High Temperature Deformation Mechanisms and Strain Heterogeneities in Calcite rocks

by

Lili Xu

Submitted to the Department of Earth, Atmospheric, and Planetary Sciences
in partial fulfillment of the requirements for the degree of

DOCTOR OF PHILOSOPHY

at the

MASSACHUSETTS INSTITUTE OF TECHNOLOGY

September 2008

Signature of Author: _____

Department of Earth, Atmospheric and Planetary Sciences

July 10, 2008

Certified by: _____

J. Brian Evans

Professor of Geophysics

Thesis Supervisor

Accepted by: _____

Maria Zuber

E.A. Griswold Professor of Geophysics

Department Head

High Temperature Deformation Mechanisms and Strain Heterogeneities in Calcite rocks

by
Lili Xu
Submitted to the Department of
Earth, Atmospheric and Planetary Sciences
on August 4th, 2008 in partial fulfillment of
the requirements for the degree of
Doctor of Philosophy

Abstract

In nature, carbonates often accumulate large amounts of strain in localized shear zones. Such marble sequences play a key role in crustal deformation processes. Despite extensive field and laboratory investigation, many questions remain concerning the mechanical behavior of these rocks. For example, the mechanical behavior of different limestones and marbles differ greatly, possibly owing to the presence of chemical impurities or solid-solutes. Thus, Chapter 2 examines the effect of Mg solute, a common impurity, on the mechanical behavior of calcite rocks. The results indicate that increasing Mg content increases the strength of calcite rocks during dislocation creep. The anisotropic nature of crystal slip usually entails variations in reorientation of individual grains and heterogeneous deformation within the polycrystalline material. In Chapter 3, a new technique including a series of sample preparation and image analysis algorithms is developed to provide quantitative measurements of the scale of heterogeneities produced, and to gain fundamental insight into polycrystalline plasticity. We place particular attention on quantifying variations of strain within grain interiors and at grain boundaries, and on recognizing the relative activities of different slip systems. The quantification of grain-to-grain interactions during straining is relevant for the improvement and verification of models of polycrystalline plasticity. The strain measurements obtained from Chapter 3 are compared with predictions of grain strain and reorientation obtained from the self-consistent viscoplastic method (Chapter 4). The results suggest that the self-consistent model gives a good description of global texture, but does not always predict lattice rotation and deformation within individual grains. To predict the actual deformation of individual grains will require a quantitative consideration of the effects on local strain of grain-boundary misorientation, local strain/stress state, grain-boundary sliding, and deviations in grain geometry.

Thesis Supervisor: J. Brian Evans
Title: Professor of Geophysics

Contents

6

Chapter 1: Background, Context, and Goals

1.1. Understanding and predicting the mechanical behavior of carbonate rocks

1.1.1 Relating laboratory measurements into natural conditions

In many orogenic belts, carbonate formations accumulate large strains along localized shear zones that involve deformation by non-cataclastic processes. Owing to the extreme localization, the deformation of these marble sequences must play a key role in the overall energy budget of orogenic events. For deformation by crystal plastic processes, forward predictions of strength can be made using constitutive laws measured in the laboratory, provided that appropriate thermodynamic conditions are carefully controlled, and that the same deformation mechanisms operated both in nature and the laboratory (see reviews by Kohlstedt et al., 1995; Paterson, 2001; Ranalli and Murphy, 1987).

Given the extensive field and experimental studies of calcite rocks, we can compare the mechanical data for various limestones and marbles. Interestingly, when the power-law creep description is used, the parameters determined for different calcite rocks differ greatly (see review by Renner and Evans, 2002). Many experimental tests have been duplicated indicating that this difference does not result from experimental artifacts. The extrapolated strain rates can vary by more than three orders of magnitude at a given stress and temperature (Brodie and Rutter, 2000; Kohlstedt et al., 1995). The lack of a general constitutive law is of great concern when extrapolating the flow laws to geological conditions and reconstructing paleo-deformation conditions from microstructural imprints. Resolving the differences among the various experimental

11

studies on different aggregates can contribute to a better understanding of the dynamics

shaping the continental crust.

1.1.2 Deformation mechanism of calcite

From laboratory experiments of calcite rocks, three major regimes of plastic flow have

been delineated (Fig. 1) (Rutter, 1974; Schmid, 1977; Schmid et al., 1980; Walker et al.,

1990). There is a low-temperature plasticity or power-law breakdown regime; a regime of

higher-temperature creep where recovery, cross slip (de Bresser and Spiers, 1993), and

boundary sliding are important (Walker et al., 1990); and a highest-temperature,

low stress regime where diffusion creep and grain-boundary sliding dominate (Schmid,

1977; Schmid et al., 1980; Walker et al., 1990).

In this thesis, I use the term "creep" to refer to any situation in which inelastic strain

occurs during prolonged loading. That term can apply to deformation by any mechanism,

by any defect, whatsoever, as long as the material exhibits a non-zero inelastic

deformation rate under a prolonged load. Both the power law equation and the power-law

breakdown equation include thermal activation terms, and in general, any mechanical

constitutive law that includes Boltzmann kinetics will exhibit creep behavior. Sometimes,

the power-law breakdown equation is called "plasticity". But "plastic" strictly means that

there is no sensitivity of strength to strain rate, and although the sensitivity of strength to

strain rate in the power-law breakdown mechanism is reduced from the power law case, it

is never zero.

1.1.3 Crystallography of calcite

The primitive unit cell of calcite single crystal is trigonal (rhombohedral or 'R'), and the point group is R$\bar{3}$c. Although triply degenerate, a structural hexagonal unit cell with a = 4.99 $\overset{\circ}{A}$ and c = 17.06 $\overset{\circ}{A}$ is most commonly used. Planes are represented by four-digit Miller-Bravais indices (hkil), where i=-(h+k). At temperatures lower than 0.3 T_m, plastic deformation in this material is due to the glide of dislocations on crystallographic slip planes which cause displacements in the direction of the dislocation Burgers vector. Figure 2 shows the stereographic projection of calcite showing the most important slip planes and directions in calcite. The intracrystalline deformation mechanism is very important in natural deformation of marble and limestone; and the development of crystallographic preferred orientation (CPO) and texture has been widely studied in both laboratory and field settings. The texture developed during crystal plastic deformation requires specification of all potential slip and twinning systems and the critical resolved shear stress (CRSS), i.e., the shear stress on the slip plane resolved in the slip direction necessary to produce dislocation motion. For a given uniaxial applied stress, the resolved shear stress is related to a geometric function called the Schmid factor, $S = \cos\theta \cdot \cos\varphi$ (Azuma & Higashi 1985), where θ is the angle between the direction of the applied force and normal to the slip plane, and φ is the angle between the applied force and the slip direction (Burgers vector).

1.2. Methodology and laboratory experiments

1.2.1 Conventional triaxial testing apparatus

Our experimental studies were conducted in a gas-medium apparatus (Paterson Instruments), equipped with an internal furnace and a servo-controlled pore-pressure system (Paterson, 1990). Displacement of the axial loading piston is quantified using a linear variable differential transformer (LVDT), which can detect a minimum displacement increment of 0.3 µm, i.e., a minimum detectable strain increment of 1.5×10^{-5}. The load is measured internally with uncertainty of 20 N (i.e., about 0.3 MPa in axial stress). The strength of the metal shell (iron/copper) at the experimental conditions was taken into account (Frost and Ashby, 1982). The absolute uncertainty in stress owes to uncertainties in the load cell readings, sample diameter, and jacket correction, but is low (on the order of 1 MPa). When two experiments are compared, differences between the nominal and actual temperature of ±2 K probably add the same order of magnitude in uncertainty in strength. Most of samples were subjected to a confining pressure of 300 MPa. Samples were deformed either at constant strain rate or by stepping intervals of loading at constant stresses. Temperatures ranged between 400 and 850ºC. When stepped loading intervals were applied, stress was successively increased, but, occasionally, low-stress conditions were revisited.

1.2.2 Description of microscope and imaging technique

The dislocation structures introduced by the deformation were observed using a transmission electron microscope (TEM, JEOL-200cx). TEM uses electrons as

low wavelength "light source" to achieve much better resolution than obtained with a standard light microscope. In Chapter 2, thin sections made from the as-deformed samples of Mg-calcites were examined first using an optical microscope and then ion-thinned to make TEM samples. Dislocation structures were studied and dislocation densities were measured using the foil intercept length method (Underwood, 1970, p.170, equation (6.10)).

Despite the lower resolution of optical microscopy, the observation of deformed samples in reflected and transmitted light is a useful and efficient method to measure grain shapes, grain sizes, and other microstructures. In Chapter 3, we used a Hirox KH-7700 digital optical microscope to study the surface topography developed during the deformation of an originally planar surface. This microscope takes images from different focal planes and digitally merges them into a single image with an extended depth of focus. This can be done manually by taking multiple images manually at different focal planes and merging them, or automatically by setting upper and lower limits of focal planes and specifying the number of images to be captured in-between. The through-focus images provide surface elevation data. In Chapter 3, sample surfaces of Carrara marble were marked with a grid of Au/C spots. 2D gray-scale images and a through-focus series of micrographs of the surfaces before and after deformation were collected in the digital microscope at a magnification of 700x, using reflected light with crossed polarizers.

Grain orientation data is obtained from electron back-scattered diffraction (EBSD)

patterns using a JEOL 840 scanning electron microscope (SEM). The diffraction patterns are used to measure crystal orientation. When the beam is scanned in a grid across a polycrystalline sample and the crystal orientation is measured at each point, the resulting map will reveal the constituent grain morphology, orientations, and boundaries. EBSD data can also be used to show the preferred crystal orientations (texture) in the material. EBSD patterns of deformed/undeformed Carrara marble samples were obtained (Chapter 4) and automatically indexed using the program Channel 5 from HKL software. This program searches for an indexing solution: a lattice orientation, for the mineral structure input into the program. Maps of orientation data can be processed to remove erroneous data and provide a more complete microstructural reconstruction of the sample.

1.3. Thesis overview

Natural carbonate rocks show variations in strength that may arise from differences in grain size, accessory minerals, porosity, or chemical impurities. These variations are of great concern when extrapolating flow laws into natural conditions or reconstructing paleo-deformation conditions from the interpretation of microstructures. For example, non-soluble, solid second phases can suppress grain growth by boundary pinning and change the overall strength of material (Evans et al., 2001; Knipe, 1980; Olgaard and Evans, 1988; Tullis and Yund, 1982). If solid solution is possible, dissolved impurities could also affect grain-growth kinetics and creep behavior (Freund et al., 2001; Freund et al., 2004; Herwegh et al., 2003; Tetard et al., 1999). Mg is one, among several, possible cation solutes in calcite rocks, e.g., Mn, Fe, Sr; and these solutes may affect the creep

behavior, as briefly demonstrated by de Bresser (1991).

In chapter 2, we studied the influence of Mg solute impurity on grain-growth and the high-temperature creep of calcite aggregates. Synthetic samples of Mg-calcites were prepared from reaction-grade powders of calcite and dolomite. The hot isostatic pressing (HIP) treatment resulted in high-magnesium calcite aggregates with Mg content ranging from 0.5 to 17 mol%. Both back-scattered electron images and chemical analysis suggested that the dolomite phase was completely dissolved, and that Mg distribution was homogeneous throughout the samples at the micron scale. Grain size and time were related using a normal grain growth equation, with exponents from 2.5 to 4.7, for samples containing 0.3 to 17.0 mol% Mg, respectively. The deformation data indicated a transition in mechanism from diffusion creep to dislocation creep. At stresses below 40 MPa, the strength was directly proportional to grain size and decreased with increasing Mg content due to the reductions in grain size. At about 40 MPa, the sensitivity of log strain rate to log stress, (n), became greater than 1 and eventually exceeded 3 for stresses above 80 MPa, the stress at which that transition occurred was larger for samples with higher Mg content and smaller grain size. For constant strain rate and fixed grain size, the strength of calcite in the dislocation creep regime increased with solute content, while the strength in the diffusion creep regime was independent of Mg content.

The crystal-plastic deformation of rocks in the laboratory is also often inhomogeneous at the microstructure scale, a particular example being given by the extensive studies of microstructures and mechanical behaviors of Carrara marble (Pieri et al., 2001b; Rutter,

1974; Rutter, 1998; Rutter et al., 1994; Schmid et al., 1980).   In this material, grains favorably orientated for slip deformation clearly deform more than other grains in the harder orientations (Wenk, 2002; Wu et al., 2006).   The quantification of grain-to-grain interactions during straining is relevant for the improvement and verification of models of polycrystalline plasticity.   Such models are valuable for understanding the textures produced during deformation of complex, polycrystalline materials with multiple phases, i.e., rocks. One method in particular, the self-consistent model, has been widely used to understand the texture development of materials during plastic deformation (Lebensohn and Tome, 1993; Molinari et al., 1987; Wenk et al., 1987).   The comparison of results from such experiments and simulations will provide useful insight into the accuracy and efficacy of the polycrystalline homogenization models and constrain our knowledge of the physics of inelastic deformation (Chapters 3 and 4, Fig. 3).

In Chapter 3, the spatial distribution of strain heterogeneity during the plastic deformation of Carrara marble is studied. Cylindrical samples of Carrara marble were drilled and machined from a block of the Lorano Bianco variety, a proposed laboratory standard (Pieri et al., 2001a). Strain development during deformation of Carrara marble was studied at the local microstructure scale using a high resolution surface mapping technique. This technique uses grid markers and computerized image analysis to evaluate local strain heterogeneity. The image processing technique gives us a high accuracy of strain measurement. This method is based on: (1) depositing grid markers on the polished surface of a half-cylinder of Carrara marble, (2) performing conventional triaxial

compression tests on composite samples of two half-cylinders, (3) comparing the positions of each grid marker in both undeformed and deformed samples, and (4) computing micro-scale strain distributions (Fig. 3). Our results show large heterogeneities of strain at the microstructural scale. The minimum and maximum local strain can vary by a factor of 3 or more from the mean imposed strains. In general, strain distributions within the grain interiors are more homogeneous than those in vicinity of grain-boundaries. Deformation is clearly localized at both twin and grain boundaries, indicating a strong influence of microstructure on the local strain distribution. The variation of strain averaged over individual grains is less than that measured locally within grains, indicating that grain boundaries are important in accommodating strain incompatibility between neighboring grains. This study also suggested that grain-boundary sliding may be active at a temperature of ~600ºC.

EBSD measurements were analyzed in Chapter 4, where we applied visco-plastic self consistent (VPSC) techniques to model the texture development in the compression tests. The VPSC models were used to understand the active slip systems in compressional tests. In agreement with earlier studies, our results suggested a dominant activation of r<sd> slip system at these conditions. Individual grains were tracked before and after deformation to study the change of crystallographic orientations due to deformation process. The changes of orientations of individual grains measured by EBSD were compared to results simulated by VPSC modeling. Even when three separate CRSS models are used, only a small number of grains can be successfully predicted by the

VPSC simulation, suggesting that models using a simple homogeneous effective medium theory (HEM) cannot predict local microstructures effectively.   Changing the CRSS of different slip systems may change the predicted grain rotation behavior significantly, and might improve the reliability of VPSC modeling in predicting the deformation behavior of single crystals within polycrystals, but intragranular heterogeneities will not be captured by this modeling.

1.4. References

Bestmann, M. and Prior, D.J., 2003. Intragranular dynamic recrystallization in naturally deformed calcite marble: Diffusion accommodated grain-boundary sliding as a result of subgrain rotation recrystallization. Journal of Structural Geology, 25(10): 1597-1613.

Brodie, K.H. and Rutter, E.H., 2000. Deformation mechanisms and rheology: Why marble is weaker than quartzite. Journal of the Geological Society, 157: 1093-1096.

de Bresser, J.H.P., 1991. Intracrystalline deformation of calcite. Geologia Ultrajectina 79: 1-191.

de Bresser, J.H.P. and Spiers, C.J., 1993. Slip systems in calcite single-crystals deformed at 300-800-degrees-c. Journal of Geophysical Research-Solid Earth, 98(B4): 6397-6409.

Evans, B., Renner, J. and Hirth, G., 2001. A few remarks on the kinetics of static grain growth in rocks. International Journal of Earth Sciences, 90(1): 88-103.

Freund, D., Rybacki, E. and Dresen, G., 2001. Effect of impurities on grain growth in synthetic calcite aggregates. Physics and Chemistry of Minerals, 28(10): 737-745.

Freund, D., Wang, Z.C., Rybacki, E. and Dresen, G., 2004. High-temperature creep of synthetic calcite aggregates: Influence of Mn-content. Earth and Planetary Science Letters, 226(3-4): 433-448.

Frost, H.J. and Ashby, M.F., 1982. Deformation-mechanism maps: The plasticity and creep of metals and ceramics. Pergamon Press, Oxford.

Herwegh, M., Xiao, X.H. and Evans, B., 2003. The effect of dissolved magnesium on diffusion creep in calcite. Earth and Planetary Science Letters, 212(3-4): 457-470.

Knipe, R.J., 1980. Distribution of impurities in deformed quartz and its implications for deformation studies. Tectonophysics, 64(1-2): T11-T18.

Kohlstedt, D.L., Evans, B. and Mackwell, S.J., 1995. Strength of the lithosphere - constraints imposed by laboratory experiments. Journal of Geophysical

Research-Solid Earth, 100(B9): 17587-17602.

Lebensohn, R.A. and Tome, C.N., 1993. A self-consistent anisotropic approach for the simulation of plastic-deformation and texture development of polycrystals - application to zirconium alloys. Acta Metallurgica Et Materialia, 41(9): 2611-2624.

Molinari, A., Canova, G.R. and Ahzi, S., 1987. A self-consistent approach of the large deformation polycrystal viscoplasticity. Acta Metallurgica, 35(12): 2983-2994.

Olgaard, D.L. and Evans, B., 1988. Grain-growth in synthetic marbles with added mica and water. Contributions to Mineralogy and Petrology, 100(2): 246-260.

Paterson, M.S., 1990. Rock deformation experimentation. Geophysical Monograph, 56(Rock deformation experimentation): 187-194.

Paterson, M.S., 2001. Relating experimental and geological theology. International Journal of Earth Sciences, 90(1): 157-167.

Pieri, M., Burlini, L., Kunze, K., Stretton, I. and Olgaard, D.L., 2001a. Rheological and microstructural evolution of Carrara marble with high shear strain: Results from high temperature torsion experiments. Journal of Structural Geology, 23(9): 1393-1413.

Pieri, M., Kunze, K., Burlini, L., Stretton, I., Olgaard, D.L., Burg, J.P. and Wenk, H.R., 2001b. Texture development of calcite by deformation and dynamic recrystallization at 1000 k during torsion experiments of marble to large strains. Tectonophysics, 330(1-2): 119-140.

Ranalli, G. and Murphy, D.C., 1987. Rheological stratification of the lithosphere. Tectonophysics, 132(4): 281-295.

Renner, J. and Evans, B., 2002. Do calcite rocks obey the power-law creep equation? . S. de Meer, M.R. Drury, J.H.P. de Bresser and G.M. Pennock (Editors), Deformation mechanisms, rheology and tectonics: Current status and future perspectives. , Geological Society, London.: 293-307.

Rutter, E.H., 1974. Influence of temperature, strain rate and interstitial water in experimental deformation of calcite rocks. Tectonophysics, 22(3-4): 311-334.

Rutter, E.H., 1998. Use of extension testing to investigate the influence of finite strain on the rheological behaviour of marble. Journal of Structural Geology, 20(2-3): 243-254.

Rutter, E.H., Casey, M. and Burlini, L., 1994. Preferred crystallographic orientation development during the plastic and superplastic flow of calcite rocks. Journal of Structural Geology, 16(10): 1431-1446.

Schmid, S.M., 1977. Superplastic flow in fine-grained limestone. Tectonophysics, 43(3-4): 257-291.

Schmid, S.M., Paterson, M.S. and Boland, J.N., 1980. High temperature flow and dynamic recrystallization in Carrara marble. Tectonophysics, 65(3-4): 245-280.

Tetard, F., Bernache-Assollant, D. and Champion, E., 1999. Pre-eutectic densification of calcium carbonate doped with lithium carbonate. Journal of Thermal Analysis and

Calorimetry, 56(3): 1461-1473.

Tullis, J. and Yund, R.A., 1982. Grain-growth kinetics of quartz and calcite aggregates. Journal of Geology, 90(3): 301-318.

Underwood, E.E., 1970. Quantitative stereology [by] ervin e. Underwood. . Addison-Wesley series in metallurgy and materials

Walker, A.N., Rutter, E.H. and Brodie, K.H., 1990. Experimental study of grain-size sensitive flow of synthetic, hot-pressed calcite rocks. In: R.J. Knipe and E.H. Rutter (Editors), Deformation mechanisms, rheology and tectonics. Geological Society Special Publications, pp. 259-284.

Wenk, H.R., 2002. Texture and anisotropy, Plastic deformation of minerals and rocks. Reviews in mineralogy & geochemistry, pp. 291-329.

Wenk, H.R., Takeshita, T., Bechler, E., Erskine, B.G. and Matthies, S., 1987. Pure shear and simple shear calcite textures - comparison of experimental, theoretical and natural data. Journal of Structural Geology, 9(5-6): 731-745.

Wu, A., De Graef, M. and Pollock, T.M., 2006. Grain-scale strain mapping for analysis of slip activity in polycrystalline b2rual. Philosophical Magazine, 86(25-26): 3995-4008.

1.5. Figures
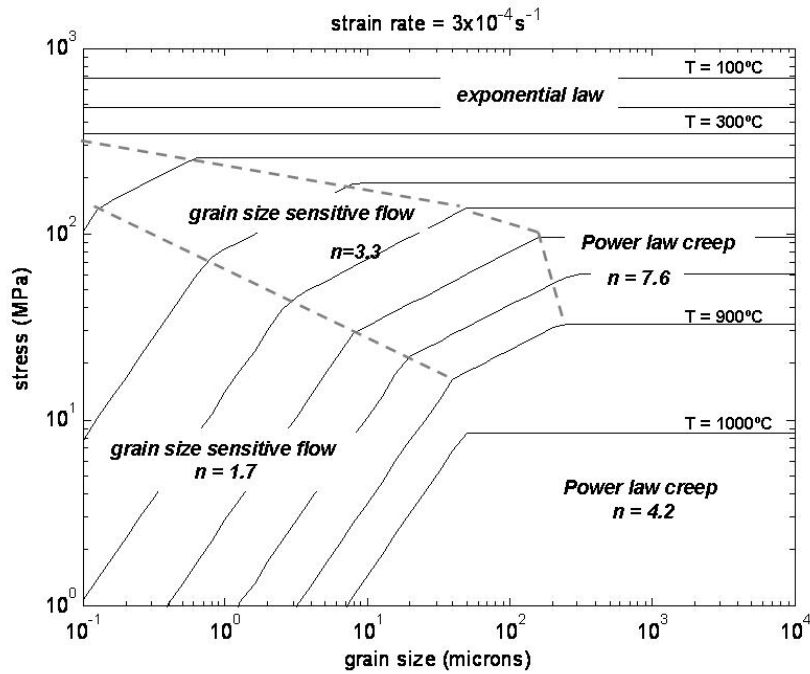
Figure 1. Deformation mechanism map of calcite for constant shear strain rate of $3 \times 10^{-4} s^{-1}$ with temperature contour at 100 k intervals. Figure after Schmid et al., (1980) and Walker et al., (1990).

twinning systems

e'{1̄018}<404̄1>

r'{101̄4}<2̄021>

f{1̄012}<101̄1̄>

slip systems

r⁺{101̄4}<2̄021>

r{101̄4}<1̄21̄0>*

r"{101̄4}<202̄1̄>

f{1̄012}<22̄01>

f⁺{1̄012}<101̄1>

f'{1̄012}<2̄201̄>
<022̄1>

f"{1̄012}<22̄01>
<02̄21̄>

c(0001)<1̄21̄0>

a{1̄21̄0}<2̄021>

m{101̄0}<1̄21̄0>
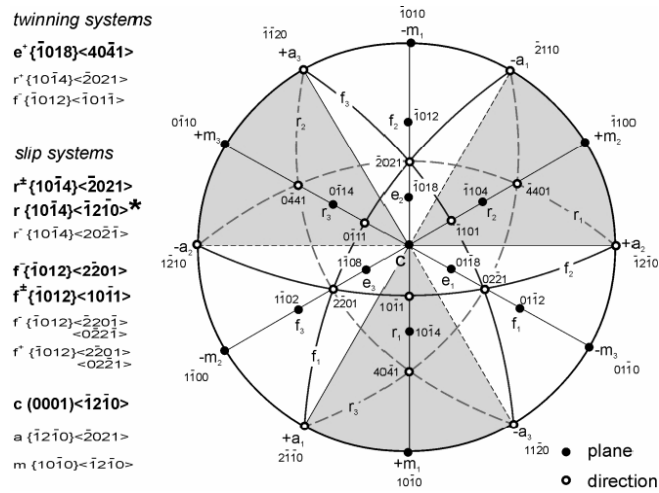
Figure 2. Stereographic (upper hemisphere, equal angle) projections of calcite showing the important planes and directions, including the known slip systems (de Bresser and Spiers, 1993). Bold letters highlight important slip systems. Asterisk indicates a slip system proposed by Pieri et al (2001b), but not experimentally verified. Shading illustrates trigonal symmetry point group 3̄m of calcite (image from Fig. 1, Bestmann and Prior, 2003).

surface topography
(3D digital microscope)

3D grid position
(image analysis)

surface straining mapping
(3-point strain analysis)

grain orientation
(electron back-scattered diffraction pattern)

preferred orientation simulation
(VPSC modeling)
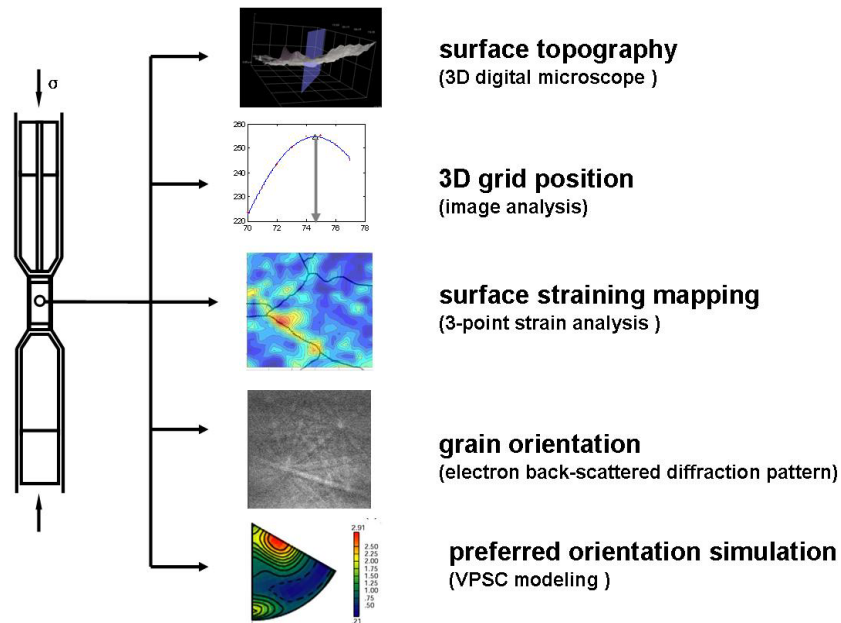
Figure 3. Flow chart of the data processing procedure including (1) 3D surface topography from 3D digital microscope, (2) grid marker position determination using image analysis techniques, (3) strain distribution mapping from n-point strain analysis technique, (4) grain orientation from electron back-scattered diffraction pattern, and (5) texture analysis using visco-plastic self consistent modeling. Procedures (1-3) and (4-5) are main topics of Chapters 3 and 4, respectively.

Chapter 2: The effect of dissolved magnesium on creep of calcite:

Transition from diffusion creep to dislocation creep

Lili Xu

Jörg Renner

Marco Herwegh

Brian Evans

Abstract

We extended a previous study on the influence of Mg solute impurity on diffusion creep in calcite to include deformation under a broader range of stress conditions and over a wider range of Mg contents. Synthetic marbles were produced by hot isostatic pressing (HIP) mixtures of calcite and dolomite powders for different intervals (2 to 30 hrs) at 850ºC and 300 MPa confining pressure. The HIP treatment resulted in high-magnesian calcite aggregates with Mg content ranging from 0.5 to 17 mol%. Both back-scattered electron images and chemical analysis suggested that the dolomite phase was completely dissolved, and that Mg distribution was homogeneous throughout the samples at the scale of about two micrometers. The grain size after HIP varied from 8 to 31 μm, increased with time at temperature, and decreased with increasing Mg content (> 3.0 mol%). Grain size and time were consistent with a normal grain growth equation, with exponents from 2.4 to 4.7, for samples containing 0.5 to 17.0 mol% Mg, respectively. We deformed samples after HIP at the same confining pressure with differential stresses between 20 and 200 MPa using either constant strain rate or stepping intervals of loading at constant stresses in a Paterson gas-medium deformation apparatus. The deformation tests took place at between 700-800 ºC and at strain rates between 10^{-6} and $10^{-3} \, s^{-1}$. After deformation to strains of about 25%, a bimodal distribution of large protoblasts and small recrystallized neoblasts coexisted in some samples loaded at higher stresses. The deformation data indicated a transition in mechanism from diffusion creep to dislocation creep. At stresses below 40 MPa, the strength was directly proportional to grain size and decreased with increasing Mg content due to the reductions in grain size. At about 40 MPa, the sensitivity of log strain rate to log stress, (n), became greater than 1 and eventually exceeded 3 for stresses above 80 MPa. At a given strain rate and temperature, the stress at which that transition occurred was larger for samples with higher Mg content and smaller grain size. At given strain rates, constant temperature,

and fixed grain size, the strength of calcite in the dislocation creep regime increased with solute content, while the strength in the diffusion creep regime was independent of Mg content. The results suggest that chemical composition will be an important element to consider when solid substitution can occur during natural deformation.

2.1. Introduction

In many orogenic belts, carbonate formations accumulate large strains along localized shear zones that involve deformation by non-cataclastic processes (Bestmann et al., 2000; Burkhard, 1990; Burkhard, 1993; Busch and Vanderpluijm, 1995; Carter, 1992; Heitzmann, 1987; Herwegh and Kunze, 2002; Molli et al., 2000; Molli and Heilbronner, 1999; Pfiffner, 1982; Schenk et al., 2005; Vanderpluijm, 1991; Yin, 1996). Owing to the extreme localization, the deformation of these marble sequences must play a key role in the overall energy budget of orogenic events.

Despite extensive field and laboratory investigations (Covey-Crump, 1998; Covey-Crump, 2001; de Bresser and Spiers, 1993; de Bresser et al., 2001; Goetze and Kohlstedt, 1977; Griggs and Miller, 1951; Heard, 1963; Heard and Raleigh, 1972; Renner et al., 2002; Rutter, 1972; Rutter, 1999; Spiers, 1979; Walker et al., 1990), many questions remain concerning the exact rheology appropriate to describe natural deformation of carbonates (de Bresser et al., 2002). Various studies have focused on mechanical behavior at large strains (Barnhoorn et al., 2004; Pieri et al., 2001; Rybacki et al., 2003), the influence of porosity and pore fluids on deformation (de Bresser et al., 2005; Heard, 1960; Rutter, 1972; Rutter, 1984; Siddiqi et al., 1997; Xiao and Evans, 2003; Zhu et al., 1999), and the effect of solid second phases on strength (Bruhn et al., 1999; Dresen et al., 1998; Jordan, 1987; Olgaard and Evans, 1986; Renner et al., 2007; Rybacki et al., 2003; Walker et al., 1990).

In this study, we investigated the strength of high-magnesium calcite of varying Mg

contents. We preformed deformation experiments using both creep and constant displacement rate loading at temperatures between 700 and 800°C, in a conventional triaxial machine at a confining pressure of 300 MPa and at strain rates between 10^{-6} and 10^{-3} s^{-1}. The conditions of these experiments are similar to those previously reported by Herwegh et al. (2003), but the current data were collected over an increased range of differential stresses -- up to 200 MPa and over a slightly wider range of chemical compositions. About 80 creep experiments were performed on 17 different synthetic calcite samples with Mg contents ranging from 0.5 to 17.0 mol%. Previous work suggested that deformation under these conditions of stress, temperature, and pressure occurs by a combination of diffusion creep and dislocation creep (Herwegh et al., 2003; Walker et al., 1990). The contribution to deformation by dislocation motion becomes much larger as the differential load increases. We do not attempt to provide a complete rheological description of deformation by all dislocation mechanisms (see discussion by Davis et al., 2005; de Bresser, 2002; Renner and Evans, 2002), but instead we focus on the relative effect of the impurity content on strength during dislocation deformation and on the conditions at which the transition between diffusion creep and dislocation creep occurs. In order to separate the contributions of diffusion and dislocation creep mechanisms, a composite flow law was fit to the data using a non-linear inversion technique. We also performed additional grain-growth experiments under hydrostatic loading to investigate further the effect of solute impurities on growth kinetics.

2.1.1 Solid solutes and physical properties

Minerals often contain impurities that substitute in varying amounts for the usual ion expected from the chemical formula (Nesse, 2000; Wenk and Bulakh, 2004). In such cases, the impurity ions are solutes, dissolved into the crystal lattice, and when the impurities take the place of one of the stoichiometric ions, the mineral can be regarded as a substitutional solid solution. For example, natural carbonates often contain varying amounts of divalent impurity cations, for example, Fe, Mg, Mn, and Sr, which substitute for Ca (Essene, 1983; Mackenzie et al., 1983). The physical properties of ceramics and semiconductors, including grain-boundary mobility, diffusion coefficients, electrical conductivity, and strength are known to be very strongly affected by solid solutes (e.g., Chiang et al., 1997; Lücke and Stüwe, 1971), and similar effects may be evident in mineral solid solutions (Bai et al., 1995; Hiraga et al., 2007; Hitchings et al., 1989; Hobbs, 1984; Kohlstedt, 2006). For example, the solution of Fe in forsterite increases the creep rate under anhydrous conditions by factors of as much as 1400 times (Zhao et al., in press, 2008).

Some studies intimate that the physical properties of carbonates will also be strongly affected by solid solutes. Natural carbonate rocks tested in the laboratory are often stronger than synthetic ones, which likely contain fewer impurities (Heard and Raleigh, 1972; Renner et al., 2002; Rutter, 1974; Schmid, 1977; Schmid et al., 1980; Walker et al., 1990). Freund and co-workers (Freund et al., 2001; Freund et al., 2004; Wang et al.,

1996) have suggested that trace amounts of dissolved Mn (10–670 ppm) decrease the strength of calcite during both dislocation and diffusion creep, although the effect in the former regime may be small.   Larger amounts of dissolved Mg do not directly affect the flow strength of the calcite aggregates in the diffusion creep regime (Herwegh et al., 2003), but, in those experiments, high Mg content correlated with smaller grain size, and this, in turn, is expected to reduce the aggregate strength during Coble creep.   Mn and Mg solutes also have opposite effects on normal grain growth of calcite.   The addition of Mn (less than 670 ppm) increases growth rates (Freund et al., 2001), but the addition of Mg (>7 mol%) decreases boundary mobility (Herwegh et al., 2003).

2.1.2 Rheological descriptions of diffusion and dislocation creep:

Here we are interested in the effect of solute impurities on the creep behavior of calcium carbonate rocks.   For deformation by non-cataclastic (crystal-plastic) processes, forward predictions of the strength of naturally deformed rocks can be made using constitutive laws calibrated by laboratory experiments, provided that appropriate thermodynamic conditions are simulated and controlled, and that the deformation mechanisms that operate in the experiments are also relevant to the geological processes (Kohlstedt et al., 1995; Paterson, 1976; Paterson, 2001; Ranalli and Murphy, 1987).   For a general framework of constitutive laws, see Frost and Ashby (1982).   The deformation mechanisms involved are probably, in general, sensitive to strain rate and temperature and have variously been termed crystal plasticity; ductile, viscous, plastic deformation; or

creep. To emphasize the effect of prolonged loading, we use the generic term, creep deformation, to refer to all rate-dependent deformation occurring by motion of any crystal defect.

Three classes of equations are commonly used to represent steady-state creep of rocks. At high temperatures, small grain sizes, and/or low stresses, rocks may deform by diffusion creep:

$$\dot{\varepsilon}_{diff} = \dot{\varepsilon}_{diff\,o} \frac{\sigma^r}{d^s} \exp\left(-\frac{Q_{diff}}{RT}\right) \tag{1}$$

where r is usually nearly equal to 1, s may be 1-3, Q_{diff} is the activation enthalpy for self-diffusion of the slowest constituent of the mineral along the fastest available path, and $\dot{\varepsilon}_{diff\,o}$ is a factor that may be weakly dependent on temperature or more strongly dependent on details of the point defect chemistry.

As temperatures decrease, or grain size and stresses increase, the creep deformation will be dominated by dislocation motion. The most common constitutive equation used to describe dislocation creep in rocks at elevated temperature and slow strain rates is the power-law equation:

$$\dot{\varepsilon}_{pwr} = \dot{\varepsilon}_{pwro} \sigma^n \exp\left(-\frac{Q_{pwr}}{RT}\right) \tag{2}$$

where $\dot{\varepsilon}_{pwr0}$ is a pre-exponential factor, perhaps containing a dependence on chemical fugacity; σ is the differential stress; $n = \partial \ln \dot{\varepsilon} / \partial \ln \sigma$ is the stress exponent of strain rate;

RT is the standard Boltzmann term, with gas constant, *R*, and absolute temperature, *T*;

and $Q_{pwr} = -R\partial \ln \dot{\varepsilon} / \partial (1/T)$ is the activation enthalpy for creep.

At low-temperatures, high stresses or fast strain rates (as defined by Frost and Ashby, 1982), creep deformation may be limited either by cross-slip (de Bresser and Spiers, 1993) or dislocation glide (Renner and Evans, 2002). The latter authors used an empirical equation for the power-law breakdown region of the form:

$$\dot{\varepsilon}_{plb} = A_{plb} \sigma^2 \exp\left(\frac{\sigma}{\sigma_p}\right) \exp\left(-\frac{Q_{plb}}{RT}\right) \tag{3}$$

where A_{plb} is a material constant, Q_{plb} is the activation energy for dislocation creep, and $\sigma_p = \left(\Sigma_{p,0} + Kd^{-m_p}\right)\left(T_m - T\right)$ is the resistance to glide, which is composed of an intrinsic Peierls stress and a grain-size dependent back stress. T_m denotes the melting temperature (Renner et al., 2002). Several other formulations for stress-activated deformation might also be used (Renner and Evans, 2002), and we do not regard this formulation as definitive. In this study, we use (3) as an empirical fit to data in the dislocation creep regime, but suggest caution in using this creep law to extrapolate to natural conditions.

In the discussion below we identify these regimes as diffusion creep, high-temperature dislocation creep, and low-temperature dislocation creep, respectively. The low-temperature creep equation is sometimes called plastic, but, in fact, all three equations can be said to be creep equations because they each predict a non-zero inelastic

34

strain rate under prolonged load. Some caution in using the equations is appropriate, however. Diffusion creep of carbonates at high temperatures seems to be described well by Eq. (1), but the high-temperature dislocation creep equation (2) does not accurately represent the mechanical behavior over a significant range of conditions (see reviews by de Bresser, 2002; Walker et al., 1990). For example, n values found by fitting data to (2) are usually between 3 and 9, but these values increase with increasing stress and are not constant even over small intervals in stress. Eq. (3) is successful in fitting most of the experimental data for several calcite rocks, but it is largely empirical. In fact, none of the current constitutive models are capable of adequately explaining all the details of the mechanical behavior for dislocation creep of carbonate rocks. Further work is needed to formulate a set of robust constitutive equations, which are firmly based on observable microstructure variables and fundamental microphysics. Because of this uncertainty, in the following discussion, we may often simply refer to deformation by dislocation motion, as dislocation creep, without making a distinction between high and low temperature regimes.

2.2. Methodology of experiments

2.2.1 Sample preparation and apparatus

Samples were prepared from mixtures of reagent-grade calcite powder (5 μm grain size, Mallinckrodt Inc.) and ground natural dolomite powder (Microdol Super from Alberto Luisoni Mineralstoffe; 2 μm grain sizes). The hot isostatic pressing (HIP) technique

was described in detail previously (Herwegh et al., 2003; Renner et al., 2002). Powders were mixed in proportions to produce marbles with magnesium solute contents (after HIP) of 0.5, 3.0 to 17.0 mol% (Fig. 1). The different Mg-calcites will be referred to as Mgcc-20, -40, …, -80, where the numbers indicate the temperature at which the solid-solution is at saturation (e.g., Mgcc-20 has 0.5 mol% Mg dissolved in the calcite lattice; calcite with that composition is saturated in Mg at 200°C). After mixing, powders were dried in an oven at 110°C and cold-pressed into thin-walled (0.3 mm) iron shells using a uniaxial stress of about 100 MPa. The cold-pressed aggregates, whose initial porosity was about 25%, were dried overnight and then loaded into an iron jacket along with Al_2O_3 and ZrO_2 pistons (Fig. 2).

2.2.2 HIP

To fabricate the synthetic marbles, the sample assembly was pressurized to about 225 MPa and then heated to 850°C at a rate of 15°C/min in an internally heated Paterson apparatus (Paterson, 1990). The HIP step lasted from 2 to 30 hrs at 850°C and 300 MPa confining pressure. To monitor densification, we applied an axial stress of less than 3 MPa (<0.2 KN) and measured changes in sample length during heat-up, pressurization, and the isothermal HIP. The temperature was monitored by three Pt-Pt/Rh thermocouples inserted in the furnace and by an additional chromel-alumel thermocouple reaching the top of the sample through a bore in the ceramic pistons. The temperature at the top of the sample varied less than ± 5°C throughout the experiments. Before the

experiments, we calibrated the furnace to guarantee a flat thermal profile along the sample (spatial temperature variations are estimated to be $< \pm 2°C$).

During the initial portion of the HIP, Mg-calcite is formed from the mixture of calcite and dolomite powders by a complex combination of densification, grain-boundary diffusion, volume diffusion, and chemically induced grain-boundary migration (see Herwegh et al., 2003).   During this short transition period, a dense compact aggregate of high-magnesian calcite is formed with an average grain size that is smaller than the original powder sizes.   Additional heat-treatment under isostatic stress (longer HIP time) resulted in normal grain growth.   By interrupting the HIP process at very short times, we ascertained that normal grain growth was underway after 1000s and that the average grain size of the aggregate was about 5 μm.   Ten additional HIP experiments of durations up to 18 hours were conducted to investigate normal grain growth rates.

Chemical analyses of the mixtures after HIP treatments were done in electron microprobe (JEOL JXA 733) with spatial resolution of ~2 micron through X-ray emission spectrometry.   At the scale of the probe dimensions, (~2 μm), the aggregates were spatially homogeneous.   The microprobe results provide quantitative checks on the Mg content of the synthetic marbles.   The microprobe measurements also indicate the presence of trace impurities of Fe, Mn, and Sr.   These three cations are present in amounts much less than 0.1%; i.e., concentrations that are too small to be measured very accurately in the microprobe.   Because these impurities are probably contained within the natural dolomite powder, their concentrations in the aggregates are likely to co-vary

with the Mg content.

2.2.3 Deformation Tests

We performed deformation tests on other samples immediately after the HIP step by reducing the temperature at 15°C/min to the run temperature (800, 750, or 700°C) and then allowing the thermal profile to equilibrate for about 20 min. The confining pressure was adjusted to 300 MPa, if necessary, and maintained at that value throughout the experiment. Displacement of the axial loading piston is quantified using a linear variable differential transformer (LVDT), which can detect a minimum displacement increment of 0.3 μm, i.e., a minimum detectable strain increment of 1.5×10^{-5}. The load is measured internally with uncertainty of 20 N (i.e., about 0.3 MPa in axial stress). The strength of the metal shell (iron) at the experimental conditions was taken into account using a correction procedure from Renner et al. (2002); more details of the apparatus can also be found there.

Deformation tests were done either with constant strain rate or constant stress (Table 1). Strain rates varied from $\sim 10^{-6}$ to 10^{-3} s^{-1}; and the total inelastic strain of the sample was about 20% or less for most tests. When subsequent examination indicated that the sample had barreled, the mechanical data were discarded to prevent artifacts induced by inhomogeneous deformation. The duration of a deformation test was usually less than 1 hr. After deformation, samples were unloaded first and quenched immediately after unloading by reducing the confining pressure and turning off the furnace simultaneously.

38

The temperature in the sample drops from 700 to 300° C in less than one minute. Recovery experiments in heavily deformed calcite single crystals indicate that dislocation densities are reduced by less than 20% over a period of 2 hours at 600° C (Liu and Evans, 1997). Thus, the dislocation microstructure is probably affected very little by the quench procedure.

At the end of each hydrostatic or triaxial experiment, a polished thin section was made to measure the grain size. Micrographs were recorded from optical observations made in reflected polarized light, and a tracing of the grain boundaries in the sample was made by hand, using Imagepro software and some manual adjustment. Using the software, the area of each grain was calculated, and the grain size recorded as the diameter of a circle with equivalent area. In each sample at least 300 grains were measured. To compare with previous grain growth studies that used mean intercept length (e.g., Covey-Crump, 1997; Schmid, 1977; Tullis and Yund, 1982), we also calculated the mean intercept length (D_{2D}) using equation $D_{2D} = \pi \overline{A}_{\alpha}/\overline{L}_{p}$ (Underwood, 1970, p42), where $\overline{A}_{\alpha}$ is the mean area of grains in the 2D image and $\overline{L}_{p}$ is their mean perimeter length. The sample porosity after the experiment was calculated using either a geometric method, i.e., weighing a sample with known dimensions, or by calculating the area fraction of porosity from an SEM image. Dislocation structures of HIPed and deformed samples were studied using a transmission electron microscope (TEM) operating at 200 kV.

2.3. Results

2.3.1 Microstructures formed under hydrostatic and conventional triaxial loading

After the initial period of reaction and mixing, normal grain growth occurs. Fig. 3 (a-c) shows photomicrographs of Mgcc-20, Mgcc-60, and Mgcc-80 after HIP for 2hrs at 850°C and 300 MPa. Grain boundaries are slightly curved; triple junctions have angles of approximately 120°. The grain sizes appear to be approximately in lognormal distribution (Fig. 4). The grain size after HIP increases with longer hot-pressing time and lower bulk impurity content (Mg content >3.0 mol%, Fig. 5), consistent with earlier observations (Herwegh et al., 2003). The total porosity of samples after HIP is usually between 0.5 and 1%, and does not systematically correlate with Mg content. During deformation, both grain growth and grain refinement occur (Figs. 3d-f, Fig. 4). The magnesium content in Figs. 3d-f varies in the same order as in Figs. 3a-c. The grain sizes of different samples range from 8 to 31 μm.

We did not perform detailed quantitative analysis of the dislocation structure of these samples, but cursory inspection does not indicate an obvious variation of the dislocation morphology with variations in magnesium content. Bright field TEM micrographs of a deformed sample (Mgcc-20) show free dislocations, microtwins, and dislocation networks (Fig. 6). Free dislocations of various orientations (Fig. 6a) indicate the activation of multiple slip systems. Cell structures and sub-grain boundaries (Fig. 6b) probably indicated that recovery processes, such as climb, were operating. Our starting

material has relatively low dislocation densities, well below $1 \cdot 10^{13} \text{m}^{-2}$, but those

increased during deformation to greater than $2 \cdot 10^{13} \text{m}^{-2}$. Such densities are comparable

to those in natural calcite rocks deformed in the laboratory (de Bresser, 1996; Goetze and

Kohlstedt, 1977; Schmid et al., 1980). Microtwins (Fig. 6d, < 1 µm thick) are

infrequently observed; these are usually observed in natural calcite that deformed at less

than 150°C (Burkhard, 1993).

2.3.2 Creep of High-Magnesium Calcite

If the duration of the test is short compared to the time necessary for the grain size to

evolve, then the test can be regarded as occurring at a fixed grain size. Additionally the

same creep conditions can be revisited at the beginning and end of the test (as described

immediately below). For samples with Mg content of 0.5 to 17.0 mol%, grain sizes in

the range of 20 and 12 µm could be produced by varying the HIP time intervals from 2 to

30 hrs. The strength of Mg-calcites determined from these constant strain rate tests

($\sim 3.1 \text{-} 8.5 \cdot 10^{-4}$ s^{-1} at 800°C and 300 MPa) indicated that the strength of calcite increases

with magnesium content (Fig. 7a). The strain rates are high and all these samples

deformed in dislocation creep regime.

Typical differential stress ($\sigma_1 \text{-} \sigma_3$) versus strain rate data are shown in Fig. 7b. Both

the grain size and the magnesium content affect the strength. At low strain rates, the

strength of Mg-calcite correlates with grain size, rather than Mg content; and n values are

nearly unity (Fig. 7b), consistent with previously published results. At higher strain

rates, the flow strength of calcite strongly depends on the Mg content, although the data

for the high Mg-calcites show more scatter.   In general, n values increase with stress, but

decrease with increasing Mg content at higher stresses used in these experiments.

Magnesium solute could affect the mechanical behavior of calcite in at least three ways:

first, the elastic modulus of calcite increases with increasing Mg content (Zhang and

Reeder, 1999); second, the strength of calcite in the diffusion creep regime is indirectly

affected by the suppression of grain growth (Herwegh et al., 2003); and third, Mg solutes

may interact with dislocations as individual obstacles or solute clouds.   The first two

effects and the effect of temperature can be eliminated by normalizing the strength by the

appropriate shear modulus (G) and by multiplying strain rate by $\exp(Q_{diff}/RT)\cdot d^s$, where

Q_{diff} and s are the activation energy and grain size sensitivity factor in the diffusion creep

regime (Herwegh et al., 2003) and d is the grain size.

Three distinctive regimes of mechanical behavior may be identified in Figs. 7c: First,

at low stresses, $\sigma/G <\sim 10^{-3}$, the strength is directly proportional to the cube of the grain

size and the stress exponent of strain rate, n, is about 1, behavior that we interpret to

indicate Coble creep. The normalized strain rate, $\dot{\varepsilon}_{normal} = \dot{\varepsilon} \exp(Q_{diff}/RT)d^3$, is a linear

function of normalized stress, $\sigma_{normal}=(\sigma_1-\sigma_3)/G$, and shows less scatter than the raw data

because the effect of grain size has been removed.   The difference in normalized

strength at a fixed normalized strain rate is small and does not vary systematically with

Mg content.   Second, at intermediate stresses (normalized stress $\sim 10^{-3}$–$2\cdot10^{-3}$), n varies

from about 1 to greater than 3, a region we interpret as transitional between diffusion

creep and dislocation creep. Third, at high stresses (normalized strength $>2 \cdot 10^{-3}$), n is greater than 3; the normalized strengths vary directly with Mg content; and we suppose that deformation occurs by dislocation creep. At a fixed temperature and strain rate, the transition between the region of linear stress/strain rate behavior and the highly non-linear region occurs at higher stresses and larger grain sizes for calcite with higher Mg concentration (Fig. 11).

To study the effect of loading history (accumulated strain and elapsed time) on the strength of Mg-calcite, we revisited the initial deformation conditions on samples subjected to multiple strain rate steps. The small effect of the accumulated strain on the strength of low Mg-calcite is consistent with previous studies on pure synthetic calcite (Renner et al., 2002). By contrast, high Mg-calcite tends to exhibit increased strain rates after deformation in the intermediate- to high-stress regime (Table 1). In one test (C859), the sample was shortened in compression, extended at different conditions, and then shortened under the initial conditions. It was weaker than the unstrained sample by about 29% after the intermediate cycle in tension. In fact, most samples became weaker at low stress conditions when subjected to intermediate deformation at higher stresses (Fig. 8). Revisiting lower stresses after deformation in the intermediate- to high-stress regime affected the strength of high Mg-calcite more than that of low Mg-calcite (e.g., step 5 for sample Mgcc-70). Also, notice that there is also strain weakening in high Mg-calcites (Mgcc-60 and Mgcc-80) over a strain interval of about 20%. Optical micrographs of some of these samples, i.e., deformed at higher stress levels, show many

fine recrystallized grains (Fig. 3e-f).

2.4. Discussion

Both the grain-growth kinetics and the strength of calcite during dislocation creep are strongly affected by the addition of solutes from the dolomite. Interestingly, the diffusion creep strength does not seem to be affected, provided that comparisons are done at similar grain size (Herwegh et al., 2003). Within the dislocation creep regime, absolute values of strength at a given strain rate correlated directly with the Mg solute content, and, we argue below that the transition from diffusion creep to dislocation creep occurred at larger grain sizes when the Mg content was elevated. In some cases, the relation between stress and strain rate changed when lower stresses were revisited during the stress-step experiment. This result suggests an evolution of some mechanically important state variable, probably grain size. One possibility for this change is an increased contribution of diffusion creep within the population of small recrystallized grains formed during deformation at higher stresses. But, other explanations are also tenable. For example, there might be changes of the fine-scale impurity distribution. It is known that submicron-scale chemical modulations exist in dolomite and high-magnesium calcite (e.g., Wenk et al., 1983). Weakening could also occur, if, during the experiment, the dislocation structure or mobility evolved in ways that were not directly proportional to the applied stress, for example owing to release of an impurity cloud around dislocations. Further study is needed to determine the exact cause. In the

remainder of this paper, we exclude any strength data that may have exhibited such changes and concentrate only on data taken during constant loading conditions, or when stresses were monotonically increased.

An additional caveat should be recognized. The dolomite used in this study comes from a natural mineral source, and contains some traces of Fe, Mn, Al, and Sr. Chemical compositions of minerals were determined by wavelength dispersive spectrometry with a JEOL JXA-733 electron microprobe. The microprobe measurements of those impurity concentrations (<0.1%) are semi-quantitative and the concentrations do not appear to vary from one aggregate to another. But, because the impurities are contained within the dolomite, it is most likely that all the impurities actually co-vary with the Mg content. Without considerable additional work, we cannot definitively implicate one or another cation as the cause of the strengthening. However, it is universally true that deformation tests indicate that all dolomites are stronger than calcites under the same conditions (Davis et al., 2005); and thus, as a first approximation, it seems the simplest interpretation to assume that Mg is indeed the source of strengthening. Still, one should remember that other ions contained within the dolomite at the trace level might have an influence on strength.

2.4.1 Effect of Mg on Grain growth of Calcite

Grain-growth rates can be influenced by many factors, including pores, fluids, solute impurities, and second phases (Atkinson, 1988; Drury and Urai, 1990; Evans et al., 2001;

Urai et al., 1986; Yan et al., 1977).   In metals and ceramics, solid solutes may either increase grain growth rates, as happens with segregation of Al to boundaries in tetragonal zirconia stabilized by yttria (Chokshi et al., 2003), or they may exert solute drag on the boundary, as occurs with the addition of magnesia to alumina (Bae and Baik, 1994; also see reviews by Powers and Glaeser, 1998; Rollett, 2004; and Yan et al., 1977).

For calcite rocks, grain growth in Solnhofen limestone is slow compared to synthetic marbles, whether doped with Mg or not (Fig. 9a) (Evans et al., 2001; Olgaard and Evans, 1988; Schmid, 1977; Tullis and Yund, 1982).   Previous studies suggest that the reduced grain-growth rate of Solnhofen limestone can be attributed to the influence of second phases, solute impurities, and the reactions of accessory minerals.   In general, synthetic marbles with added water have higher grain-growth rates than samples with the same porosity, but no added water (Covey-Crump, 1986; Olgaard, 1989).   Samples with lower porosity grow faster than those with many pores (Covey-Crump, 1997; Olgaard and Evans, 1988), and samples grow more slowly with increasing melt fraction (Renner et al., 2002).

Grain growth is often represented by an equation of the form:

$$d^p - d_0^p = k(t - t_0) \tag{4}$$

where k is a kinetic parameter, d and d_o are the average grain sizes at time, t and t_o, respectively.   The exponent p is determined by the mechanisms operating during grain growth (Atkinson, 1988; Brook, 1976; Evans et al., 2001).   Since our samples undergo a

chemical reaction at the initial stage (Herwegh et al., 2003), we chose d_0 and t_0 to be 5

µm and 1000 s (see above) and invert for p and k.   Best-fit values for p vary from 2.4 to

4.7 for different Mg-calcites (Table 2).   Such exponents are compatible with solute-drag

($p = 3$) (Evans et al., 2001; Yan et al., 1977) or pore-drag ($p = 2$-4) (Covey-Crump, 1997;

Spears and Evans, 1982).   Our HIPed samples have porosities of less than 1%; the

porosity does not appear to correlate with Mg content.   Some pore shapes do suggest

boundary drag, however, so both solute-drag and pore-drag controlled mechanisms may

be active in controlling the overall grain growth rate of Mg-calcite.

In agreement with earlier results (Herwegh et al., 2003), our data clearly indicate that

grain-boundary mobility is inversely related to the Mg content (Fig. 9b).   Here, we have

calculated mobility using $M = \dfrac{1}{2} \cdot \dfrac{d}{\gamma} \cdot \dfrac{\partial d}{\partial t}$, where grain-boundary energy, γ, is taken as

0.1 J/mol (Janczuk et al., 1983).   Notice, however, that the addition of other solid solutes

might have different effects on boundary mobility.   For example, Freund et al. (2001)

found the grain-growth rate of synthetic calcite made from powders ground from a single

crystal containing elevated levels of Mn were faster than those made from crystals with

less Mn.   At present, the reason for this difference is not clear.   Both Mn and Mg have

ionic radii smaller than Ca, so the effect is not simply due to a change of sign of the misfit

elastic strain of the solute.   Unlike Mg, Mn may be an aliovalent substitution and might

thus affect the concentration of some point defect.   Additionally, the bulk level of

impurity in the two studies differs by an order of magnitude: i.e., <0.1 mol% Mn, versus

up to 17 mol% Mg. Although our samples do not show chemical inhomogeneity at the level of electron microprobe observations, finer scale modulations of chemistry may be present in high Mg-calcite (Reeder, 1983; Wenk et al., 1983). Tetard et al. (1999) found increased grain-growth rates in calcite doped with <1 wt% $LiPO_4$, but lower rates at higher concentrations (>2 wt%); they posited that solute was segregated into grain boundaries at high solute concentrations. However, it should be noted that lithium and calcium carbonates form a eutectic system at temperatures above 650°C, especially if the system contains water.

Using the elastic distortion model (Blundy and Wood, 1994), we can estimate the amount of solute segregated into grain boundaries owing to elastic misfit of the solute to be about 5 times the concentration in the bulk material. The mobility predicted by such solute models (Blundy and Wood, 1994; Blundy and Wood, 2003; Hiraga et al., 2004) is

$M = \dfrac{D_s \cdot \Omega}{2\delta \cdot k \cdot T(C_s e^{U/RT})}$, where D_s is the lattice diffusion coefficient of the solute, Ω is

the unit cell volume, δ is the grain boundary thickness, C_s is the concentration of solute at grain boundaries, and U is the energy associated with the partitioning of the solute into the grain boundary. In this case, boundary mobility should be reduced by about one order of magnitude when high Mg-calcite (17.0 mol%) is compared to low Mg-calcite (0.5 mol%). However, the mobility predicted by this relation is much slower than that determined from the grain growth data ($2 \cdot 10^{-16}$-$3 \cdot 10^{-15}$ versus $2 \cdot 10^{-14}$-$7 \cdot 10^{-13}$ (m^2/s)/(J/m^2)). Other factors might also influence boundary mobility. For example, if

48

pore drag is important in grain coarsening, then surface diffusion, rather than grain-boundary diffusion might limit growth. Thus, although it is clear that boundary mobility is adversely affected by additions in Mg solute, it is difficult to be definite about the exact cause of the reduction.

2.4.2 Composite flow law

The conditions of the experiments span a transition in mechanical behavior, which we interpret to involve a transition from diffusion creep to dislocation creep. In the transitional regime, both mechanisms may be active under a given set of loading conditions. To separate the effect of solutes on the individual mechanisms, we used a nonlinear generalized inversion method (Sotin and Poirier, 1984) to fit the experimental data to eq. (5); eqs. (1) and (3) used to describe diffusion and dislocation creep respectively.

A number of different schemes can be used to compute the total strain rate of a material deforming by two mechanisms. For example, if there are two separate fractions within the aggregate, each of which are deforming exclusively by either diffusion or dislocation creep, the total strain rate can be estimated as the volume weighted sum (Ter Heege et al., 2004):

$$\dot{\varepsilon}_{tot} = v_{disl}\dot{\varepsilon}_{disl} + v_{diff}\dot{\varepsilon}_{diff} \qquad (5)$$

where $\dot{\varepsilon}_{disl}$ is given either by eq. (2) or (3), and $\dot{\varepsilon}_{diff}$ is given by eq. (1); v_{disl} and v_{diff} are the volume fractions deforming by a particular mechanism. Alternatively, one might postulate that all grains are the same size and capable of deforming by both mechanisms, in which case $v_{disl} = v_{diff}=1$ and the total deformation rate is simply the sum of the two creep laws. The estimate gained from this model is equivalent to a Sachs model where all grains in the aggregate are loaded under the same stress and can deform by either or both mechanisms.

In the following data inversions, we assume all grains are the average grain size and that all grains deform at rates set by eqs. (1) and (3). In order to minimize the number of variables in the inversions, some other informed choices of the materials parameters had to be made. The activation energy for diffusion creep has been estimated as 200±30 kJ/mol (Herwegh et al., 2003), and 210kJ/mol for Solnhofen limestone (Schmid, 1977). In these fits, we used a constant value of 212 kJ/mol for Q_{diff}, which we derive at a differential stress of ~20 MPa and temperatures of 700–800 C using equation $Q_{diff} = -R\, \partial \ln \dot{\varepsilon} \big/ \partial (1/T)\big|_{\sigma}$. This value is higher than Hewrwegh at al.'s number but within the error limits, ±30 kJ. If we fix Q_{diff} to be 200 kJ/mol, the quality of fit changes only slightly.

The melting temperature T_m of calcite is reduced by the addition of Mg impurity (Byrnes and Wyllie, 1981; Irving and Wyllie, 1975). Variables in the dislocation creep law (3), which are essentially an empirical fit to many data sets, are not well known. We

assumed that the grain size exponent m_p in the expression used for the Peierl stress in eq.(3) is either 0.5 or 1. Fortunately, the results of the inversion vary only slightly when different values for m_p are used (Table 3). In general, within experimental uncertainties and sample-to-sample variations, the data can be fit well by the unconstrained inversion (Table 3 and Fig. 10). Fig. 10 shows the best fits of the composite flow law to both Mg-calcite and synthetic calcite. The experimental data of Mn-calcite (Freund et al., 2004; Wang et al., 1996) are also plotted for comparison. Other constitutive laws for dislocation creep can also be used to fit the data, e.g., the power law (Eq.(2) and Table 3) or a stress activated law for cross slip. The relative effect of Mg concentration on the strength is similar for all the flow laws.

The apparent activation energies for dislocation creep from the inversion vary slightly for different Mg-calcites (~200 kJ/mol, see Table 3). Rather than inverting for the activation energies, they may also be calculated using $Q_{disl} = -R\,\partial \ln \dot{\varepsilon} \big/ \partial (1/T)\big|_{\sigma}$. At a differential stress of ~90 MPa and temperatures of 700–800 C, the activation energies are 300 ± 74 kJ/mol, 203 ± 64 kJ/mol, and 145 ± 60 kJ/mol for Mgcc-60, Mgcc-70, and Mgcc-80, respectively; these values might be biased because grain sizes, and, therefore, strength evolve with different rates during the experiments. For example, the activation energy will be underestimated if it is determined from tests on samples where the initial grain size is systematically smaller at lower temperatures. Since dynamic recrystallization is prominent in Mgcc-80 (Fig. 3f) after deformation, its activation energy is likely to be underestimated using this method. Our derived values (Q_{plb}) are

comparable to the activation energies for dislocation recovery kinetics of calcite single crystals (184 ± 22 kJ/mol, Liu and Evans, 1997), and for dislocation creep of various calcite aggregates; e.g., about 200 kJ/mol for pure crystal aggregates (Renner et al., 2002), but are smaller than that for determined for dislocation creep of single crystals, 350 kJ/mol (de Bresser and Spiers, 1993; Rutter, 1974).

2.4.3 Effect of Mg on creep strength of high-magnesian calcite

Comparing our results with previous studies, we find that the strengths of synthetic aggregates (Renner et al., 2002), Solnhofen limestone (Schmid, 1976; Schmid, 1977), and Mg-calcite (this study) are nearly the same when grain sizes are less than 10 μm (Fig. 11). At a given strain rate and temperature, the strength varies inversely with the average grain size cubed, suggesting a Coble creep mechanism. For coarser-grained carbonates, dislocation creep dominates and the relation between grain size and strength is similar to a Hall-Petch relation. Increasing the magnesium content increases both the creep strength and the grain size at which the transition between the two deformation regimes occurs. In addition, we note that, in the high stress regime, both Yule marble (Heard, 1963; Heard and Raleigh, 1972) and Carrara marble (Covey-Crump, 1997; de Bresser et al., 2001; Rutter, 1995; Schmid et al., 1980) are stronger than the synthetic aggregates and single crystals.

To understand the strengthening behavior of calcite with Mg solute, we first notice that dolomite is much stronger than the high-magnesian calcite (Davis et al., 2003). There

are several possible reasons for such strengthening, including larger elastic constants, solid-solution hardening, and precipitation hardening. The elastic modulus of calcite does increase with Mg concentration (Zhang and Reeder, 1999), but only by ~16%, whereas, we observe increases in flow strength in the magnesian calcites of about 500% (Fig. 12). This solute hardening is very intriguing because of the possibility of complex interactions between solute cations and anions that might significantly alter the activity on different slip systems (Poirier, 1985). Solid solutes might affect the strength by affecting dislocation climb if the solutes affect point defect concentrations, or by decreasing dislocation mobility owing to impurity drag. It is also possible that the addition of magnesium solute introduces precipitates or sub-microscopic regions of cation order (Reeder, 2000; Wenk et al., 1991), and that these structures act as impediments (discrete obstacles) to dislocation motion.

Solid-solute hardening, either by impurity drag or discrete obstacles, seems most probable. It is common for metal alloys and ceramics (Duong et al., 1993; Duong et al., 1994; Mohamed and Langdon, 1975) to exhibit solute-hardening behavior during glide-controlled dislocation creep. Defects, including dislocations and grain boundaries, may generate solute atmospheres which retard dislocation glide (Cottrell and Jaswon, 1949). The actual retarding force depends on the details of the concentration profiles, diffusivities, and activation energies, but in general, the strain rate is inversely proportional to the impurity concentration. At a fixed strain rate of $10^{-3}s^{-1}$ and 800°C, the strength of calcite monotonically increases with Mg concentration (Fig. 12) and is

53

proportional to the cube root of the solute concentration C_{Mg}.   However, if we predict the strength of the Mg-calcite using the solute-drag model of Kitabjian et al. (1999), then the predicted strength is an order of magnitude greater than that observed.   The obstacle mechanisms is also possible: natural high-magnesian calcite is known to exhibit nano-meter scale modulations in cation chemistry (Wenk et al., 1991), such modulations may be present in the synthetic samples, too.

In contrast to the results for Mg doping, a previous study (Freund et al., 2004) indicated that Mn solute seemed to decrease the diffusion creep strength.   The reason for this difference between the two solutes is not clear, but Mn solute is multivalent and could affect charge neutrality conditions, and thus, the defect concentrations.

2.4.4 Natural applications

Natural carbonate rocks show variations in strength that may arise from differences in grain size, accessory minerals, porosity, or chemical impurities.   These variations are of great concern when extrapolating flow laws into natural conditions or reconstructing paleo-deformation conditions from the interpretation of microstructures.   For example, non-soluble, solid second phases can suppress grain growth by boundary pinning and change the overall strength of material (Evans et al., 2001; Knipe, 1980; Olgaard and Evans, 1988; Tullis and Yund, 1982).   If solid solution is possible, dissolved impurities could also affect grain-growth kinetics and creep behavior (Freund et al., 2001; Freund et al., 2004; Herwegh et al., 2003; Tetard et al., 1999).   Mg is one, among several, possible

cation solutes in calcite rocks, e.g., Mn, Fe, Sr; and these solutes may affect the creep behavior, as briefly demonstrated by de Bresser (1991). The experiments clearly indicate that Mg doping increases strength in the dislocation creep regime; and the transition from diffusion to dislocation creep at a fixed strain rate also occurs at a larger grain size as well.   In at least some natural carbonates, the effects of magnesium content may be evident in the microstructure.   We extrapolate the flow law of Mg-calcite to geological strain rates (10^{-12}s^{-1}) and compare this with pure calcite (Fig. 13).   Naturally deformed carbonates also show evidence of chemical influences on strength.   For example, Fig. 14 shows a porphyroblasts of high-magnesian calcite grains from echinoderm fossils that are much less deformed than surrounding carbonate matrix with lower Mg content.   It seems clear that solute impurities will affect the strength of carbonates and that field interpretations will need to take this effect into account.

2.5 Summary

Previous results (Herwegh et al., 2003) indicated that diffusion creep in high-magnesian calcite was not sensitive to the Mg content, but that grain growth was reduced by the addition of that solute.   The results of this study corroborate those in the earlier work.   Additional analyses indicate that the grain-growth rate of calcite is suppressed by >3.0 mol% Mg solute; and the grain growth exponent, p, ranges from 2.4 to 4.7 for different Mg-calcites.   There are several mechanisms that might be active in controlling the overall grain growth rate, including solute-drag or pore-drag.   No direct

measurements of grain-boundary chemistry were made here, but solute segregation, if it occurs, is likely to reduce the grain-boundary mobility and would explain the reduced grain growth rate. Nano-scale modulations in cation chemistry within the crystals might also be responsible. Reduction in grain size and suppression of grain-growth rate of Mg on calcite rocks might also be important for strain localization. Thus, variations in dolomite content within layered carbonate sediments might drastically affect calcite grain size during metamorphic process.

Although these experiments show that there is no obvious effect of Mg content on the strength of calcite in the diffusion creep regime (σ <40 MPa) at temperature of 700 800°C, the transition between diffusion to dislocation creep regimes occurs at higher stresses for samples with higher Mg content and smaller grain size. In addition, the additional data collected here and the non-linear inversion of these data indicate that the Mg solute strengthens calcite in the dislocation creep regime, possibly as a result of local lattice distortions or owing to interactions between dislocations and solute ions/nanometer-scale domains of ordered cations. Our data suggest that, for a fixed temperature, strain rate, and grain size, the strength of calcite deforming by dislocation creep will depend on the cube root of the Mg concentration. Such chemical influences should be taken into account in field situations.

TEM observations indicate that dislocation recovery processes occur under the conditions of these experiments, and it is plausible that both dislocation climb and glide play important roles in controlling the overall strength of Mg-calcite in the dislocation

creep regime.

Acknowledgements

2.6 References

Anovitz, L.M. and Essene, E.J., 1987. Phase-equilibria in the system caco3-mgco3-feco3. Journal of Petrology, 28(2): 389-414.

Atkinson, H.V., 1988. Theories of normal grain-growth in pure single-phase systems. Acta Metallurgica, 36(3): 469-491.

Bae, S.I. and Baik, S., 1994. Critical concentration of mgo for the prevention of abnormal grain-growth in alumina. Journal of the American Ceramic Society, 77(10): 2499-2504.

Bai, Q., Wang, Z.C. and Kohlstedt, D.L., 1995. Manganese olivine .1. Electrical conductivity. Physics and Chemistry of Minerals, 22(8): 489-503.

Barnhoorn, A., Bystricky, M., Burlini, L. and Kunze, K., 2004. The role of recrystallisation on the deformation behavior of calcite rocks: Large strain torsion experiments on Carrara marble. Journal of Structural Geology, 26(5): 885-903.

Bestmann, M., Kunze, K. and Matthews, A., 2000. Evolution of a calcite marble shear zone complex on Thassos island, Greece: Microstructural and textural fabrics and their kinematic significance. Journal of Structural Geology, 22(11-12): 1789-1807.

Blundy, J. and Wood, B., 1994. Prediction of crystal-melt partition-coefficients from elastic-moduli. Nature, 372(6505): 452-454.

Blundy, J. and Wood, B., 2003. Partitioning of trace elements between crystals and melts. Earth and Planetary Science Letters, 210(3-4): 383-397.

Brook, R.J., 1976. Controlled grain growth. In: F.-Y. Wang (Editor), Ceramic fabrication procedures. Academic Press, New York.

Bruhn, D.F., Olgaard, D.L. and Dell'Angelo, L.N., 1999. Evidence for enhanced deformation in two-phase rocks: Experiments on the rheology of calcite-anhydrite aggregates. Journal of Geophysical Research-Solid Earth, 104(B1): 707-724.

Burkhard, M., 1990. Aspects of the large-scale Miocene deformation in the most external part of the Swiss Alps (sub-Alpine molasse to Jura fold belt). Eclogae Geologicae Helvetiae, 83(3): 559-583.

Burkhard, M., 1993. Calcite twins, their geometry, appearance and significance as stress-strain markers and indicators of tectonic regime - a review. Journal of Structural Geology, 15(3-5): 351-368.

Busch, J.P. and Vanderpluijm, B.A., 1995. Calcite textures, microstructures and rheological properties of marble mylonites in the bancroft shear zone, Ontario, Canada. Journal of Structural Geology, 17(5): 677-688.

Byrnes, A.P. and Wyllie, P.J., 1981. Subsolidus and melting relations for the join caco3-mgco3 at 10-kbar. Geochimica et Cosmochimica Acta, 45(3): 321-328.

Carter, K.E., 1992. Evolution of stacked, ductile shear zones in carbonates from midcrustal levels - Tuscan nappe, n-apennines, Italy. Journal of Structural Geology, 14(2): 181-192.

Chiang, Y.-M., Dunbar, B. and Kingery, W.D., 1997. Physical ceramics: Principles for ceramics science and. Engineering. Mit series in materials science & engineering. John Wiley and Sons, Inc., New York, 522 pp.

Chokshi, A.H., Yoshida, H., Ikuhara, Y. and Sakuma, T., 2003. The influence of trace elements on grain boundary processes in yttria-stabilized tetragonal zirconia. Materials Letters, 57(26-27): 4196-4201.

Cottrell, A.H. and Jaswon, M.A., 1949. Distribution of solute atoms round a slow dislocation. Proceedings of the Royal Society of London. Series A, Mathematical and Physical Sciences 199: 104-114.

Covey-Crump, S.J., 1997. The normal grain growth behavior of nominally pure calcitic aggregates. Contributions to Mineralogy and Petrology, 129(2-3): 239-254.

Covey-Crump, S.J., 1998. Evolution of mechanical state in Carrara marble during deformation at 400 degrees to 700 degrees c. Journal of Geophysical Research-Solid Earth, 103(B12): 29781-29794.

Covey-Crump, S.J., 2001. Variation of the exponential and power law creep parameters with strain for Carrara marble deformed at 120 degrees to 400 degrees c. Geophysical Research Letters, 28(12): 2301-2304.

Davis, N., Kronenberg, A. and Newman, J., 2005. Plasticity and diffusion creep of dolomite. American Geophysical Union, Fall Meeting 2005, abstract# MR33A-0152.

Davis, N.E., Newman, J. and Kronenberg, A.K., 2003. High temperature deformation of stoichiometric dolomite. AGU 2003: S22A-0433.

de Bresser, H., Evans, B. and Renner, J., 2002. Estimating the strength of calcite rocks under natural conditions. In: S. de Meer, M.R. Drury, J.H.P. de Bresser and G. Pennock (Editors), Deformation mechanisms, rheology, tectonics, current status future perspectives. Geolog. Society of London, London, UK, pp. 293-307.

de Bresser, J.H.P., 1991. Intracrystalline deformation of calcite. Geologia Ultrajectina 79: 1-191.

de Bresser, J.H.P., 1996. Steady state dislocation densities in experimentally deformed calcite materials: Single crystals versus polycrystals. Journal of Geophysical Research-Solid Earth, 101(B10): 22189-22201.

de Bresser, J.H.P., 2002. On the mechanism of dislocation creep of calcite at high temperature: Inferences from experimentally measured pressure sensitivity and

strain rate sensitivity of flow stress. Journal of Geophysical Research-Solid Earth, 107(B12).

de Bresser, J.H.P. and Spiers, C.J., 1993. Slip systems in calcite single crystals deformed at 300-800ºc. J. Geophys. Res. - Sol. Earth, 98(B4): 6397-6409.

de Bresser, J.H.P., Ter Heege, J.H. and Spiers, C.J., 2001. Grain size reduction by dynamic recrystallization: Can it result in major theological weakening? International Journal of Earth Sciences, 90(1): 28-45.

de Bresser, J.H.P., Urai, J.L. and Olgaard, D.L., 2005. Effect of water on the strength and microstructure of Carrara marble axially compressed at high temperature. Journal of Structural Geology, 27(2): 265-281.

Dresen, G., Evans, B. and Olgaard, D.L., 1998. Effect of quartz inclusions on plastic flow in marble. Geophysical Research Letters, 25(8): 1245-1248.

Drury, M.R. and Urai, J.L., 1990. Deformation-related recrystallization processes. Tectonophysics, 172(3-4): 235-253.

Duong, H., Beeman, M. and Wolfenstine, J., 1993. Creep-behavior of potassium-chloride rubidium chloride solid-solution alloys. Journal of the American Ceramic Society, 76(1): 185-191.

Duong, H., Beeman, M. and Wolfenstine, J., 1994. High-temperature creep-behavior and substructure in kcl-kbr solid-solution alloys. Acta Metallurgica Et Materialia, 42(3): 1001-1012.

Essene, E.J., 1983. Solid solutions and solvi amoun metamorphic carbonates with applications to geologic thermobarometry. In: R.J. Reeder (Editor), Carbonates: Mineralogy and chemistry. Reviews in mineralogy. American Mineralogical Society, Washington, D. C., pp. 77-96.

Evans, B., Renner, J. and Hirth, G., 2001. A few remarks on the kinetics of static grain growth in rocks. International Journal of Earth Sciences, 90(1): 88-103.

Freund, D., Rybacki, E. and Dresen, G., 2001. Effect of impurities on grain growth in synthetic calcite aggregates. Physics and Chemistry of Minerals, 28(10): 737-745.

Freund, D., Wang, Z.C., Rybacki, E. and Dresen, G., 2004. High-temperature creep of synthetic calcite aggregates: Influence of Mn-content. Earth and Planetary Science Letters, 226(3-4): 433-448.

Frost, H.J., 1982. Deformation mechanism and fracture mechanism maps. Cim Bulletin, 75(842): 110-110.

Goetze, C. and Kohlstedt, D.L., 1977. Dislocation-structure of experimentally deformed marble. Contributions to Mineralogy and Petrology, 59(3): 293-306.

Griggs, D. and Miller, W.B., 1951. Deformation of Yule marble: Part I - compression and extension experiments on dry Yule marble at 10,000 atmospheres confining pressure, room temperature. Geological Society of America Bulletin 62(8): 853-862.

Heard, H.C., 1960. Transition from brittle to ductile flow in Solnhofen limestone as a function of temperature, confining pressure, and interstitial fluid pressure Rock

deformation: Geological Society of America Memoir, 79: 193-226.

Heard, H.C., 1963. Effect of large changes in strain rate in the experimental deformation of Yule marble. J. Geol., 71: 162-195.

Heard, H.C. and Raleigh, C.B., 1972. Steady-state flow in marble at 500 degrees to 800 degrees c. Geological Society of America Bulletin, 83(4): 936-956.

Heitzmann, P., 1987. Calcite mylonites in the central Alpine root zone. Tectonophysics, 135(1-3): 207-215.

Herwegh, M. and Kunze, K., 2002. The influence of nano-scale second-phase particles on deformation of fine grained calcite mylonites. Journal of Structural Geology, 24(9): 1463-1478.

Herwegh, M., Xiao, X.H. and Evans, B., 2003. The effect of dissolved magnesium on diffusion creep in calcite. Earth and Planetary Science Letters, 212(3-4): 457-470.

Hiraga, T., Anderson, I.M. and Kohlstedt, D.L., 2004. Grain boundaries as reservoirs of incompatible elements in the earth's mantle. Nature, 427(6976): 699-703.

Hiraga, T., Hirschmann, M.M. and Kohlstedt, D.L., 2007. Equilibrium interface segregation in the diopside-forsterite system ii: Applications of interface enrichment to mantle geochemistry. Geochimica et Cosmochimica Acta, 71(5): 1281-1289.

Hitchings, R.S., Paterson, M.S. and Bitmead, J., 1989. Effects of iron and magnetite additions in olivine pyroxene rheology. Physics of the Earth and Planetary Interiors, 55(3-4): 277-291.

Hobbs, B.E., 1984. Point defect chemistry of minerals under a hydrothermal environment. Journal of Geophysical Research, 89(B6): 4026-4038.

Irving, A.J. and Wyllie, P.J., 1975. Subsolidus and melting relationships for calcite, magnesite and join caco3-mgco3 to 36 kb. Geochimica et Cosmochimica Acta, 39(1): 35-53.

Janczuk, B., Chibowski, E. and Staszczuk, P., 1983. Determination of surface free-energy components of marble. Journal of Colloid and Interface Science, 96(1): 1-6.

Jordan, P.G., 1987. The deformational behavior of bimineralic limestone-halite aggregates. Tectonophysics, 135(1-3): 185-197.

Kitabjian, P.H., Garg, A., Noebe, R.D. and Nix, W.D., 1999. High-temperature deformation behavior of NiAl(Ti) solid-solution single crystals. Metallurgical and Materials Transactions a-Physical Metallurgy and Materials Science, 30(3): 587-600.

Knipe, R.J., 1980. Distribution of impurities in deformed quartz and its implications for deformation studies. Tectonophysics, 64(1-2): T11-T18.

Kohlstedt, D.L., 2006. The role of water in high-temperature rock deformation, Water in nominally anhydrous minerals. Reviews in mineralogy & geochemistry, pp. 377-396.

Kohlstedt, D.L., Evans, B. and Mackwell, S.J., 1995. Strength of the lithosphere - constraints imposed by laboratory experiments. Journal of Geophysical

Research-Solid Earth, 100(B9): 17587-17602.

Liu, M. and Evans, B., 1997. Dislocation recovery kinetics in single-crystal calcite. Journal of Geophysical Research-Solid Earth, 102(B11): 24801-24809.

Lücke, K. and Stüwe, H.P., 1971. On the theory of impurity controlled grain boundary motion. Acta metall., 19: 1087-99.

Mackenzie, F.T., Bischoff, W.D., Bishop, F.C., Loijens, M., Schoonmaker, J. and Wollast, R., 1983. Magnesian calcites: Low-temperature occurrence, solubility, and solid-solution behavior. In: R. Reeder (Editor), Carbonates: Mineralogy and chemistry. Reviews in mineralogy. Mineralogical Society of America, Washington DC, pp. 97-144.

Mohamed, F.A. and Langdon, T.G., 1975. Creep-behavior of ceramic solid-solution alloys. Journal of the American Ceramic Society, 58(11-1): 533-534.

Molli, G., Conti, P., Giorgetti, G., Meccheri, M. and Oesterling, N., 2000. Microfabric study on the deformational and thermal history of the Alpi apuane marbles (Carrara marbles), Italy. Journal of Structural Geology, 22(11-12): 1809-1825.

Molli, G. and Heilbronner, R., 1999. Microstructures associated with static and dynamic recrystallization of Carrara marble (Alpi apuane, nw tuscany, Italy). Geologie En Mijnbouw-Netherlands Journal of Geosciences, 78(1): 119-126.

Nesse, W.D., 2000. Introduction to mineralogy. Oxford University Press, New York, 442 pp.

Olgaard, D.L. and Evans, B., 1986. Effect of 2nd-phase particles on grain-growth in calcite. Journal of the American Ceramic Society, 69(11): C272-C277.

Olgaard, D.L. and Evans, B., 1988. Grain-growth in synthetic marbles with added mica and water. Contributions to Mineralogy and Petrology, 100(2): 246-260.

Paterson, M.S., 1976. Some current aspects of experimental rock deformation. Philosophical Transactions of the Royal Society of London Series a-Mathematical Physical and Engineering Sciences, 283(1312): 163-172.

Paterson, M.S., 2001. Relating experimental and geological theology. International Journal of Earth Sciences, 90(1): 157-167.

Pfiffner, O.A., 1982. Deformation mechanisms and flow regimes in limestones from the helvetic zone of the Swiss Alps. Journal of Structural Geology, 4(4): 429-442.

Pieri, M., Burlini, L., Kunze, K., Stretton, I. and Olgaard, D.L., 2001. Rheological and microstructural evolution of Carrara marble with high shear strain: Results from high temperature torsion experiments. Journal of Structural Geology, 23(9): 1393-1413.

Poirier, J.P., 1985. Creep of crystals; high-temperature deformation processes in metals, ceramics and minerals.

Powers, J.D. and Glaeser, A.M., 1998. Grain boundary migration in ceramics. Interface Science, 6(1-2): 23-39.

Ranalli, G. and Murphy, D.C., 1987. Rheological stratification of the lithosphere. Tectonophysics, 132(4): 281-295.

Reeder, R.J., 1983. Tem as a tool in study of carbonate crystal-chemistry. Aapg Bulletin-American Association of Petroleum Geologists, 67(3): 538-539.

Reeder, R.J., 2000. Constraints on cation order in calcium-rich sedimentary dolomite. Aquatic Geochemistry, 6(2): 213-226.

Renner, J. and Evans, B., 2002. Do calcite rocks obey the power-law creep equation? In: S. de Meer, M.R. Drury, J.H.P. de Bresser and G.M. Pennock (Editors), Deformation mechanisms, rheology and tectonics: Current status and future perspectives. Special publications. Geological Society, London, pp. 293-307.

Renner, J., Evans, B. and Siddiqi, G., 2002. Dislocation creep of calcite. Journal of Geophysical Research-Solid Earth, 107(B12).

Renner, J., Siddiqi, G. and Evans, B., 2007. Plastic flow of two-phase marbles. Journal of Geophysical Research-Solid Earth, 112(B7).

Rollett, A.D., 2004. Modeling the impact of grain boundary properties on microstructural evolution, Recrystallization and grain growth, pts 1 and 2. Materials science forum, pp. 707-714.

Rutter, E.H., 1972. The influence of interstitial water on the rheological behavior of calcite rocks Tectonophysics 14(1): 13-33.

Rutter, E.H., 1974. Influence of temperature, strain rate and interstitial water in experimental deformation of calcite rocks. Tectonophysics, 22(3-4): 311-334.

Rutter, E.H., 1984. The influence of temperature, strain rate, and interstitial water in the experimental deformation of calcite rocks. Tectonophysics, 43: 311-334.

Rutter, E.H., 1995. Experimental study of the influence of stress, temperature, and strain on the dynamic recrystallization of Carrara marble. Journal of Geophysical Research-Solid Earth, 100(B12): 24651-24663.

Rutter, E.H., 1999. On the relationship between the formation of shear zones and the form of the flow law for rocks undergoing dynamic recrystallization. Tectonophysics, 303(1-4): 147-158.

Rybacki, E., Paterson, M.S., Wirth, R. and Dresen, G., 2003. Rheology of calcite-quartz aggregates deformed to large strain in torsion. Journal of Geophysical Research-Solid Earth, 108(B2): -.

Schenk, O., Urai, J.L. and Evans, B., 2005. The effect of water on recrystallization behavior and grain boundary morphology in calcite-observations of natural marble mylonites. Journal of Structural Geology, 27(10): 1856-1872.

Schmid, S.M., 1976. Rheological evidence for changes in the deformation mechanism of solenhofen limestone towards low stresses. Tectonophysics, 31(1-2): T21-T28.

Schmid, S.M., 1977. Superplastic flow in fine-grained limestone. Tectonophysics, 43(3-4): 257-291.

Schmid, S.M., Paterson, M.S. and Boland, J.N., 1980. High temperature flow and dynamic recrystallization in Carrara marble. Tectonophysics, 65(3-4): 245-280.

Siddiqi, G., Evans, B., Dresen, G. and Freund, D., 1997. Effect of semibrittle deformation on transport properties of calcite rocks. Journal of Geophysical Research-Solid

Earth, 102(B7): 14765-14778.

Sotin, C. and Poirier, J.P., 1984. Ananlysis of high-temperature creep experiments by generalized nonlinear inversion. Mechanics of Material, 3(4): 311-317.

Spears, M.A. and Evans, A.G., 1982. Microstructure development during final intermediate stage sintering .2. Grain and pore coarsening. Acta Metallurgica, 30(7): 1281-1289.

Spiers, C.J., 1979. Fabric development in calcite polycrystals deformed at 400-degrees-c. Bulletin De Mineralogie, 102(2-3): 282-289.

Ter Heege, J.H., de Bresser, J.H.P. and Spiers, C.J., 2004. Composite flow laws for crystalline materials with log-normally distributed grain size: Theory and application to olivine. Journal of Structural Geology, 26(9): 1693-1705.

Tetard, F., Bernache-Assollant, D. and Champion, E., 1999. Pre-eutectic densification of calcium carbonate doped with lithium carbonate. Journal of Thermal Analysis and Calorimetry, 56(3): 1461-1473.

Tullis, J. and Yund, R.A., 1982. Grain growth kinetics of quartz and calcite aggregates. J. Geology, 90(3): 301-318.

Urai, J.L., Means, W.D. and Lister, G.S., 1986. Dynamic recrystallization of minerals. In: B.E.H. Hobbs and C. Hugh (Editors), Mineral rock deformation: Laboratory studies, paterson volume. Geophysical Monograph, Washington D. C., pp. 161-200.

Vanderpluijm, B.A., 1991. Marble mylonites in the bancroft shear zone, Ontario, Canada - microstructures and deformation mechanisms. Journal of Structural Geology, 13(10): 1125-1135.

Walker, A.N., Rutter, E.H. and Brodie, K.H., 1990. Experimental study of grain-size sensitive flow of synthetic, hot-pressed calcite rocks. In: R.J. Knipe and E.H. Rutter (Editors), Deformation mechanisms, rheology and tectonics. Geological Society Special Publications, pp. 259-284.

Wang, Z.C., Bai, Q., Dresen, G. and Wirth, R., 1996. High-temperature deformation of calcite single crystals. Journal of Geophysical Research-Solid Earth, 101(B9): 20377-20390.

Wenk, H.R., Barber, D. and Reeder, R., 1983. Microstructures in carbonates. In: R. Reeder (Editor), Carbonates: Mineralogy and chemistry. Reviews in mineralogy. American Mineralogical Society, Washington DC, pp. 301-369.

Wenk, H.R. and Bulakh, A., 2004. Minerals, their constitution and origin. University Press, Cambridge, 646 pp.

Wenk, H.R., Hu, M.S., Lindsey, T. and Morris, J.W., 1991. Superstructures in ankerite and calcite. Physics and Chemistry of Minerals, 17(6): 527-539.

Xiao, X.H. and Evans, B., 2003. Shear-enhanced compaction during non-linear viscous creep of porous calcite-quartz aggregates. Earth and Planetary Science Letters, 216(4): 725-740.

Yan, M.F., Cannon, R.F. and Bowen, H.K., 1977. Grain boundary migration in ceramics.

In: R.M. Fulrath and J.A. Pask (Editors), Ceram. Microstructures - 76. Westview Press, Boulder, CO, pp. 276-307.

Yin, X.L., 1996. The deformation mechanism of marble mylonites in the dashankou shear zone. Journal of Geomechanics, 2(4): 61-67.

Zhang, J.Z. and Reeder, R.J., 1999. Comparative compressibilities of calcite-structure carbonates: Deviations from empirical relations. American Mineralogist, 84(5-6): 861-870.

Zhao, Y.H., Zimmerman, M. and Kohlstedt, D.L., in press, 2008. Effect of iron content on the creep behavior of olivine:1. Anhydrous conditions.

Zhu, W.L., Evans, B. and Bernabe, Y., 1999. Densification and permeability reduction in hot-pressed calcite: A kinetic model. Journal of Geophysical Research-Solid Earth, 104(B11): 25501-25511.
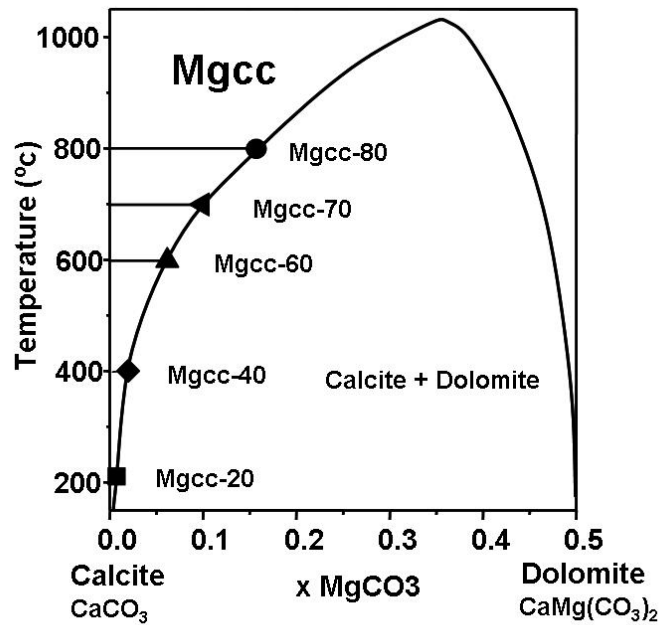
2.7 Figures and tables

Figure 1. Calcite-dolomite solid-solution system; after Anovitz and Essene(1987). Symbols indicate the molar concentration of Mg in calcite for the various samples and the temperature at which each composition would saturated in Mg.   The labeling is the same as in Herwegh et al., (2003).   Two new composition Mgcc-20 and Mgcc-40 have been added in this study.   All samples were produced using HIP at 850°C; all solid solutions used in this study should be stable for deformation at 800°C.   The most-concentrated solid solutions (Mgcc-80) may have undergone exsolution during deformation at 700-800°C; but the remainder should have been stable at all conditions.
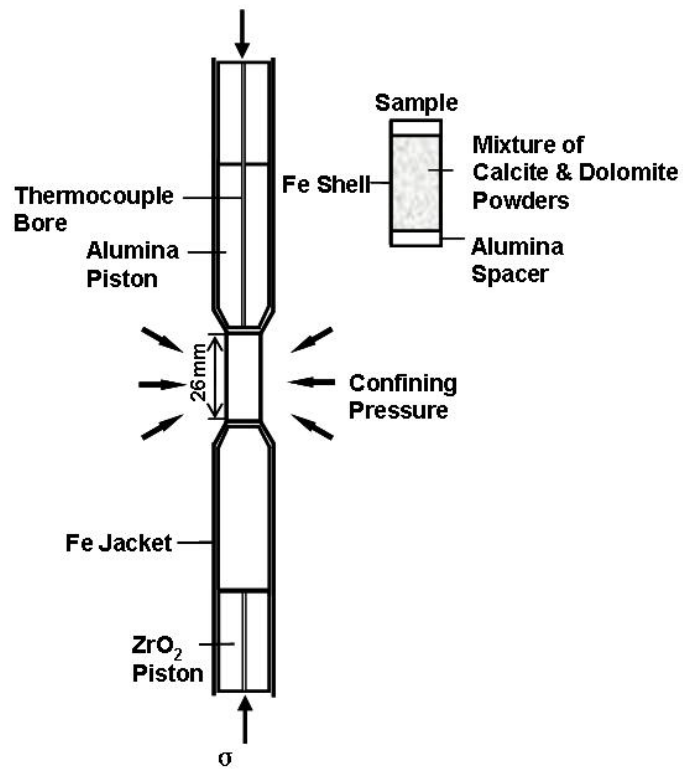
Figure 2. Schematic cross-section of the sample assembly for the grain growth and deformation experiments. See (Renner et al., 2002) for a complete description of the apparatus and of the accuracy of the measurements.
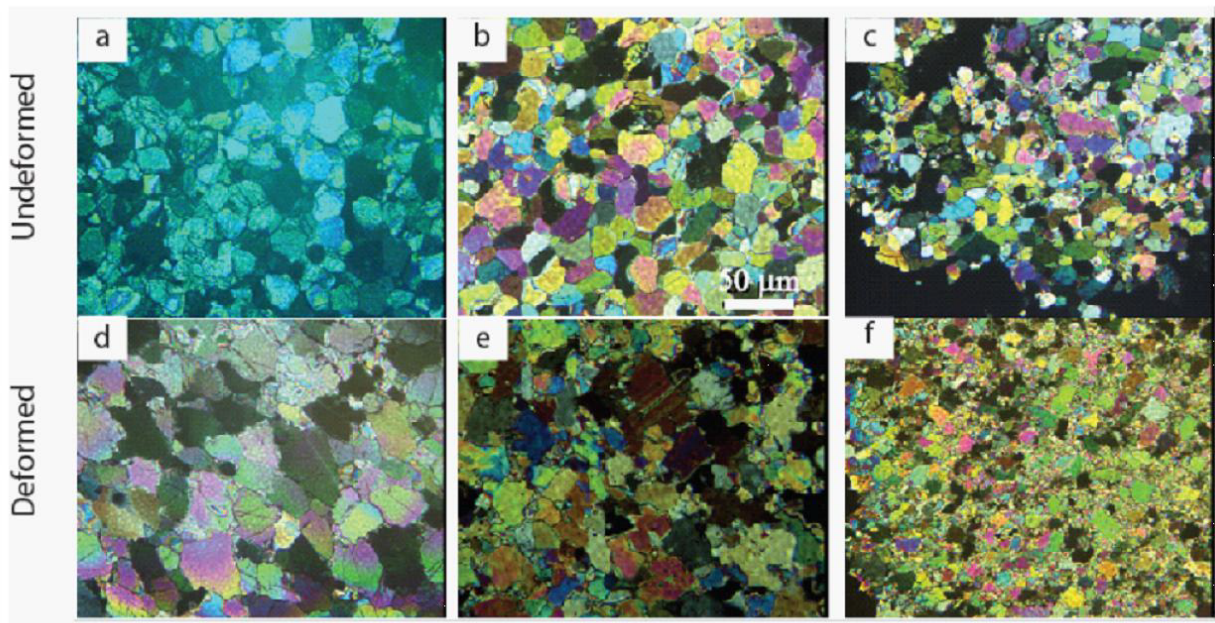
Figure 3. Optical micrographs in cross-polarized light for undeformed (a-c) and deformed (d-f) samples with Mg concentration of 0.5 mol% (a and d), 7.0 mol% (b and e), and 17.0 mol% (c and f). All were prepared using a HIP step of 2 hours. Undeformed (a-c) samples contain isometric grains with straight or gently curved boundaries. The deformed samples (d-f) shown here were deformed under multiple stress conditions, at relatively high stresses. They contain small recrystallized neoblasts, along with larger grains that have undulate boundaries. See Fig. 4 for grain size distribution analysis. Scale bar for all micrographs shown in (b). Note that the magnesium content in Figs. 3d-f (samples C948, C814, and C820) varies in the same order as in Figs. 3a-c.
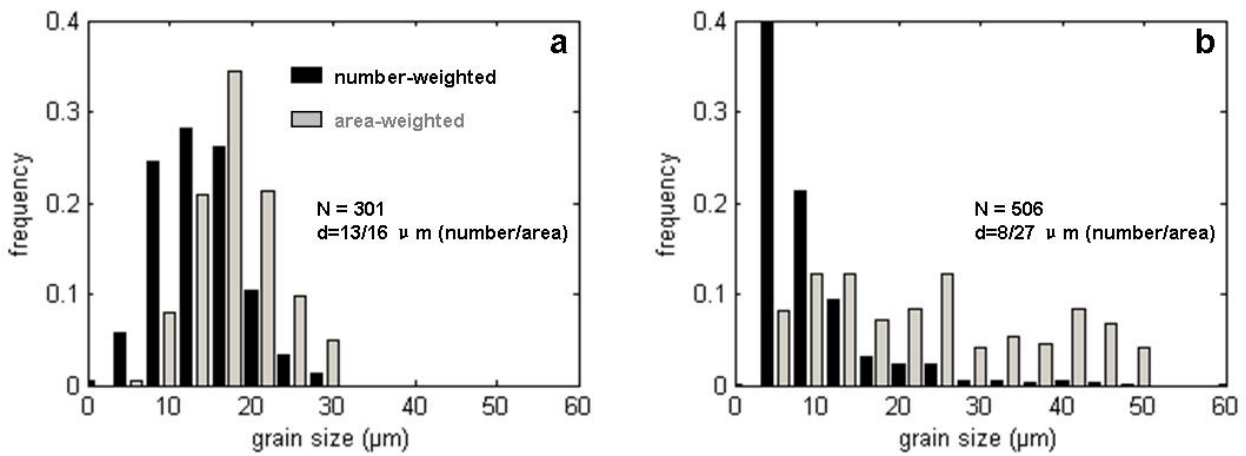
Figure 4. Grain size distributions of samples with 7.0 mol% Mg after HIP for 2hrs at 850ºC (a) and after deformation ((b), ~ 9% strain).   Black bars and gray bars represent number-weighted and area-weighted grain size distributions, respectively.   The average grain sizes are indicated.   In each sample, at least 300 grains were measured; the grain dimension is determined by calculating the diameter of a circle with an area equivalent to that particular grain.   The distribution of the undeformed HIP sample is roughly similar to a lognormal distribution.   Note that the deformed sample contains a large number of small grains but also a few large grains that covers a considerable area fraction.
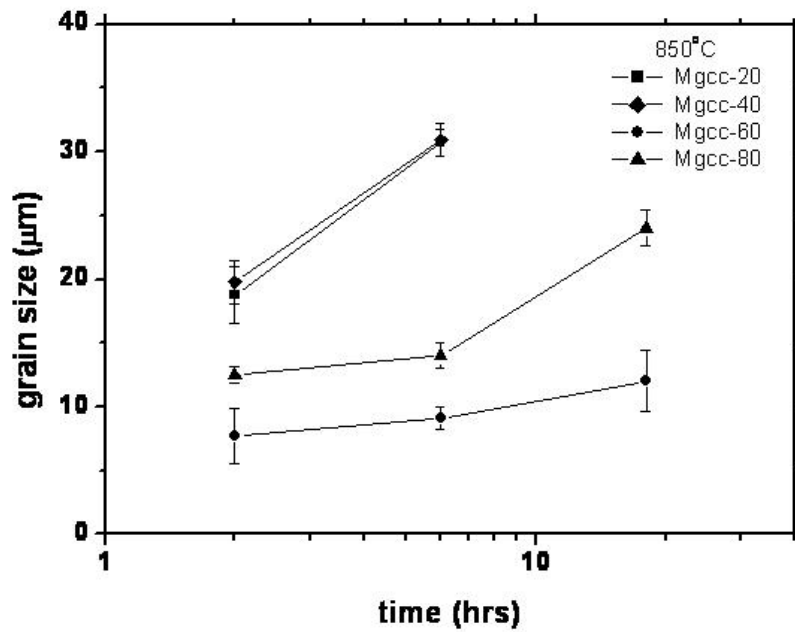
Figure 5. Evolution of grain size for samples of different compositions as a function of the duration of the HIP step (at 850°C).   All samples were loaded under isostatic stresses only and held for different times at constant temperature.   Slower grain growth rates correlate with higher magnesium content.
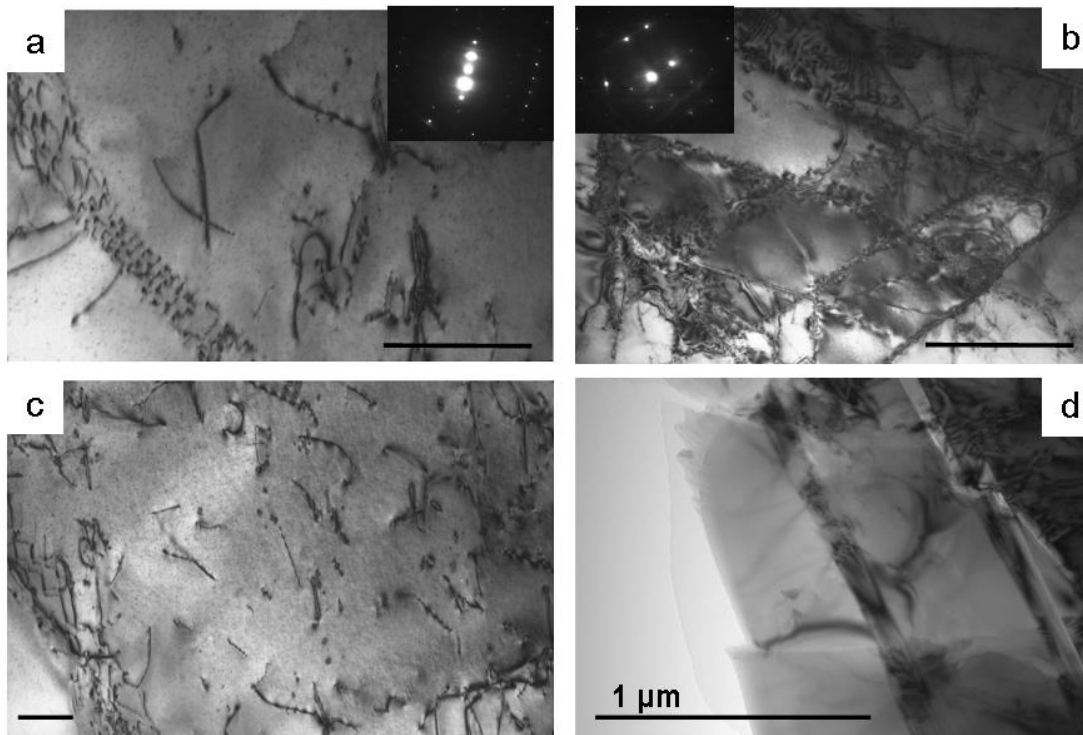
Figure 6. Transmission electron microscope (TEM) micrographs of a sample (C942) deformed in dislocation creep regime. Scale bars in each micrograph are 1 μm. In general, the samples show widely spaced sub-grain networks (a-c) that interact with each other (b) and with dislocations within the interior of the subgrains. Dislocations of various orientations indicate slip on several systems. The free dislocation density is relatively low (c). A few microtwins (d), with widths of about 30-100 nm, are infrequently observed.
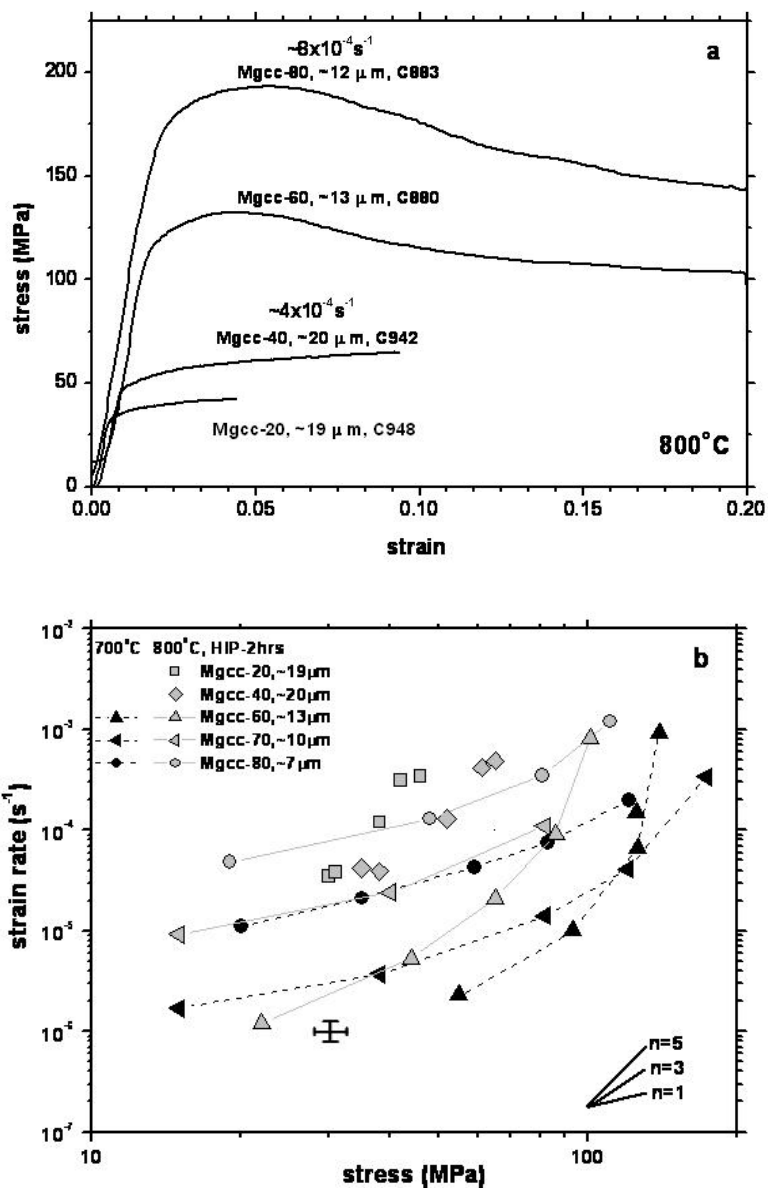
Figure 7. (a) Constant displacement rate tests on different Mg-calcites at 800°C and 300 MPa. The strain rates are high and all these samples deformed in dislocation creep regime. Strain weakening is obvious in some of the tests at high differential stress (> 100 MPa). Grain sizes at the starting of the deformation are estimated from the grain growth data and shown as indicated. (b) Mechanical data from stress-stepping and

creep tests after HIP for 2 hrs at 850˚C and deformation at 800˚C (gray symbols) and 700˚C (black symbols).   The crossed error bars represent the absolute uncertainty of the data points.   The data are scattered because both grain size and Mg content varies. There are, however, systematic trends.   Notice that the stress sensitivity of strain rate (*n*) increases with differential stress, and that the transition from diffusion creep to dislocation creep (identified by the change in slope) is shifted to higher stress for samples with higher Mg content (i.e., 700°C).
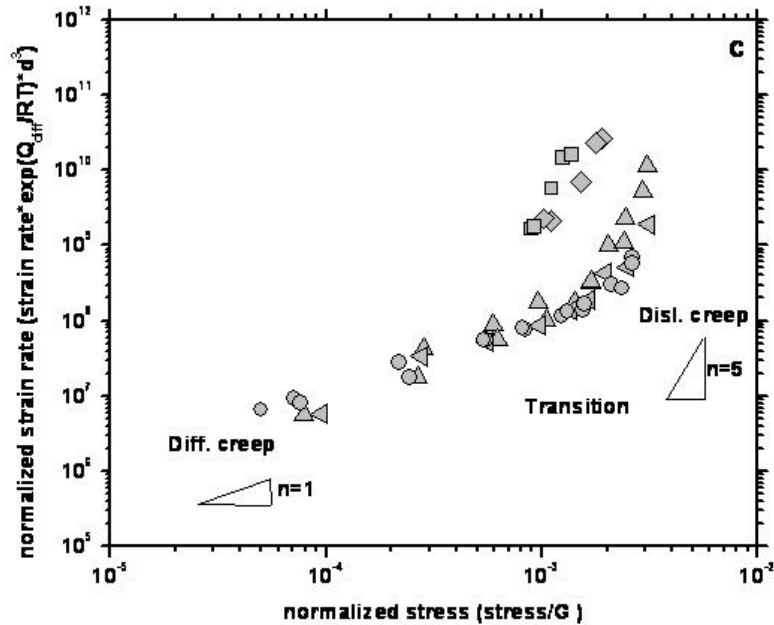
Figure 7 (c) Normalized strain rate vs. normalized stress. When the differential stress is normalized by the shear modulus adjusted to reflect changes in the elastic modulus owing to different compositions, and strain rate is normalized by grain size and a kinetic term appropriate for diffusion creeps, much of the scatter seen in 7b is removed. The normalization of the strain rate removes the effect of grain size which is systematically smaller in the high Mg calcites. Notice that the low Mg-calcite aggregates are weaker in the dislocation creep region. The strength of calcite increases with Mg content in dislocation creep regime, but not in the diffusion creep regime.
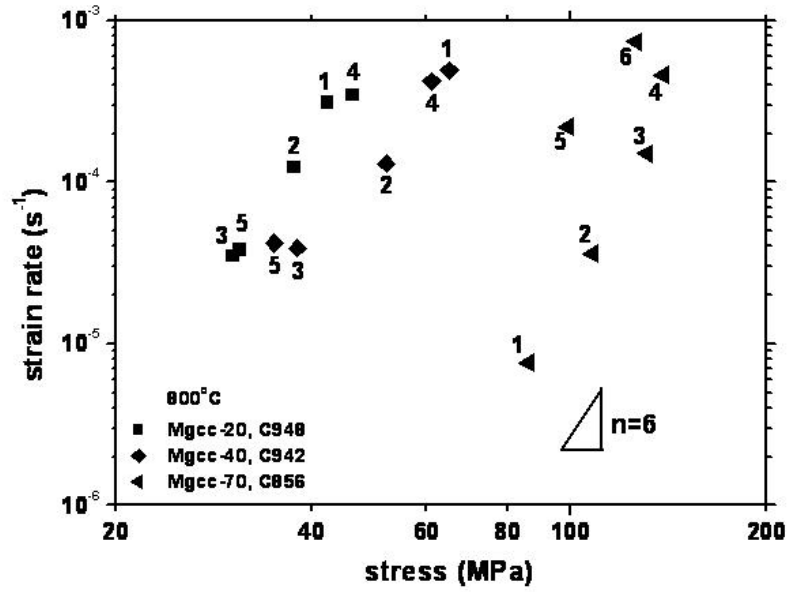
Figure 8. Data reproducibility is shown by creep step tests. Numbers indicate the order in which the tests were conducted. The sample with the highest magnesium content indicates a strength that changed when the initial stress was revisited.
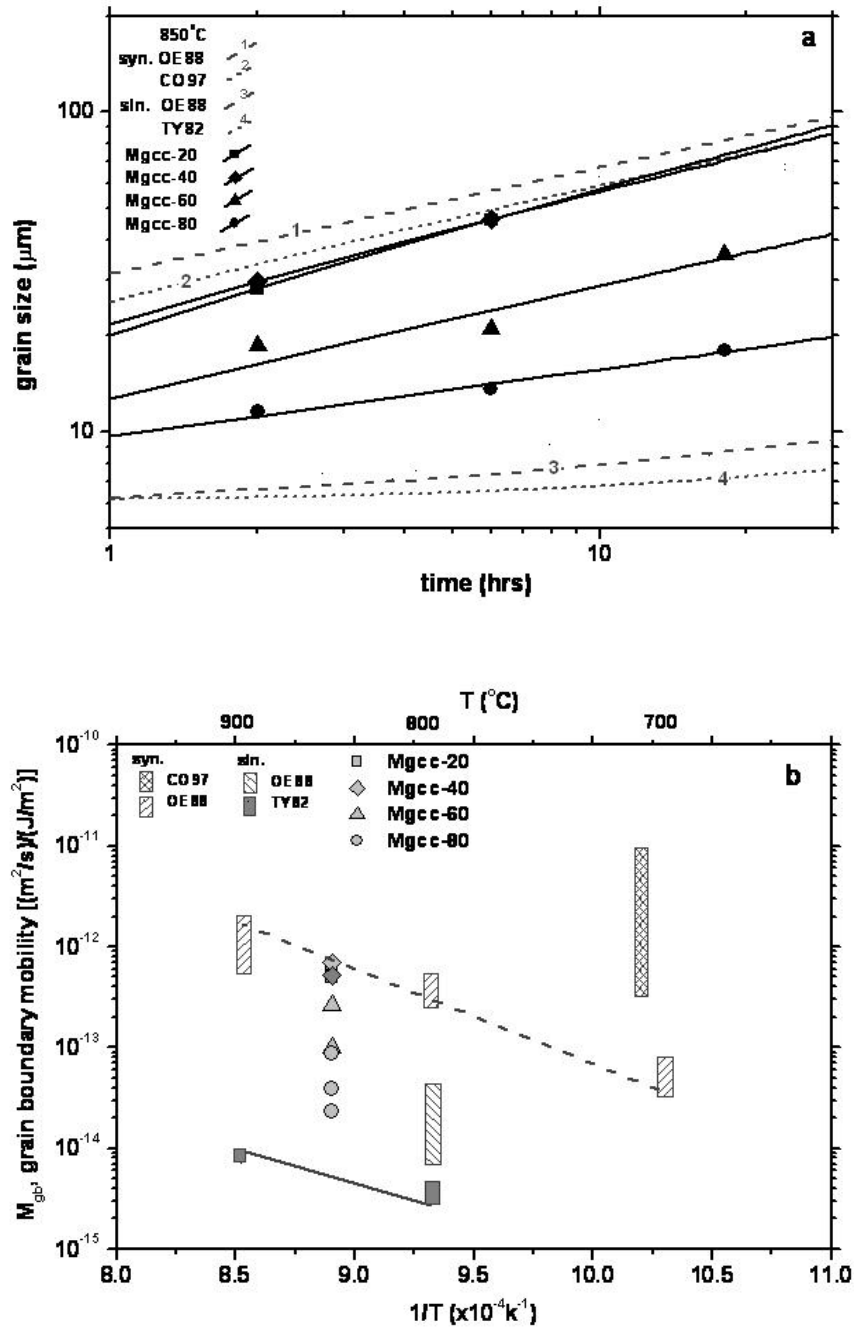
Figure 9. (a) Grain growth data compiled for pure synthetic calcite from Olgaard &

Evans, 1988 (OE88, line 1), Covey-Crump, 1997 (CO97, line 2); for Solnhofen limestone

from Olgaard and Evans, 1988, and Schmid, 1977 (line 3), Tullis and Yund, 1982 (TY82,

line 4); and for synthetic Mg-calcite (symbols with solid lines; this study).   Details of

grain growth kinetics are compiled in Table 2.   (b) Grain boundary mobility $(m^2/s)/(J/m^2)$

as a function of inverse temperature (1/T) for different calcite rocks.   Mobility is

estimated from normal grain growth data using equation $M = \frac{1}{2} \cdot \frac{\bar{d}}{\gamma} \cdot \frac{\partial \bar{d}}{\partial t}$.
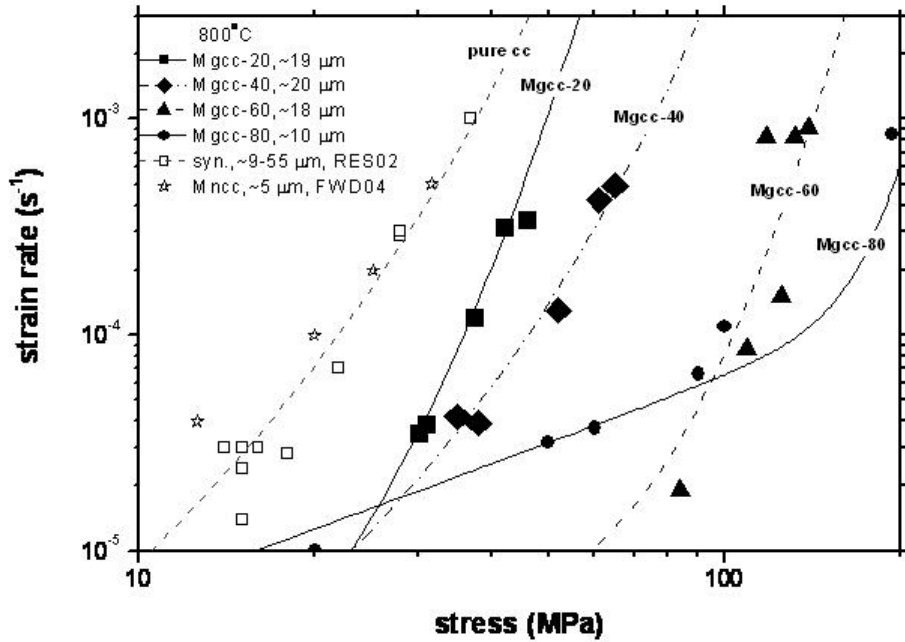
Figure 10.   Strength data and the curves fit using composite flow law (eqs. (1), (3), and (5)).   Parameters used see Table 3.   The experimental data of Mn-calcite (Freund et al., 2004) and synthetic calcite (Renner et al., 2002) are also plotted for comparison.
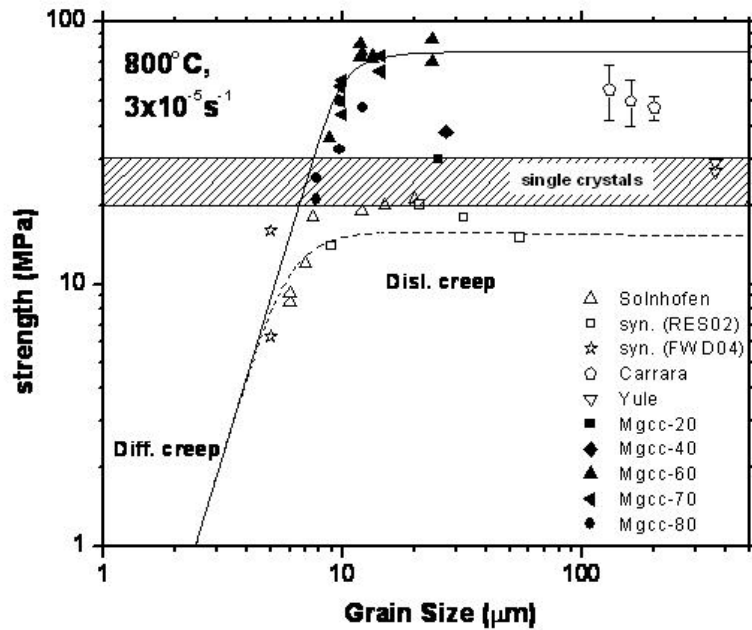
Figure 11. Flow strength vs. grain size for deformation of Mg-calcite (solid symbols) and previous studies on calcite aggregates (open symbols) at strain rate of $3 \cdot 10^{-5} s^{-1}$. When grain size is small, flow strength is approximately proportional to the grain size with grain size sensitivity factor ($m \approx 3$). The flow strength is inversely proportional to the grain size for large grains (Hall-Petch relation) in most calcite aggregates. References: Solnhofen limestone (Schmid, 1976; Schmid, 1977); synthetic marbles (syn., Renner et al., 2002 (RES02); Freund et al., 2004 (FWD04)); Carrara marble (Covey-Crump, 1997 (147 µm); de Bresser, 2002 (200 µm); Rutter, 1995 (130 µm); Schmid et al., 1980 (150 µm)); Yule marble (Heard, 1963; Heard and Raleigh, 1972); and single crystals (de Bresser and Spiers, 1993). The dashed line represents the best fit of the hybrid law to the data for Solnhofen limestone (Parameters see Table 3).
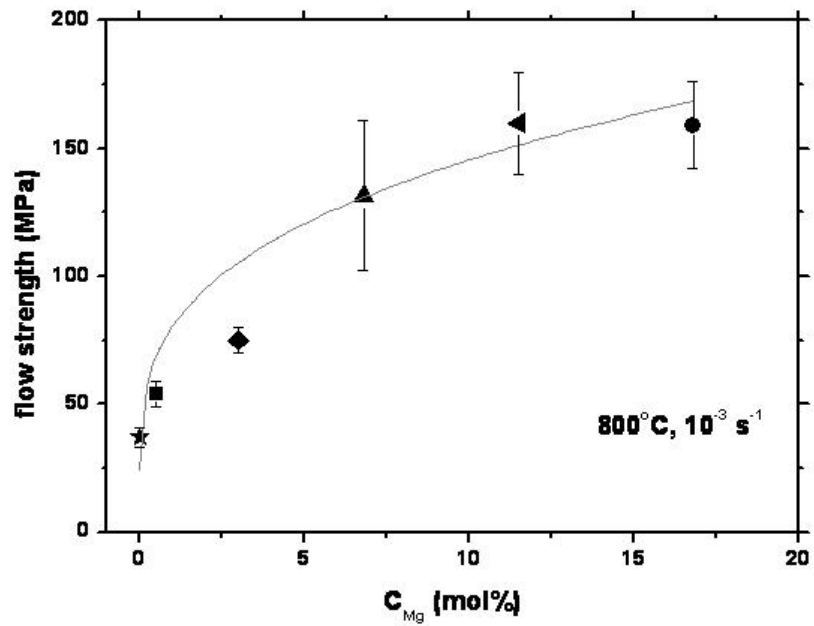
Figure 12. Correlation between flow strength and Mg-content. At a temperature of 800°C and strain rate of 10^{-3} s^{-1}, the samples deform in dislocation creep regime. The flow strength of calcite increases with Mg concentration. Dashed line shows the flow strength as a function of the solute concentration (C_s) to the 1/3 power.
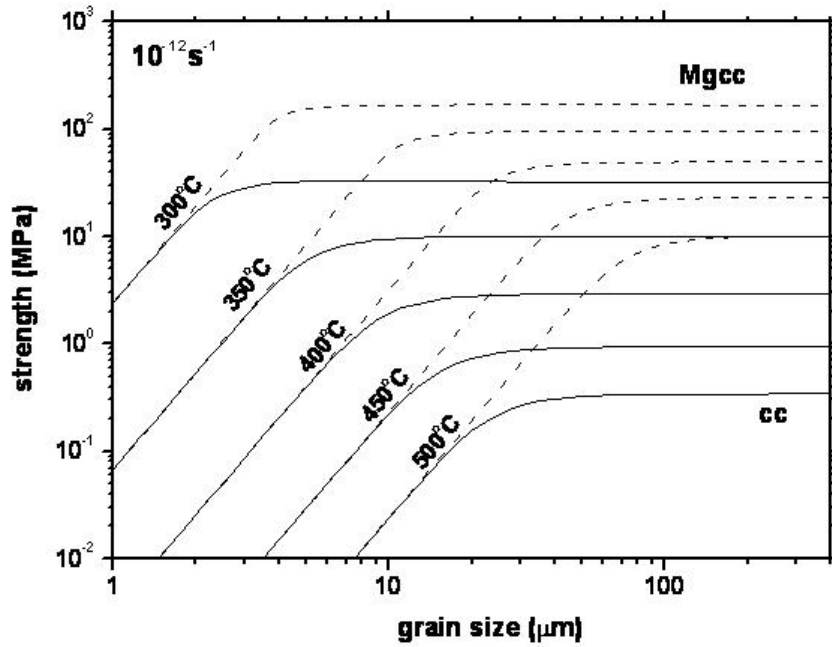
Figure 13. Curves of stress vs. grain size extrapolated to a strain rate of $10^{-12}s^{-1}$ at temperatures from 300 to 500°C. Mg-calcite and calcite are represented by the dashed lines and solid lines, respectively. High-magnesian calcite is much stronger compared with pure calcite in the dislocation creep regime; the transition from diffusion to dislocation moves to much higher stress.

Figure 14. Optical micrograph of carbonate mylonite from the Urgonian of the Morcles Nappe (Andreas), which contains echinoderms. These echinoderm fragments (center and lower left) consist of Mg-calcite and are stronger and thus less deformed than the surrounding fine-grained and completely recrystallized calcite matrix.

Table 1 Conditions and results of the deformation experiments

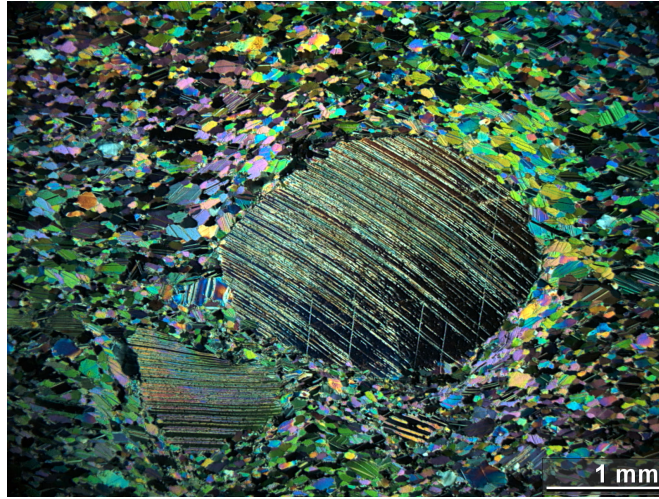| Run #	T (°C)	Stress (MPa)	Strain rate (s⁻¹)	Strain (%)	Grain sizes[a]	Porosity[b]	Description
C814	794	22 creep	$1.2 \cdot 10^{-6}$	0.8	16.0±3.1	1.5% (2.4%)	Mgcc-60,
		44	$5.3 \cdot 10^{-6}$	1.7			HIP-2 hrs
		65	$2.1 \cdot 10^{-5}$	2.6			
		86	$9.2 \cdot 10^{-5}$	4.1			
	691	93	$1.0 \cdot 10^{-5}$	4.7			
		126	$6.7 \cdot 10^{-5}$	8.1			
		104*	$3.2 \cdot 10^{-5}$	8.9			
		77*	$9.1 \cdot 10^{-6}$	8.8			
		64*	$8.0 \cdot 10^{-6}$	8.5			
		39*	$2.5 \cdot 10^{-6}$	8.9			
C817	Mgcc-70, HIP-2 hrs, load-cell signal unstable						
C818	795	15 creep	$9.2 \cdot 10^{-6}$	1.1	6.7±0.9	0.5%	Mgcc-70,
		40	$2.4 \cdot 10^{-5}$	2.5			HIP-2 hrs
		82	$1.1 \cdot 10^{-4}$	4.3			
	694	15	$1.7 \cdot 10^{-6}$	6.8			
		38	$3.7 \cdot 10^{-6}$	7.3			
		82	$1.4 \cdot 10^{-5}$	8.3			
		120	$4.1 \cdot 10^{-5}$	9.6			
		173	$3.4 \cdot 10^{-4}$	14.1			
C819	Mgcc-80, HIP-0.5hrs, jacket leak						
C820	801	19 creep	$4.8 \cdot 10^{-5}$	2.5	7.0±1.6	0.7%	Mgcc-80,
		48	$1.3 \cdot 10^{-4}$	4.8		(2.7%)	HIP-2hrs
		81	$3.5 \cdot 10^{-4}$	8.5			
		111	$1.3 \cdot 10^{-3}$	15.7			
	697	22	$1.1 \cdot 10^{-5}$	17.8			
		35	$2.1 \cdot 10^{-5}$	18.5			
		59	$4.3 \cdot 10^{-5}$	19.6			
		83	$7.5 \cdot 10^{-5}$	20.8			
		129	$2.0 \cdot 10^{-4}$	24.3			
C826	799	49 Creep	$1.0 \cdot 10^{-6}$	0.7	17.7±3.0	(0.7%)	Mgcc-60,
		66	$2.1 \cdot 10^{-6}$	1.0			HIP-20hrs
		91	$6.2 \cdot 10^{-6}$	1.5			
		108	$1.9 \cdot 10^{-5}$	2.1			
		124	$5.6 \cdot 10^{-5}$	3.1			
		140	$1.7 \cdot 10^{-4}$	5.0			
		151*	$3.7 \cdot 10^{-4}$	8.1			
		161*	$1.3 \cdot 10^{-3}$	19.6			

ID	Temp	Stress	Rate	Value	±value	%	Condition
C827	982	55 creep	$2.3\cdot10^{-6}$	5.7	11.7±1.7	0.5% (4.9%)	Mgcc-60, HIP-2hrs
		125	$1.5\cdot10^{-4}$	10.1			
		139*	$9.1\cdot10^{-4}$	33.3			
C855	Mgcc-60, HIP-20min, jacket leak						
C856	695	86	$7.6\cdot10^{-6}$	1.0	8.7±1.6	(3.3%)	Mgcc-70, HIP-2hrs
		108	$3.6\cdot10^{-5}$	3.2			
		131	$1.5\cdot10^{-4}$	7.5			
		139	$4.6\cdot10^{-4}$	16.3			
		99*	$2.2\cdot10^{-4}$	20.2			
		126*	$7.4\cdot10^{-4}$	27.5			
C857	801	104	$5.3\cdot10^{-4}$	4.9	8.5±2.0	0.5% (3.3%)	Mgcc-80, HIP-6hrs, weakening
		100	$1.1\cdot10^{-3}$	17.4			
		72	$7.0\cdot10^{-4}$	21.9			
C859	800	67	$1.2\cdot10^{-4}$	+16.8	13.1±3.0	(1.8%)	Mgcc-65, HIP-2hrs
		52	$8.5\cdot10^{-5}$	-15.5			
		59	$1.1\cdot10^{-4}$	+19.3			
		57	$1.0\cdot10^{-4}$	-5.9			
C869	807	85	$1.1\cdot10^{-4}$	3.8	12	0.5%	Mgcc-80, HIP-18hrs weakening
		96	$2.1\cdot10^{-4}$	7.4			
	756	97	$1.0\cdot10^{-4}$	10.5			
	695	73	$1.4\cdot10^{-5}$	12.3			
		97	$2.1\cdot10^{-5}$	13.3			
	805	79	$1.8\cdot10^{-4}$	16.8			
		100*	$3.3\cdot10^{-4}$	21.9			
C870	800	76	$2.4 10^{-4}$	4.6	9		Mgcc-60, HIP-2hrs
		85	$6.3\cdot10^{-4}$	9.9			
	751	89	$2.4\cdot10^{-4}$	13.0			
		98	$3.5\cdot10^{-4}$	16.8			
	694	164	$3.2\cdot10^{-4}$	20.8			
C880[c]	804	132	$8.2\cdot10^{-4}$	5.0	7	0.5%	Mgcc-60, HIP-2hrs
		115		10.0			
		101		20.0			
		90*		43.3*			
C883[c]	797	193	$8.5\cdot10^{-4}$	5.0	7	0.5%	Mgcc-80, HIP-30hrs
		176		10.0			
		143		20.0			
		127*		31.8			
C900	792	124	$7.8\cdot10^{-4}$	6.6	17	0.5%	Mgcc-60, HIP-4hrs
	745	159	$8.1\cdot10^{-4}$	11.3			

	695	208	$8.5 \cdot 10^{-4}$	15.8			
	743	179	$9.3 \cdot 10^{-4}$	20.6			
C942	785	65	$4.9 \cdot 10^{-4}$	7.0	25		Mgcc-40, HIP-2hrs
		52	$1.3 \cdot 10^{-4}$	10.8			
		38	$3.9 \cdot 10^{-5}$	15.8			
		61	$4.2 \cdot 10^{-4}$	21.4			
		35	$4.2 \cdot 10^{-5}$	24.2			
C948	800	42	$3.1 \cdot 10^{-4}$	4.4	27	3.8%	Mgcc-20, HIP-2hrs
		38	$1.2 \cdot 10^{-4}$	8.1			
		30	$3.5 \cdot 10^{-5}$	10.8			
		46	$3.4 \cdot 10^{-4}$	15.5			
		31	$3.8 \cdot 10^{-5}$	18.6			
C1038[c]	800	143	$8.9 \cdot 10^{-4}$	5.0	22	0.5%	Mgcc-60 HIP-18hrs
		151		10.0			
		128		14.7			

Table 2 Some laboratory determination of grain growth parameters in calcite aggregates

	T (°C)	P (MPa)	k (μm^n/s)	n	Q (kJ/mol)	t_0 (s), d_0 (μm)	Reference
Solnhofen	800	300	0.02-0.2	>7	190	0, 6.1	Schmid et al., 1977a
	900	300	0.08-0.4	4.8	190		
	800	1500	0.05-0.5	5.1	200	0, 6.1	Tullis & Yund,
	900	1500	0.8-1.0	3.0	200		1982
	800	300	0.03-0.13	5.2		0, 6.1	Olgaard & Evans, 1988
	900	300	0.1				
Syn. cc	800	300	2.4-2.8	2.6±0.1	180±50	0, 7	Olgaard & Evans, 1988
	706	185	0.15	2	232	1000, 12	Covey-Crump, 1997
Mgcc-20	850	300	0.17	2.4		1000, 5	This study
Mgcc-40	850	300	0.43	2.7		1000, 5	This study
Mgcc-60	850	300	0.15	2.9		1000, 5	This study
Mgcc-80	850	300	1.73	4.7		1000, 5	This study

Table 3 Fitting the data using hybrid flow law

	N	m_p	lnA_{plb}(MPa^{-2}s^{-1})	$\Sigma_{p,0}$(MPa^{-1}kK^{-1})	lnk(MPa μm^m kK^{-1})	Q_{plb}(kJ mol^{-1})	$\aleph_\sigma$
Solnhofen	32	0.5	6.1±0.5	19.9±11.0	4.7±0.2	205±24	1.005± 0.102
		1*	5.9±0.6	29.7±9.5	5.1±0.2	205±14	1.005±0.098
Syn. cc	82	1	4.3±0.5	23.5±1.5	2.8±0.7	191±24	1.015± 0.128
Mgcc-20	5	0.5	4.4±1.1	8	5	201±10	1.003± 0.107
		1	1.7±1.2	8	5	201±10	1.002± 0.021
Mgcc-40	5	0.5	3.5±1.1	8	5	201±10	1.001± 0.044
Mgcc-60	54	0.5	3.2±0.6	41.2±4.2	4.1±0.2	201±15	1.025± 0.160
			-3.3±1.1	8	5	180±10	1.043±0.175
		1	-2.0±0.7	30.7±5.3	0.6±4.3	197±20	1.028± 0.152
Mgcc-70	42	0.5	-2.1±1.3	35.5±11.2	2.0±0.9	196±20	1.018± 0.157
		1	-1.2±0.9	45.1±6.3	0.7±1.1	198±22	1.007± 0.057
Mgcc-80	43	0.5	2.0±0.6	12.0±11.7	7.8±0.3	181±12	1.027± 0.213
			-4.6±1.2	8	5	202±10	0.984± 0.036
		1	2.1±0.6	11.9±11.7	9.3±0.3	182±15	1.026± 0.211

	N	$\ln \dot{\varepsilon}_{pwr0}$ (MPa^{-2}s^{-1})	n	Q_{pwr} (kJ mol^{-1})	$\aleph_\sigma$
Solnhofen	32	2.6±0.6	3.4±0.1	209±4	1.014± 0.158
Syn. cc	82	-0.8±0.5	4.3±0.1	196±16	1.017± 0.140
Mgcc-20	5	-0.7±2.2	3.9±0.6	201±5	1.011±0.097
Mgcc-40	5	-0.4±1.9	3.6±0.5	201±5	1.009± 0.082
Mgcc-60	54	-12.5±1.3	5.6±0.3	202±18	1.032± 0.154
Mgcc-70	42	-9.6±1.7	5.0±0.4	200±20	1.018± 0.119
Mgcc-80	43	0.1±0.8	2.6±0.1	188±15	1.015± 0.183

* We use 1327°C and 1241°C as melting temperatures (T_m) for Mgcc-20 and Mgcc-80, respectively (Byrnes and Wyllie 1981; Irving and Wyllie 1975).

Chapter 3: Strain Heterogeneity during Dislocation Creep in Carrara Marble Using a Micro Scale Strain Mapping Technique

Abstract

By combining a high resolution surface mapping technique with the split cylinder technique, local strain heterogeneities can be quantitatively measured in deformation experiments of Carrara marble at 400-700°C, 300 MPa confining pressure, and at strain rates of 10^{-4} to 10^{-5} s^{-1}. This micro-scale mapping technique uses grid markers and computerized image analysis to evaluate local strain heterogeneity at a scale of micrometers. This method is based on: (1) depositing grid markers on the polished surface of a half-cylinder of Carrara marble, (2) performing conventional triaxial compression tests on composite samples of two half-cylinders, (3) comparing the positions of each grid marker in both undeformed and deformed samples, and (4) computing micro-scale strain distributions. In this material under these conditions, strain heterogeneities at the scale of grains and smaller are observed to be as large as 300% of the bulk aggregate strain. Localized deformation occurs along twins and grain boundaries, but can also be observed as pathy strain variations in intragranular regions. Although the amount of heterogeneity is more pronounced at scales smaller than grains, the strain averaged over individual grains may also vary by 50% of the bulk strain. Schmid factor analysis indicates that c and r<sd> are the two most active slip systems in the compression test of Carrara marble at 600ºC.

3.1 Introduction:

Natural deformation of rocks is usually inhomogeneous, and often occurs over a wide variety of spatial scales. Thus, a full understanding of tectonics and orogenic processes will necessarily involve understanding the causes and influences of localization, material heterogeneities, and mechanical anisotropy. It is easy to rationalize spatial heterogeneity in deformation during cataclastic faulting and frictional sliding processes. By contrast, dislocation mechanisms are often regarded as being non-localized. In fact, however, the anisotropic nature of crystal slip usually entails variations in reorientation of individual grains and heterogeneous deformation within the polycrystalline material, even under homogeneous and gradient-free external loadings. This mechanical anisotropy, which tends to be exaggerated in low-symmetry minerals, may lead to large spatial heterogeneities in strain and grain orientation.

At the thin-section scale, the quantification of grain-to-grain interactions during straining is relevant for the improvement and verification of models of polycrystalline plasticity. Such models are valuable for understanding the textures produced during deformation of complex, polycrystalline materials with multiple phases, i.e., rocks. The inverse problem is also of critical importance: insight into the production of texture is a valuable tool in unraveling the deformation history of rocks based on their current microstructure. One method in particular, the self-consistent model, has been widely used to understand the texture development of materials during plastic deformation (Molinari

et al., 1987; Wenk et al., 1987; Lebenson & Tome, 1993). These models are called self-consistent because they compute the mechanical interaction between each grain and an average equivalent background. Self-consistent model generally provides a good description of the production of global textures, but they do not always predict local aspects of the actual deformation, e.g., individual lattice rotations or grain deformation sometimes are not completely consistent with experimental observations of the evolution of strength or of the intensity or of the details of orientation distribution functions.

To understand the vagaries of local strain distribution, several recent studies have focused on producing quantitative descriptions of the spatial heterogeneity of inelastic strain and crystal orientation at microstructural scales (Biery et al., 2001; Raabe et al., 2001; Sachtleber et al., 2002; Wu et al., 2006). Often in these metallic materials, large strain tends to be accommodated by weak grains in preferred slip directions, but the heterogeneity may even extend to scales smaller than the grains. Depending on the material, loading conditions and geometry, strain can be partitioned in regions near grain boundaries, or even, at the boundary itself. The comparison of results from such experiments and simulations will provide useful insight into the accuracy and efficacy of the polycrystalline homogenization models and constrain our knowledge of the physics of inelastic deformation. The crystal-plastic deformation of rocks in the laboratory is also often inhomogeneous at the microstructure scale, a particular example being given by the extensive studies of microstructures and mechanical behaviors of Carrara marble (Pieri et al., 2001; Rutter, 1974; Rutter, 1998; Rutter et al., 1994; Schmid et al., 1980). In this

material, grains favorably orientated for slip deformation clearly deform more than other grains in the harder orientations (Wenk, 2002; Wu et al., 2006). Recent torsion experiments on Carrara marble (Pieri et al., 2001) suggested that its texture continues to evolve to a shear strain of 5 where the sample reaches a steady state condition and is characterized by fully recrystallized grains in easy slip orientations. The texture simulations of Carrara marble using visco-plastic self consistent (VPSC) model suggest that recrystallization is an important process in both torsion and compression tests (Barber et al., 2007; Lebensohn et al., 1998; Pieri et al., 2001). At lower temperatures, faster strain rates, and higher stresses, twinning is an important deformation mechanism, and accommodates strain in an extremely localized fashion (Turner et al., 1954; Weiss and Turner, 1972). At higher temperatures, grain boundary sliding mechanism can be important in accommodating strain incompatibility between neighboring grains (Schmid et al. 1980; Rutter, 1995).

In this paper, we investigated heterogeneous deformation of Carrara marble produced during conventional triaxial deformation tests implementing a strain mapping technique recently developed for metals (Biery et al., 2001; Park and Schowengerdt, 1983; Wu et al., 2006). The goals of this study are to examine the crystal-plastic processes responsible for creep deformation of Carrara marble by plastic behavior in greater detail, to develop a quantitative understanding of the scale of heterogeneities produced, to gain fundamental insight into polycrystalline plasticity, and to understand the mechanisms by which strain localizes. We place particular attention on quantifying variations in strain within grain

interiors and at grain boundaries, and on recognizing the relative activities of different slip systems.

   The strain distribution mapping technique usually includes a series of image processing algorithms (Biery et al., 2001; Park and Schowengerdt, 1983). By studying the change of grid marker positions due to deformation process, 2D strain distribution map can be derived. By using the surface mapping capability of a digital microscope, we developed a new procedure which allows us to characterize the full, 3D strain tensor. The main steps of our strain distribution mapping technique include: (1) acquire 2D gray-scale images of the grain structure and superpose test grids on a flat surface on a half-cylinder, (2) reconstruct a cylindrical sample from two half-cylinders and deform under conventional triaxial loading at temperatures between 400-800°C, confining pressures of 300 MPa, and strain rates of $\sim 10^{-5}$-10^{-4} s^{-1}, up to about 25% strain, (3) recover the sample, and determine new grid marker positions using an image reorganization technique, (4) calculate the full strain tensor at each position using the relative displacements of the grid markers before and after deformation and an n-point averaging technique, and (5) mapping the strain distribution at the micrometer scale. Most of the image processing and strain mapping procedure was done in Matlab. For comparison with the strain mapping, the grain orientation map of an interested area is acquired using the electron back-scattered diffraction pattern. The relative activity of different slip systems can be inferred from the relative strain and rotation produced during the compression tests and compared to the resolved shear stresses produced by the bulk loading on each grain.

Considerable development of laboratory technique and data analysis methods was necessary to implement the measurements, and this development limited the number of experiments that could be analyzed. However, the concept and experimental design can be considered to be proven, and the results which are available are quite interesting and provocative.

3.2 Methodology:

3.2.1 Experimental procedure:

Our samples were constructed from blocks of Carrara marble, a coarse-grained, nearly pure calcium carbonate rock of Liassic age quarried from the northwestern Alpi Apuane region of the Appenines fold and thrust belt in Italy (Coli, 1989). These rocks contain accessory phases of quartz, albite, white mica, and some opaques, in amounts that vary spatially, but are never more than 5% of the total. The particular sample that we used could be classed as a type A, "granoblastic" microfabric, with roughly equiaxed grains (Molli et al., 2000). Consideration of structural field relations and geochemical measurements suggests that rocks from this location with this fabric have probably been exposed to metamorphic temperatures sufficient to coarsen the grains, under small or no deviatoric stresses (Molli and Heilbronner, 1999). Although marbles with type A fabrics are largely isotropic, there may be a weak preferred orientation inherited from earlier deformation episodes, and some of the grain boundaries are mildly undulose. This material is useful as a test material for these experiments, because it has been studied

extensively by many investigators, is nearly a single mineral phase, and has large, equi-axed grains.

The strain mapping technique relies on calculating the relative displacements of identifiable points in the deformed and undeformed configurations. To produce a simple configuration for the undeformed state, we constructed a grid of electro-deposited carbon or gold spots on a flat, polished surface of a half cylinder, 20 mm in length and 5 mm in radius (Fig. 1). We called the surface with the grid markers surface A (Fig. 1a). The deformation sample was completed by mating a second half-cylinder (surface B) to the first (Fig. 1b-c). In addition, we put a copper foil in between the two half cylinders to separate them more easily after the deformation test. This copper foil has a window shape, so that most of surfaces A and B are in contact with each other during deformation at pressure and temperature conditions. The half-cylinders are formed from immediately adjacent sections of the block. Because the kerf of the diamond saw used to cut the billets for the two halves is much smaller than the grain size of the sample, the grain structure of the two half cylinders is nearly contiguous across the reference surface. Both flat surfaces are prepared by polishing using alumina grit on cloth laps. In the final polishing procedure of surface A, we use colloidal silica (~0.03 microns) on automatic wheels for several hours.

The sample cylinders are then loaded into a copper jacket, pressurized to about 220-240 MPa and heated to 400-800ºC at a rate of 25ºC/min in a Paterson deformation apparatus (Paterson, 1995). The final confining pressure is kept at 300 MPa except one

experiment at 100 MPa (CM08). Compression tests are performed at constant strain rate of $\sim 10^{-5}$ to 10^{-4} s^{-1} to a final strain of $\sim$5-25%.   See Table 1 for a detailed description of the experimental conditions; detailed discussion of the conventional triaxial deformation tests can be found in Renner et al. (2002). After the deformation test, the sample is removed from the outer pressure jacket and then split open along the internal copper foil to recover the deformed internal surface, which, strictly speaking, is no longer planar.

The grain microstructure intersected by the internal surface was observed in reflected polarized light, both before and after deformation (Fig. 2 shows CM17). Before deformation, gold or carbon markers are deposited onto surface A using a commercially available nickel mesh grid with 2000 wires/inch.   Grid markers are shown as the light square dots (Fig. 3a, CM18 before deformation). Before deformation the markers are squares with sides about 5 µm long; the distance between the centers of two grid markers is 12.64µm.   A few narrow twins are visible in the undeformed starting material. Notice that some grid markers are missing in the micrograph due to imperfections of the undeformed sample surface.   We put additional scratches onto this surface in order to identify the grid area before and after deformation.

The starting Carrara marble sample has roughly equiaxial grains (Fig. 2a) and the grain size distribution is similar to a lognormal distribution (Fig. 2c).   Grain size is analyzed by tracing the grain boundaries in ImageJ, measuring the grain area, and computing the diameter of a circle having equivalent area. The number-weighted mean grain size (equivalent area) of the starting Carrara marble is $\sim$130 µm. The deformation test

introduces thick twin bands (Fig. 2b, sample CM17). The distribution of grain size (equivalent area) of the deformed sample shows only a slight variation from the undeformed material.

After the grid region is located in the deformed sample, 2D gray-scale images and a through-focus series of micrographs are collected at 700x magnification using reflected light with crossed polarizers in a Hirox KH-7700 digital microscope. The through-focus images provide surface elevation data (Fig. 3b). The three dimensional coordinates of each grid marker are then identified by the analyzing 2D gray-scale images and 3D surface data (as described below in section 2.2). The resolution of 2D images at 700x magnification is 3.6 pixels/micron.

We identify the same grid markers in the deformed sample by looking for the same grain near the scratched lines and then comparing the grain boundary geometry with the undeformed sample. The change of grid marker positions owing to the deformation process will provide us information of the strain distribution in the microstructure scale. Of course, we can only image a single surface within the sample, and strain can be analyzed only for a small portion of the sample.

The final step in characterization is to coat the surface with Au/Pt, polish it to generate a more conductive surface, and use EBSD techniques to map crystallographic orientation. Thus far, only a single polished surface (surface A) has been studied in SEM (JEOL 840).

3.2.2 Producing the strain distribution map:

In order to get the strain distribution map, there are four procedures: image acquisition, grid-marker location, strain-tensor calculation using an n-point strain analysis method (P-Y F. Robin, personal communication), and strain-distribution mapping. Both 2D gray-scale images and 3D surface data are acquired using the 3D digital microscope as described above. The positions of the grid markers are assigned three-dimensional coordinates and a descriptor of the gray-scale distribution in their proximity.

The center point of each individual grid-point is located using a pattern recognition technique (Fig. 4). First we locate the grid marker positions in the two images using a convolution algorithm, namely, by convolving the image with a kernel that contains a reference marker (Biery, 2003). The reference marker is chosen as an average of 4 grid markers. By convolving the kernel with the entire image, we are able to identify the maximum of the peaks in the filtered image as the center position of the grid marker. This convolution step is sufficient to locate all grid markers to within 1 pixel using a 2D 256-gray-scales image. Then we use the x and y coordinates of each grid point to look up the third, z coordinate using the surface elevation data from the 3D digital microscope (Fig. 5a). Since the grid marker is square 18 pixels on a side in the 2D gray-scale image, we then find the surface elevation of a certain grid maker by taking the average within a certain window size. Our data shows that the average surface elevation is not sensitive to the window size (Fig. 5b).

The grid-marker coordinates are then stored in a list, which is ordered so that each grid marker in the reference image is matched to a corresponding grid marker in the distorted image. This might seem to be a trivial problem; but it takes computational time to trace the same grid marker in the distorted image because the sample size (10×20 mm^2) is much larger than the size of the grid marker (5 μm^2). This process is done by identifying a particular grain near the scratched lines and then comparing the grain boundary geometry in the undeformed and deformed samples. The 3D strain tensor can then be calculated using the grid marker positions in both undeformed and deformed samples.

Recovering the grid markers also proved to be challenging and we have been successful only for a few deformed samples (Table 1). For example, at high pressure and temperatures (>600ºC), the contacting surfaces of the two half cylinders tend to be welded together, and it is hard to recover the grid markers. If surfaces A and B can be separated successfully, some grid markers may be transferred from surface A (Fig. 6a) to surface B (Fig. 6b). In order to get a better coverage of grid marker positions in the deformed sample, we use a 3-point analysis to combine two surface images. After applying a mirror reflection, we choose 3 features that are distinctive and can be observed clearly in both surface images (e.g. color dots in Fig. 6). Then we use a least-squares method to decide the horizontal shifts and rotation angle between the two images. This procedure allows us to identify more grid markers in the deformed samples and thus a more detailed deformation map.

97

3.2.3 n-point strain analysis:

We calculate the local strain using an n-point strain analysis method by Robin (2007, personal communication), which calculates local strain tensor from the displacement of any number of grid markers (n>3) relative to each other.   Suppose we have the positions of n grid markers at two time intervals: the position of the ith grid marker $X_i^0 = [x_i, y_i, z_i]^0$ at time = 0 in the undeformed sample, and $X_i^1 = [x_i, y_i, z_i]^1$ at time 1 in the deformed sample.   There are two steps we need to calculate the strain tensor for that certain area: (1) recalculate the positions of each point i, X_i^0 and X_i^1, with respect to their moving centroid, C^0 and C^1, i.e., $\overline{X}^0 = X^0 - C^0$, and $\overline{X}^1 = X_i^1 - C^1$, (2) find a deformation gradient matrix, U ∍

$$\overline{X}^{1*} = U\,\overline{X}^0.$$

The best-fitting coefficients of U are those that minimize the sum of the squares of the distances between $\overline{X}^{1*}$ and $\overline{X}^1$, i.e., minimize χ^2 where

$$\chi^2 = \sum_{i=1}^{n} \left| \overline{X}_i^1 - \overline{X}_i^{1*} \right|^2 = \sum_{i=1}^{n} \left| \left(\overline{X}_i^{1T} - \overline{X}_i^{0T} U^T \right) \left(\overline{X}_i^1 - U \overline{X}_i^0 \right) \right|.$$

A 3-points grid analysis is sufficient to solve the problem, but we can use more neighboring grids to get the average of larger areas.   The strain tensor ε can be found from the deformation gradient tensor by

$$\varepsilon = \frac{1}{2}\left(\mathbf{U} + \mathbf{U}^T\right) - \mathbf{I}$$

98

The maximum compression stress lies in the x (or 1) direction in the x-y plane so that ε_{11} will be the maximum compression strain; displacements perpendicular to the test plane, i.e., the z direction, will give rise to strain components (ε_{i3}). We assume that there is no volumetric strain during the plastic deformation ($\varepsilon_{11} + \varepsilon_{22} + \varepsilon_{33} = 0$). The Von Mises effective strain can then be calculated using

$$\varepsilon_{eff} = \sqrt{\frac{2}{3}\varepsilon_{ij}\varepsilon_{ij}} \ .$$

3.2.4 Error analysis:

During some of tests, grid markers originally deposited on the A face of one hemi-cylinder are transferred to the B face of the mating hemi-cylinder. In some cases, a particular marker or a patch of them will appear on both A and B faces, in other cases, the marker(s) are entirely missing on one face. When a patch of markers appears on the B face and not the A face, we have used image processing to superpose the marker grids and obtain better areal coverage. When the markers can be found on both surfaces, we can use cross-correlation to provide information about the precision of the determination of grid-marker position (Fig. 7). For sample CM18, the correlation coefficients of displacement components in the x, y, z directions are 0.99956, 0.99971, and -0.51344, respectively. The correlation coefficient is close to 1 for the in-plane components indicating that good resolution in the 2D grid marker positions, but the correlation in z-direction is not as good. Displacements in the z direction might be less precise for

several reasons, including: (1) imperfection in grid marker shape, (2) errors during the surface data acquisition, (3) de-trending process in leveling the surface, and (4) departures from planarity of the test surface, either originally present on the polished surface or created by compacting small mismatches in the two mating surfaces during pressurization and deformation. Since the 2D grid marker positions can be correlated very well, the effect of imperfections in grid marker shape are probably small, unless there are significant and undetected variations in the profile of the marker in the z direction. The de-trending process in leveling the surface can be improved by increasing the size of sampling area. The error in the surface elevation probably mostly comes from the surface data acquisition procedure from the 3D digital microscope or from departures from planarity. Estimates of both effects suggest that the accuracy in the z direction will be no better than $\pm 0.5\mu$ m.

The resolution of strain-mapping technique relies on the image resolution and strain calculation algorithm. The minimum detectable strain can be defined as the ratio of minimum detectable marker shift to original marker spacing. Since we are able to locate the grid marker position to within 1 pixel using a pattern reorganization technique, the minimum detectable strain can be less than 1% for our study. Suppose that we apply a 3-point strain analysis and the deformation is homogeneous within that area, the total error in strain estimation can be the same as the minimum detectable strain. One can average over a larger number of grid points and obtain the average strain within a larger area. The precision of the measurement increases, but, of course, the cost is a sacrifice of

information about the local heterogeneity.   See Table 2 for detailed information of the strain resolution.

An example of the effects of averaging is shown in Fig. 8, where four contour maps of strain distributions were made of the same area using averages of 3 to 9 points (see Table 2).   It is clear that the strain heterogeneity decreases with increased averaging; the local heterogeneities are lost in the 9-point analysis. The difference in the ratios of the maximum/minimum strain values with respect to the average strain decreases from 7 to 2 from Fig. 8a to 8d; resolution is one issue, but this result probably also indicates increasing strain heterogeneity at smaller length scales.

3.3 Results

All the deformation tests for this study were conventional triaxial compression tests performed with confining pressures of 300 MPa and at constant temperatures between 400-800ºC (Table 1).   The tests were done in constant displacement-rate mode to strains between 5% and 25%. After yielding, the marbles may either strengthen or weaken (Fig. 9), but both effects are quite mild over this strain interval. The stress vs. strain diagrams agree well with previous tests on Carrara marble (Fig. 9c) (Covey-Crump, 1997; de Bresser et al., 2001; Rutter, 1995; Schmid et al., 1980), suggesting that the effect on the mechanical properties of putting a copper foil in between two half cylinders is small.

3.3.1 Strain mapping:

The strain mapping analysis has not been successful at temperatures above 700ºC,

because the two contacting surfaces of the half cylinders tend to weld together at higher pressures and temperatures. Consequently, it is difficult to expose the grid markers. Although it is possible that improved recovery techniques might remove this obstacle, at present, detailed analyses are available only for samples CM09, 11, 12, and 18, and we concentrate this discussion on those samples.

Using the grid marker positions from the image data and the n-point strain analysis technique, we can derive the spatial distribution and heterogeneity of strain along the test plane (Figs 8, 10-18). Notice that, in all the 2D images, the axis of maximum shortening (and greatest compression) of the aggregate lies along the vertical direction. Several different visualization techniques can be used to analyze the deformation: Fig. 10a shows a 2-D displacement gradient map for sample CM18, which was deformed at $3x10^{-5}$ s^{-1} to 10% strain at 400ºC and 300 MPa, while Fig. 10b shows the 2D gray-scale image of the undeformed sample, a 3D displacement-gradient map, and a 3D strain tensor map, all of the same area. The 2D displacement-gradient map shows the direction and magnitude of movement of the grid markers, in the original test plane, relative to a center point. In general, the displacement-gradient map is characterized by a flow pattern from the upper and lower planes, i.e., parallel to the direction of shortening of the aggregate, to the periphery of the grid, parallel to the direction in which bulk sample is expanding. But, notice that there are lots of local heterogeneities. One example can be seen in the upper right corner, where the magnitude of displacement is larger than in the other corners. Apparently, grains in that region accommodate more strain, probably because they are in

a weak crystallographic orientation. Finally, the 3D displacement-gradient map shows both the in-plane and out-of-plane deformation, and the 3D strain map shows the distribution of the local strain tensor (Fig. 10b).

Contour maps of the strain tensor components provide information about the heterogeneity in local strain.   The magnitudes of the individual components of the strain tensor are shown in Fig. 11a-b, and Fig. 11c-d, for samples CM18 and CM11, respectively. Those samples were deformed at 400 and 600ºC to a final strain of ~10%. In both samples, the contour maps indicate substantial heterogeneities at microstructure scale.   Even though the sample is deformed is in compression (imposed strain ε_{11}~-0.10), there are local areas deforming in a sense opposite to the imposed overall deformation. Because the mechanical response of each grain depends on both its crystallographic orientation, and the constraints due to the neighboring grains, spatial variations in modulus, strength, and geometry can give rise to local variations in stress and inelastic strain. For sample CM18 (Fig. 11a-b), the variation in components of the strain tensor follow: ε_{11} is ~-7%$\pm$8%, ε_{22} is ~2%$\pm$5%, ε_{33} is ~4%$\pm$10%, ε_{12} is ~0%$\pm$5%, ε_{13} is ~0%$\pm$6%, and ε_{23} is ~0%$\pm$6%. For sample CM11 (Fig. 11c-d), the strain tensor components: ε_{11} is ~-12%$\pm$11%, ε_{22} is ~8.1%$\pm$13%, ε_{33} is ~4%$\pm$16%, ε_{12} is ~0%$\pm$8%, ε_{13} is ~-1%$\pm$8%, and ε_{23} is ~0%$\pm$9%.   The minimum and maximum strain varied by a factor of ~6-8 compared to the imposed aggregate strain.   Such large heterogeneities of strain also suggest substantial variations in stress at the grain scale.   On average, however, the strain components are roughly consistent with the bulk deformation.

Notice that the average magnitude of ε_{11} is roughly twice the average magnitude of ε_{22} and ε_{33}, and that the shear components are smaller than the principal strain components, both generalizations that one would expect for this geometry.

Strain is accommodated in a spatially heterogeneous fashion for both CM18 (400ºC) and CM11 (600ºC). The magnitudes of the variation of the von Mises effective strain are also similar; and both materials seem to have concentrated deformation near the grain boundaries (Fig. 12). While some grains carry less than 5% strain in their interiors, some local areas have accumulated strains above 20%. The grain boundaries often show concentrations of high strain compared with the grain interiors, and the strain magnitudes there are often more than twice that of the imposed strain. By comparing Fig. 12b with its optical micrograph, we also find high strain concentrations within the middle large grain where twin/slip lines exist in NW-to-SE direction, and the strain contour maps clearly show strain localization near both twin bands and grain boundaries. By contrast, the strain distribution in grain interiors is usually more homogeneous. It will be interesting to see if this anecdotal evidence can be demonstrated to occur as a general rule.

Strain ellipses show that the magnitude of finite strain and the direction of the principal stretching directions. If the sample is deformed homogeneously, the theoretical finite strain ellipse after 10% strain in compression will look like Fig. 13a, and will be the same everywhere. The deviation of strain ellipses in Fig. 13b from Fig. 13a gives us information of the strain heterogeneity and the local stress conditions. The principal

stretching direction varies in local areas indicating the possible relationship between the local stress and the microstructures. It is of interest that the grain boundaries don't show obviously a higher shear deformation than the grain interiors.

3.3.2 Average grain strain:

We are also interested in the average strain of individual grains, which will provide us information about the single crystal behavior inside polycrystal. Average grain strain is computed using 4 steps: (1) trace grain boundaries, (2) discretize individual grains, (3) find grid markers that belong to a certain grain, and (4) average strains inside individual grains. In Fig. 14 we show 3D strain ellipsoids, accompanied by average Von Mises strains, superposed on the grain outline. The imaged area is the same as in Fig. 13b. For comparison, strain ellipsoids for three strain states with the principal compression direction lying along the x, y, and z axes. Notice that the axis of greatest compression in the aggregate, shown in blue arrows, is rotated by 90 ° from our usual convention in both Fig. 14a and b. The accumulated strains vary from grain to grain with variations of ~ 0.1% to 8% strain in neighboring grains, still significant, but less than the local point to point variations.

We analyzed the strain distribution maps for 6 additional images from sample CM11 and calculated the average strain of 73 grains in total. The distribution of the magnitude of the principal strains for 73 grains from sample CM11 is shown in Fig. 15. The principal strain of maximum shortening (black bars) for each grain varies between -30%

to -5%, and the median of the distribution is at -15%. The other two axes suffer tensile deformation with magnitudes about half of that in compression direction. The strain ellipsoid of the aggregate has an oblate shape with values shown by the dashed lines. The distribution of the magnitude of the effective Von Mises strain for the same grains is shown in Fig. 16. The average strain varies from ~4% to 19% and is more homogeneous than the local strain distribution. The majority of grains are deforming in accordance to the imposed strain (12%).

3.4 Discussion:

At temperatures above 400°C and below 700°C, confining pressures of a few hundred MPa, and laboratory strain rates, Carrara marble deforms by dislocation creep processes (Covey-Crump, 1998; Rutter, 1974; Schmid et al., 1980), conditions satisfied in all of our experiments. In addition to dislocation generation, migration and annihilation, twinning may occur, particularly at the lower part of this temperature range, and diffusion creep will become increasingly important at higher temperatures. Recovery processes might include grain boundary migration, dislocation cross-slip, and dislocation climb (de Bresser, 1996; Goetze and Kohlstedt, 1977; Liu and Evans, 1997). For example, at 600°C, the 2D gray scale images indicate that there is a slight change in the average grain size after deformation (CM 17, Fig. 2) and there are changes in the grain shapes at even lower temperatures.

The strain mapping results indicate that the strain heterogeneity increases as the scale

decreases, and there appears to be a strong influence of local microstructure on the strain distribution (Figs. 11-14).   Heterogeneity in both the average grain strain and the strain within grains are observed in all the samples. The amount of heterogeneity is more pronounced among grids within grains than among grains within polycrystal.

3.4.1 Intragranular deformation:

Both twinning and grain boundary sliding can contribute a few percent strains to the total deformation and thus are important in interpreting the strain heterogeneities.   The strain introduced by twinning can be estimated by parameters like twin spacing, thickness of the twin lamella, and angle of the rotation from the untwined to the twinned position (Groshong, 1972).   The contribution of twinning to the total deformation becomes less with increasing temperature. Twins are widely observed in these samples, and these tend to be thicker at higher temperatures. High strains are observed in the maps at twin and grain boundaries (Fig. 12), and strain heterogeneities may exceed the mean aggregate strains by a factor of 3 or more.

In addition, grain boundary sliding can contribute to the total deformation and the accommodated strain can be calculated using $\varepsilon_{gbs} = gv/d$, where g is the geometrical factor relating the displacement at the grain boundary to the shortening strain, v is the grain boundary displacement, and d is the average grain size (Schmid et al., 1980).   In sample CM11, we found that some grid markers that show obvious shift along the grain boundaries (Fig. 17b).   The Von Mises strain contour map (Fig. 17c) also shows that

some grain-boundary areas accommodate strains as much as 35%, about 3 times the mean imposed strain.   This result is consistent with earlier studies: Schmid et al (1980) studied the topographic relief at the deformed grain boundaries in split cylinders of Carrara marble and suggested that grain boundary sliding at temperatures above 800ºC might contribute as much as 14% to the overall strain. Rutter (1995) has also suggested that the grain boundary sliding is present at 700ºC.

In addition to the strain accumulations along the boundaries, samples deformed at 600 C (CM12) also indicate patchy elements of strain with orientation changes of less than 5° in many of the grain interiors. These small variations of crystallographic orientation within a single grain probably indicate dislocation substructure. The development of substructures during the dislocation creep of calcite may indicate that, with increasing strain, recovery process is active and forming low angle boundaries (substructure walls, misorientaion of less than 5°).   If the sample is deformed to a higher strain, the subgrain rotation will produce higher angle subgrain boundaries (Bestmann and Prior, 2003; Kruse et al., 2001; Urai et al., 1986).   This supposition begs verification by TEM observation, but unfortunately, we have not yet done that.

3.4.2 Average grain strains:

The average grain strain also varies from grain to grain, by a smaller, but still substantial, factor of 50%.   For example, the average Von Mises effective strain of individual grains varies from 4% to 19% under applied strain of 12% (Fig 16). Some

grains show a relatively homogeneous strain field inside the grain boundaries (Fig. 12), which indicates that they respond as mechanical entities to the externally imposed load. It is observed that the smallest grains present the biggest discrepancies with respect to the imposed deformation. For example, large grains (e.g., grains #6 and 11 in Fig. 14) deform according to the applied strain field, while small grains (grains #4 and 9) have a large deviation from the homogenization model. The deformation of individual grain is a combination of the activation of multiple twin/slip systems, grain-to-grain interaction, grain boundary sliding and etc. The grains reorient and their shapes change during the deformation process. Fig. 19 shows an example of the change of grain boundary geometry during compression test of Carrara marble at 400°C (CM18) as well as the abundance of slip lines on the sample surface.

More highly strained grains are probably oriented in a direction such that one or more easy slip systems can be activated. The crystal orientation can be identified by EBSD study, and Schmid factor analysis can be used to gain information about the relative strength of different slip systems, indicate which slip systems are active, and perhaps explain the strain heterogeneities among single crystalline grains (Wu et al., 2006). In sample CM11, which was deformed at 3×10^{-5} s^{-1} to 12% strain at 600ºC and 300 MPa, we observe an obvious twinning in the grain #6 from the optical micrograph. Schmid factor analysis shows the possible twin/slip plane traces (Fig. 20b). The $r\left(0\bar{1}14\right)$ plane trace lies in the same direction (NW-to-SE) as that in the optical micrograph and has the largest Schmid factor value (0.40), thus providing a nice example that the local strain behavior is

109

sensitive to individual grain orientation.

In a second example, Fig. 20a shows that grain #4 accumulated more strain than its neighboring grains, indicating that it may be orientated in a direction so that slip on a weak slip system is favored. The Schmid factor analysis of possible slip systems from grain orientation data showed that grain #4 has the largest Schmid factors for $r\langle\bar{2}02\bar{1}\rangle^{\pm}$ and $f\langle\bar{2}20\bar{1}\rangle^{\pm}$ (LT) slip systems. Grains #2 and 11 show the largest Schmid factors for $c\langle\bar{1}2\bar{1}0\rangle^{\pm}$ slip systems. In addition, Schmid factors for $r(0\bar{1}14)$ toward $a\langle\bar{1}2\bar{1}0\rangle$ slip system are generally larger than 0.4 for these 5 grains. The resolved shear stress on different slip systems indicated that the basal slip $c\langle\bar{1}2\bar{1}0\rangle^{\pm}$ and $r\langle\bar{2}02\bar{1}\rangle^{\pm}$ are important slip systems during the compression deformation of Carrara marble at ~600° C.

The quantification of microstructural strain distribution during the plastic deformation of Carrara marble clearly shows the heterogeneous strain distribution at the grain scale even under homogeneous and gradient-free external loadings. The results provide us a better understanding of the spatial heterogeneity in terms of strain and crystal orientation under certain loading conditions. These are valuable information for the prediction of texture development during the plastic deformation of polycrystalline material and it allows us to calibrate the limitations of the homogenization models with the assumptions of uniform stress/strain fields. The anisotropic nature of crystal slip, grain-to-grain interaction, twinning, and grain boundary sliding are important factors and should be taken into account in order to predict the texture development of calcite rocks. These will be the topics in Chapter 4.

3.5 Conclusions:

Following the demonstration of split cylinder experiments by Schmid (1980) and the micro-strain mapping of Wu et al. (2006), we combined and extended the techniques to enable microstrain mapping in confined, triaxial deformation tests of Carrara marble at 400-600° C, 300 MPa confining pressure, and strain rates of 10^{-4} to 10^{-5} s^{-1}. Briefly, the conclusions of this study are as follows:

1. The displacement-mapping technique is capable of accurately measuring strain distributions on the scale of microstructure.

2. The strain distribution contour maps indicate high heterogeneity of strain distribution at grain level, indicating some grains are more or less intact than others.

3. The minimum and maximum principal strains in a small, local region can vary by a factor of 3 or more from the mean imposed strains. The strains averaged over a particular grain show less dramatic variations, but may still be as much as 50%.

4. There is a strong influence of microstructure on the distribution of strain. High strains are often observed near twin bands and grain boundaries, indicating these are weak areas and localize strain.

5. Grain boundary sliding may be active at temperatures as low as 600ºC. Substructures within grains are also observed and may also owing to recovery processes. Local strain heterogeneities can be a combination of the activation of

multiple slip systems, grain boundary sliding, and stress variations owing to the grain-to-grain interactions.

Considerable development of technique and refinement of data analyses was required to implement the technique, and consequently, the analyses are available for only a small number of samples. That information is quite encouraging, because these observations agree with previous suppositions about the mechanisms of dislocation creep in carbonates, and, importantly, because, for the first time, quantitative information on strain heterogeneity in confined, high-temperature experiments has been obtained. As an example of the use of this data, in the following chapter, we compare the strain measurements obtained here with predictions of grain strain and reorientation obtained from the self-consistent viscoplastic method.

Further developments of the microstrain mapping technique could involve developing improved methods for measuring the vertical displacements of the markers, broadening the measurements to increased strains, temperature ranges, and strain rate conditions. The technique could easily be used to investigate deformation of other materials. Comparison of the microstrain measurements with observations made using CIP or EBSD to make local orientation measurements of the same samples will be quite important. Verifications of the dislocation microstructure should also be made using transmission electron microscopy.

3.6 References

Barber, D.J., Wenk, H.R., Gomez-Barreiro, J., Rybacki, E. and Dresen, G., 2007. Basal slip and texture development in calcite: New results from torsion experiments. Physics and Chemistry of Minerals, 34(2): 73-84.

Bestmann, M. and Prior, D.J., 2003. Intragranular dynamic recrystallization in naturally deformed calcite marble: Diffusion accommodated grain boundary sliding as a result of subgrain rotation recrystallization. Journal of Structural Geology, 25(10): 1597-1613.

Biery, N.E., De Graef, M. and Pollock, T.M., 2001. Influence of microstructure and strain distribution on failure properties in intermetallic tial-based alloys. Materials Science and Engineering a-Structural Materials Properties Microstructure and Processing, 319: 613-617.

Coli, M., 1989. Litho-structural assemblage and deformation history of "Carrara marble:. Bolletino della Societa Geologica Italiana, 108: 581-590.

Covey-Crump, S.J., 1997. The normal grain growth behavior of nominally pure calcitic aggregates. Contributions to Mineralogy and Petrology, 129(2-3): 239-254.

Covey-Crump, S.J., 1998. Evolution of mechanical state in Carrara marble during deformation at 400 degrees to 700 degrees c. Journal of Geophysical Research-Solid Earth, 103(B12): 29781-29794.

de Bresser, J.H.P., 1996. Steady state dislocation densities in experimentally deformed calcite materials: Single crystals versus polycrystals. Journal of Geophysical Research-Solid Earth, 101(B10): 22189-22201.

de Bresser, J.H.P., Ter Heege, J.H. and Spiers, C.J., 2001. Grain size reduction by dynamic recrystallization: Can it result in major theological weakening? International Journal of Earth Sciences, 90(1): 28-45.

Goetze, C. and Kohlstedt, D.L., 1977. Dislocation-structure of experimentally deformed marble. Contributions to Mineralogy and Petrology, 59(3): 293-306.

Kruse, R., Stunitz, H. and Kunze, K., 2001. Dynamic recrystallization processes in plagioclase porphyroclasts. Journal of Structural Geology, 23(11): 1781-1802.

Lebensohn, R.A., Wenk, H.R. and Tome, C.N., 1998. Modelling deformation and recrystallization textures in calcite. Acta Materialia, 46(8): 2683-2693.

Liu, M. and Evans, B., 1997. Dislocation recovery kinetics in single-crystal calcite. Journal of Geophysical Research-Solid Earth, 102(B11): 24801-24809.

Molli, G., Conti, P., Giorgetti, G., Meccheri, M. and Oesterling, N., 2000. Microfabric study on the deformational and thermal history of the Alpi apuane marbles (Carrara marbles), Italy. Journal of Structural Geology, 22(11-12): 1809-1825.

Molli, G. and Heilbronner, R., 1999. Microstructures associated with static and dynamic recrystallization of Carrara marble (Alpi apuane, nw tuscany, Italy). Geologie En Mijnbouw-Netherlands Journal of Geosciences, 78(1): 119-126.

Park, S.K. and Schowengerdt, R.A., 1983. Image-reconstruction by parametric cubic

convolution. Computer Vision Graphics and Image Processing, 23(3): 258-272.

Paterson, M.S., 1995. A theory for granular flow accommodated by material transfer via an intergranular fluid. Tectonophysics, 245(3-4): 135-151.

Pieri, M., Kunze, K., Burlini, L., Stretton, I., Olgaard, D.L., Burg, J.P. and Wenk, H.R., 2001. Texture development of calcite by deformation and dynamic recrystallization at 1000 k during torsion experiments of marble to large strains. Tectonophysics, 330(1-2): 119-140.

Raabe, D., Sachtleber, M., Zhao, Z., Roters, F. and Zaefferer, S., 2001. Micromechanical and macromechanical effects in grain scale polycrystal plasticity experimentation and simulation. Acta Materialia, 49(17): 3433-3441.

Renner, J., Evans, B. and Siddiqi, G., 2002. Dislocation creep of calcite. Journal of Geophysical Research-Solid Earth, 107(B12).

Rutter, E.H., 1974. Influence of temperature, strain rate and interstitial water in experimental deformation of calcite rocks. Tectonophysics, 22(3-4): 311-334.

Rutter, E.H., 1995. Experimental study of the influence of stress, temperature, and strain on the dynamic recrystallization of Carrara marble. Journal of Geophysical Research-Solid Earth, 100(B12): 24651-24663.

Rutter, E.H., 1998. Use of extension testing to investigate the influence of finite strain on the rheological behaviour of marble. Journal of Structural Geology, 20(2-3): 243-254.

Rutter, E.H., Casey, M. and Burlini, L., 1994. Preferred crystallographic orientation development during the plastic and superplastic flow of calcite rocks. Journal of Structural Geology, 16(10): 1431-1446.

Sachtleber, M., Zhao, Z. and Raabe, D., 2002. Experimental investigation of plastic grain interaction. Materials Science and Engineering a-Structural Materials Properties Microstructure and Processing, 336(1-2): 81-87.

Schmid, S.M., Paterson, M.S. and Boland, J.N., 1980. High temperature flow and dynamic recrystallization in Carrara marble. Tectonophysics, 65(3-4): 245-280.

Turner, F.J., Griggs, D. and Heard, H.C., 1954. Experimental deformation of calcite crystals. Geological Society of America Bulletin, 65: 883-934.

Urai, J.L., Means, W.D. and Lister, G.S., 1986. Dynamic recrystallization of minerals. In: B.E.H. Hobbs and C. Hugh (Editors), Mineral rock deformation: Laboratory studies, paterson volume. Geophysical Monograph, Washington D. C., pp. 161-200.

Weiss, L.E. and Turner, F.J., 1972. Some observations on transition gliding and kinking in experimentally deformed calcite and dolomite. AGU Geophysical Monograph, 16: 95-107.

Wenk, H.R., 2002. Texture and anisotropy, Plastic deformation of minerals and rocks. Reviews in mineralogy & geochemistry, pp. 291-329.

Wu, A., De Graef, M. and Pollock, T.M., 2006. Grain-scale strain mapping for analysis of slip activity in polycrystalline b2rual. Philosophical Magazine, 86(25-26):

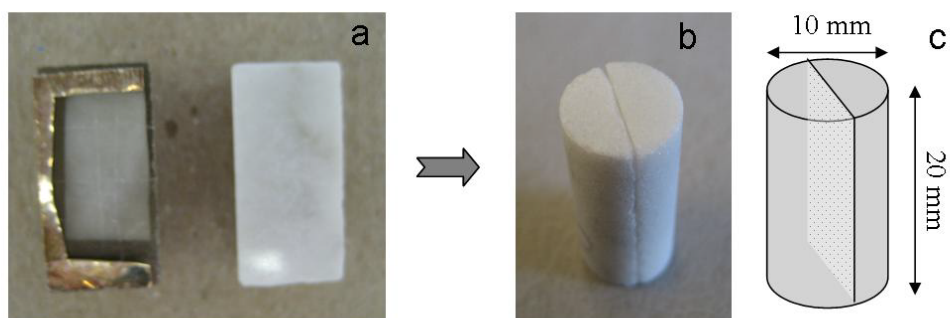3995-4008.

3.7 Figures and tables

Figure 1. (a) Carrara marble samples are cut into two half cylinders. Both surfaces are polished and one surface is coated with Au/C grid marker (surface on left, white area). A copper foil window is put in-between the two half cylinders. (b) The starting sample has a cylindrical shape with 20 mm in length and 10 mm in diameter. (c) A schematic diagram shows the split sample with the middle cross section coated with Au/C grid markers.
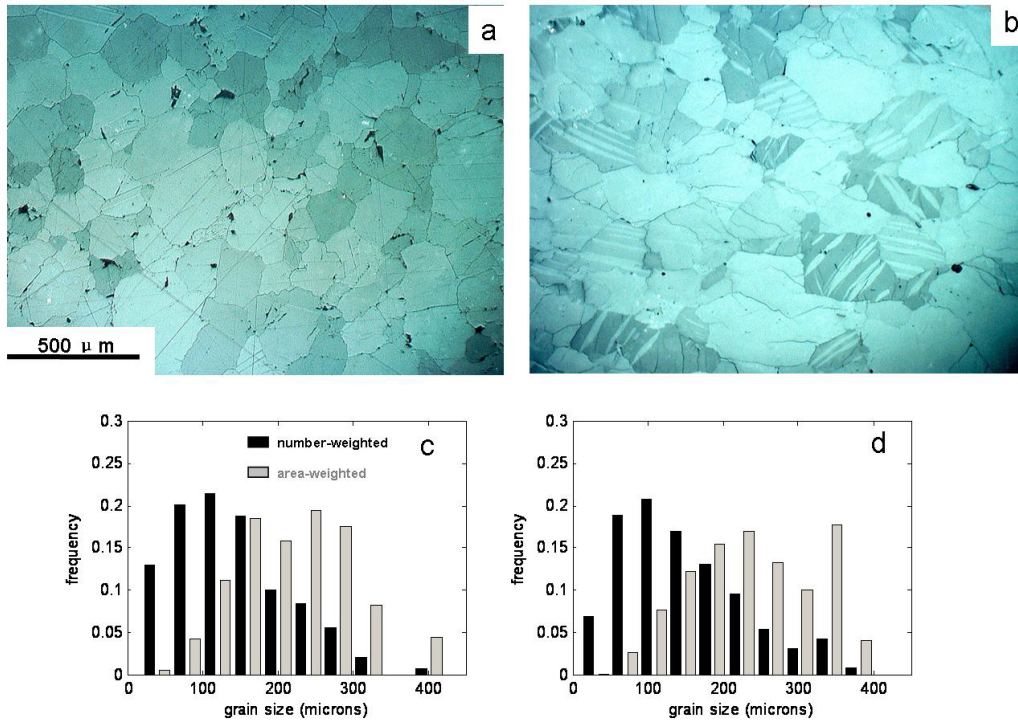
Figure 2. Optical micrographs of both undeformed (a) and deformed (b) Carrara marble (sample CM17, compressed to 25% strain at 600℃). The deformation test introduces thick twin bands. (c) and (d) show grain size distribution histograms of both undeformed and deformed sample, respectively. Black and gray bars represent number-weighted and area-weighted grain size distributions. Grain size is analyzed by tracing the grain boundaries in ImageJ, measuring the grain area, and computing the diameter of a circle having equivalent area. The number-weighted mean grain size (equivalent area) of the starting Carrara marble is ~130 µm. The distribution of grain size (equivalent area) of the deformed sample shows only a slight variation from the

117

undeformed material.
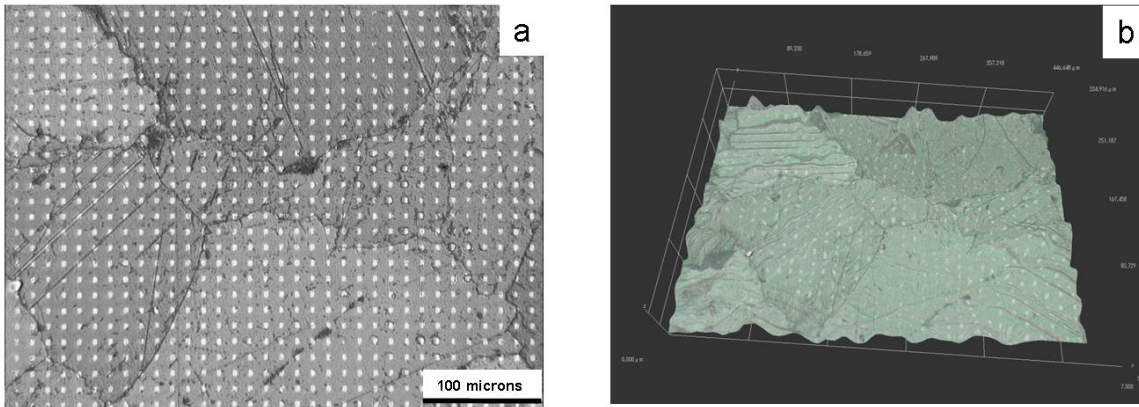
Figure 3. (a) 2D gray-scale image of undeformed sample (CM18), bright spots are the grid markers. Before deformation the markers are squares with sides about 5 μm long; the distance between the centers of two grid markers is 12.64μm. A few narrow twins are visible in the undeformed starting material. Notice that some grid markers are missing in the micrograph due to imperfections of the undeformed sample surface. (b) 3D image of the same sample after deformation.
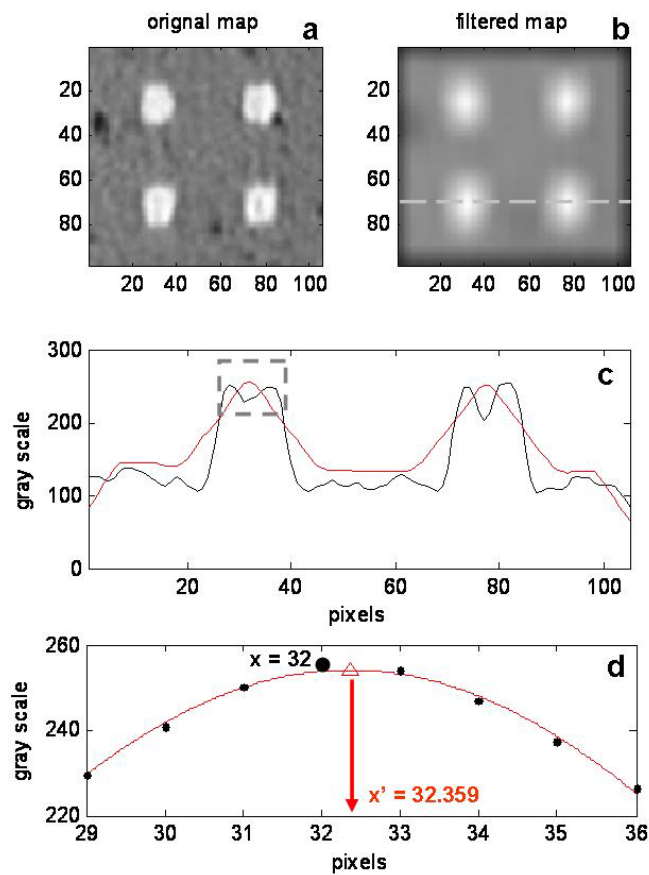
Figure 4. Grid marker positions are determination by convolving the original image (a) with a kernel that contains a reference marker. The filtered image is shown in (b). (c) shows the line profiles (at the dashed line in b) from both unfiltered (black line) and filtered images (red line). See the blow-up image of the windowed peak area in (d). Grid positions are recognized as the peaks in the filtered image. This convolution step is sufficient to locate all grid markers to within 1 pixel using a 2D 256-gray-scales image.

surface height matrix (*.csv)

4.8995	4.9072	4.9296	4.9531	4.9742
4.9017	4.9038	4.9239	4.9501	4.9736
4.8986	4.9007	**4.9166**	4.9415	4.9680
4.8790	4.8874	4.9078	4.9293	4.9554
4.8373	4.8462	4.8768	4.9065	4.9269

window size = 5x5

window size = 15x15
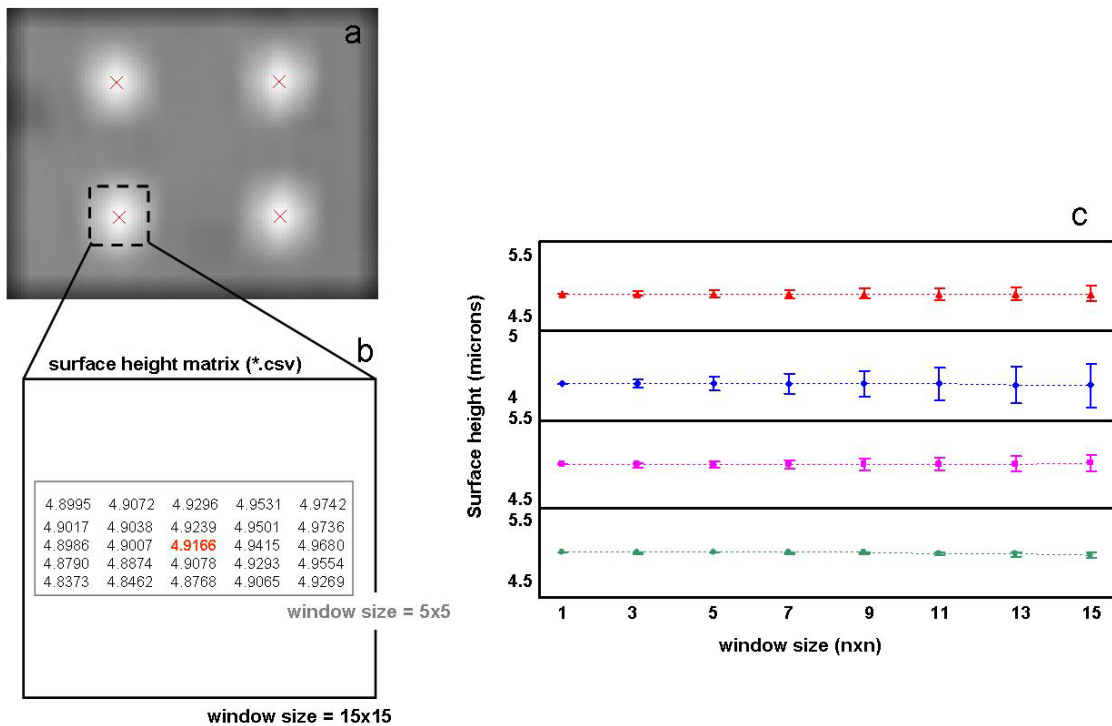
Figure 5. The grid marker positions (red crosses) in 2D coordinates (a) are used to find the third coordinate using the surface elevation data (.csv files) from the 3D digital microscope (b). Number in red color represents the surface elevation at the exact marker position. (c) The average surface elevation with increasing window size indicates that it is not sensitive to the window size.
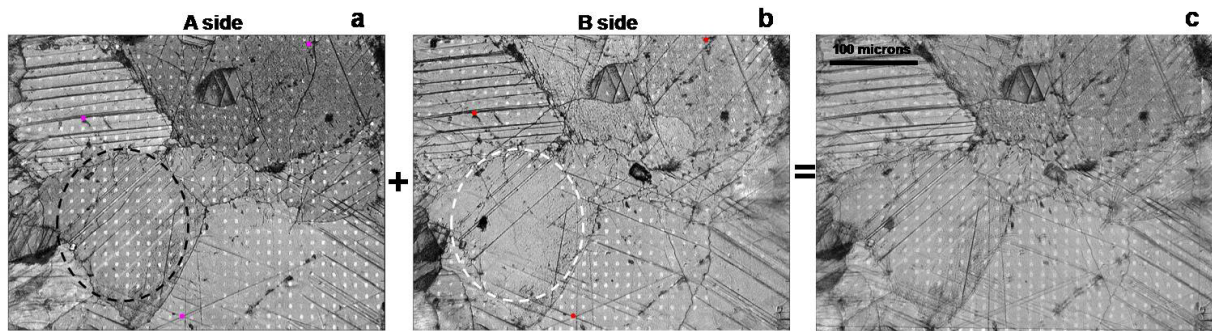
Figure 6. (a) and (b) 2D images of the two facing surfaces in the deformed sample (CM18). Some grid markers are present on both sides of the sample; while some are shown only on one side (e.g. inside the circled window). (c) The two images are overlapped together using a 3-point analysis (color dots in (a) and (b)), which gives us a better coverage in grid marker positions. All images shown in 2D have a compression direction in the vertical direction.
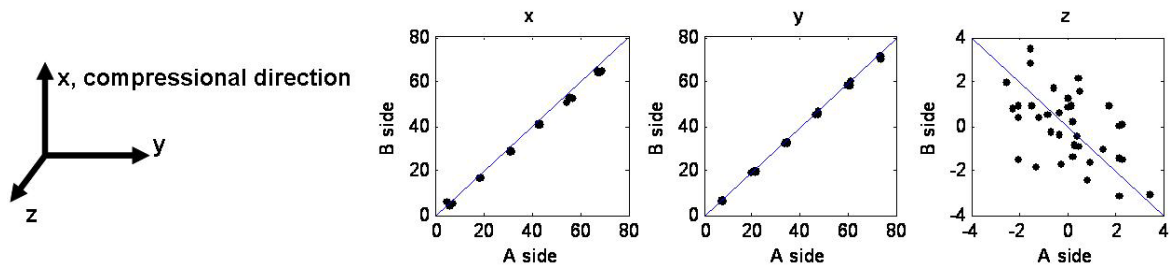
Figure 7. The correlation of grid marker positions from corresponding grid markers on A and B sides of the sample (Fig. 6, (a) and (b)). The correlation coefficients in x, y, z directions are 0.99956, 0.99971, and -0.51344, respectively. The poor correlation in z-direction indicates that we may have a limited resolution in the z-direction strain components. See text for more details about the resolution.
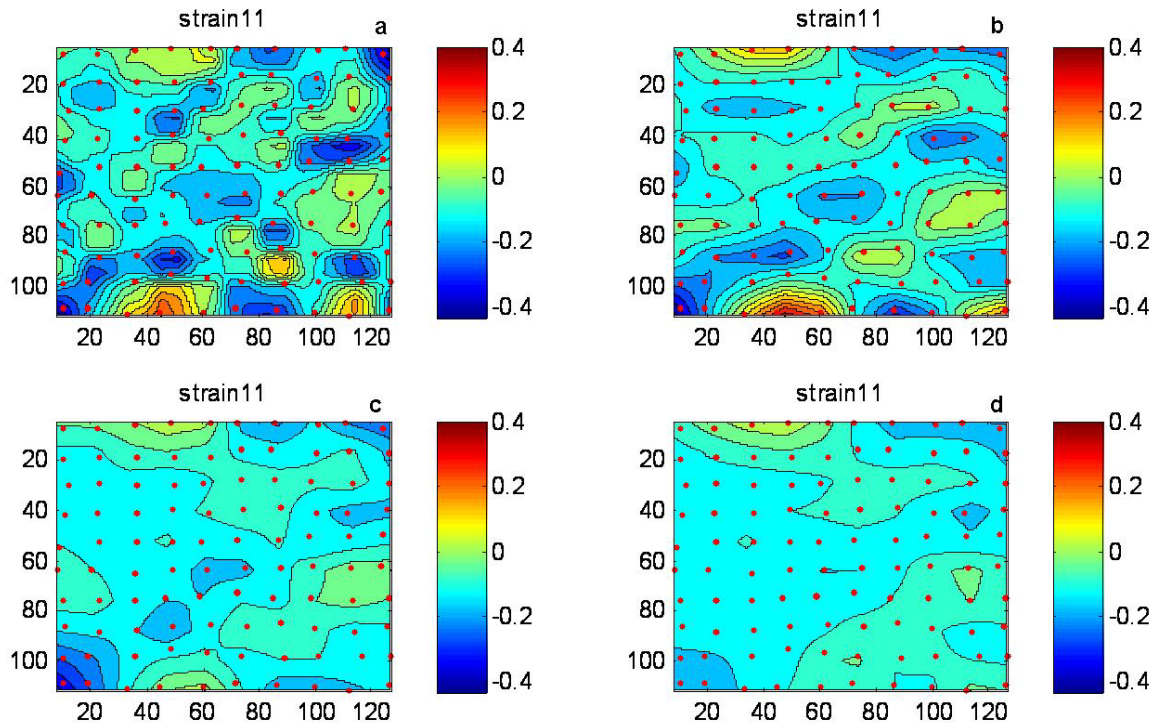
Figure 8. Contour maps of strain component using (a) method 1, 3-point, (b) method 2, 4-point, (c) method 3, 5-point, and (d) method 4, 9-point strain analysis technique. Red dots are the grid markers positions for strain calculation. The strain heterogeneity decreases with increased averaging; the local heterogeneities are lost in the 9-point analysis. The difference in the ratios of the maximum/minimum strain values with respect to the average strain decreases from 7 to 2 from (a) to (d).
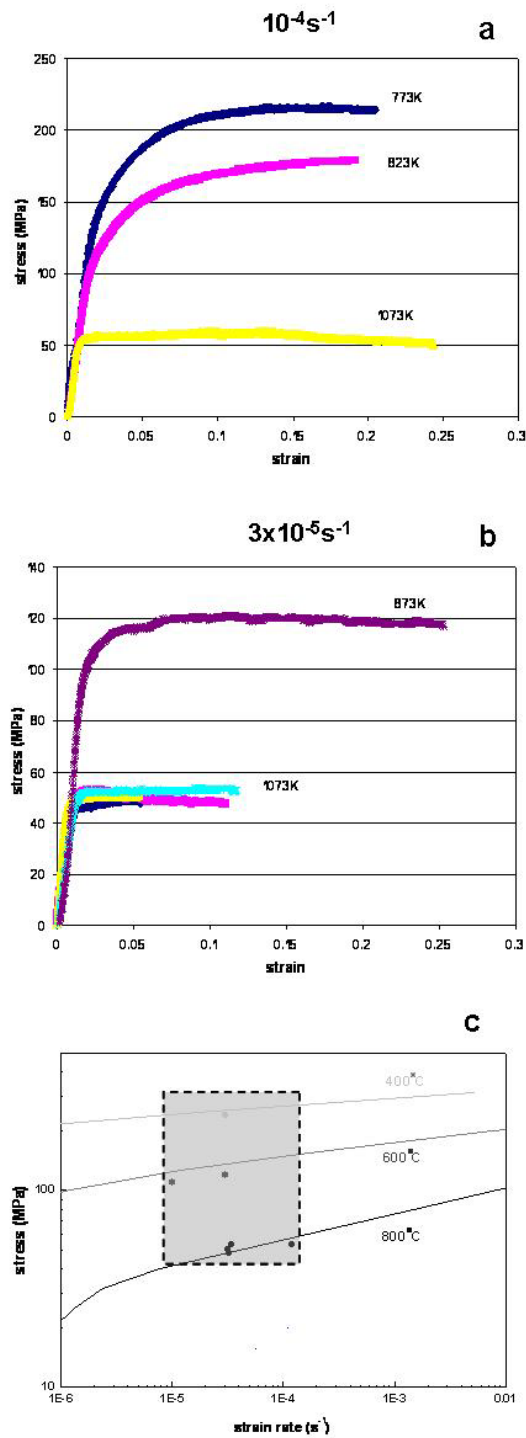
Figure 9. (a) and (b) Stress vs. strain diagrams from compression tests on Carrara marble samples. See Table 1 for a summary of the deformation tests. (c) Our data (dots) is in agreement with previous deformation tests (solid lines) on Carrara marble samples

(Covey-Crump, 1997; de Bresser et al., 2001; Rutter, 1995; Schmid et al., 1980).
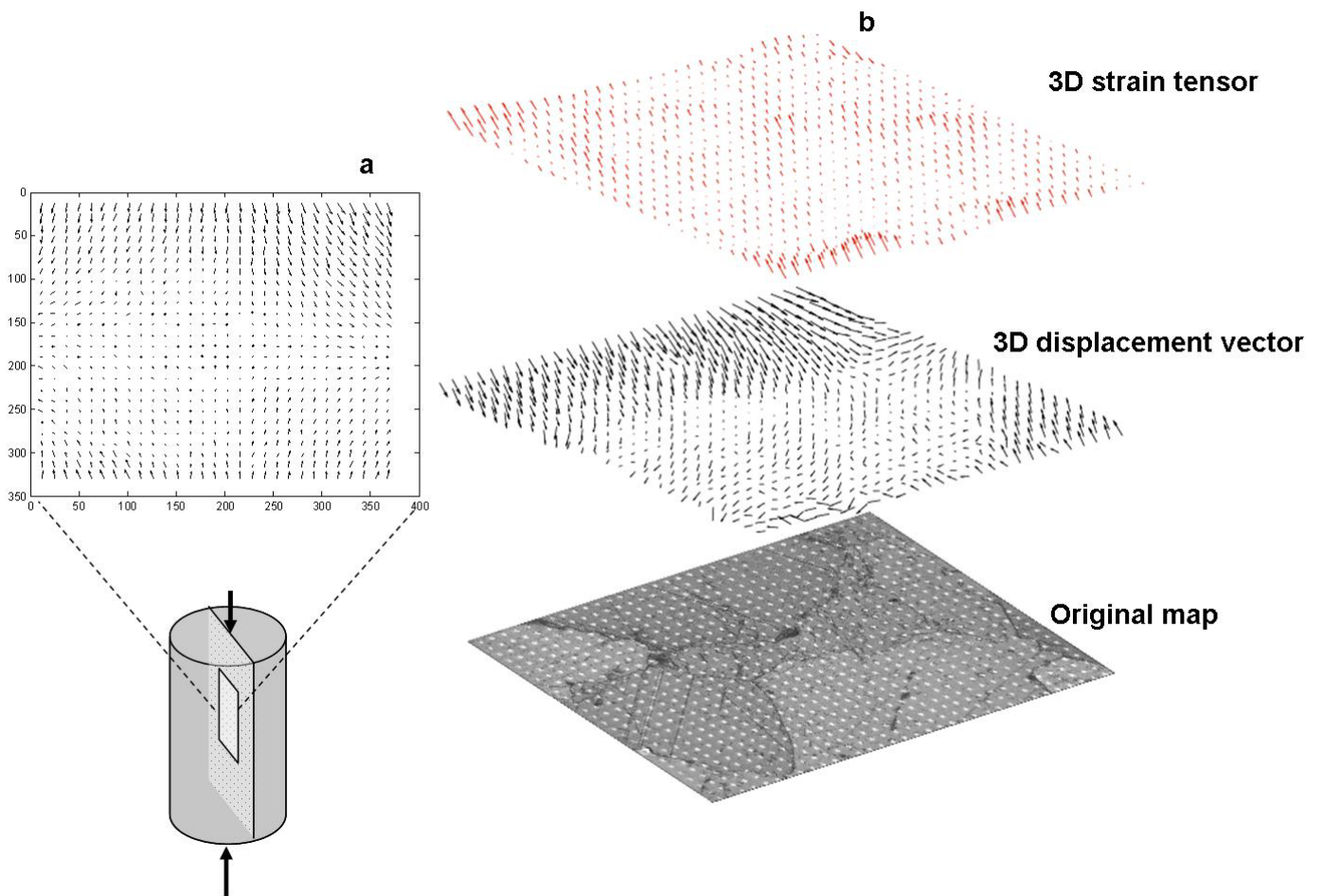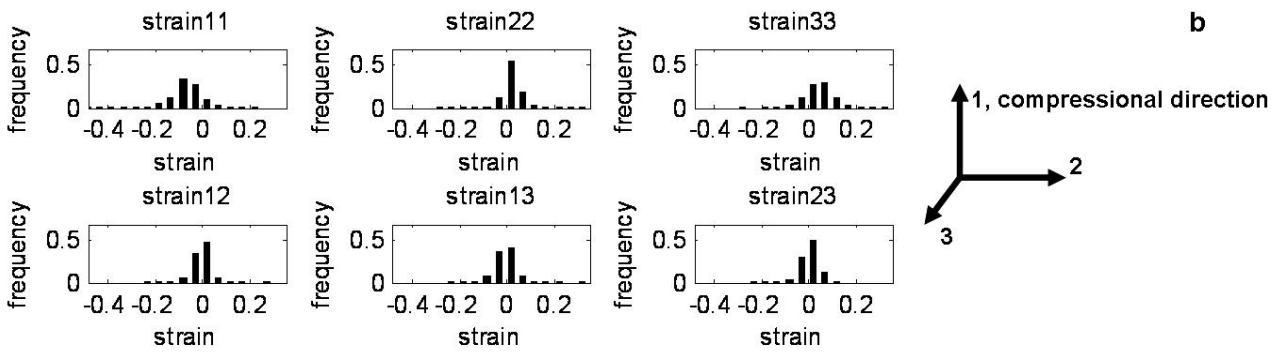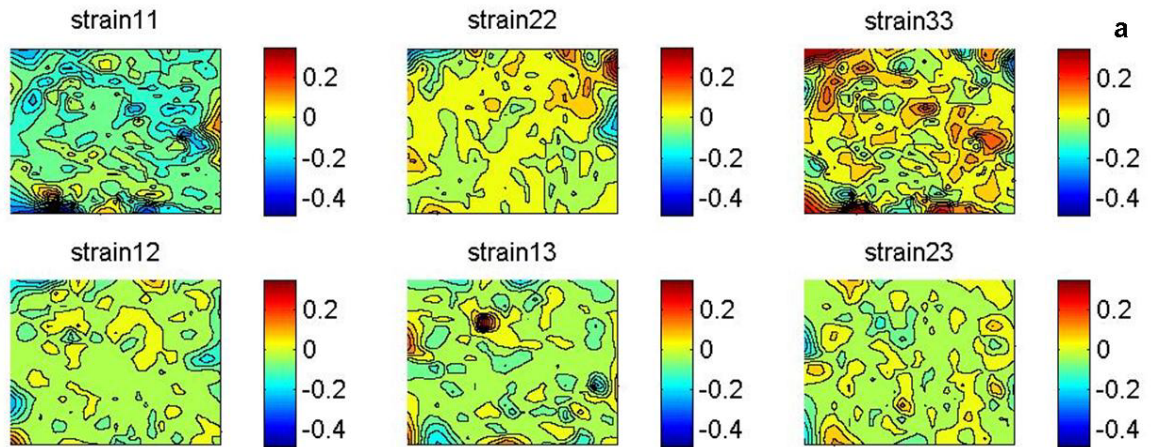

Figure 10. (a) 2D displacement gradient map (sample CM18), arrows show the movement of grid markers relative to a center point due to the deformation process. The deformation gradient map is characterized by a flow pattern from the two end sides where the compression deformation applies to the periphery of the sample. (b) The original map, the 3D displacement vector map, and 3D strain tensor map of the same area.
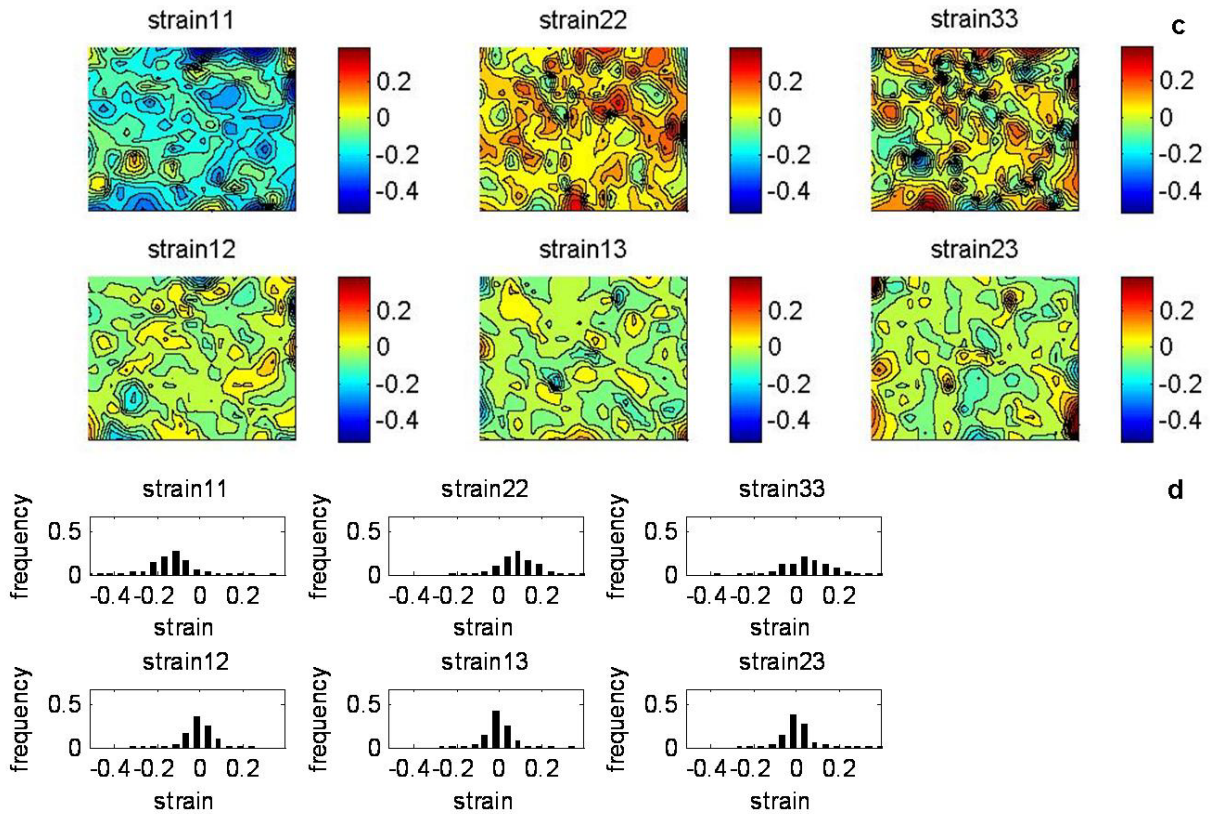
125

strain11 strain22 strain33 **a**

strain12 strain13 strain23

strain11 strain22 strain33 **b**

frequency
0.5
0
-0.4 -0.2 0 0.2
strain

frequency
0.5
0
-0.4 -0.2 0 0.2
strain

frequency
0.5
0
-0.4 -0.2 0 0.2
strain

1, compressional direction

2

3

strain12 strain13 strain23

frequency
0.5
0
-0.4 -0.2 0 0.2
strain

frequency
0.5
0
-0.4 -0.2 0 0.2
strain

frequency
0.5
0
-0.4 -0.2 0 0.2
strain

126

Figure 11. 2D contour maps of strain tensor distributions for samples CM18 (a-b) and CM11 (c-d). Strains show large heterogeneities (a) and (c): while the sample is compressed in vertical direction (imposed strain, $\varepsilon_{11}<0, \varepsilon_{22}>0$), there are local areas which are deformed in the opposite sense from the loading condition. The minimum and maximum strain varied by a factor of ~6-8 compared to the imposed strain. (b) and (d) The distribution histograms of 6 strain components. Strain component ε_{11} is roughly twice the magnitude as ε_{22} and ε_{33}.
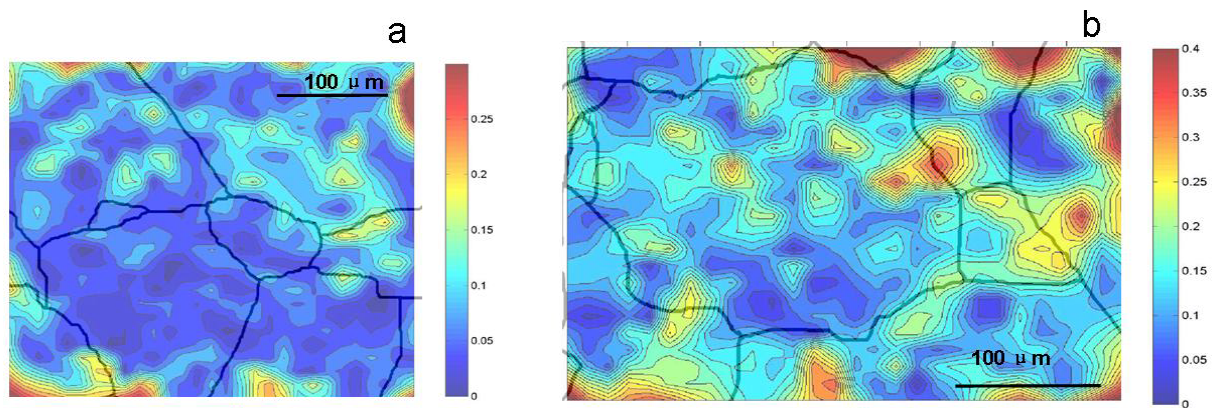
Figure 12. Von Mises strain distribution for samples CM18 (a) and CM11 (b). Grain boundaries are shown in solid black lines. Notice the heterogeneity of strain distribution; and high strain concentration near twin and grain boundaries. The high heterogeneity of strain distribution at grain level indicating some grains are more or less intact than others.
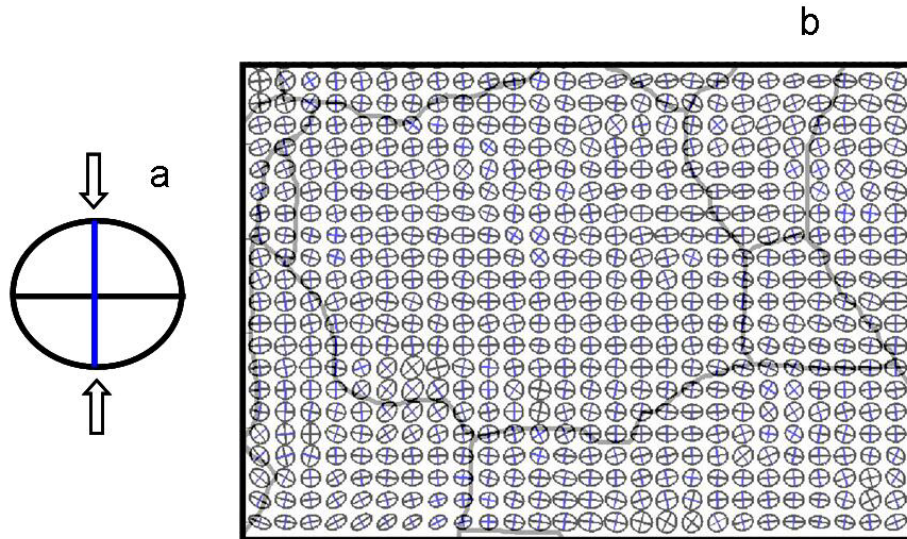
Figure 13. (a) Theoretical finite strain ellipse with 10% strain in vertical direction. (b)

2D finite strain ellipse map for sample CM11. The principal stretching and compression

directions are shown as the main axes of the ellipse with the principal compression

direction shown as blue lines. Notice that the principal stretching direction varies in local
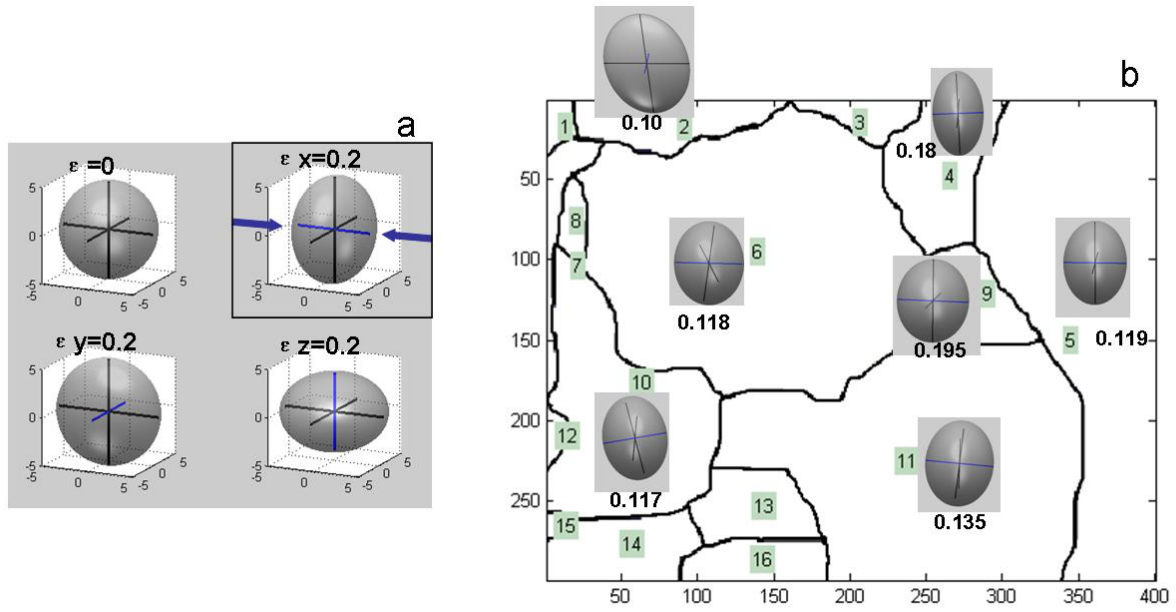
areas.

Figure 14. (a) Strain ellipsoid before deformation and after compression deformation in 3 different directions. The windowed subplot shows the compression directions in blue arrows, which is the same as in Fig. 15b. (b) Average 3D strain ellipsoids of individual grains (sample CM11); numbers shown are the average Von Mises strains (same area as in Fig. 13b).
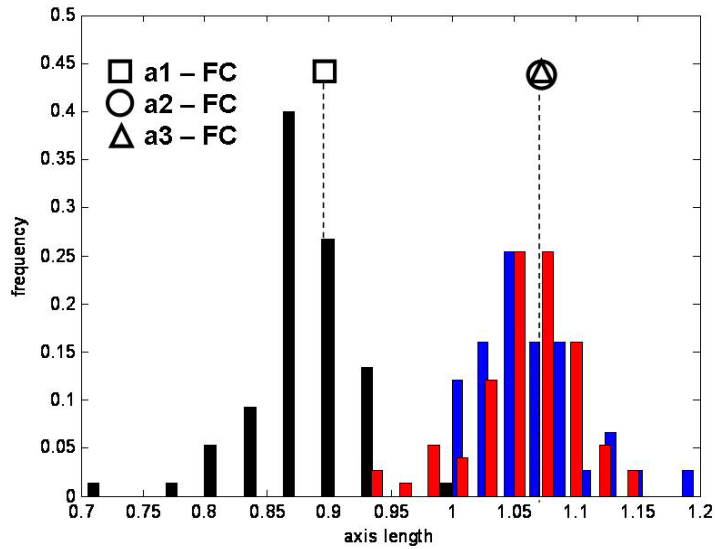
Figure 15. Equivalent 3D strain ellipsoid axis distribution of 73 grains (sample CM11).

The main axis in compression direction (black bars) is reduced by ~ -30% to -5% with a

maximum distribution at ~ -15%. The other two axes are under tensile deformation with

the magnitudes about half of that in the compression direction. a1, a2, a3 are the 3 main

axes of the strain ellipsoid which has an oblate shape under the imposed strain and

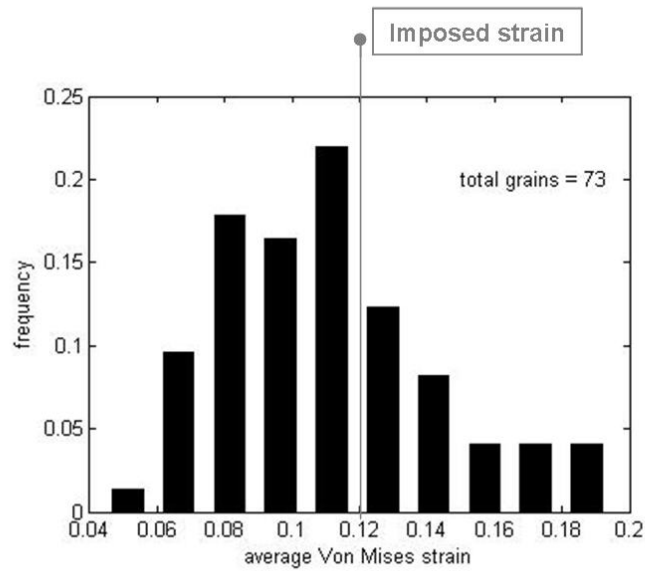full-constrained condition (see also dashed lines).

Figure 16. The average Von Mises strain distribution histogram of 73 grains (sample CM11). The average strain varies from ~4% to 19% and is more homogeneous than the local strain distribution. The majority of grains are deforming in accordance to the imposed strain (12%).
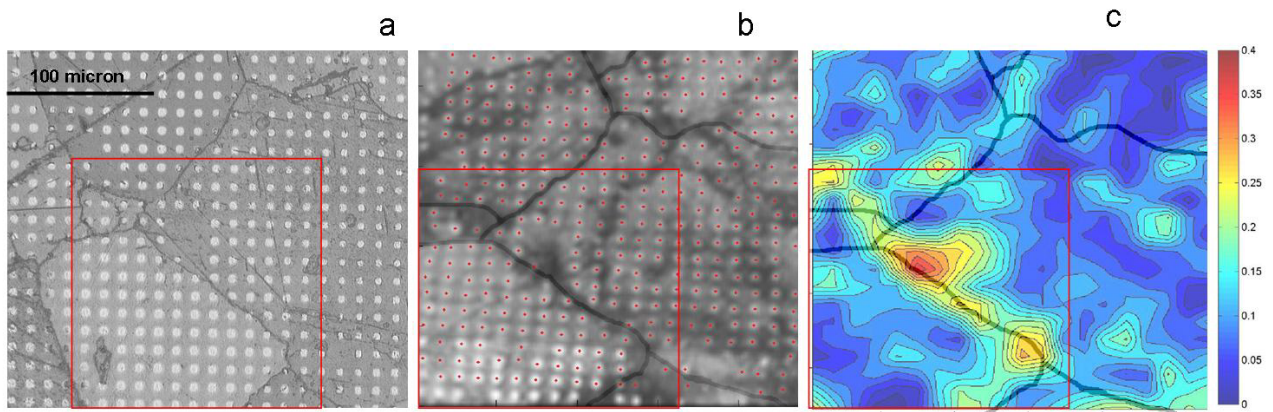
Figure 17. (a) Optical micrograph of sample CM11 before deformation. Red squared window represents the area of interest. (b) Filtered map of the deformed sample together with the identified grid marker positions in red dots. Grain boundaries are shown in solid black lines. (c) 2D Von Mises strain contour map with grain boundaries in solid black lines. It shows that the grain boundary accommodates a large amount of deformation.
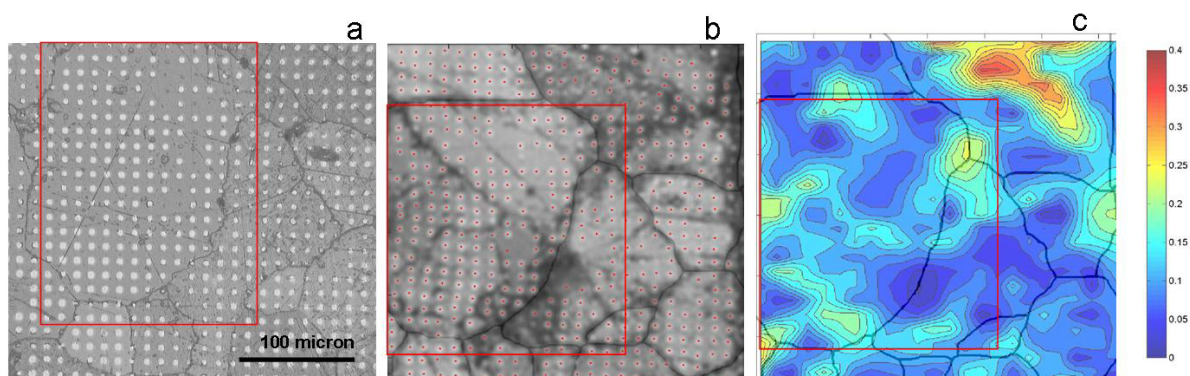
Figure 18. Same as in Fig. 17 except for another study area. Red squared window represents the area of interest. It shows the grid marker lines change their orientations in the grain interior, indicating the development of substructures due to the compression deformation.
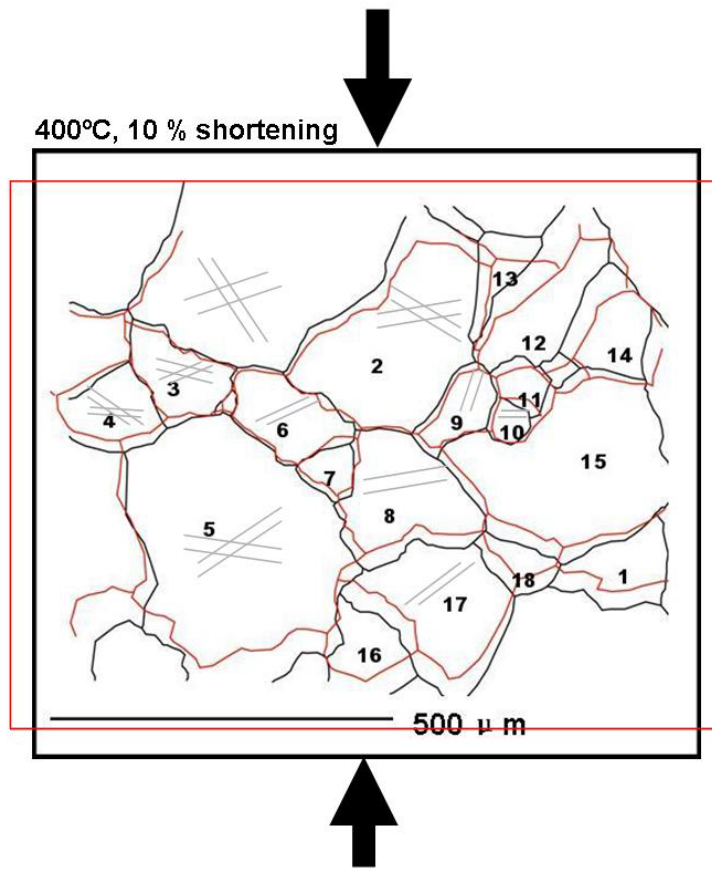
Figure 19. Change of grain shape as well as slip activities due to the compression deformation of Carrara marble. Sample CM18 is deformed at 400°C and 300 MPa confining pressure, the total strain is 10% at strain rate of $3x10^{-5}s^{-1}$. Grain boundaries are shown in black and red colors representing the sample before and after deformation, respectively. Major slip line traces are shown within individual grains, grain numbers are indicated. Compression direction is in vertical.

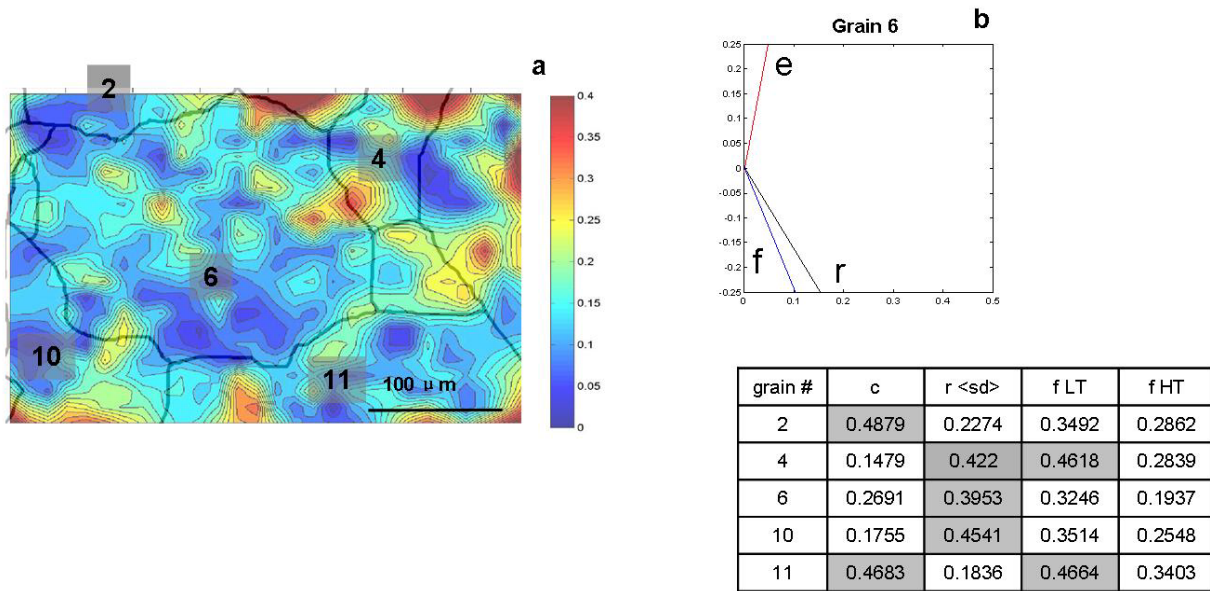| grain #	c	r <sd>	f LT	f HT
2	0.4879	0.2274	0.3492	0.2862
4	0.1479	0.422	0.4618	0.2839
6	0.2691	0.3953	0.3246	0.1937
10	0.1755	0.4541	0.3514	0.2548
11	0.4683	0.1836	0.4664	0.3403
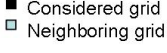
Figure 20. Schmid factor analysis of individual grains (CM11). (a) Area of interest, grain numbers indicated are used the same as in Fig. 14. (b) Computed orientations of the e-twinning, $r(10\bar{1}4)$, and $f(\bar{1}012)$ plane traces for grain #6. Compression direction is vertical. The $r(10\bar{1}4)$ plane trace lies in the same direction (NW-to-SE) as that in the optical micrograph, and it has the largest schmid factor value (0.40). Table shows the schmid factors of individual slip systems.

136

Table 1. List of experiments

	grid	Cp(Mpa)	T (ºC)	strain rate	strain	EBSD	Grid recovered?
CM01	C	300	800	3.2E-05	6%		
CM02	Au	300	800	3.3E-05	11%		
CM03	W	300	800	3.2E-05	5%		
CM04	Au	300	800	1.0E-04	20%		
CM05	Au	300	700	1.0E-04	20%		
CM06	C	300	800	1.2E-04	24%		
CM07	C	300	700	1.0E-04	20%		y
CM08	C	100	550	1.2E-04	19%		y
CM09	C	300	500	8.0E-05	21%		y
CM10	C	300	600	0	0		y
CM11	C	300	600	1.0E-05	12%	y	y
CM12	C	300	600	1.0E-05	6%	y	
CM18	Au	300	400	3.0E-05	10%	y	y
CM13	Au	300	800	3.4E-05	12%	y	
CM17	Au	300	600	3.7E-05	25%	y	

Table 2. Resolution of the n-point strain analysis technique

■ Considered grid □ Neighboring grid	Method 1	Method 2	Method 3	Method 4
Averaging area (μm^2)	80	160	313	643
Equivalent distance (μm)	9	13	18	25
Error I - minimum detectable marker shift/original marker spacing (<1%) ; Error II - 3-point strain analysis (< 0.1%) Strain resolution = Error I + Error II (~1%)				
$\varepsilon_{heterogeneity}$	-	~6-7%	~19-25%	~21-26%

* The resolution of strain-mapping technique relies on the image resolution (Error I) and strain calculation algorithm Error II.   One can average over a larger number of grid points and obtain the average strain within a larger area. The precision of the measurement increases, but, of course, the cost is a sacrifice of information about the local heterogeneity ($\varepsilon_{heterogeneity}$).

Table 3. Statistics of Von Mises effective strain maps of Carrara marble

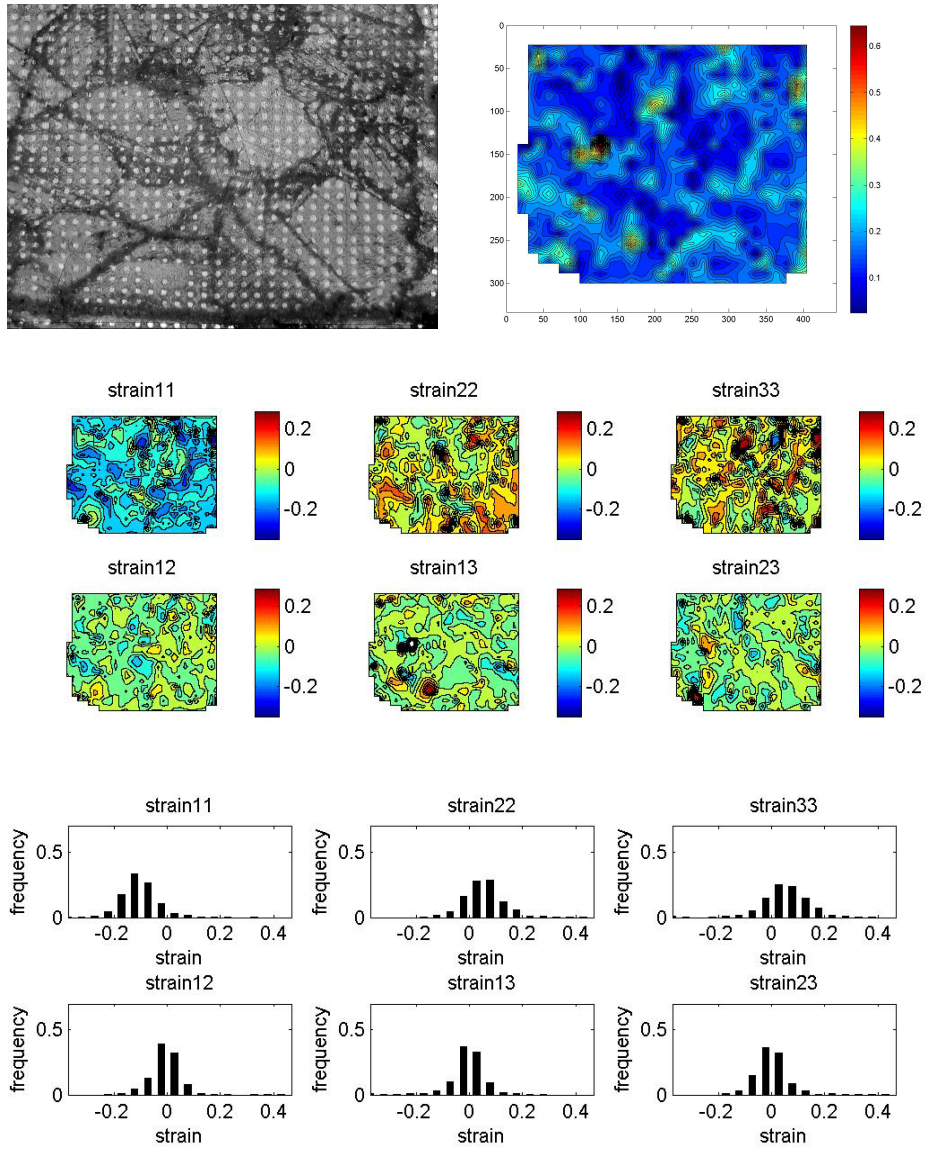|	Nominal imposed strain	Average strain in the map	Std dev of avg strain	Max strain in the map	Max/Avg	Min strain in the map	Min/Avg
CM09	20%	25%	9%	68%	27	4%	0.2
CM11	12%	23%	11%	79%	3.4	3%	0.1
CM18	10%	15%	8%	58%	3.8	2%	0.2

3.8. Appendix

Figure A1. (Top row) sample CM11, microstructure after deformation (left) and the Von Mises effective strain distribution (right). (Middle row) 2D contour maps of strain tensor distributions. (Bottom row) distribution histograms of 6 strain tensor components. Strain component ε_{11} is roughly twice the magnitude as ε_{22} and ε_{33}.

D:\Research\rock\images\grid_analysis\IDL\to_print\CM11_after\result_2n

Figure A2. Sample CM11, see Fig. A1 for figure caption.

D:\Research\rock\images\grid_analysis\IDL\to_print\CM11_after\result_3n

Figure A3. Sample CM11, see Fig. A1 for figure caption.

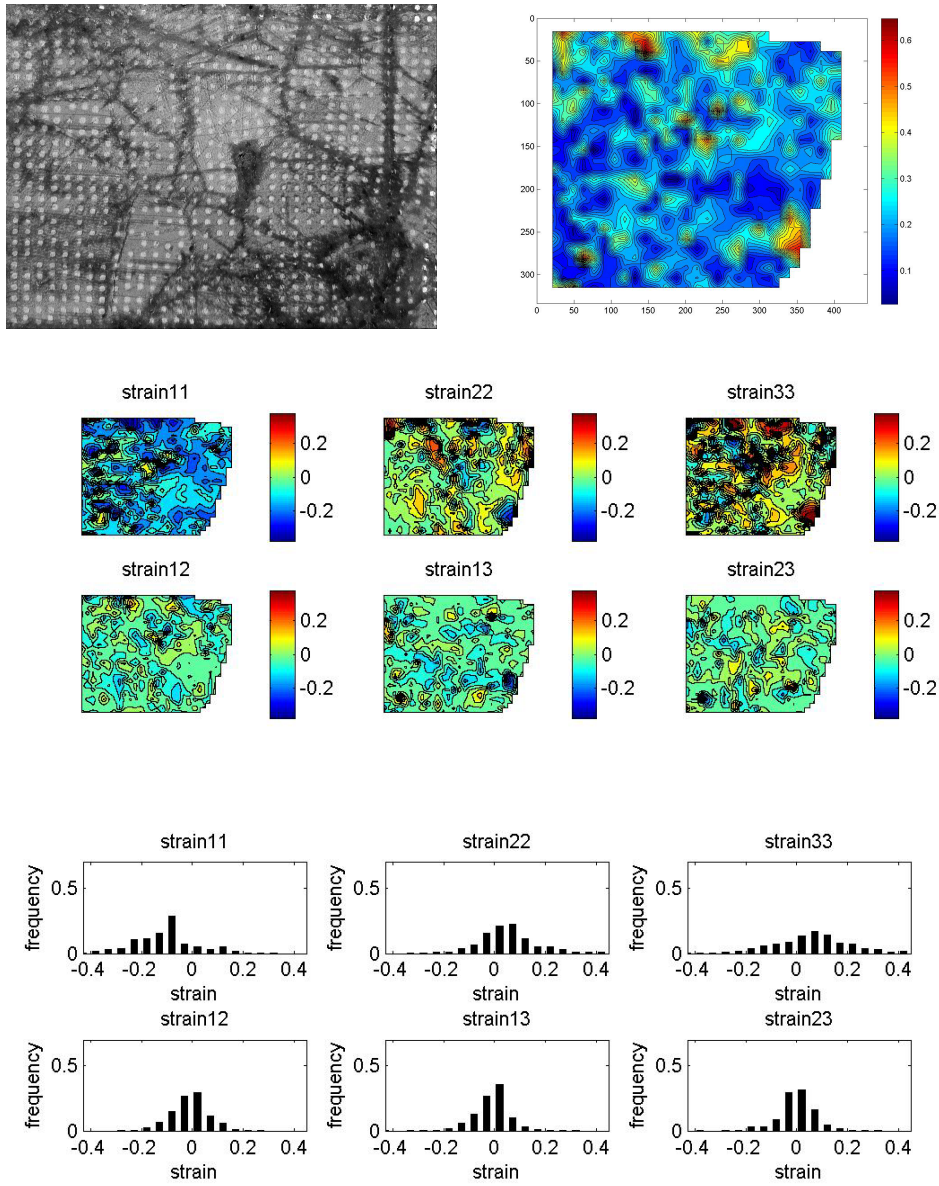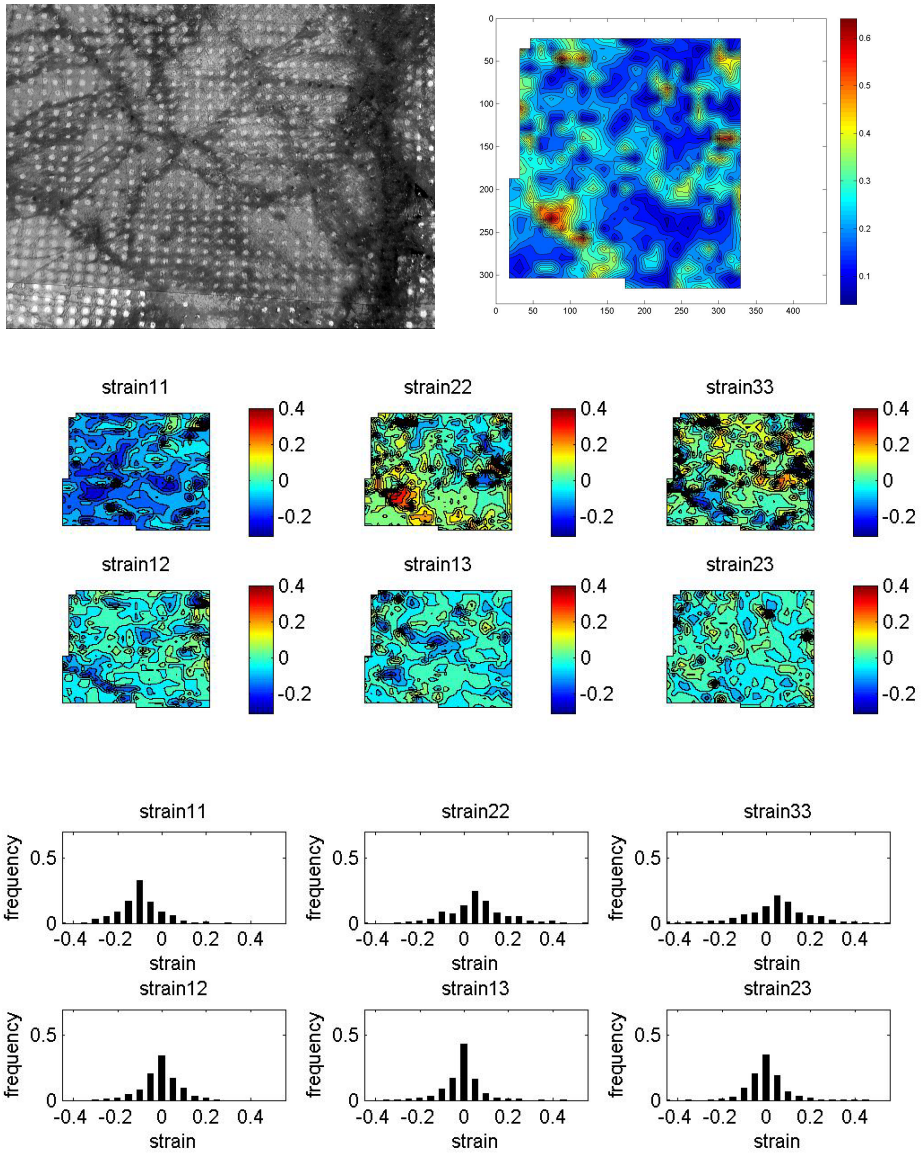D:\Research\rock\images\grid_analysis\IDL\to_print\CM11_after\result_4n

Figure A4. Sample CM11, see Fig. A1 for figure caption.

D:\Research\rock\images\grid_analysis\IDL\to_print\CM11_after\result_5n

Figure A5. Sample CM11, see Fig. A1 for figure caption.

D:\Research\rock\images\grid_analysis\IDL\to_print\CM11_after\result_7n

144

Figure A6. Sample CM11, see Fig. A1 for figure caption.

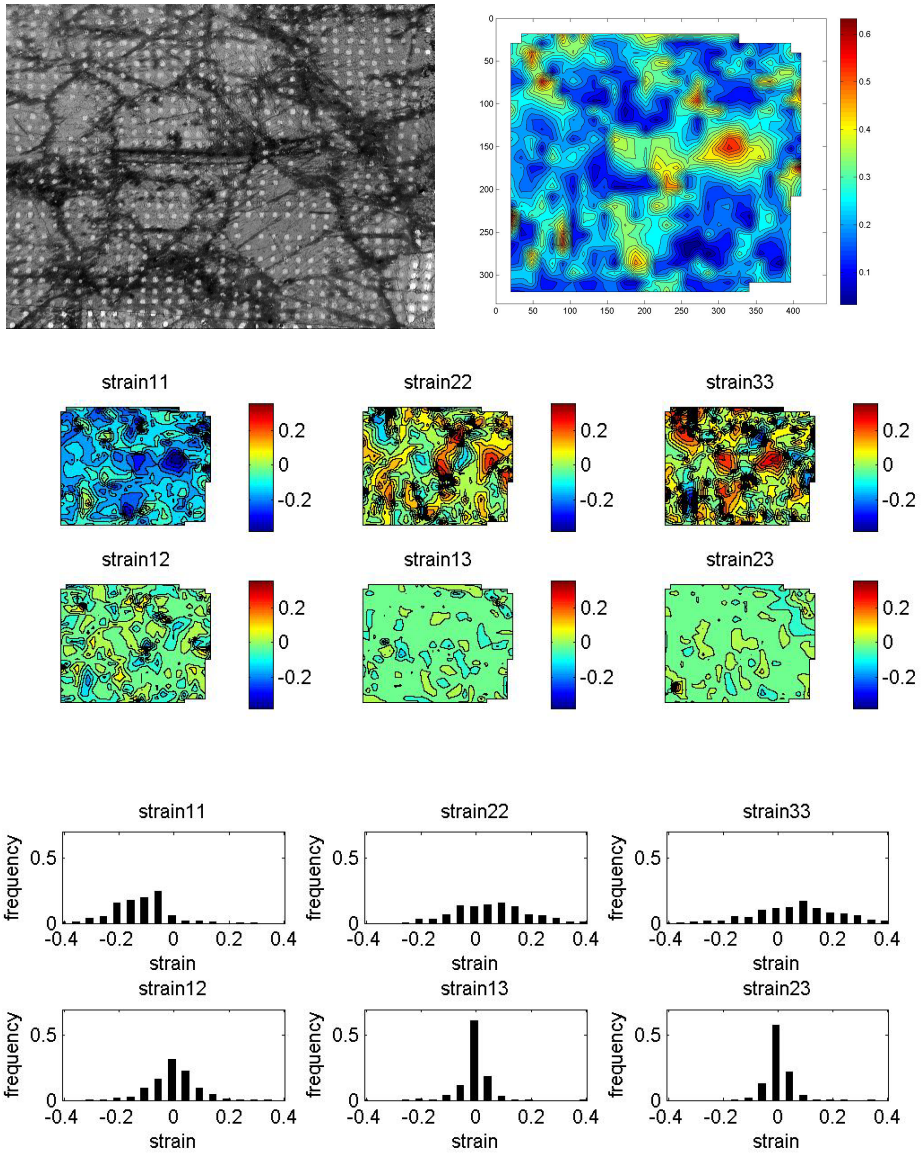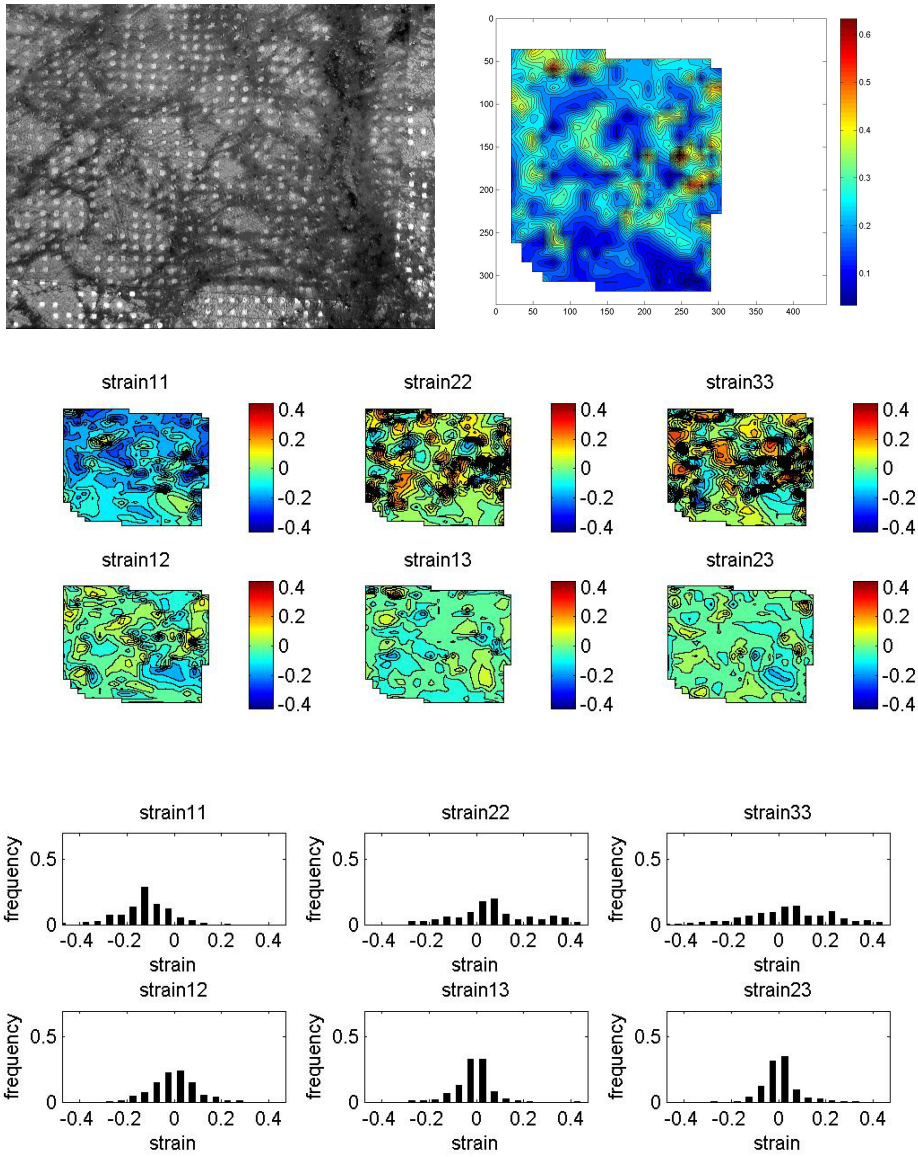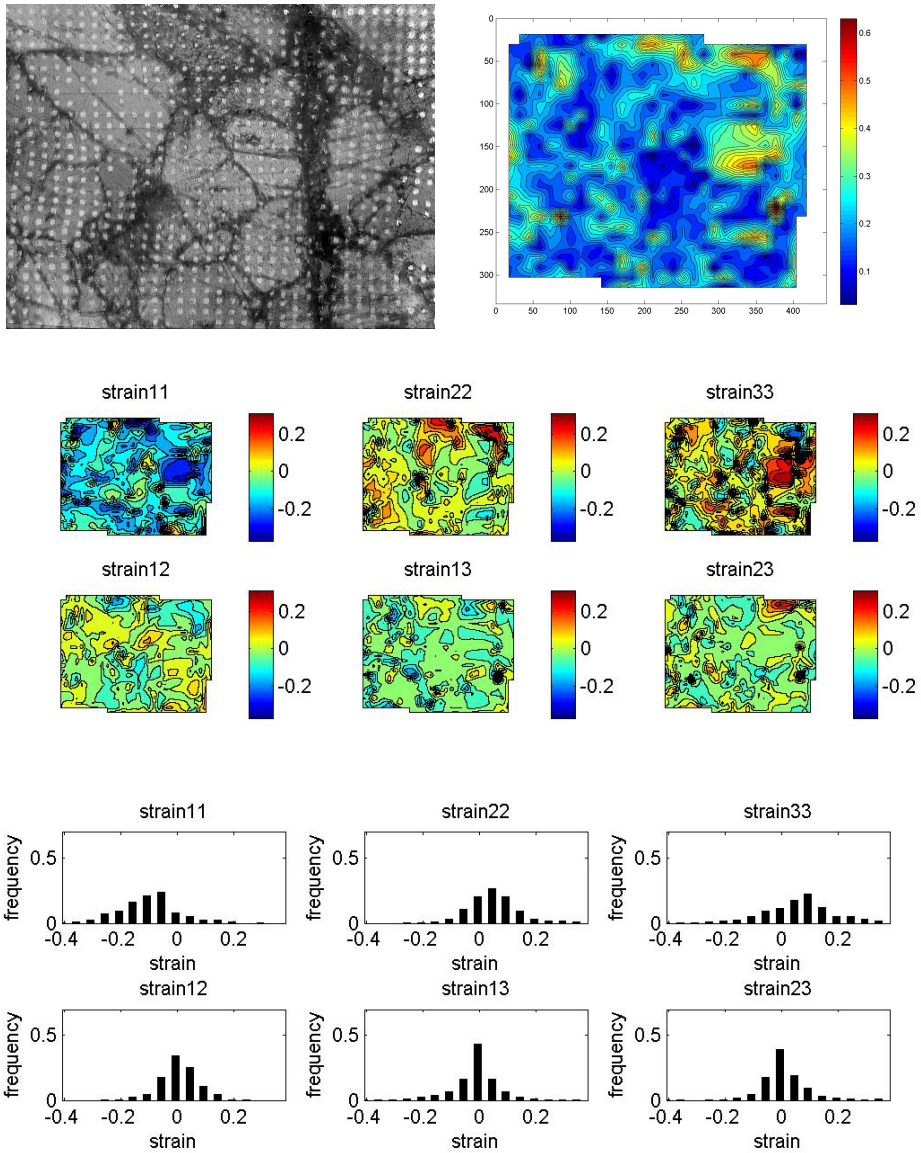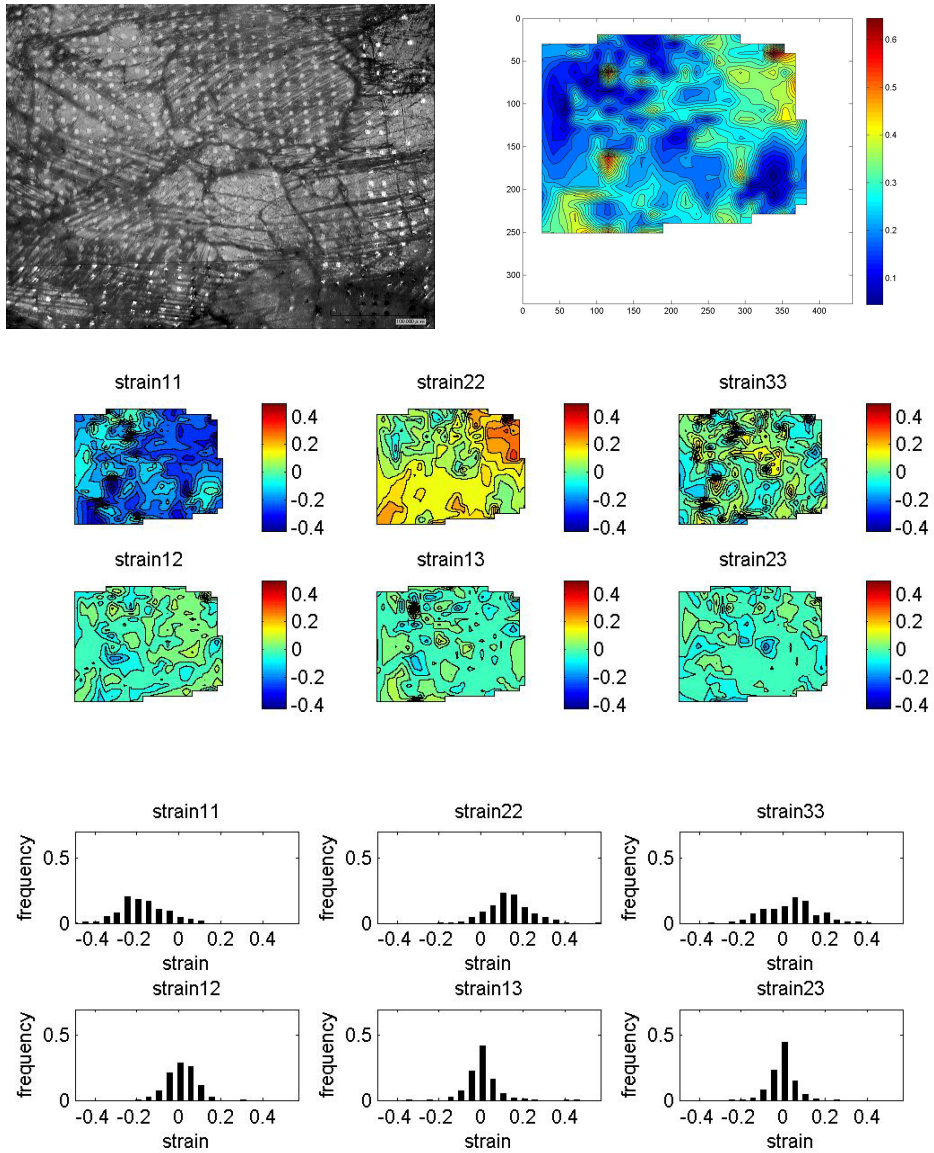D:\Research\rock\images\grid_analysis\IDL\to_print\CM11_after\result_9n

145

Figure A7. Sample CM09, see Fig. A1 for figure caption.

D:\Research\rock\images\grid_analysis\IDL\to_print\CM09_after\result_8n\
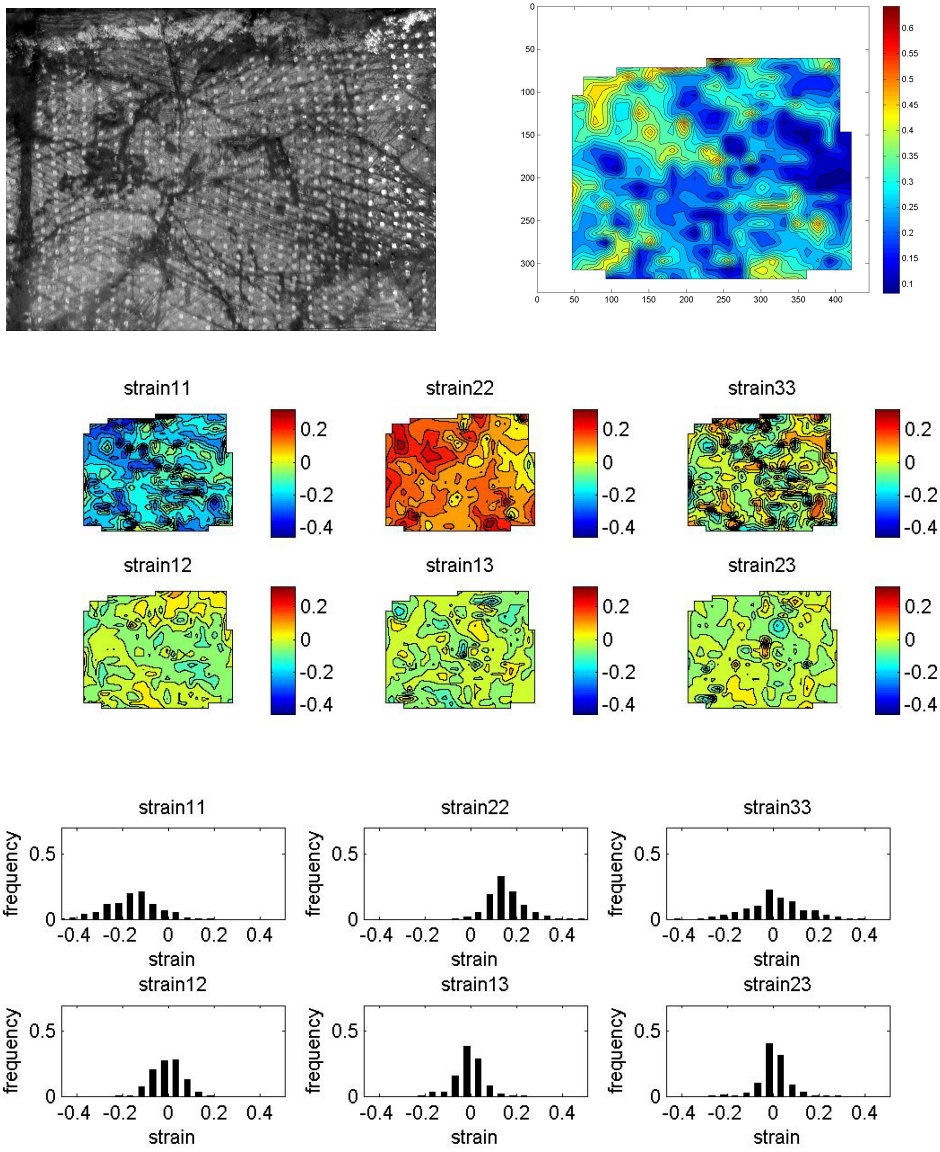
Figure A8. Sample CM09, see Fig. A1 for figure caption.

D:\Research\rock\images\grid_analysis\IDL\to_print\CM09_after\result_9n\

Chapter 4: Development of Carbonate Texture during Deformation using Visco-Plastic Self-Consistent Modeling

Abstract

Carrara marble samples are compressed to 5-25% at 400-800ºC and 300 MPa. The texture development was studied using Electron Back Scattered Diffraction (EBSD) analysis. Visco-plastic self-consistent (VPSC) modeling is applied to understand the active slip systems in compression tests of calcite. Our results suggest dominant activations of r<sd> and basal c slip systems at current deformation conditions. Individual grains are traced before and after deformation to study the change of crystallographic orientations due to deformation process. The predicted grain rotation behavior from VPSC simulation can be changed significantly by varying the critical resolved shear stress values of different slip systems. The comparison between the observed grain rotation behavior from EBSD data and that from VPSC simulation shows that only a small number of grains can be successfully predicted by the VPSC simulation. Our result suggests that VPSC modeling is not very successful in predicting the deformation behavior of individual grains especially small grains, indicating that other factors, including deformation heterogeneity and grain to grain interaction, need to be taken into account and that cares must be taken in using the homogeneous effective medium theory to predict the microscopic deformation of polycrystals.

4.1 Introduction

Interpreting the structure of rocks deformed in natural settings is an important task in field structural geology, and it has long been appreciated that the crystallographic preferred orientation in rocks contains detailed information about the mechanical history (Sander, 1950; see also a review by Wenk, 2002). Recent developments in the understanding of deformation mechanisms in minerals, in techniques of optical and electron microscopy, and in the polycrystal plasticity theories, now allow detailed calculations of the production of texture, quantitative observations of textures, and comparison of fabrics of naturally deformed rocks, of experimentally deformed samples, and of those calculated. In particular, the development of preferred orientation patterns during plastic deformation of calcite has been a subject of many experimental and theoretical investigations (Burlini and Kunze, 2000; de Wall et al., 2000; Khazanehdari et al., 1998; Pieri et al., 2001a; Ratschbacher et al., 1991; Rutter, 1974; Rutter et al., 1994; Schmid et al., 1980; Wagner et al., 1982; Wenk and Shore, 1974; Wenk et al., 1986; Wenk et al., 1981).

The deformation mechanisms identified in deformation experiments of single crystal of calcite (de Bresser and Spiers, 1997; Griggs et al., 1960) are an important element in predicting the development of preferred orientation. Based on the deformation behavior of individual slip systems, fabrics in naturally deformed carbonate rocks can be interpreted in terms of paleostress (Lacombe and Laurent, 1992; Rowe and Rutter, 1990)

and deformation history (Burlini et al., 1998; Dietrich, 1986; Erskine et al., 1993). Previous experimental studies (Barber et al., 2007; de Bresser and Spiers, 1997; Turner et al., 1954) established the relative importance of multiple slip systems in calcite rocks at different temperatures, including twinning on $e\langle40\bar{4}1\rangle$, slip on $r\langle\bar{2}021\rangle$, $f\langle\bar{2}021\rangle$ at low temperature, $f\langle0\bar{1}11\rangle$ at high temperature, and $c\langle12\bar{1}0\rangle$.

Two end member descriptions of deformation of a polycrystalline material are the Taylor model, which assumes a homogeneous strain (Turner et al., 1954), and the Sachs model, which assumes a uniform stress state throughout the polycrystal (Wagner et al., 1982; Wenk et al., 1987). The Taylor assumption is reasonable for material with many slip systems of comparable strength, using it in other conditions can lead to prediction of excessively high stresses and incorrect textures. This approach is known as an upper bound. With the Sachs approach, only the most favorable slip systems are activated, and thus the stress is low. This approach is known as a lower bound.

A large part of the complexity in predicting texture development of minerals with low symmetrylike calcite arises from the fact that different slip systems in these materials have highly disparate flow strengths, and thus, the individual grains within the polycrystal will strain differently. In addition, the understanding of the critical resolved shear stresses necessary to activate different slip systems is limited (de Bresser and Spiers, 1997; Griggs et al., 1960; Turner et al., 1954), and, thus, it has been considerably more difficult to simulate texture evolution in calcite rocks than that in metallic materials (Beausir et al., 2008; Lebensohn and Tome, 1993).

Unlike the Taylor and Sachs models which assume either strain compatibility or stress equilibrium, the VPSC formulation allows the local stress and strain-rate to be different from the corresponding macroscopic magnitudes, according to their directional plastic properties (Lebensohn et al., 1998; Molinari et al., 1987; Wenk and Christie, 1991). Grains are allowed to have different stress and strains, neighboring grains are rotating differently and related to each other using a homogeneous effective medium theory (HEM).

The VPSC modeling has been widely used to understand the texture development during the shear and torsion experiments in calcite rocks (Barnhoorn et al., 2002; Casey et al., 1998; Pieri et al., 2001b). Compression tests on carbonate rocks at different temperatures show pronounced changes in preferred orientation patterns (Wenk et al., 1973); but the texture simulation to understand these compression test results has been less successful (Barber et al., 2007; Lebensohn et al., 1998; Pieri et al., 2001a; Wenk et al., 1987).

Despite the increasing application of VPSC modeling in predicting the texture development during rock deformation (Barber et al., 2007; Casey et al., 1998; Pieri et al., 2001b; Tome et al., 1991; Wenk et al., 1987), no studies have been made to understand the effectiveness of VPSC simulation in predicting the deformation behavior of individual grains during the plastic deformation of rocks. This is largely due to the difficulties in conducting the experiments. The strain mapping technique (Chapter 3) and the following EBSD study allow us to get insights into the microstructural deformation.

The quantification of grain-to-grain interactions during straining is relevant for the improvement and verification of polycrystalline homogenization models (Jia et al., 2008), which is valuable for the prediction of deformation texture of polycrystalline bulk material.

In this investigation, we studied the texture development of Carrara marble samples during compression tests using EBSD data and compared our observations with the simulated texture from VPSC modeling. Different CRSS values are tested to find the best-fitting models. The EBSD data also provides us information of the grain rotation during the plastic deformation; and, in addition, the strain mapping results from Chapter 3 can provide information about the local strain heterogeneities. Using these data, the grain rotation and strain distribution of individual grains can be compared with the simulation results from self-consistent modeling, providing new insights into the grain-to-grain interactions and the ability of VPSC modeling in predicting the grain rotation during the plastic deformation of rocks.

4.2 Methodology

The texture observations were collected from the Carrara marble samples discussed in the previous chapter by analyzing backscattered diffraction patterns in the scanning electron microscope, a technique called EBSD. These rocks were deformed under triaxial loading at 400-800℃, and 300 MPa confining pressure using Paterson gas-medium apparatus. The strain rate varies from 10^{-5} to $10^{-4}\,s^{-1}$; the samples are compressed to 5-25

% strain under constant strain rate tests (see Table 1, Chapter 3). At these strain rates and temperatures below 800ºC, Carrara marble probably deforms by dislocation creep (Covey-Crump, 1998; Rutter, 1974; Schmid et al., 1980) .

4.2.1 Observation of Grain Rotation Using EBSD:

After the strain mapping analyses described in chapter 3, we repolished the samples using colloidal silica (~0.03 microns) on automatic wheels for several hours. The sample was coated with Au/Pt and then gently polished again. EBSD patterns were obtained using a JEOL 840 SEM operating at an accelerating voltage of 15 kv, a beam current of ~30-60 nA and a working distance of 23 mm. EBSD patterns were collected either with steps of 15-25 microns over a large surface or one point per grain, depending on the success rate of pattern identification. Diffraction patterns were acquired and automatically indexed using the program Channel 5 from HKL software. This program searches for an indexing solution: a lattice orientation, for the mineral structure input into the program. Maps of orientation data can be processed to remove erroneous data and provide a more complete microstructural reconstruction of the sample.

The orientation of individual grains can be defined completely by the orientation matrix g_{ij}, which is a function of Euler angles ($\varphi_1, \phi, \varphi_2$):

$$g = \begin{bmatrix} \cos\varphi_2 & -\sin\varphi_2 & 0 \\ \sin\varphi_2 & \cos\varphi_2 & 0 \\ 0 & 0 & 1 \end{bmatrix} \begin{bmatrix} 1 & 0 & 0 \\ 0 & \cos\phi & -\sin\phi \\ 0 & \sin\phi & \cos\phi \end{bmatrix} \begin{bmatrix} \cos\varphi_1 & -\sin\varphi_1 & 0 \\ \sin\varphi_1 & \cos\varphi_1 & 0 \\ 0 & 0 & 1 \end{bmatrix} \quad (1).$$

The same areas before and after deformation are recognized using scratch lines and/or ink markers. Based on the grain-orientation measurements on both the undeformed and deformed samples, the evolution of micro-texture in calcite is analyzed by calculating the rotation axis and angle (Mainprice et al., 1993; Randle and Ralph, 1986; Wheeler et al., 2001).

The rotation that transforms the orientation g_{ij} of the grain into the reference coordinate system (identity matrix) is given by the transverse matrix $g_{ij}^T = g_{ji}$. The misorientation Δg between two grains (A and B) is presented by the misorientation matrix M_{ij} $(= g_A^T g_B)$. From the misorientation matrix, the misorientation axis/angle (m/θ) can be calculated using (Kruse et al., 2001; Lloyd et al., 1997)

$$\theta = \cos^{-1}\left\{[g_{11} + g_{22} + g_{33} - 1]/2\right\} \tag{2a}$$

$$m = \left[\frac{g_{23} - g_{32}}{2\sin\theta}, \frac{g_{31} - g_{13}}{2\sin\theta}, \frac{g_{12} - g_{21}}{2\sin\theta}\right] \tag{2b}$$

The same calculation can be performed on an individual grain before and after deformation test to get the grain rotation angle. The EBSD data is able to resolve misorientation angles of ~1° (Humphreys et al., 2001).

4.2.2 Visco-plastic self-consistent Modeling

The texture development is simulated here using the visco-plastic self-consistent modeling of Lebensohn, Wenk and co-workers (Lebensohn and Tome, 1993; Molinari et

al., 1987; Wenk et al., 1987). We assume an aggregate of 1,000 crystals, a particular set of slip systems (see Table 1) and critical resolved shear stresses and strain rate sensitivity (stress exponent n = 5, Rybacki et al. 2003) based on previous determinations for calcite crystals. Each grain is embedded in a homogeneous effective medium (HEM) that represents the average over all orientations (Molinari et al., 1987). The orientation of different slips systems in an individual grain can be calculated from Euler angle analysis (Bunge, 1982).

Each grain has the freedom to deform differently, depending on its orientation and its interaction with the surrounding material. The local strain-rate can be described by the visco-plastic equation (Lebensohn et al., 1998; Molinari et al., 1987) if the geometry and critical stresses of the active slip and twinning systems in each grain are known,

$$\dot{\varepsilon}_k = \gamma_0 \sum_{s=1}^{S} m_k^s \left(\frac{m_j^s \sigma_j^{'}}{\tau_c^s} \right)^n \quad where \ k = 1...5 \tag{3}$$

where the sum is carried over all the slip systems in the grain, and m, γ_0, τ_c, n, σ are the Schmid tensor, a reference shear-rate, the critical stress of the particular slip or twinning system, the stress sensitivity factor, and microscopic stress, respectively.

The VPSC modeling considers each grain of the polycrystal as a visco-plastic inclusion deforming in a visco-plastic homogeneous effective medium. The medium has the average properties of the polycrystal and is based on the determination of the interaction tensor $\tilde{M}$:

156

$$\tilde{M} = (I - S)^{-1} SM^{(tg)} \tag{4}$$

where S is the visco-plastic Eshelby tensor (Lebensohn and Tome, 1993), which depends on the grain shape and the plastic properties of the HEM, and $M^{(tg)}$ is the tangent modulus which is not known and has to be determined self-consistently. This interaction tensor relates the deviations in stress and strain-rate from the average, and is used to predict the local state. The interaction tensor depends both explicitly and implicitly (via the Eshelby tensor) on the macroscopic modulus.

The reorientation of each grain due to slip and twinning can be updated at each deformation step; the formulation allows each grain to deform by different amount. The lattice rotation of each grain is given by:

$$\dot{\omega}_{ij} = \dot{\Omega}_{ij} + \Pi_{ijkl} S_{klmn}^{-1} \dot{\tilde{\varepsilon}}_{mn} - \sum_s \frac{1}{2} \left(b_i n_j - b_j n_i \right)^s \dot{\gamma}^s \tag{5}$$

where the first term is the antisymmetric component of the macroscopic distortion rate, the second term is the reorientation of the associated ellipsoid, and the last term is the antisymmetric component of the plastic distortion rate. A texture development calculation is carried out by imposing incremental steps of deformation.

Three alternative models for the slip system strengths have been postulated (Barber et al., 2007; de Bresser and Spiers, 1997; Pieri et al., 2001b). The relative strength of different slip systems in the VPSC models (i.e., the critical resolved shear stress, CRSS)

has been measured by de Bresser et al. (1997). The only parameter we insert into their model (model 3) is the CRSS of r<a> slip system, which has not been measured. The inverse pole figures predicted from the various VPSC simulations are then compared to the experimental results in an attempt to determine the relative importance of the CRSS's and the mutual influence between deformations by different slip systems are reinterpreted. The rotation angles are then compared with the simulated results from VPSC calculations using the slip system models.

4.3 Results

After yielding at 3-4% strain, the strength of Carrara marble at 300 MPa, 400-800℃, and laboratory strain rates, is nearly constant over the interval of strain from 4% to 25%. Some samples do show slight strain weakening or strengthening. Experiments done over much larger strain intervals do indicate that carbonate rocks may continue to harden up to strains of 1-3, and may weaken by as much as 1/3 after the peak strength (Paterson and Olgaard, 2000; Pieri et al., 2001a). In the samples examined here, for the relatively short time that they are deformed, the average grain size did not vary; boundaries could be observed to migrate, however, and most grains changed shape (see Chapter 3). Previous studies (Rutter, 1995; Schmid et al., 1980) indicated that Carrara marble deforms by dislocation creep under the conditions used here.

4.3.1 Texture development of Carrara Marble

For sample CM05, which was deformed at 700℃ and 300 MPa to 20% strain in

compression, the inverse pole figure (Fig. 1b) shows a maximum near $e(01\bar{1}8)$, a result very similar to that from previous experiments by Wenk et al. (1973). In that work, the maximum concentration of compression poles shifts from near (0001) towards $e(01\bar{1}8)$ as temperature increases (Fig. 2). At even higher temperatures, maximum of compression axes moves nearer to the high-angle positive rhombs $r(10\bar{1}4)$ (Fig. 2c).

The simulated inverse pole figures obtained from three different VPSC models are shown in Fig. 3. Each VPSC model is characterized by a set of CRSS values and slip systems (Barber et al., 2007; de Bresser and Spiers, 1997; Pieri et al., 2001b) (Table 1). No significant differences exist in the inverse pole figures produced by the simulations, and it is difficult to choose the best-fitting model by simply looking for similarities between the observed and calculated textures. For example, all the inverse pole figures show a maximum near $e(01\bar{1}8)$. Perhaps the second model (Fig. 3b) is less favored, because it has a second maximum near $a\langle 1\bar{1}\bar{2}0\rangle$, whereas the observed inverse pole figure (Fig. 1b) has a second maximum between $r(10\bar{1}4)$ and $m(10\bar{1}0)$. The observed feature may be more comparable to secondary peaks in the first model (Fig. 3a).

The variations in the CRSS values from model to model (Table 1) affect the relative activities of the slip systems, obtained by normalizing and averaging the shears associated with each system (Fig. 4). Models 1 and 3 have relatively weak $r\langle\bar{2}021\rangle$ and $f\langle\bar{2}20\bar{1}\rangle$ slip systems while model 2 has similar CRSS values for all the active slip systems. The slip system activities from models 1 and 3 are similar, and $r\langle\bar{2}021\rangle$ and basal slip c are the

most active, while the second model has $f\langle \bar{2}20\bar{1}\rangle$ as the most active slip system. Although model 1 seems to describe the inverse pole figures slightly than model 3, we will suggest below that model 3 is more successful in predicting grain rotations.

4.3.2 Grain Reorientation due to deformation process

Grain rotation rates depend directly on slip system activities, and, thus, individual grain rotations might vary from model to model, even under the same loading. In Fig. 5, trajectories for 18 grains of various orientations are predicted by each model for compression to 30% strain. Notice that some orientations are quite sensitive to model parameters, but others are not; and, in fact, in some orientations, both the axis of rotation and the magnitude of the angle of rotation may be quite different, even for models 1 and 3, which are very similar.

By using the strain mapping technique and EBSD measurements, we measured individual grain rotations and compared them to the VPSC calculations. To measure the total angle of grain rotation owing to deformation requires determination of the orientations of a particular grain before and after deformation from the gray-scale images and EBSD experiments. As discussed in chapter 3, grains can be identified by using the scratched lines on the gray-scale images and by comparing the grain boundary geometries. Fig. 6 (a-b) shows the grain orientation maps of sample CM12 (undeformed and deformed) from HKL software after extrapolation and filtering. Fig. 6 (c-d) shows the grain-misorientation profiles across the microstructure (see Fig. 6) and that within 9

grains. All the misorientation angles are calculated relative to the first point. These profiles show that there are substructures inside grains with characteristic size of ~ 20–80 microns and misorientation angles of less than 5º. If the rotation axis is not in the 2D plane, it can be shown as a rotation of grid markers of certain angles in the 2D surface (Fig. 18, Chapter 3).

The rotation angles of 18 individual grains before and after deformation were calculated using equations 1-2 (Table 2).   Since the rotation angles are small (<5º), we need to be very careful in the grain orientation analysis. The two main resources of error are: (1) resolution in the rotation angle determination and (2) sample misalignment inside the virtual camber. The resolution of the rotation angle can be improved by increasing the number of patterns on each grain. Our step size in EBSD measurements vary from 15 to 25 μm. For grains larger than ~200 μm, we will have about 100 samples per grain, which may then be averaged. Because small grains (identified by red dots in Fig. 7c) have larger uncertainties in the grain rotation angles, those orientation data are not considered further .The second source of error is misalignment of the sample in the SEM sample holder: a few degrees uncertainty is important for grain reorientation measurement. We correct the sample misalignment manually by calculating the orientations of a certain direction (e.g. c (0001)) in the same grains on two surfaces and find the minimum misfit between the two surfaces.

A comparison of grain rotation angles observe in the EBSD study and that calculated from the VPSC simulations for the three models is given in Table 3 and correlations of

161

misorientation angles for Model 3 and the observations are shown in Fig. 7. The grain rotation angles observed from EBSD vary from 1.7 to 4.5°, values that are slightly larger than those predicted by VPSC simulation (0.8-3.3°). As expected some grains are predicted accurately in both magnitude and direction, and the comparison fails for other grains. Several factors could contribute to the discrepancies: (1) errors in determination of the angle of grain rotation from EBSD data; (2) heterogeneous deformation within a grain; (3) grain boundary sliding; and (4) grain-grain interactions not predicted by the homogeneous effective medium (HEM) theory. These factors are discussed in more detail in section 4.2.

The trajectories for 18 individual grains observed by EBSD (Table 2) and calculated from our VPSC simulations using model 3 (Table 3) are plotted in Fig. 8. We consider the comparison to be good (Category 1) when both the axis and magnitude of rotation of the observed and simulated rotations agree, to be OK (Category 2) if either magnitude or orientation are predicted, and poor (Category 3) if neither agree: grains 3, 6, and 15 fall into the first category; grains 4, 8, 12, 13, and 17 fall into the second category; and grains 1, 2, 9, 7, and 14 fall into the third category. The comparison shows that only a small number of grains can be successfully predicted in detail by the VPSC simulation (Fig. 8 and Table 3) even for the best model (3); Model 2 predicts the fewest grains successfully.

4.4 Discussion

4.4.1 CRSS for VPSC simulation

The inverse pole figure from the compression test on Carrara marble at temperature of 700ºC is characterized by a maximum near $e\left(01\bar{1}8\right)$, i.e., on the border between $r_1\left(10\bar{1}4\right)$ and $r_2\left(1\bar{1}04\right)$, and in reasonably good agreement with results of previous axial compression experiments on marble and limestone (Spiers, 1979; Wenk et al., 1973). In this position, both r_1 and r_2 slip can be activated, allowing the compression orientation to stabilize in the vicinity of $e\left(01\bar{1}8\right)$. Note that neither slip plane is normal to the compression direction. The compression direction never reaches the slip plane normal, because in that orientation, the Schmid factor is zero, and an infinitely high stress is required to activate slip (Wenk and Christie, 1991). We note that many grains have multiple slip systems with Schmid factors greater than 0.4 under the current loading conditions, indicating multiple slip; slip systems on c and r <sd> have the highest Schmid factors.

Simulated textures for the aggregate for all three visco-plastic self-consistent (VPSC) models agree with the observed texture (e.g. Figs. 1-3), and we infer that this comparison does not discriminate between the models. By contrast, in at least some cases, the rotations of some single grains seem to be more sensitive to variations in the CRSS values of different slip systems. Thus, the comparison between the observed grain reorientation and that from VPSC simulation is potentially useful to discriminate different

163

VPSC models and test the homogenous effective medium theory. In the ensemble of 13 grains shown in Fig. 8, in only three grains, i.e., 3, 6 and 16, do the observed and simulated rotations agree well.

4.4.2 HEM theory

In order to relate the mechanical behavior of single crystals to that of macroscopic polycrystals, averaging assumptions including stress equilibrium (Sachs model), strain compatibility assumptions (Taylor model), or the self-consistent model (HEM theory) must be made (Lebensohn et al., 1998; Wagner et al., 1982; Wenk et al., 1986). The self-consistent model is a distinct improvement over the simpler Sachs and Taylor models because it introduces heterogeneous deformation by assuming that the single crystal is embedded in a homogeneous effective medium (equations 3-4).

For the grain orientations measured in sample CM11 (12% strain at 10^{-5} s^{-1}, 600ºC and 300 MPa), we calculated the Von Mises effective strains using both the Sachs model and the homogeneous effective medium theory (Figs. 9 a-b), and compare those results to the strains obtained using the mapping technique (Fig. 9c). It is obvious that the self-consistent model is able to characterize the strain distribution more realistically than the Sachs model. Cross-correlations between the calculated strains from the self-consistent model and the strain mapping analysis (Fig. 10) indicate that large grains follow the homogeneous effective medium theory more closely, while small grains show a lot of scattering in the data. Three reasons are possible: small grains may be affected

more strongly by stress heterogeneity in the medium; they may be influenced more by strain heterogeneities, such a boundary sliding, or they may simply be prone to larger errors in orientation determinations.

Previous studies suggest that the grain rotations during the plastic deformation of polycrystalline aggregates are highly dependent on the stress state at the grain boundaries, the grain boundary misorientations, intracrystalline and intercrystalline strain heterogeneities, and grain boundary sliding (Barbe et al., 2001a; Barbe et al., 2001b; Rutter, 1995; Zhang and Tong, 2004). In this VPSC modeling, many slip systems (e.g., 4.5 in average for VPSC modeling of calcite compression tests, Figs. 3-5) are activated within individual grains during the deformation of polycrystalline calcite, the grain rotations is usually hard to predict and largely dependent on the CRSS values for different slip systems, even withstanding the other mechanisms mentioned above.

The comparison between the observed grain rotation behavior due to deformation and that predicted from different VPSC models (Fig. 7) show that only a small number of grains can be successfully predicted by the VPSC simulation. Since the actual grain rotations within polycrystals are affected by heterogeneous deformation in the microstructural scale, grain boundary sliding, and stress state at the grain boundaries, it is hard to test the ability of homogeneous effective theory (HEM) in predicting the actual deformation of individual grains inside polycrystalline material without a better understanding of these effects.

The strain mapping results (Chapter 3) shows heterogeneity in both intracrystalline and

intercrystalline deformation. The heterogeneous deformation during plastic deformation of material sometimes can be shown as the reorientation of crystal lattice within grains. If the neighboring grains are under different amount of strain, it is likely that the grain can rotate differently from what the homogeneous effective medium theory predicts. In addition, if the grain boundary sliding is present, which is likely true from grid marker analysis (Chapter 3), the deformation heterogeneity at neighboring grains can be accommodated by the grain boundary sliding. The grain boundary sliding can also be responsible for the weakening of the initially strong CPO, and increase in the mean misorientation angle between neighboring grains and random misorientation axes (Bestmann and Prior, 2003; Fliervoet et al., 1997; Jiang et al., 2000).

4.5 Conclusions:

Specific conclusions of this study are

1. In agreement with several previous studies, the inverse pole figure from compression test of Carrara marble at temperature of ~700℃ is characterized by a maximum near $e\left(01\bar{1}8\right)$, indicating a dominant activation of r<sd> slip system.

2. Simulated textures from visco-plastic self-consistent (VPSC) modeling can provide a good comparison to the observed texture, particularly using CRSS values from de Bresser and Spiers (1997). However, the predictions of the aggregate textures using different VPSC models may be quite similar, making it difficult to identify the best CRSS model based solely on comparison of pole figures alone.

3. The simulated grain rotation behavior is very sensitive to the CRSS values in VPSC modeling, and the comparison of the grain rotation behavior between VPSC simulation and EBSD observation is a potentially useful method to discriminate different VPSC models and test the homogenous effective medium theory.

4. The strain distribution observed from strain mapping and that predicted from Sachs and self-consistent model indicate that large grains can be described by the effective medium theory better than the small grains. The small grains may be more affected by the heterogeneity in stress and strain in the surrounding medium or by localized deformation along the grain boundaries, but it is also possible that the scattered results are simply from data resolution issues.

5. The comparison between the observed grain rotation behavior from EBSD study and that predicted from different VPSC models shows that only a small number of grains can be successfully predicted by the VPSC simulation.

The self-consistent model gives a good description of global texture, but not always for individual lattice rotation and deformation of the grains. Perhaps this result is not surprising because the model considers only the interaction between a single grain and an average equivalent background, and neglects interactions between neighboring grains, deviations from an equiaxed grains shapes, and local heterogeneities of strain distribution in grain interiors or along boundaries. To predict the actual deformation of individual grains inside polycrystalline material in more details will require a quantitative consideration of the effects on local strain of grain boundary misorientation, local

167

strain/stress state, grain boundary sliding, and deviations in grain geometry.

4.6 References

Barbe, F., Decker, L., Jeulin, D. and Cailletaud, G., 2001a. Intergranular and intragranular behavior of polycrystalline aggregates. Part 1: Fe model. International Journal of Plasticity, 17(4): 513-536.

Barbe, F., Forest, S. and Cailletaud, G., 2001b. Intergranular and intragranular behavior of polycrystalline aggregates. Part 2: Results. International Journal of Plasticity, 17(4): 537-563.

Barber, D.J., Wenk, H.R., Gomez-Barreiro, J., Rybacki, E. and Dresen, G., 2007. Basal slip and texture development in calcite: New results from torsion experiments. Physics and Chemistry of Minerals, 34(2): 73-84.

Barnhoorn, A., Bystricky, M., Burlini, L. and Kunze, K., 2002. The role of recrystallization on the deformation behaviour of calcite rocks: High strain torsion experiments on Carrara marble. (poster) Gordon Conference on Rock Deformation.

Beausir, B., Suwas, S., Toth, L.S., Neale, K.W. and Fundenberger, J.J., 2008. Analysis of texture evolution in magnesium during equal channel angular extrusion. Acta Materialia, 56: 200-214.

Bestmann, M. and Prior, D.J., 2003. Intragranular dynamic recrystallization in naturally deformed calcite marble: Diffusion accommodated grain boundary sliding as a result of subgrain rotation recrystallization. Journal of Structural Geology, 25(10): 1597-1613.

Bunge, H.J., 1982. Texture analysis in materials science: Mathematical methods p593.

Burlini, L. and Kunze, K., 2000. Fabric and seismic properties of Carrara marble mylonite. Physics and Chemistry of the Earth Part a-Solid Earth and Geodesy, 25(2): 133-139.

Burlini, L., Marquer, D., Challandes, N., Mazzola, S. and Zangarini, N., 1998. Seismic properties of highly strained marbles from the splugenpass, central Alps. Journal of Structural Geology, 20(2-3): 277-292.

Casey, M., Kunze, K. and Olgaard, D.L., 1998. Texture of Solnhofen limestone deformed to high strains in torsion. Journal of Structural Geology, 20(2-3): 255-267.

Covey-Crump, S.J., 1998. Evolution of mechanical state in Carrara marble during deformation at 400 degrees to 700 degrees c. Journal of Geophysical Research-Solid Earth, 103(B12): 29781-29794.

de Bresser, J.H.P. and Spiers, C.J., 1997. Strength characteristics of the r, f, and c slip systems in calcite. Tectonophysics, 272(1): 1-23.

de Wall, H., Bestmann, M. and Ullemeyer, K., 2000. Anisotropy of diamagnetic susceptibility in Thassos marble: A comparison between measured and modeled data. Journal of Structural Geology, 22(11-12): 1761-1771.

Dietrich, D., 1986. Calcite fabrics around folds as indicators of deformation history. Journal of Structural Geology, 8(6): 655-668.

Erskine, B.G., Heidelbach, F. and Wenk, H.R., 1993. Lattice preferred orientations and microstructures of deformed cordilleran marbles - correlation of shear indicators and determination of strain path. Journal of Structural Geology, 15(9-10): 1189-1205.

Fliervoet, T.F., White, S.H. and Drury, M.R., 1997. Evidence for dominant grain-boundary sliding deformation in greenschist- and amphibolite-grade polymineralic ultramylonites from the redbank deformed zone, central australia. Journal of Structural Geology, 19(12): 1495-1520.

Griggs, D., Turner, F.J. and Heard, H.C., 1960. Deformation of rocks at 500 to 600°c. Geological Society of America Bulletin, 79: 39-105.

Humphreys, F.J., Bate, P.S. and Hurley, P.J., 2001. Orientation averaging of electron backscattered diffraction data. Journal of Microscopy-Oxford, 201: 50-58.

Jia, N., Lin Peng, R., Chai, G., Johansson, S. and Wang, Y., 2008. Direct experimental mapping of microscale deformation heterogeneity in duplex stainless steel Materials Science and Engineering, 491(1-2): 425-433.

Jiang, Z.T., Prior, D.J. and Wheeler, J., 2000. Albite crystallographic preferred orientation and grain misorientation distribution in a low-grade mylonite: Implications for granular flow. Journal of Structural Geology, 22(11-12): 1663-1674.

Khazanehdari, J., Rutter, E.H., Casey, M. and Burlini, L., 1998. The role of crystallographic fabric in the generation of seismic anisotropy and reflectivity of high strain zones in calcite rocks. Journal of Structural Geology, 20(2-3): 293-299.

Kruse, R., Stunitz, H. and Kunze, K., 2001. Dynamic recrystallization processes in plagioclase porphyroclasts. Journal of Structural Geology, 23(11): 1781-1802.

Lacombe, O. and Laurent, P., 1992. Determination of principal stress magnitudes using calcite twins and rock mechanics data. Tectonophysics, 202(1): 83-93.

Lebensohn, R.A. and Tome, C.N., 1993. A self-consistent anisotropic approach for the simulation of plastic-deformation and texture development of polycrystals - application to zirconium alloys. Acta Metallurgica Et Materialia, 41(9): 2611-2624.

Lebensohn, R.A., Wenk, H.R. and Tome, C.N., 1998. Modelling deformation and recrystallization textures in calcite. Acta Materialia, 46(8): 2683-2693.

Lloyd, G.E., Farmer, A.B. and Mainprice, D., 1997. Misorientation analysis and the formation and orientation of subgrain and grain boundaries. Tectonophysics, 279(1-4): 55-78.

Mainprice, D., Lloyd, G.E. and Casey, M., 1993. Individual orientation measurements in quartz polycrystals - advantages and limitations for texture and petrophysical property determinations. Journal of Structural Geology, 15(9-10): 1169-1187.

Molinari, A., Canova, G.R. and Ahzi, S., 1987. A self-consistent approach of the large deformation polycrystal viscoplasticity. Acta Metallurgica, 35(12): 2983-2994.

Paterson, M.S. and Olgaard, D.L., 2000. Rock deformation tests to large shear strains in torsion. Journal of Structural Geology, 22(9): 1341-1358.

Pieri, M., Burlini, L., Kunze, K., Stretton, I. and Olgaard, D.L., 2001a. Rheological and microstructural evolution of Carrara marble with high shear strain: Results from high temperature torsion experiments. Journal of Structural Geology, 23(9): 1393-1413.

Pieri, M., Kunze, K., Burlini, L., Stretton, I., Olgaard, D.L., Burg, J.P. and Wenk, H.R., 2001b. Texture development of calcite by deformation and dynamic recrystallization at 1000 k during torsion experiments of marble to large strains. Tectonophysics, 330(1-2): 119-140.

Randle, V. and Ralph, B., 1986. A practical approach to the determination of the crystallography of grain-boundaries. Journal of Materials Science, 21(11): 3823-3828.

Ratschbacher, L., Wenk, H.R. and Sintubin, M., 1991. Calcite textures - examples from nappes with strain-path partitioning. Journal of Structural Geology, 13(4): 369-384.

Rowe, K.J. and Rutter, E.H., 1990. Paleostress estimation using calcite twinning - experimental calibration and application to nature. Journal of Structural Geology, 12(1): 1-17.

Rutter, E.H., 1974. Influence of temperature, strain rate and interstitial water in experimental deformation of calcite rocks. Tectonophysics, 22(3-4): 311-334.

Rutter, E.H., 1995. Experimental study of the influence of stress, temperature, and strain on the dynamic recrystallization of Carrara marble. Journal of Geophysical Research-Solid Earth, 100(B12): 24651-24663.

Rutter, E.H., Casey, M. and Burlini, L., 1994. Preferred crystallographic orientation development during the plastic and superplastic flow of calcite rocks. Journal of Structural Geology, 16(10): 1431-1446.

Rybacki, E., Paterson, M.S., Wirth, R. and Dresen, G., 2003. Rheology of calcite-quartz aggregates deformed to large strain in torsion. Journal of Geophysical Research-Solid Earth, 108(B2): -.

Sander, B., 1950. Einführung in die gefügekunde der geologischen körper, zweiter teil: Die korngefüge. Springer Verlag, 409 pp.

Schmid, S.M., Paterson, M.S. and Boland, J.N., 1980. High temperature flow and dynamic recrystallization in Carrara marble. Tectonophysics, 65(3-4): 245-280.

Spiers, C.J., 1979. Fabric development in calcite polycrystals deformed at 400-degrees-c. Bulletin De Mineralogie, 102(2-3): 282-289.

Tome, C.N., Wenk, H.R., Canova, G.R. and Kocks, U.F., 1991. Simulations of texture development in calcite - comparison of polycrystal plasticity theories. Journal of Geophysical Research-Solid Earth and Planets, 96(B7): 11865-11875.

Turner, F.J., Griggs, D. and Heard, H.C., 1954. Experimental deformation of calcite crystals. Geological Society of America Bulletin, 65: 883-934.

Wagner, F., Wenk, H.R., Kern, H., Vanhoutte, P. and Esling, C., 1982. Development of preferred orientation in plane-strain deformed limestone - experiment and theory. Contributions to Mineralogy and Petrology, 80(2): 132-139.

Wenk, H.R., 2002. Texture and anisotropy, Plastic deformation of minerals and rocks. Reviews in mineralogy & geochemistry, pp. 291-329.

Wenk, H.R. and Christie, J.M., 1991. Comments on the interpretation of deformation textures in rocks. Journal of Structural Geology, 13(10): 1091-1110.

Wenk, H.R. and Shore, J., 1974. Preferred orientation in experimentally deformed dolomite. Transactions-American Geophysical Union, 55(4): 419-419.

Wenk, H.R., Takeshita, T., Bechler, E., Erskine, B.G. and Matthies, S., 1987. Pure shear and simple shear calcite textures - comparison of experimental, theoretical and natural data. Journal of Structural Geology, 9(5-6): 731-745.

Wenk, H.R., Takeshita, T., Vanhoutte, P. and Wagner, F., 1986. Plastic anisotropy and texture development in calcite polycrystals. Journal of Geophysical Research-Solid Earth and Planets, 91(B3): 3861-3869.

Wenk, H.R., Venkitas.Cs and Baker, D.W., 1973. Preferred orientation in experimentally deformed limestone. Contributions to Mineralogy and Petrology, 38(2): 81-114.

Wenk, H.R., Wagner, F., Esling, C. and Bunge, H.J., 1981. Texture representation of deformed dolomite rocks. Tectonophysics, 78(1-4): 119-138.

Wheeler, J., Prior, D.J., Jiang, Z., Spiess, R. and Trimby, P.W., 2001. The petrological significance of misorientations between grains. Contributions to Mineralogy and Petrology, 141(1): 109-124.

Zhang, N. and Tong, W., 2004. An experimental study on grain deformation and interactions in an al-0.5%Mg multicrystal. International Journal of Plasticity, 20(3): 523-542.
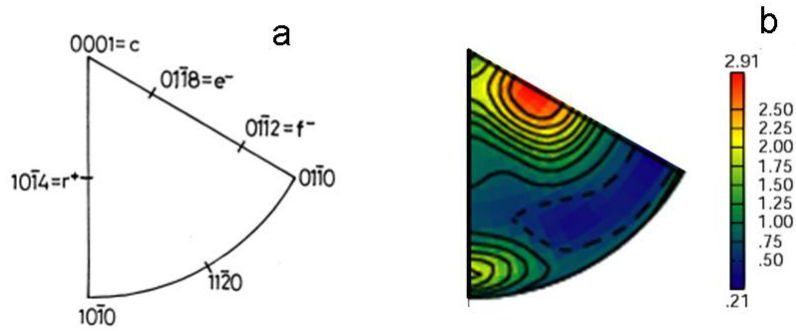
4.7 Figures and tables

Figure 1. (a) Schematic diagram of main crystallographic orientations (plane normal, in Miller-Bravis notation) and symbols in calcite. (b) Inverse pole figure from compression test of sample CM05 (20% strain at 10^{-4} s^{-1}, 700°C, and 300 MPa). Colors correspond to the intensity values.
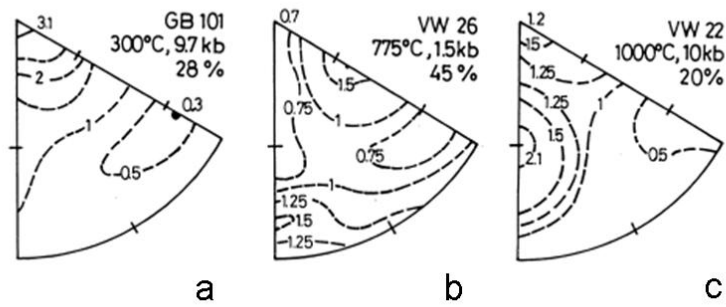
Figure 2. Experimental deformation of calcite limestone from previous compression tests (Wenk et al., 1973). Inverse pole figures (in equal area projection) for (a) low temperature (300° C), (b) intermediate (775° C), and (c) high temperature (1000° C). Numbers shown together with the contour lines are the intensity values.
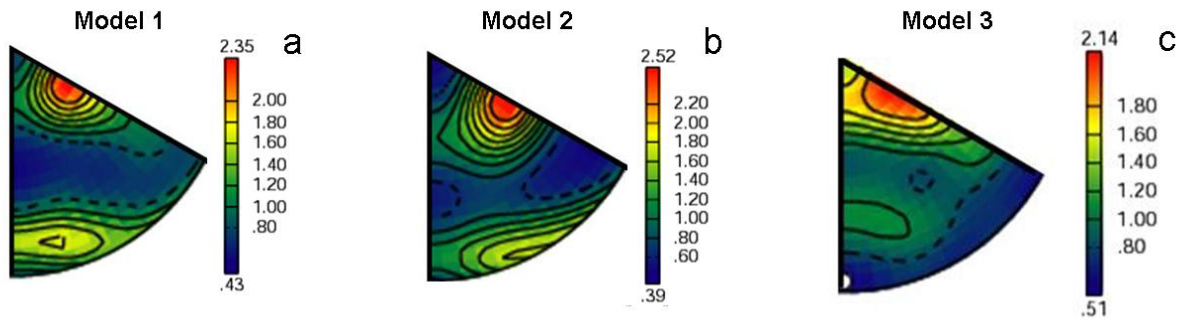
Figure 3. Inverse pole figures from VPSC simulations using 3 different models. See
Table 1 for the CRSS values in these models. The temperature conditions correspond to
experimental studies at intermediate temperature (Figs. 1b and 2b).
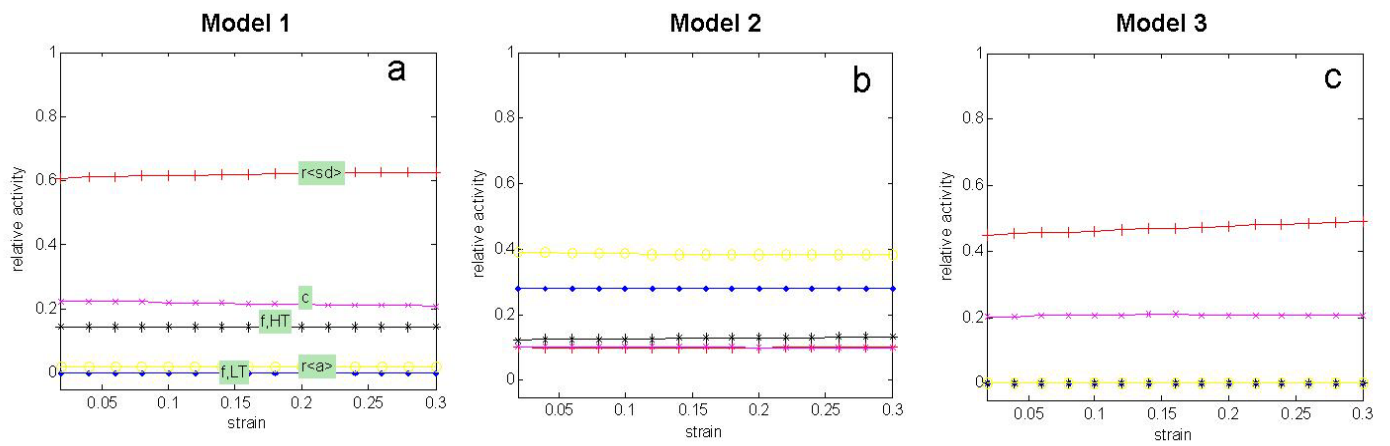
Figure 4. Relative activities of different slip systems from VPSC simulations using 3 different models (Table 1, see corresponding inverse pole figures in Fig. 3). Different colors represent different slip systems. r<sd> and c are the two most active slip systems during the compression deformation in models (a) and (c), while r<a> is the most active slip system in model (b).
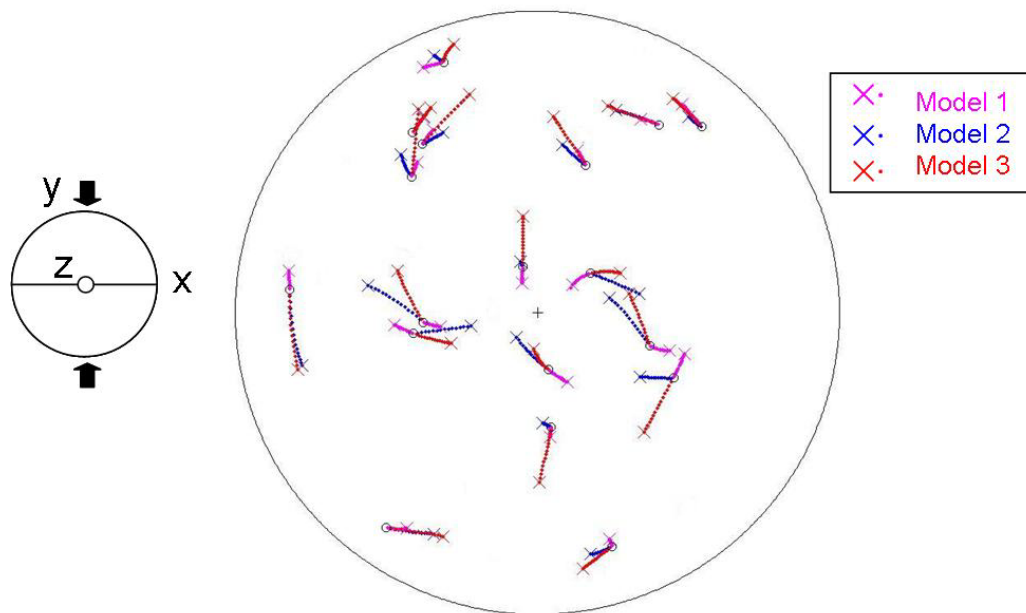
Figure 5. Change of grain orientations (shown here the c direction) during compression test of calcite after 30% strain from VPSC simulations (Table 1, see corresponding inverse pole figures in Fig. 3). Different colors represent different models; the starting and final positions of 18 grains are shown as small circles and large cross symbols, respectively. Compression direction is vertical, which is shown in the small diagram on the left. Notice that grains rotate differently in both directions and magnitudes.
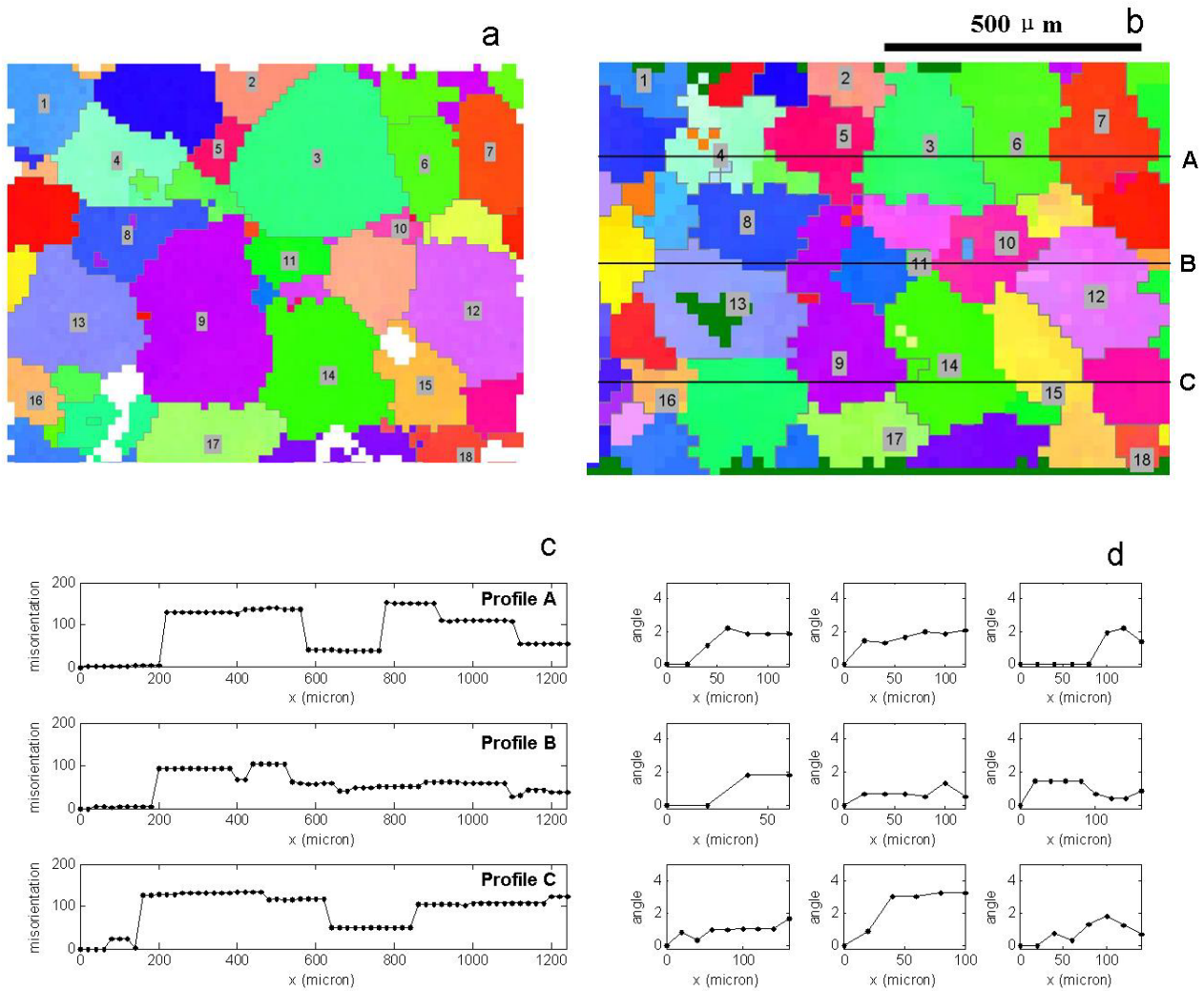
Figure 6. Grain orientation maps from EBSD study of sample CM12 (6% strain at 10^{-5} s^{-1}, 700ºC and 300 MPa) before (a) and after (b) deformation. Scale bar shown in (b) is the same at both images. Grains are numbered and 3 profiles (A-C) are drawn in (b) to study the change of crystallographic orientation in the microstructure. (c) misorientation profiles in Fig. 8b. (d) misoriention profiles across individual grains. All the misorientation angles are calculated relative to the first point.

177
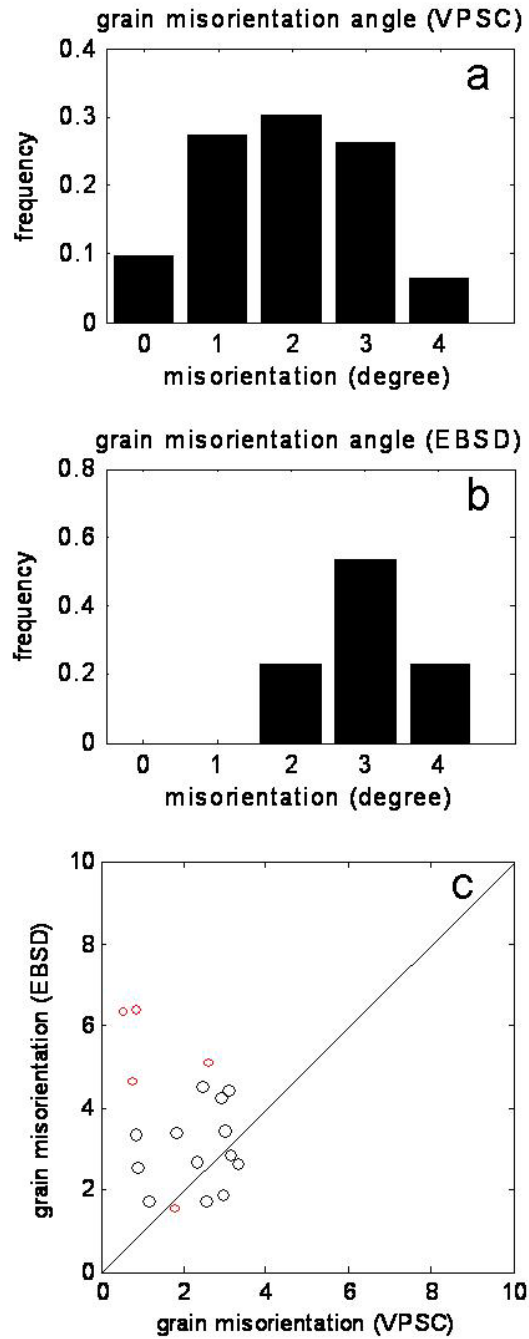
Figure 7. (a-b) Distributions of the misorientation angles from VPSC simulation (a) and EBSD data (b). (c) Correlations of misorientation angles (calculated using the same

grain before and after deformation) from VPSC simulation (Model 3, Table 1) and EBSD

data (sample CM12). Straight line is plotted as a reference of 1:1 correlation. Small red

circles and large black circles represent data from small and large grains, respectively.

Notice the improvement of data comparison after tilt correction, and the generally better

correlation of large grains.
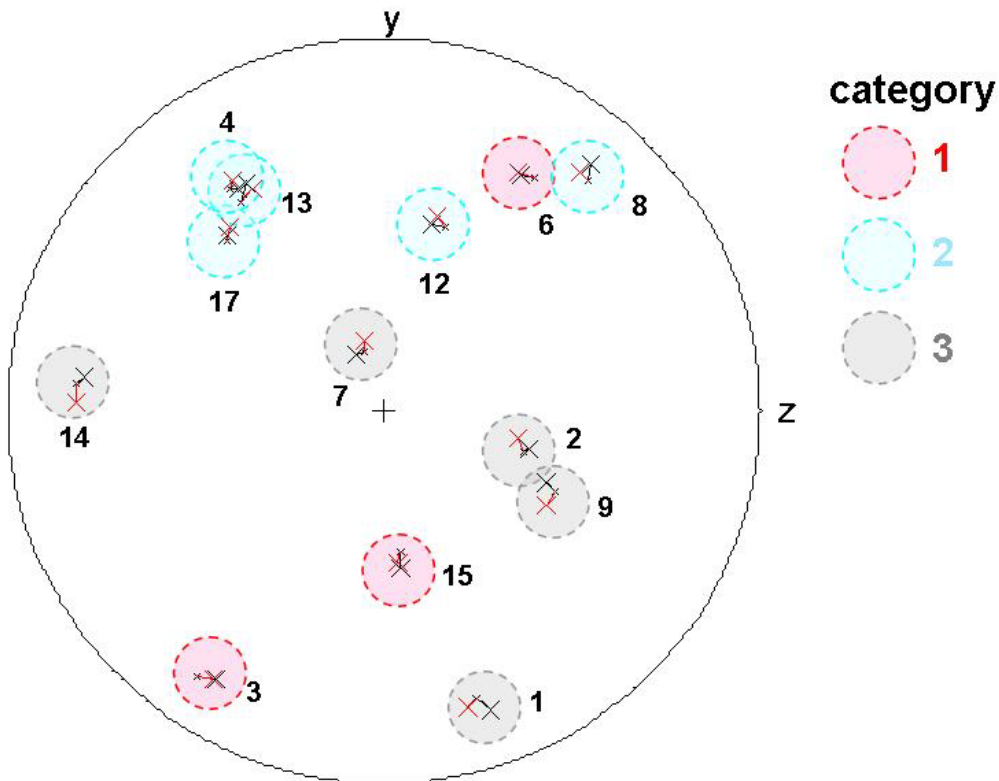
Figure 8. Comparison of grain reorientation results from VPSC simulations (Red crosses) and EBSD data (black crosses, sample CM12). The cross symbols represent the grain orientation after 6% strain in compression. The initial grain orientations in the undeformed (Small cross symbols) sample are the same as in Fig. 5, except that 13 grains are used instead of 18 grains. We choose large grains as shown in Fig. 7 (large black circles).   We consider the comparison to be good (Category 1) when both the axis and magnitude of rotation of the observed and simulated rotations agree, to be OK (Category 2) if either magnitude or orientation are predicted and poor (Category 3) if neither agree. The comparison shows that only a small number of grains can be successfully predicted in detail by the VPSC simulation.

180
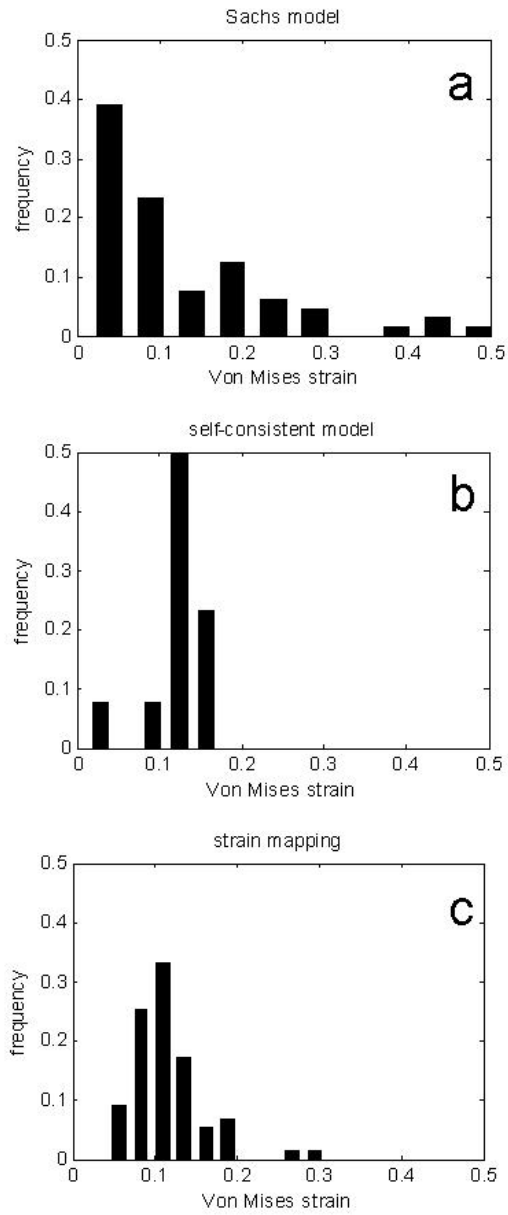
Figure 9. Von Mises strain distribution using (a) Sachs model assuming homogeneous stress distribution; (b) self-consistent model using homogeneous effective medium theory; and (c) strain mapping technique on sample CM11 (12% strain at 10^{-5} s^{-1}, 600°C and 300 MPa).
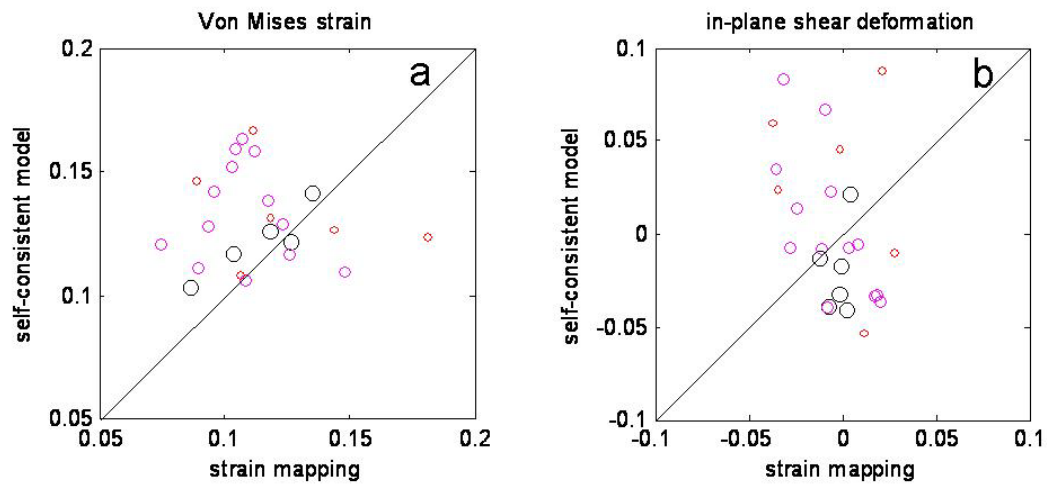
Figure 10. Correlations between the calculated strains (sample CM11) from self-consistent model and strain mapping analysis, shown here both the Von Mises strain (a) and in-plane shear strain (b). Small red circles, medium magenta circles, and large black circles represent grains sizes of <100 μm, ~100-200 μm, and >200 μm, respectively.

Table 1. Critical resolved shear stresses for different slip systems in 3 VPSC models (relative to CRSS for r <sd> or r <a>).

	r<sd> (10-14)[-2021]		f,LT (01-12)[-2021]		f,HT (01-12)[0-111]		c<a> (0001)[-1-120]		r<a> (10-14)[-12-10]		e-twin (-1018)[40-41]	
	CR+	CR-	CR+	CR-	CR+	CR-	CR+	CR-	CR+	CR-	CR+	CR-
Model 1	1.3	1.0	9.0	9.0	1.5	1.5	1.6	1.6	4.5	4.5		
Model 2	1.5	1.5	1.5	1.5	1.5	1.5	1.5	1.5	1.0	1.0		
Model 3	1.0	1.0	9.0	3.8	4.2	4.2	1.6	1.6	3.0	3.0	0.8	9.0

Model 1: Barber et al., 2007; Model 2: Pieri et al., 2001; Model 3: de Bresser & Spiers, 1997

Table 2. Summary of the crystallographic orientation changes of individual grains for sample CM12 (grain numbers same as Fig. 6)

Grain #	Initial orientation (E1,E2,E3)			Final orientation (E1,E2,E3)'			Rot. Ang. (°) no tilt corr.	Rot. Ang. (°) with tilt corr.
1	12.4	72.7	93.3	7.3	70.3	98.0	6.2	3.4
2	75.5	49.7	84.6	74.3	45.7	84.3	4.3	1.7
3	9.7	124.8	46.1	10.9	120.8	47.3	4.1	4.4
4	158.3	122.7	83.1	154.5	119.6	78.3	5.3	2.5
6	160.0	58.7	6.7	159.6	60.3	4.9	2.6	2.9
7	107.4	95.5	91.0	105.2	95.3	90.9	2.2	2.6
8	165.2	49.5	84.6	170.0	50.2	79.0	4.5	3.3
9	60.0	43.9	68.9	60.6	42.5	67.8	1.6	2.7
12	143.0	75.3	56.0	142.4	77.0	53.4	3.3	3.5
13	154.1	121.6	25.7	154.9	117.9	23.3	4.7	4.3
14	115.3	167.7	53.3	110.1	163.3	49.8	4.9	1.9
15	48.4	85.4	40.4	42.3	83.9	44.0	6.9	4.5
17	145.4	127.2	114.7	144.3	125.3	112.9	2.4	1.7

Table 3. Rotation angles of individual grains due to deformation process, predicted from VPSC simulation (see Table 1 for CRSS values in 3 models).

Grain #	Model I Rotation angle	Category*	Model 2 Rotation angle	Category*	Model 3 Rotation angle	Category*
1	1.2	3	0.4	3	1.8	3
2	4.0	3	1.9	3	1.1	3
3	2.8	1	1.3	3	3.1	1
4	0.9	3	1.3	3	0.9	2
6	2.7	1	1.4	3	3.1	1
7	0.6	3	1.4	3	3.3	3
8	0.7	3	1.9	3	0.8	2
9	2.0	3	1.7	3	2.3	3
12	1.5	2	1.2	3	3.0	2
13	1.0	3	1.0	3	2.9	2
14	4.4	3	0.7	3	3.0	3
15	0.6	3	0.5	3	2.4	1
17	1.1	2	0.7	3	2.5	2

Category *: 1. good; 2. ok; 3. bad

Appendix: Crustal velocity structure of southeastern Tibetan Plateau using receiver function method

Lili Xu

Stéphane Rondenay

Robert D. van der Hilst

Abstract

Southeastern Tibet marks the site of presumed clockwise rotation of the crust due to the India-Eurasian collision and abutment against the stable Sichuan basin and South China block. Knowing the structure of the crust is a key to better understanding crustal deformation and seismicity in this region. Here, we analyze recordings of teleseismic earthquakes from 25 temporary broadband seismic stations and one permanent station using the receiver function method. We find that crustal thickness decreases gradually from the Tibetan plateau proper to the Sichuan basin and Yangtze platform but that significant (intra-)crustal heterogeneity exists on shorter lateral scales (<1000 km). Most receiver functions reveal a time shift of ~0.2s in the direct P arrival and negative phases between 0 and 5 s after the first arrival. Inversion of the receiver functions yields S-velocity profiles marked by near-surface and intra-crustal low-velocity zones (IC-LVZs). The shallow low-velocity zones are consistent with the wide distribution of thick surface sedimentary layers. The IC-LVZ varies laterally in depth and strength; it becomes thinner toward the east and southeast and is absent in the Sichuan basin and the southern part of the Yangtze platform. Results from slant-stacking analysis show a concomitant decrease in crust thickness from ~60 km in the Songpan-Ganze fold system to ~46 km in the Sichuan basin and ~40 km in the Yangtze platform. High Poisson's ratios (> 0.30) are detected beneath the southeastern margin of Tibet but in the Sichuan basin and southestern Yangtze platform the values are close to the global average. Combined with high regional heat flow and independent evidence for mid-crustal layers of high (electric) conductivity, the large intra-crustal S-wave velocity reduction (12–19%) and the intermediate-to-high average crustal Poisson's ratios are consistent with partial melt in the crust beneath parts of southeastern Tibet. These results could be used in support of deformation models involving intra-crustal flow, with the caveat that

significant lateral variation in location and strength of this flow may occur.

A.1. Introduction

Geological structures suggest that deformation in the central part of the Tibetan plateau, directly north of the Indian subcontinent, has largely been the result of north-south convergence (Molnar and Tapponnier, 1975; Rowley, 1996). However, east of the Himalayan syntaxis, the east-west trending structural features of central Tibet bend southeastward as a consequence of the extrusion of crustal elements from central Tibet, their abutment against the Sichuan basin and South China block, and the stress field caused by subduction under the Burma ranges (King et al., 1997; Chen et al., 2000; Wang et al., 2001; Lev et al., 2006). The left-lateral Xianshuihe-Xiaojiang fault system forms the eastern boundary of the clockwise rotation (Avouac and Tapponnier, 1993; Wang and Burchfiel, 2000).

Following Chen et al. (1987) and Wang et al. (2003) we recognize four major geological units southeast of the Tibetan plateau proper: the Yangtze Platform, the Songpan-Ganze fold system, the Sanjiang fold system, and the Bomi-Tengchong fold system (Figure 1). The Songpan-Ganze and Sanjiang fold belts are separated from the Yangtze Platform by the Longmen Shan fault and the Red River fault, respectively. The Sichuan basin is located to the east of the Longmen Shan fault and is part of the Yangtze platform. Surface sediments of up to 10 km thickness are widespread throughout the study region (Leloup et al., 1995; Song and Lou, 1995; Burchfiel and Wang, 2003). The Tengchong area belongs to the Bomi-Tengchong fold system, with volcanic activity in the Cenozoic.

189

The crustal structure in Tibet has been debated. For example, previous shear-wave splitting studies (e.g., McNamara et al., 1994; Sandvol et al., 1997) indicated that the mantle anisotropy is aligned with surface structures. These results were interpreted by Silver (1996) and Sandvol et al. (1997) to represent, at least in central Tibet, a high degree of mechanical coupling between the upper crust and the upper mantle, or, at least, that the lower crust is strong enough to transfer shear stresses between the crust and mantle over horizontal length scales of tens of kilometers. In contrast, geologic and GPS studies (Burchfiel et al., 1995; Chen et al., 2000; Wang et al., 2001) showed little to no convergence across a large part of eastern Tibet, implying that eastern Tibet has been uplifted without appreciable shortening of the upper crust, and that crustal thickening involved primarily shortening within the deep crust. Royden and co-workers explained this observation as well as the evolution in shape of river streams with a channel flow model in which the deep crust is weak and in which there is little correlation between the crustal and upper mantle deformation (Royden et al., 1997; Clark and Royden, 2000; Roy and Royden, 2000a and b; Clark et al., 2005).

Regional shear-wave splitting measurements are consistent with some level of decoupling of crust and upper mantle beneath parts of the study region (Lev et al., 2006). The interpretation of teleseismic shear-wave splitting measurements is often ambiguous, however. Indeed, opposite conclusions have been reached from joint modeling of shear-wave splitting and GPS results, using a thin viscous sheet approach (Silver, 1996; Holt, 2000; Flesch et al., 2005).

190

Receiver function studies in central Tibet (Kind et al., 1996; Nelson et al., 1996; Yuan et al., 1997; Ozacar and Zandt, 2004) presented evidence for a crustal low-velocity zone. This could be, and has been, used in support of the crust-mantle decoupling and middle/lower crustal flow, but to date the observations have been too sparse to determine whether this crustal low-velocity zone extends into the southeastern part of the Tibetan plateau. Moreover, as we will show here, it is likely that neither end-member model is correct and that significant lateral variation exists in the nature of crust-mantle coupling and – if present at all – in the depths where intra-crustal flow might occur.

To date, most estimates of crustal thickness for southeastern Tibet are derived from deep seismic sounding profiles and from the coherence between gravity anomalies and topography (e.g., Lin et al., 1993; Li and Mooney, 1998; Wang et al., 2003). Previous receiver function studies in the Yunnan province (Hu et al., 2003; He et al., 2004) suggest that a crustal low-velocity zone exists in the upper and/or lower crust of the western Yangtze platform. Furthermore, the high average crustal Poisson's ratio of > 0.30 (Hu et al., 2003) for this area suggests the existence of partial melt in the crust (Owens and Zandt, 1997). Body-wave tomography (Huang et al., 2002; Wang et al., 2003) revealed low velocity anomalies in the crust and upper mantle of various areas (e.g., the western Sichuan plateau and the Panxi tectonic zone). Such intra-crustal low-velocity zones (IC-LVZs) are also apparent in results of high-resolution surface wave array tomography (Yao et al., 2006, 2007). In combination, these previous studies suggest that the crust beneath southeastern Tibet is highly heterogeneous.

191

In order to improve the characterization of this heterogeneity we analyze data from a regional network of 25 temporary broadband seismometers (Figure 1). We use receiver function analysis, which has been used previously to characterize the crust (including IC-LVZs) in a variety of tectonic environments (e.g., Langston, 1979; Gurrola et al., 1995; Owens and Zandt, 1997; Yuan et al., 1997; Bostock, 1998; Zorin et al., 2002). We first use a simultaneous deconvolution approach to obtain the average crustal impulse response (Gurrola et al., 1995; Bostock, 1998). Then we use a slant-stacking method to constrain simultaneously the crustal thickness (H) and P-to-S wave velocity ratio (V_P/V_S) (Zhu and Kanamori, 2000; Chevrot and van der Hilst, 2000). Finally, we derive S-wave velocity profiles through least-squares inversion of the receiver function waveforms and simplify the derived models into fewer layered models (Owens et al., 1984; Ammon et al., 1990; Kind et al., 1995). Such inversions have been used in previous studies to image low velocity layers within the crust (e.g., Kind et al., 1996; Frederiksen et al., 2003; Hetland et al., 2004) and can be used to estimate both the depth to and thicknesses of the IC-LVZs.

A.2. Methodology

A.2.1 Receiver functions

The receiver function technique derives a source-equalized teleseismic waveform, in which source, far field path, and instrument effects are removed by deconvolving the vertical component from the radial/transverse components (Langston, 1979; Gurrola et al.,

1995; Bostock, 1998). The resulting receiver function waveform is an estimate of the ground's impulse response. For stations MC01-MC25, the gains were the same on all channels, whereas for station KMI they differed by < 3% between channels. No equalization before rotation was performed for the latter due to the small difference in gain, which we believe does not strongly affect our results. In this study, the following processing steps are applied to derive the receiver functions: rotation, deconvolution, moveout correction, stacking, and filtering. First, all teleseismic traces are rotated from an E-N-Z coordinate system to an R-T-Z system (Figure 2). Second, we deconvolve the vertical components from both the radial and transverse components to remove the effects of the source and the instrument. During this process, which is conducted in the frequency domain, we apply a water level to stabilize the spectral division (e.g., Langston, 1979; Bostock, 1998). The water level is adjusted to the quality of the original seismogram and the stability of the equalization; it varies from 10^{-3} to 10^{-1}. Third, a Gaussian filter with width of 2.0 Hz is applied in the frequency domain after decovolution to remove high frequency noise in the seismogram. To improve the overall signal-to-noise ratio and ensure stability of the deconvolution process, we simultaneously deconvolve all seismograms along moveout curves, which depend on the horizontal slowness and the depth of phase conversion (Bostock, 1998); this provides an average ground impulse response of the sampling area.

The lateral offset between the surface recording point and conversion point at depth is a function of the ray parameter, the crustal thickness, and the average crustal velocity.

For example, for a ray parameter of 0.0586 s/km (*P*-wave from a source at 67° distance), crust thickness of 40 km, and crust velocities V_P = 6.2 km/s and V_S = 3.6 km/s, the $P_m s$ phases sample the Moho ~9 km from the stations, while multiples sample it ~40 km away.

A.2.2 Slant-stacking method

Crust thickness *H* and average V_P/V_S of the crust can be estimated from the relative timing of *P*-to-*S* conversions and reverberations (see Figure 2). Here, we follow the approach of Zhu and Kanamori (2000) and use the travel times of three phases relative to the direct *P* (see Figure 2 for definitions): $P_h s$, $PpP_h s$, and $PpS_h s$ (or $PsP_h s$). The differential travel-time equations depend on *H*, V_P/V_S, the average crustal *P*-wave velocity ($\overline{V}_P$), and the ray parameter (*p*). We determine the ray parameter from the event depth and epicentral distance and use average crustal *P*-wave velocities of 6.2 and 6.4 km/s (Lin et al., 1993; Li and Mooney, 1998; Wang et al., 2003). At each station, we sum the amplitudes of the receiver functions at the predicted differential travel times of the *Ps*, *PpPs*, and *PpSs* (or *PsPs*) phases for a given *H* and V_P/V_S:

$$s(H, V_P/V_S) = \sum_N \left[a(t_{P-Ps}) + a(t_{P-PpPs}) + a(t_{P-PpSs}) \right], \tag{1}$$

where *N* is the number of receiver functions at each station and *a(t)* is the amplitude of a receiver function at time *t*. We perform a grid search in the V_P/V_S - *H* parameter space, and take the optimum solution to be at the maximum of the amplitude stack surface. We use the 90% contour lines as an indication of uncertainty (Hetland et al., 2004). In an

194

isotropic medium, the Poisson's ratio (v) is given by:

$$v = \frac{1}{2}\left(1 - \frac{1}{(V_P/V_S)^2 - 1}\right). \tag{2}$$

The Poisson's ratio is an important parameter for determining crustal composition because it is sensitive to mineralogy (e.g., Christensen, 1996) and the presence of fractures, fluid content, and partial melt (e.g., O'Connell and Budiansky, 1974; Mavko, 1980). .

A.2.3 Least-squares inversion and velocity modeling

A least-squares inversion of receiver function waveforms is performed to estimate the crustal velocity structure (Ammon et al., 1990). This technique is more sensitive to velocity contrasts than to the absolute magnitude of the velocities, but it requires a starting velocity model that is close to the actual velocities (Owens et al., 1984; Ammon et al., 1990). Here, we accommodate this requirement by using the seismic refraction results of Zhu et al. (personal communication, 2003) as our starting velocity models. We invert for velocity structures consisting of horizontal layers with fixed thicknesses of 2 km, not because we expect to resolve such detail, but because the receiver functions are dominated by shear-converted phases with a typical wave length of ~8 km and layers as thin as 2 km may influence the inverse modeling. Furthermore, we fix the Poisson's ratios and Moho depths at the values derived from the slant-stacking method. We invert only for the S-wave velocity; the P-wave velocity is derived from these results in

conjunction with the V_P/V_S ratio. Approximate densities (ρ) throughout the model are derived using the equation $\rho = 0.32\ V_P + 0.77$ (Berteussen, 1977).

The inversion seeks to minimize the difference between the observed and model-generated receiver function waveforms. A distribution of possible solutions is built by running the inversion for a range of starting models based on perturbations to the prescribed initial model (see Ammon et al., 1990), and the preferred solution is computed by averaging the solutions that fit the data within data uncertainty using a chi-squared test with 95% confidence (Lodge and Helffrich, 2006). At each station, we apply varying levels of smoothing until we can model the dominant phases and avoid over-complexity in the resultant model.

Since the inversion tends to overfit the data and produce solutions that may contain too much structure, we proceed by simplifying the preferred crustal model to obtain a model that is more realistic and, therefore, easier to interpret (see, e.g., Lodge and Helffrich, 2006). Simplified models are constructed by investigating the effects of isolated portions of the least-squares solution on the receiver function waveform. Velocity gradient are replaced by single, sharp discontinuities, and adjacent model layers exhibiting similar velocities are grouped to form a coarser model. Once the minimum structure has been identified, the solution to this "simplified model" is found by performing a grid-search over its parameters and computing the average of all the models that fit the data within 95% confidence (Lodge and Helffrich, 2006).

A.3. Data

We use data from a network of 25 temporary broadband seismometers operated by MIT and the Chengdu Institute of Geology and Mineral Resources (CIGMR) for one year between September 2003 and October 2004. The station distribution is shown in Figure 1. We analyze waveforms from seismic events that are selected based on the following criteria: (1) body-wave magnitude $m_b > 5.6$ to insure high signal-to-noise ratio, (2) epicentral distances (Δ) between 30° and 100° to avoid wavefield complexities due to upper mantle discontinuities or diffraction at the core-mantle boundary. In order to get relatively simple source functions, earthquakes with vertical waveforms containing two or more obvious pulses are avoided. In addition, data with poor signal-to-noise ratios are discarded. This includes, for example, data with no obvious first-*P* arrivals and/or large-amplitude surface waves in the observing time window.

With a deployment period of one year only, our array recorded data from a relatively narrow range of backazimuths. A total of 147 events, mostly from the circum-Pacific seismogenic belt (Figure 3), were used to produce 1329 individual receiver function waveforms. However, due to equipment failure, periods of high noise levels, and variable durations of station operation, only a subset of the total number of events were recorded at a particular station. In addition, we used data recorded between 1990–2002 at KMI (Kunming), a station of the China Digital Seismograph Network (CDSN). The number of events selected for analysis at each station is given in Table 1.

A.4. Results

A.4.1 Receiver functions from 25 temporary stations

At most stations, *P*-to-*S* conversions from the Moho are clearly identified on both individual and stacked receiver functions. Other prominent phases are observed after the direct *P* arrival, indicating the presence of significant intra-crustal structure. We illustrate our analysis with data from stations MC22 and MC05 (Figure 4).

Station MC22 (24.5°N; 100.2°E) was located in the Sanjiang tectonic unit, to the south of the Red River fault. The 29 receiver functions obtained for this station are plotted in Figure 4a, for backazimuths between 8° and 253°. Visual inspection reveals a clear $P_m s$ arrival at ~5 s on all 29 radial receiver functions. Subsequent arrivals include a strong positive one at ~16 s and a weak negative one at ~22 s (Figure 4a). Based on their polarity and relative arrival time, these arrivals could be the free-surface multiples of the Moho, i.e., $PpP_m s$ and $PpS_m s$ (or $PsP_m s$) phases, respectively (see Figure 2). In some receiver functions, positive arrivals observed between 9–11 s may correspond to *P*-to-*S* conversions from upper mantle discontinuities or multiples from intra-crustal discontinuities. Since there are no obvious phases corresponding to *P*-to-*S* conversions from an intra-crustal discontinuity, we interpret the arrivals at 9–11 s as *P*-to-*S* conversions from structure in the upper mantle (~80 km). The positive arrival at ~7 s in the transverse receiver function (thin blue line in Figure 4b) is likely due to *P*-to-*S* conversion from an anisotropic and/or tilted layer, either in the mantle (direct arrival) or in the crust (multiple). There are no prominent phases observed before $P_m s$

(i.e., 5 s) in the transverse receiver function, which indicates that there are no significant effects of anisotropy or tilted layers at shallow depth (Zhang et al., 1995; Savage, 1998), which – in turn – implies that our assumption of a 1-D crustal velocity structure is adequate.

Station MC05 was located at (30.0°N; 100.2°E), which is in the Songpan-Ganze fold zone. Figure 4c and d show the processed receiver functions at this station. The initial P-wave pulse is time shifted by ~0.2 s. Such shifts, which have also been observed elsewhere (see, e.g., van der Meijde et al., 2003), can be attributed to the presence of a low velocity layer near the surface (i.e., sediments) directly below the station. The arrivals at ~5 and ~7–8 s may correspond to P-to-S conversions from intra-crustal and Moho discontinuities, respectively. Stacking events over all backazimuths can produce slightly broader peaks for P_ms and its multiple phases because of the dependence of the arrival time on backazimuth. Therefore, we stack 42 events from back azimuth range of 104.5°–156.7° (Figure 4d). For the same reason we bin events for stations MC06, MC11, and KMI (see Table 1). The small-amplitude phases that arrive before the P_ms phases represent P-to-S conversions within the crust. There is a clear positive phase at ~23 s, corresponding to the arrival of PpP_ms, and a negative phase at ~30 s, which corresponds to PpS_ms (or PsP_ms) (Figure 4c). No prominent phase appears on the transverse receiver function of station MC05 (Figure 4d).

In contrast to stations MC22 and MC05, some stations have no strong crustal P_ms conversions (Figure 5). The observation of time delays of the first pulse in receiver

functions at most stations indicate that a near-surface low-velocity layer is widely distributed in our study area.   The first pulses are complicated due to interference with *P*-to-*S* conversions from the bottom of the surface layers, which arrive within ~2 s after the first pulse, e.g., MC02 and MC11 (Figure 5).   At station MC03, which is located just east of the Longmen Shan fault, the radial receiver function waveform has several low amplitude, positive phases within ~10 s after the first-*P* arrival.   The 10.2-s phase is most probably the P_ms phase because it does not depend on backazimuth and because it is consistent with a Moho depth of ~60 km inferred from refraction studies (Zhu et al., 2003, personal communication), which corresponds to a P_ms phase at > 7.0 s assuming an average crustal velocity V_P < 6.8 km/s and a Poisson's ratio ≥ 0.25.   At station KMI, which is located near N-S trending strike-slip faults (Figure 1), large-amplitude positive phases are observed at ~5 s after the main pulse, which could be P_ms.   The large variation in the radial receiver functions with backazimuth indicates a laterally heterogeneous structure beneath station KMI.

A.4.2 Slant-stacking

We classify stations into three categories depending on the reliability of the derived crustal properties.   The first category corresponds to stations for which the P_ms and PpP_ms phases are clearly visible in the radial receiver functions, and for which a clear maximum in the V_P/V_S vs. *H* diagram can be observed even if phase identification is difficult.   The second category corresponds to stations with multiple maxima in the

V_P/V_S vs. H diagram. When identification in the stacks of the maxima corresponding to Moho is ambiguous we use independent estimates of crustal thickness (Wang et al., 2003; Zhu et al, personal communication, 2003) and restrict the average crustal Poisson's ratio to reasonable values (~0.25–0.30). The third category corresponds to stations for which the records are too complex or too noisy to determine V_P/V_S and H with sufficient confidence. In this study, we only use stations in the first two categories for further S-wave velocity analysis (Table 1).

Figure 6a-b shows the slant-stacking results from station MC22. The following phases are visible: the P_ms phase at ~5 s after the first-P arrival, the PpP_ms phase at ~16 s, and (more tentatively) the PpS_ms (or PsP_ms) phases at ~22 s. Travel time curves of these phases (thick lines in Figure 6a) are derived using the combination of H and V_P/V_S that gives the maximum amplitude of the stack. There is only one global maximum in the V_P/V_S vs. H diagram, which corresponds to the optimum solution. Therefore, this station is classified in the first category. We obtain a crustal thickness of 37.5 ± 1.5 km and an average crustal Poisson's ratio of 0.25 ± 0.04 beneath this station (Figure 6b). The inferred crustal thickness of 37.5 km is slightly less than the values of 43 and 41.3 km from previous studies (Wang et al., 2003; Zhu et al., personal communication, 2003; see Table 1). The receiver function study using data from the Yunnan regional seismic network (Hu et al., 2003) yielded a crustal thickness of 36.0 ± 1.0 km at nearby station YX (24.3^o N, 100.1^o E). Hu et al. (2003) also derived a Poisson's ratio of 0.31 ± 0.01, which is larger than but not incompatible with our estimate of 0.25 ± 0.04.

Station MC05 has local maxima in addition to a global maximum in the V_P/V_S -H diagram (Figure 6c-d).   One of the local maxima yields $H = 42.5$ km and Poisson's ratio of 0.33, whereas the global maximum corresponds to a crustal thickness of 59.0 ± 1.0 km and average crustal Poisson's ratio of 0.26 ± 0.01.   Because seismic refraction data suggest a thickness of ~62.5 km (Zhu, personal communication, 2003) we select the latter values for crustal thickness (i.e., 59.0 ± 1.0 km) and Poisson's ratio (i.e., ~0.26) at station MC05.

The receiver function waveforms from stations MC12, MC18, and MC19 are too noisy to identify the P_ms phase among several pulses with similar amplitude (Figure 5). They are in the third category and thus not included in further analysis.

The slant-stacking analysis reveals that the depth to the Moho changes gradually across our array, from ~37 km in Yunnan province to ~64 km below eastern Tibet.   The average crustal Poisson's ratio varies between 0.21 and 0.32 and is the lowest in the southern Yangtze platform.   The Poisson's ratio is highest, with values consistently above 0.30, below the eastern margin of the Tibetan plateau just west of the Sichuan basin (below the latter the Poisson's ratios are generally less than 0.29).   The Songpan-Ganze fold zone, the region of high average elevation (~4 km), has a thick crust. Station MC01, situated between the Xianshuihe and Longmen Shan faults, has the thickest crust (i.e., 64 km ± 1.0 km) and a small Poisson's ratio (i.e., 0.21 ± 0.1).   On the Yangtze platform, MC02 and MC10 sample the western Sichuan basin (Figure 1).   Here the crust thickness is between ~46 and 41 km, and the Poisson's ratios between ~0.26 and

0.29.   The crust-mantle boundary of the Yangtze platform deepens northwestward from ~40 km to 56 km.   The Poisson's ratio generally decreases eastward from ~0.30 to 0.22. The Sanjiang fold zone, west of the Red River fault, has a crustal thickness of ~38–46 km and Poisson's ratio of ~0.23–0.25.

A.4.3 *S*-wave velocity profiles

S-wave velocity profiles derived from least-squares inversion and grid search through simplified models are show in Figure 7 (for 8 stations).   Low-velocity zones are identified as velocity minima on smoothed crustal velocity models beneath many stations in the southeastern part of the Tibetan plateau.   The thickness of near-surface low velocity layers (S-LVL) varies from ~0 to 10 km.   An intra-crustal low-velocity layer (IC-LVZ) is mostly observed in the Songpan-Ganze fold zone and the western Yangtze platform.   On average, the *S*-wave velocity in the IC-LVZ is ~0.5–0.8 km/s lower than that of its overlying layer. Both S-LVL and IC-LVZ are robust features: S-LVLs are well constrained by a ~0.2 s time shift of the incident *P*-wave pulse; IC-LVZs are only assigned to stations where a low-velocity layer is required both in the least-squares solution and in the simplified model to fit the measured receiver function waveform.

A.4.3.1 Songpan-Ganze fold zone (SG)

At MC01, the receiver functions synthesized from the derived *S*-wave velocity

profiles match the observed data within the observational uncertainty (Figure 7). The 68-km thick crust has a 20-km thick upper crust with *S*-wave velocity of ~3.7 km/s and a 30-km lower crust with *S*-wave velocity of 3.9 km/s. There is a low-velocity zone at ~20-40 km which is necessary to explain the negative arrival at ~2.6 s in the receiver function waveform. Our results are consistent with previous *S*-wave tomography, which yielded a small negative velocity anomaly at ~50 km beneath this station (Wang et al., 2003). MC04 and MC08 have similar velocity structures: there are no obvious low velocity layers near the surface and the *S*-wave velocities in the upper and middle crust are more or less constant. The 57-km thick crust at MC04 consists a ~32-km upper crust with *S*-wave velocity of 3.2 km/s and 25-km lower crust with *S*-wave velocity of 3.5 km/s.

Stations MC05-07 have very similar *S*-wave velocity profiles. These stations are marked by an IC-LVZ with S-wave velocity of ~3.3 km/s. The IC-LVZ extends between ~15 and 38 km depth at station MC05 (Figure 7), which is necessary to explain the negative phases at ~2 s and 6 s in the receiver function waveform. In the same region, MT studies show a high conductive layer below ~10 km (Sun et al., 2003), and *S*-wave tomography shows a low-velocity anomaly between ~10–30 km depth (Wang et al., 2003). The positive velocity gradient at ~30 km corresponds to the 5-s arrival in the receiver function waveform, which can be related to the Conrad discontinuity (i.e., ~25 km depth) inferred from deep seismic sounding (Wang et al., 2003). We note that the strong Moho multiples that appear near ~23 s and ~31 s in the synthetic waveforms

calculated from the preferred velocity model are not as clearly visible in the stacked receiver functions (Figure 7). This discrepancy is due, in large part; to the fact that receiver functions are stacked using moveout curves that account for variations in relative travel time of direct conversions, but that do not stack multiples coherently.

A.4.3.2 Yangtze platform (YZ)

Two stations sample the crust of the western Sichuan basin. Beneath station MC02, the S-LVL is ~5 km thick, which is consistent with the layers of Mesozoic sediments in the Sichuan basin (Kirby et al., 2000). The crust there has a thickness of 48 km and exhibits a fairly uniform *S*-wave velocity (average ~3.7 km/s) below the S-LVL. In contrast, station MC10 has an IC-LVZ at ~10-20 km with *S*-wave velocity of ~3.1 km/s.

In the western Yangtze platform, stations MC17, MC20, and MC23 have similar *S*-wave velocity profiles, without obvious IC-LVZs. Stations MC13 and MC15 have IC-LVZs with *S*-wave velocities ~3.1 km/s. A similar IC-LVZ had been inferred from other receiver function studies (Hu et al., 2003; He et al., 2004), except for a station at $(26.9^o N, 100.2^o E)$, which is close to MC15, where an IC-LVZ has not been previously observed (Hu et al., 2003). Stations MC03, MC09, MC11, MC16, MC25, and MC24 sample the Yangtze platform from north to south. Their *S*-wave velocity profiles are significantly different. Station MC03, located near the Longmen Shan fault, reveals an IC-LVZ at ~20–44 km and two velocity discontinues at ~44 km and 64 km (corresponding to the arrivals at ~5.2 and 10.1 s in the receiver function waveform).

205

These can be interpreted as intracrustal and Moho discontinuities, respectively. Station

MC09 has an IC-LVZ at ~15–30 km, with an *S*-wave velocity of ~3.2 km/s. Stations on

the southern Yangtze platform do not show evidence for IC-LVZs. Our results generally

agree with previous receiver function studies in southern Tibet (Hu et al., 2003; He et al.,

2004).

A.4.3.3 Sanjiang fold system (SJ)

Stations MC21 and MC22 sample the Sanjiang fold system, west of the Red River

fault. MC21 is located to the east of the Tengchong volcanic area. The crust deepens

northward by ~9 km from station MC22 to station MC21. There is no obvious IC-LVZ

and intracrustal discontinuities at both stations. Similar receiver function results were

observed by Hu et al. (2003) in the Sanjiang fold system.

A.5. Discussion

A.5.1 Crustal thickness

The crustal thickness varies between 37 and 64 km in SE Tibet and its surrounding

area (Figure 8). The thickness of the crust is large beneath the Songpan-Ganze fold

zone (~60 km) and decreases eastward to the western Sichuan basin (~46 km) and

southeastward to the Yangtze platform (~40 km). The crust beneath the Sanjiang fold

zone has a thickness of ~38-46 km.

In general, the Moho depths derived in our study are consistent with previous results

(e.g., Li and Mooney, 1998; Hu et al., 2003; Wang et al., 2003; He et al., 2004).

Specifically, Figure 9 (also Table 1) shows that for realistic values of the average crustal *P*-wave velocity (6.2–6.4 km/s) our results agree well with estimates from seismic refraction profiles (Zhu et al., personal communication, 2003) or Bouguer gravity anomaly and deep seismic sounding profiles data (Wang et al., 2003). The correlation coefficients between our Moho depth values and their estimates are 0.88 and 0.86, respectively. The only significant outliers are stations MC01 and MC03, for which we obtained thicker crust (Table 1). When we include these outliers, the root mean square of the differences between our results and those from the independent studies are about 4 km. Some of this difference can be due to the fact that the receiver function analysis and the seismic refraction study sample the crust at different locations and that the spatial resolution of two methods is different (Chevrot and van der Hilst, 2000).

Figure 10 shows *S*-velocity profiles along an east-west cross section (line 1 in Figure 1) beneath the northern part of our study region, adjacent to the Sichuan basin; the topographic slope across the east margin of the Tibetan plateau (Figure 10, top) is steep and the elevation decreases by ~3500 m over a lateral distance of 150 km. The steep topographic gradient in the western Sichuan basin was interpreted by Clark et al. (2005) to be a result of crustal material flowing around the strong lithosphere of the Sichuan block in the channel flow model. From station MC05 – on the plateau proper – to station MC02 – in Sichuan basin – the base of the crust shallows by 9.5 ± 2.0 km and the elevation decreases by ~3500 m. An Airy isostastic model predicts a change in crustal thickness of ~24 km (Braitenberg et al., 2000), which suggests that crustal material may

still be piling up at the east margin of the Tibetan plateau.   Along Line 2 (Figure 11), which transects the southeastern margin of the Tibetan plateau, the average topographic slope is smaller than across the eastern margin (line 1).   The crust shallows southeastward by 19.7 ± 6.0 km with a change in elevation of ~2300 m, in agreement with an Airy isostatic model.   Our result of Moho compensation using the Airy isostastic model (Braitenberg et al., 2000) is consistent with previous gravity anomaly studies, which indicated that the topography of the southeastern part of the Tibetan plateau is locally compensated except for the eastern margin across the Longmen Shan fault on to the western Sichuan basin (Jiang and Jin, 2005; Jordan and Watts, 2005).

A.5.2 Poisson's ratio and (average) crustal composition

Poisson's ratios can help constrain crustal mineralogy and chemical composition. Mineral physics and field constraints indicate that (1) the Poisson's ratio increases more-or-less linearly with decreasing SiO_2 content for continental crust, and (2) high ratios (> 0.30) suggest the existence of partial melt (Christensen, 1996; Owens and Zandt, 1997), especially if the perturbation in Poisson's ratio is localized to an intra crustal layer. We interpret the large range of observed Poisson's ratio (0.22–0.32) in the southeastern part of the Tibetan plateau to be a result of heterogeneity in crustal composition and, locally, the existence of partial melt.

Most of our study region has an intermediate-to-high Poisson's ratio (> 0.25) except for a few stations in the southern Yangtze platform.   The ratio is highest (> 0.30) in the

eastern margin of the Tibetan plateau, just west of the Sichuan basin (Figure 8). In the

Yangtze platform, Poisson's ratios generally decrease eastward, from ~0.30 to 0.22. The

normal-to-high values in the western Yangtze platform (~0.26-0.30) are consistent with a

mafic/ultramafic lower crust as inferred from recent geophysical surveys (Xu et al., 2001),

and may indicate the presence of partial melt in the crust, whereas low-to-intermediate

values suggest a felsic-to-intermediate composition in the southern Yangtze platform. The

ratios in the Sanjiang fold system (~0.23–0.25) are consistent with results from seismic

refraction studies and suggest an "average" crustal composition (Kan et al., 1986; Li and

Mooney, 1998).

Hu et al. (2003) estimated Poisson's ratios – using equations (1) and (2) – from

differential travel times of P_ms and PpP_ms phases at 23 temporary stations in Yunnan

province. They showed that the western Yangtze platform has Poisson's ratios of

0.30–0.35, which are higher than our values of 0.26–0.30. This discrepancy may, in part,

be due to differences in data and methodology. Our results are consistent with Zurek et

al. (personal communication, 2007), who used a slant-stacking method similar to the one

deployed here.

A.5.3 Low-velocity zones

Our results suggest the presence of complex 3-D heterogeneity in the crust beneath

SE Tibet. The most prominent features in the *S*-wave velocity profiles presented here

are the near-surface and intra-crustal low-velocity zones (Figure 7, 10, and 11). The

quasi-ubiquitous S-LVL can be related to the surface sedimentary basins (Leloup et al., 1995; Song and Lou, 1995; Burchfiel and Wang, 2003). The IC-LVZ is widely observed in the study region, but with significant lateral variation in its depth and strength. In some places the IC-LVZ corresponds to the middle crust, but in other places it marks the lower crust. In general, it becomes thinner toward the Sichuan basin and is absent in the southern part of the Yangtze platform (Figure 8). Compared to the shallow crust, the reduction of the *S*-wavespeed in IC-LVZ is in the range of ~12–19%.

The existence of IC-LVZs as inferred here is generally consistent with results from seismic sounding, seismic tomography, and previous receiver function analyses (e.g., Li and Mooney, 1998; Huang et al., 2002; Wang et al., 2003; Hu et al., 2003; He et al., 2004; Yao et al., 2007). Along line 1 (Figure 10), the IC-LVZ also coincides with one or more intra-crust layers of high (electric) conductivity inferred from MT data (Sun et al., 2003).

A.5.4 Partial melt?

Earthquake focal depths and heat flow studies both indicate a relatively high geothermal gradient in the southeastern part of the Tibetan plateau (Sun et al., 2004; Wu et al., 1988; Hu et al., 2000). In crystalline continental crust, seismic velocities generally increase with increasing depth. However, wavespeed reductions can occur in regions with steep geothermal gradients (e.g., Kern and Richter, 1981; Kono et al., 2006) and, in particular, in regions of partial melt (Meissner, 1986). In view of (i) the magnitude of the reduction in shear wavespeed in the IC-LVZs, (ii) the high average

Poisson's ratios of the crust and their possible translation into vertically localized perturbations, (iii) the correlation with a zone of high conductivity inferred from the inversion of MT data, and (iv) the association with high heat flow, we suggest that crustal partial melt exists beneath parts of the eastern margin of the Tibetan plateau, possibly with continuation into the northwesternmost part of the Yangtze platform.

In general, the *S*-wave velocity decreases and Poisson's ratio increases drastically when the temperature approaches and exceeds the solidus. Mueller and Massonne (2001) suggested that for typical mid-crustal pressures, granite starts to melt at ~650°C. If we suppose a similar composition, the inferred Poisson's ratio > 0.30 and *S*-wave velocities of ~3.0–3.2 km/s in the IC-LVZs (~10–30 km in depth) indicate a temperature of ~700–800°C and an amount of melt less than 4%. This interpretation is consistent with inferences from receiver function studies in northern Tibet (Zhu et al., 1995) and with Roger et al. (1995), who suggested that the young Konga Shan granite (~10 Ma) at the southern segment of the Xianshuihe fault (Figure 1) may have originated from partial melting of continental crust. However, our results suggest that partial melt is restricted to certain geographical regions (that is, the data do not require it for large parts of our study region) and that it involves the middle or the lower crust, and perhaps, in some locations, both (see also, Yao et al., 2007).

Previous geological and experimental studies (Leloup et al., 1995; Rabinowicz and Vigneresse, 2004) suggested that crustal partial melt may be partly due to shear heating in southeastern Tibet. Another contribution may come from the upper-mantle

decompression melting which also contributed to the young volcanism (Wang et al., 2001). Intra-crustal zones of partial melt in northern Tibet have been attributed to the extrusion of mantle-derived magma (e.g., Zhu et al., 1995; Nelson et al., 1996; Kind et al., 2002). Furthermore, a shallow IC-LVZ (~10–20 km) around the Tengchong volcano was interpreted by Wang and Gang (2004) to be the result of upper-mantle magma activity and heat conduction through the near vertical fault.

Since the viscosity of crustal rocks decreases with increasing fraction of partial melt (Bagdassarov and Dorfman, 1998), it is tempting to associate the IC-LVZ with a mechanically weak zone. This would be consistent with a model in which crustal shortening is accommodated by channel flow in the mid-to-lower crust (Royden et al., 1997; Clark and Royden, 2000; Roy and Royden, 2000a and b; Clark et al., 2005). Insofar as the association of IC-LVZs with layers of weaker rheology is correct, the results from receiver function analysis (this study) and from surface wave array tomography (Yao et al., 2007) suggest that there is substantial lateral variation in existence, strength, and position (e.g., depth range) of such zones. In turn, this suggests a complex 3-D geometry of intra-crustal channel flow.

A.6. Summary

By analyzing receiver functions from 25 temporary seismograph stations, we estimated the crustal velocity structure in the southeastern margin of the Tibetan plateau. The crust varies in thickness from ~60 km in the Songpan-Ganze fold system to ~40 km

in the southern Yangtze platform.   The gradient of the Moho discontinuity is the greatest in the eastern margin of Tibet toward the western Sichuan basin.   The crustal thickness generally follows the Airy isostatic model except toward the western Sichuan basin, which indicates that crustal material may still be piling up at the eastern margin of the Tibetan plateau.   Poisson's ratio varies greatly in our study region.   The western Yangtze platform exhibits intermediate-to-high Poisson's ratios (> 0.30), which can be related to the existence of high-velocity lower crust with a mafic/ultramafic composition and, locally, to the presence of partial melt.   In general, the overall crustal chemical composition varies between felsic and intermediate.

Arguably the most conspicuous features in the velocity profiles derived here are the pronounced low-velocity zones in the crust.   The geometry may not be well resolved, but these IC-LVZs are required by the data (the starting models used for the inversions do not have clear low-velocity structures in the crust (Figure 7)).   An IC-LVZ is widely observed in the study region, but with significant lateral variation in its depth and strength. It becomes thinner toward the Sichuan basin and is absent in the southern part of the Yangtze platform (Figure 8).   The S-wavespeed reduction in IC-LVZ is ~12–19% relative to the shallow crust.   As seismic velocities generally increase with increasing depth in crystalline continental crust, we infer the possible existence of crustal partial melt in IC-LVZ.   Our interpretation is supported by observations of crustal high-conductivity layers and high heat flow values in our study area (e.g., Wang and Huang, 1988; Hu et al., 2000; Sun et al., 2003) and by inferences from high-resolution

surface wave tomography (Yao et al., 2007).   Collectively, these observations indicate that the low-viscosity zone in the crust of the central Tibetan plateau probably extends into southeastern Tibet.   The substantial lateral variations in the existence, character, strength, and position of IC-LVZ may point to intra-crustal channel flow but with a complex 3D geometry.

A.7 References:

Ammon, C., Randall, G., and Zandt, G., 1990. On the non-uniqueness of receiver function inversions. J. Geophys. Res., 95: 15303-15318.

Avouac, J.P., and Tapponnier, P., 1993. Kinetic model of active deformation in central-Asia. Geophys. Res. Lett., 20: 895-898.

Bagdassarov, N., and Dorfman, A., 1998. Granite rheology: magma flow and melt migration. J. Geol. Soc., 155: 863-872.

Berteussen, K.A., Moho depth determinations based on spectral ratio analysis of NORSAR long-period P waves, Phys. Earth Planet. Inter., 31: 313-326, 1977.

Bostock, M.G., 1998. Mantle stratigraphy and evolution of the Slave Province. J Geophys. Res., 103: 21183-21200.

Braitenberg, C., Zadro, M., Fang, J., Wang, Y., and Hsu, H.T., 2000. The gravity and isostatic Moho undulations in Qinghai-Tibet plateau, J. Geodyn., 30 (5): 489-505.

Burchfiel, B.C., and Wang, E.C., 2003. Northwest-trending, middle Cenozoic, left-lateral faults in southern Yunnan, China, and their tectonic significance. J. Strut. Geol., 25 (5): 781-792.

Burchfiel, B.C., Chen, Z., Liu, Y., and Royden, L.H., 1995. Tectonics of the Longmenshan and adjacent regions, central China. Inter. Geol. Rev., 37 (8):661-735.

Chen, B.W., Wang, K.W., and Liu, W.X., 1987. Geotectonics in Nujiang-Lancangjiang-Jinshajiang Region (in Chinese). Geol. Publ., Beijing, 204 pp.

Chen, Z., Burchfiel, B.C., Liu, Y., King, R.W., Royden, L.H., Tang, W., Wang, E., Zhao, J., and Zhang, X., 2000. Global Positioning System measurements from eastern Tibet and their implications for India/Eurasia intercontinental deformation. J. Geophys. Res., 105(B7): 16215-16227.

Chevrot, S., and van der Hilst, R.D., 2000. The Poisson ratio of the Australian crust: geological and geophysical implications. Earth Planet. Sci. Lett., 183 (1-2): 121-132.

Christensen, N.I., 1996. Poisson's ratio and crustal seismology. J. Geophys. Res., 101

(B2): 3139-3156.

Clark, M.K., and Royden, L.H., 2000. Topographic ooze: building the eastern margin of Tibet by lower crustal flow. Geology, 28 (8): 703-706.

Clark, M.K., Bush, J.W.M., and Royden, L.H., 2005. Dynamic topography produced by lower crustal flow against rheological strength heterogeneities bordering the Tibetan Plateau. Geophy. J. Int., 162: 575-590.

Flesch, L.M., Holt, W.E., Silver, P.G., Stephenson, M., Wang, C.Y., and Chan, W.W., 2005. Constraining the extent of crust-mantle coupling in central Asia using GPS, geologic, and shear-wave splitting data. Earth Planet. Sci. Lett., 238 (1-2): 248-268.

Frederiksen, A.W., Folsom, H., and Zandt, G., 2003. Neighbourhood inversion of teleseismic Ps conversions for anisotropy and layer dip. 155 (1): 200-212.

Gurrola, H., Baker, G.E., and Minster, J.B., 1995. Simultaneous time-domain deconvolution with application to the computer of receiver functions. Geophys. J. Int., 120: 537-543.

He, Z.Q., Ye, T.L., and Su W., 2004. S-wave velocity structure of the middle and upper crust in the Yunnan region, Chinese (in Chinese). J. Geophys., 47 (5): 838-844.

Hetland, E.A., Wu, F.T., and Song, J.L., 2004. Crustal structure in the Changbaishan volcanic area, China, determined by modeling receiver function. Tectonophysics, 386: 157-175.

Holt, W.E., 2000. Correlated crust and mantle strain fields in Tibet. Geology, 28 (1): 67-70.

Hu, J.F., Su, Y.J., Zhu, X.G., and Chen, Y., 2003. S-wave velocity and Poisson's ratio structure of crust in Yunnan and its implication (in Chinese). Sci. China, Ser. B, 48 (2): 210-218.

Hu, S.B., He, L.J., and Wang, J.Y., 2000. Heat flow in the continental area of China: a new data set. Earth Planet. Sci. Lett., (2): 407-419.

Huang, J.L., Zhao, D.P., and Zheng, S.H., 2002. Lithospheric structure and its relationship to seismic and volcanic activity in southwest China. J. Geophys. Res., 107 (B10), 2255, doi: 10.1029/2000JB0000137.

Jiang, X.D., and Jin, Y., 2005. Mapping the deep lithospheric structure beneath the eastern margin of the Tibetan Plateau from gravity anomalies. J. Geophys. Res., 110, B07407, doi: 10.1029/2004JB003394.

Jordan, T.A., and Watts, A.B., 2005. Gravity anomalies, flexure and the elastic thickness structure of the India-Eurasia collisional system. Earth Planet. Sci. Lett., 236 (3-4): 732-750.

Kan, R.J., Hu, H.X., Zeng, R.S., Mooney, W.D., and McEvilly, T.V., 1986. Crustal structure of Yunnan province, Peoples-Republic-of-China, from seismic refraction profiles. Science, 234(4775): 433-437.

Kern, H., and Richter, A.E., 1981. Temperature derivates of compressional and shear wave velocities in crustal and mantle rocks at 6 Kbar confining pressure. J.

Geophys., 49 (1): 47-56.

Kind, R., Kosarev, G.L., and Petersen, N.V., 1995. Receiver functions at the stations of the German regional seismic network (GRSN). Geophys. J. Int., 121 (1): 191-202.

Kind, R., Ni, J.F., Zhao, W.J., Wu, J.X., Yuan, X.H., Zhao, L.S., Sandvol, E., Reese, C., Nabelek, J., and Hearn, T., 1996. Evidence from earthquake data for a partially molten crustal layer in southern Tibet. Science, 274: 1692-1694.

Kind, R., Yuan, X., Saul. J., Nelson, D., Sobolev, S.V., Mechie, J., Zhao, W., Kosarev, G., Ni, J., Achauer, U., Jiang, M., 2002. Seismic images of crust and upper mantle beneath Tibet: evidence for Eurasian plate subduction. Science, 298: 1219-1221.

King, R.W., Shen, F., Burchfiel, B.C., Royden, L.H., Wang, E., Chen, Z., Liu, Y., Zhang, X.Y., Zhao, J.X., and Li, Y., 1997. Geodetic measurement of crustal motion in southwest china. Geology, 25: 179-182.

Kirby, E., Whipple, K.X., Burchfiel, B.C., Tang, W.Q., Berger, G, Sun, Z.M., and Chen, Z.L., 2000. Neotectonics of the Min Shan, China: Implications for mechanisms driving Quaternary deformation along the eastern margin of the Tibetan Plateau. Geol. Soc. Am. Bull., 112 (3): 375-393.

Kono, Y., Ishikawa, M., Arima, M., 2006. Laboratory measurements of P- and S-wave velocities in polycrystalline plagioclase and gabbronorite up to $700°C$ and 1 GPa: Implications for the low velocity anomaly in the lower crust. Geophys. Res. Lett., 33, L15314, doi: 10.1029/2006GL026526.

Langston, C.A., 1979. Structure under Mount Rainier, Washington, inferred from teleseismic body waves. J. Geophys. Res., 84: 4749-4762.

Leloup, P.H., Lacassin, R., Tapponnier, P., Schärer, U., Zhong, D.L., Liu, X.H., Zhang, L.S., Ji, S.C., and Trinh, P.T., 1995. The Ailao Shan-Red River shear zone (Yunnan, China), Tertiary transform boundary of Indochina. Tectonophysics, 251: 3-84.

Lev, E., Long, M.D., and van der Hilst, R.D., 2006. Seismic Anisotropy in Eastern Tibet from shear-wave splitting reveals changes in lithospheric deformation. Earth Planet. Sci. Lett., 251 (3-4): 293:304.

Li, S., and Mooney, W.D., 1998. Crustal structure of China from deep seismic sounding profile. Tectonophysics, 288: 105-113.

Lin, Z., Hu, H., and Zhang, W., 1993. The preliminary interpretation of deep seismic sounding in western Yunnan (in Chinese). Acta Seismol. Sin., 15 (4): 282-295.

Lodge, A., and Helffrich, G., 2006. Depleted well root beneath the Cape Verde Islands, Geology, 34 (6): 449-452

Mavko, G.M., 1980. Velocity and attenuation in partially molten rocks. Geophys. J. Int., 85: 5173-5189.

McNamara, D.E., Owens, T.J., Silver, P.G., and Wu, F.T., 1994. Shear wave anisotropy beneath the Tibetan Plateau. J. Geophys. Res., 99 (B7): 13655-13665.

Meissner, R., 1986. The continental crust; a geophysical approach. Int. Geophys. Ser., 34: 426 pp.

Molnar, P., and Tapponnier, P., 1975. Cenozoic tectonics of Asia: Effect of a

continental collision. Science, 189: 419-426.

Mueller, H.J., and Massonne, H.J., 2001. Experimental high pressure investigation of partial melting in natural rocks and their influence on V_P and V_S. Phy. Chem. Earth (A), 26 (4-5): 325-332.

Nelson, K.D.,Zhao, W.J .,Brown, L.D .,Kuo, J .,Che, J.K .,Liu, X.W .,Klemperer, S.L ., Makovsky, Y., Meissner, R., Mechie, J., Kind, R., Wenzel, F., Ni, J., Nabelek, J., Chen, L.S., Tan, H.D., Wei, W.B., Jones, A.G., Booker, J., Unsworth, M., Kidd, W.S.F., Hauck, M., Alsdorf, D., Ross, A., Cogan, M., Wu, C.D., Sandvol, E., and Edwards, M., 1996. Partially molten middle crust beneath southern Tibet; synthesis of Project INDEPTH results. Science, 274: 1684-1688.

O'Connell, R.J. and Budiansky, B., 1974. Seismic velocities in dry and saturated cracked solids. J. Geophys. Res., 79: 5412-5426.

Owens, T.J., Zandt, G., and Taylor, S.R., 1984. Seismic evidence for an ancient rift beneath the Cumberland Plateau, Tennessee; a detailed analysis of broadband teleseismic P-waveforms. J. Geophys. Res., 89: 7783-7795.

Owens, T.J., and Zandt, G., 1997. Implications of crustal property variations for models of Tibetan Plateau evolution. Nature, 387: 37-43.

Ozacar, A.A., and Zandt, G., 2004. Crustal seismic anisotropy in central Tibet: Implications for deformational style and flow in the crust. Geophys. Res. Lett., 31, L23601, doi: 10.1029/2004GL021096.

Rabinowicz, M., and Vigneresse, J.L., 2004. Melt segregation under compaction and shear channeling: Application to granitic magma segregation in a continental crust. J. Geophys. Res., 109, B04407, doi:10.1029/2002JB002372.

Roger, F., Calassou, S., Lancelot, J., Malavieille, J., Mattauer, M., Xu, Z.Q., Hao, Z.W., and Hou, L.W., 1995. Miocene emplacement and deformation of the Konga Shan granite (Xianshui He fault zone, west Sichuan, China): Geodynamic implications. Earth Planet. Sci. Lett., 130 (1-4): 201-216.

Rowley, D.B., 1996. Age of initiation of collision between India and Asia: A review of stratigraphic data. Earth Planet. Sci. Lett., 145: 1-13.

Roy, M., and Royden, L.H., 2000. Crustal rheology and faulting at strike-slip plate boundaries 1. An analytic model. J. Geophy. Res., 105 (B3): 5583-5597.

Roy, M., and Royden, L.H., 2000. Crustal rheology and faulting at strike-slip plate boundaries 2. Effects of lower crustal flow, J. Geophy. Res., 105 (B3): 5599-5613.

Royden, L.H., Burchfiel, B.C., King, R.W., Wang, E., Chen, Z.L., Shen, F., and Liu, Y.P., 1997. Surface deformation and lower crustal flow in eastern Tibet. Science, 276 (5313): 788-790.

Sandvol, E., Ni, J., Kind, R., and Zhao, W.J., 1997. Seismic anisotropy beneath the southern Himalayas-Tibet collision zone. J. Geophys. Res., 102(B8): 17813-17823.

Savage, M.K., 1998. Lower crust anisotropy or dipping boundaries? Effect on receiver function and a case study in New Zealand. J. Geophys. Res., 103 (B7):

15069-15087.

Silver, P.G., 1996. Seismic anisotropy beneath the continents: Probing the depths of geology. Ann. Rev. Earth Planet. Sci., 24: 385-&.

Song, H.B., and Lou, Z.L., 1995. The study of the basement and deep geological structures of Sichuan Basin. Earth Sci. Frontier (3-4): 231-237.

Sun, J., Jin, G.W., Bai, D.H., and Wang, L.F., 2003. Sounding of electrical structure of the crust and upper mantle along the eastern border of Qinghai-Tibet Plateau and its tectonic significance. Sci. China, Ser. D, 46: 243+Suppl.

Sun, Y.S., Kuleli, S., Morgan, F.D., Rodi, W., and Toksoz, M.N., 2004. Location Robustness of Earthquakes in Sichuan Province, China. Seism. Res. Lett., 75 (1), 55-62.

van der Meijde, M., van der Lee, S., Giardini, D., 2003. Crustal structure beneath broad-band seismic stations in the Mediterranean region. Geophy. J. Int., 152:729-739

Wang, C.Y., Chan, W.W., and Mooney, W.D., 2003. Three-dimentional velocity structure of crust and upper mantle in southeastern China and its tectonic implications. J. Geophys. Res., 108 (B9), 2442, doi:10.1029/2002JB001973.

Wang, C.Y., and Gang, H.F., 2004. Crustal structure in Tengchong Volcano-Geothermal Area, western Yunnan, China. Tectonophysics, 380: 69-87.

Wang, E.C., and Burchfiel, B.C., 2000. Late Cenozoic to Holocene deformation in southwestern Sichuan and adjacent Yunnan, China, and its role in formfation of the southeastern part of the Tibetan Plateau. Geol. Soc. Am. Bull., 112(3): 413-423.

Wang, J.H., Yin, A., Harrison, T.M., Grove, M., Zhang, Y.Q., and Xie, G.H., 2001. A tectonic model for Cenozoic igneous activities in the eastern Indo-Asian collision zone. Earth Plant. Sci. Lett., 188: 123-133.

Wang, J.Y., and Huang, S.P., 1988. Compilation of heat flow data in the China continental area. Sci. Geol. Sin., 2:196-204.

Wu, Q.F., Zu, J.H., and Xie, Y.Z., 1988. Basic geothermal characteristics in Yunnan Province (in Chinese). Seismol. Geol., 10(4): 177-183.

Xu, Y.G., Menzies, M.A., Thirlwall, M.F., and Xie, G.H., 2001. Exotic lithosphere mantle beneath the western Yangtze craton: Petrogenetic links to Tibet using highly magnesian ultrapotassic rocks. Geology, 29 (9): 863-866.

Yao, H.J., van der Hilst, R.D., and de Hoop, M.V., 2006. Surface-wave array tomography in SE Tibet from ambient seismic noise and two-station analysis - I. Phase velocity maps. Geophy. J. Int., 166: 732-744.

Yao, H.J., Beghein, C., van der Hilst, R.D., 2007. Surface-wave array tomography in SE Tibet from ambient seismic noise and two-station analysis: II - Crustal and upper mantle structure. Gephys. J. Int., submitted.

Yuan, X.H.,Ni, J ., Kind, R.,Mechie, J ., and Sandvol, E., 1997. Lithospheric and upper mantle structure of southern Tibet from a seismological passive source experiment. J. Geophy. Res., 102 (B12): 27491-27500.

Zhang, J., and Langston, C.A., 1995. Dipping structure under Dourbes, Belgium, determined by receiver function modeling and inversion. Bull. Seis. Soc. Am., 85 (1): 254-268.

Zhu, L.P., Owens, T.J., and Randall, G.E., 1995. Lateral variation in crustal structure of the northern Tibetan plateau inferred from teleseismic receiver functions. Bull. Seis. Soc. Am., 85(6): 1531-1540.

Zhu, L.P., and Kanamori, H., 2000. Moho depth variation in southern California from teleseismic receiver functions. J. Geophys. Res., 105 (B2): 2969-2980.

Zorin, Yu.A., Mordvinova, V.V., Turutanov, E.Kh, Belichenko, B.G., Artemyev, A.A, Kosarev, G.L., and Gao, S.S, 2002. Low seismic velocity layers in the Earth's crust beneath Eastern Siberia (Russia) and Central Mongolia: receiver function data and their possible gological implication. Tectonophysics, 359: 307-327.
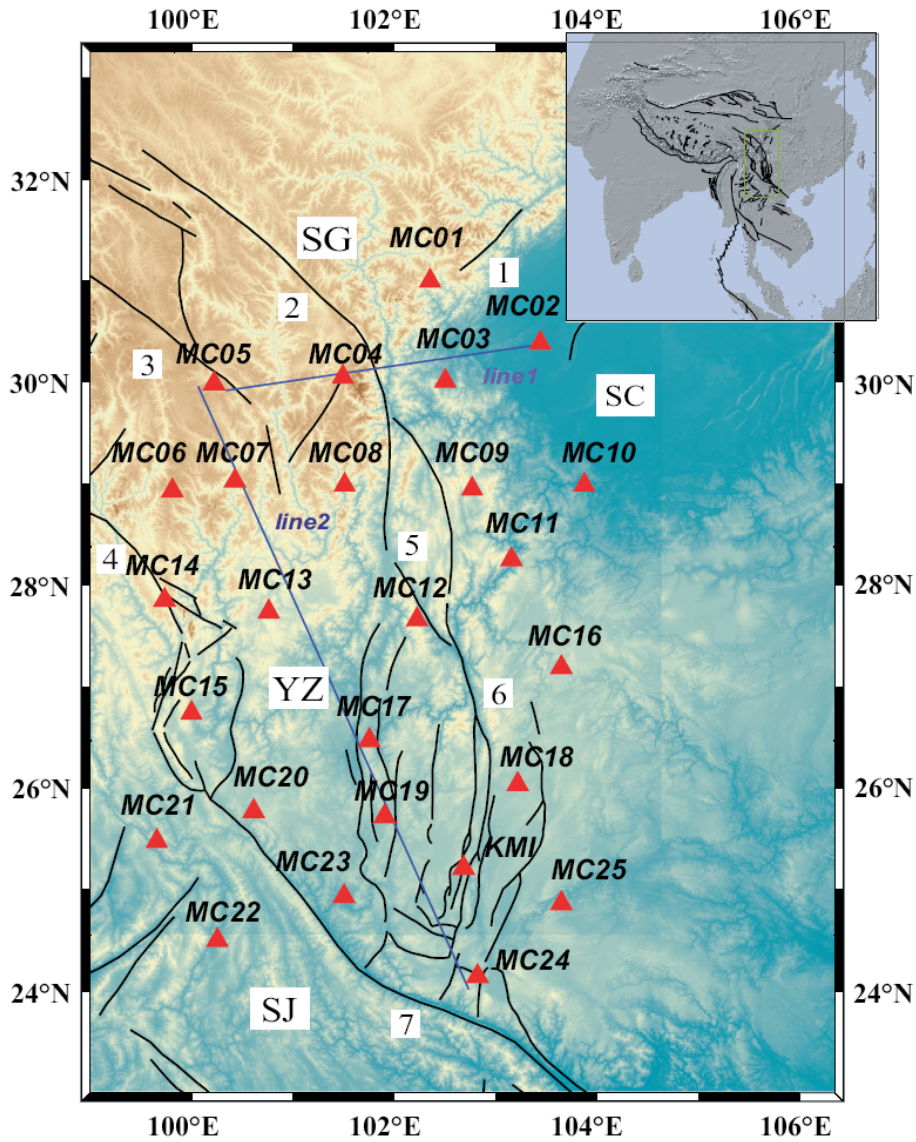
A.8 Figures and Tables

Figure 1. Location of seismic stations (red triangles) and cross-sections (blue lines) in the study region (boxed area on the inset map). Red cross represents the Konga Shan area. The background shows the topography of southeastern Tibet and the regional faults: 1. Longmen Shan fault; 2. Xianshuihe fault; 3. Lijiang fault; 4. Zhongdian fault; 5. Anninghe fault; 6. Xiaojiang fault; 7. Ailaoshan Red-River fault. The main geological

units are: SG, Songpan-Ganze fold system; YZ, Yangtze platform; SJ, Sangjiang fold zone; SC, Sichuan basin [modified from Chen et al., 1987 and Wang et al., 2003]. The Bomi-Tengchong fold system is located outside of the mapped area, starting ~ 80 km to the west of station MC21.
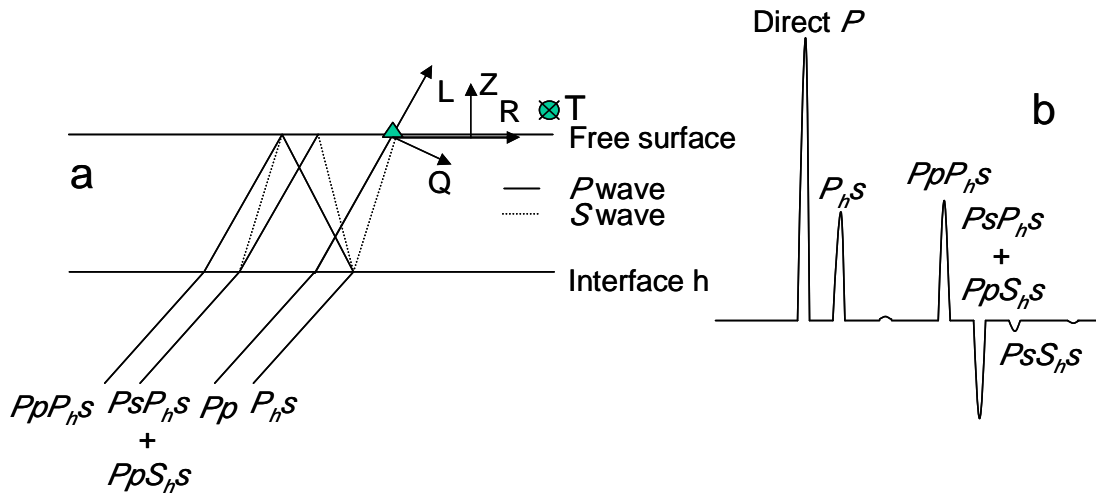
Figure 2.   A schematic representation of receiver functions: (a) simplified ray diagram showing the main *P*-to-*S* converted phases for a layer over a half-space, and (b) corresponding receiver function waveform.   Vertical, radial, and transverse components of the wavefield are denoted Z, R, and T, respectively.   Except for the first arrival, upper case letters denote downgoing travel paths, lower case letters denote upgoing travel paths, and h indicates reflection from the interface [modified from Ammon et al., 1990].
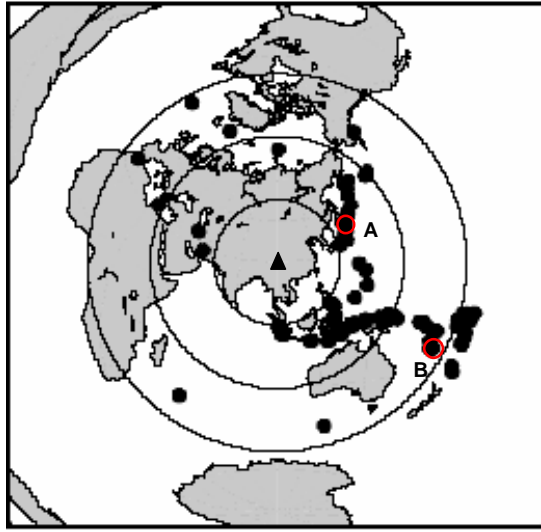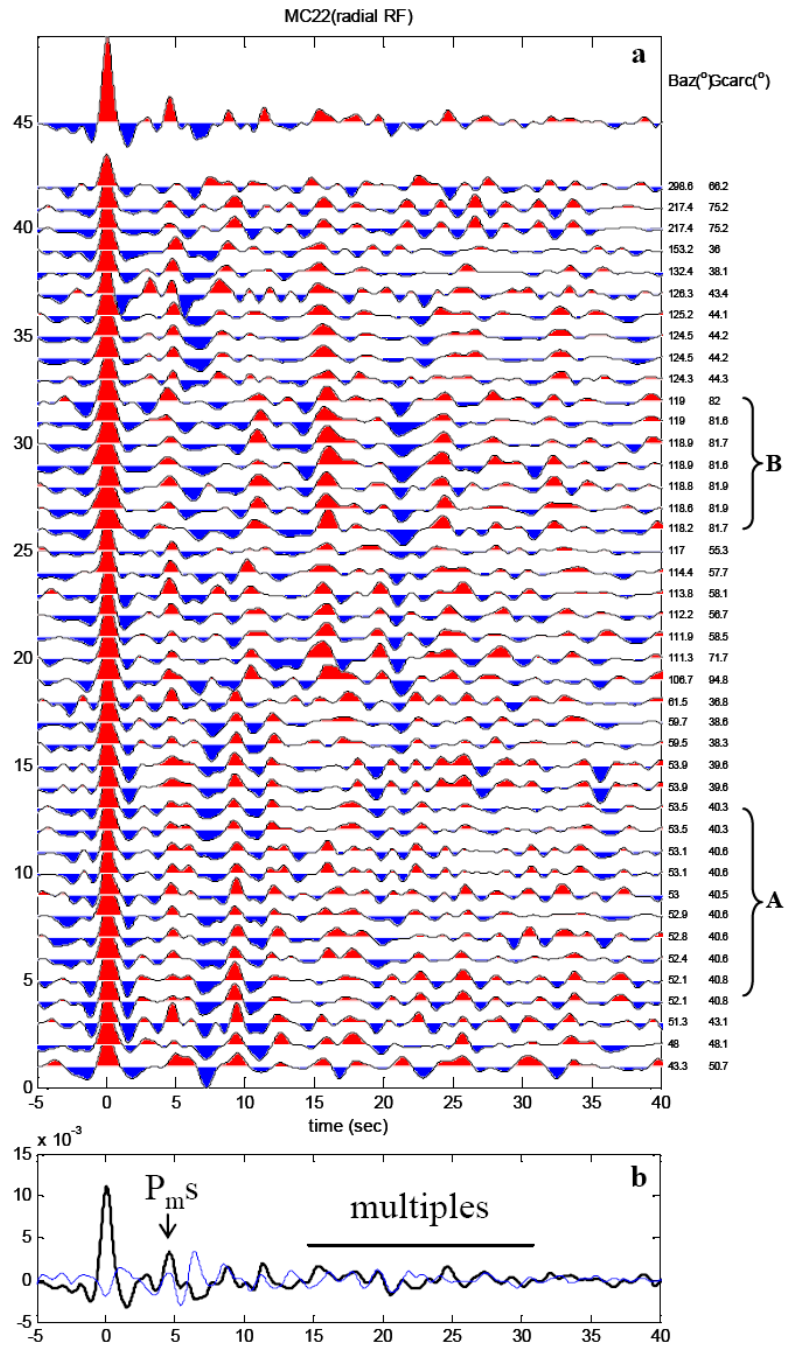
Figure 3. Azimuthal projection centered on MC08 (black triangle) showing distribution of events used in this study and recorded over the period September 2003 to October 2004. Small circles mark epicentral distance of 30º, 60º, and 90º from MC08. Two red circles (A and B) indicate regions that saw frequent seismic activity during the recording period (see also Figure 4).
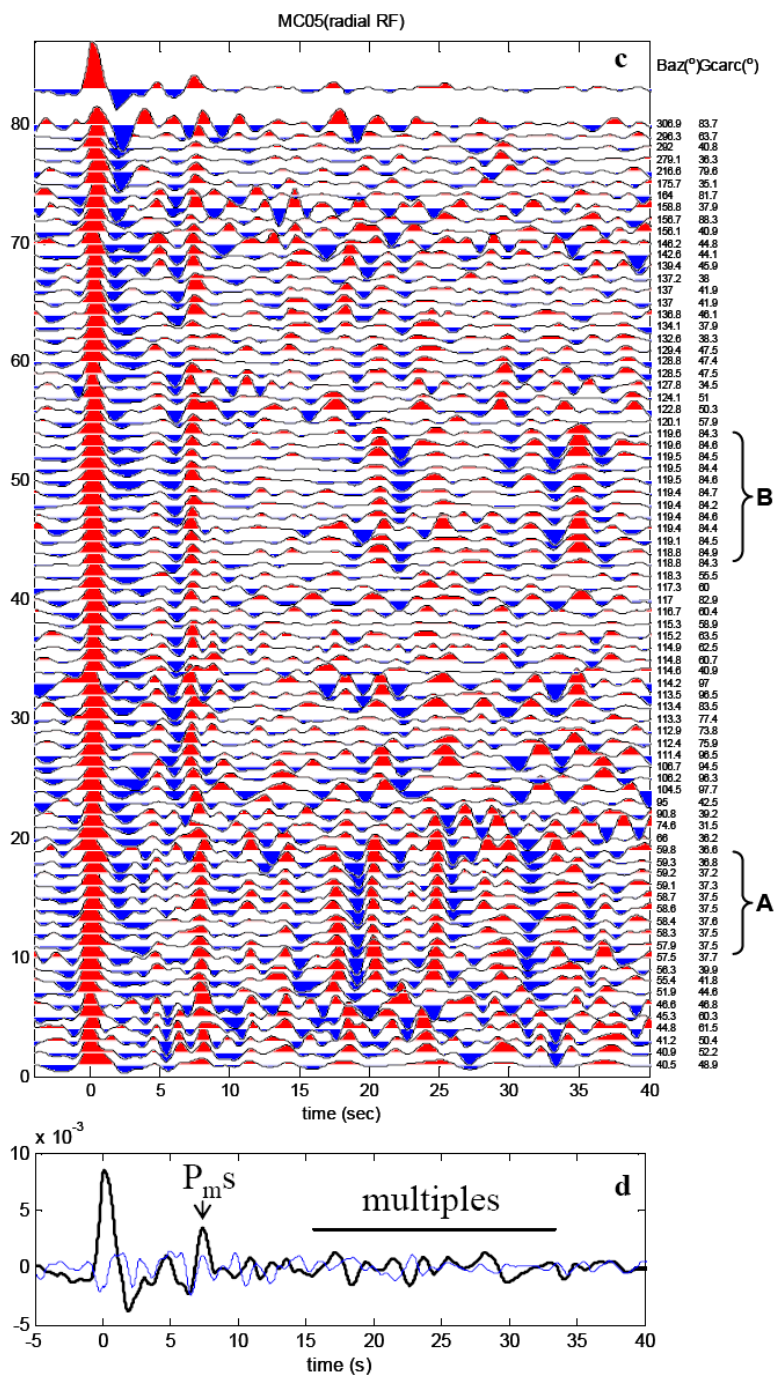
MC22(radial RF)

Baz(°) Gcarc(°)

298.6 66.2
217.4 75.2
217.4 75.2
153.2 36
132.4 38.1
126.3 43.4
125.2 44.1
124.5 44.2
124.5 44.2
124.3 44.3
119   82
119   81.6
118.9 81.7
118.9 81.6
118.8 81.9
118.6 81.9
118.2 81.7
117   55.3
114.4 57.7
113.8 58.1
112.2 58.7
111.9 58.5
111.3 71.7
106.7 94.8
61.5   36.8
59.7   38.6
59.5   38.3
53.9   39.6
53.9   39.6
53.5   40.3
53.5   40.3
53.1   40.6
53.1   40.6
53   40.5
52.9   40.6
52.8   40.6
52.4   40.6
52.1   40.8
52.1   40.8
51.3   43.1
48   48.1
43.3   50.7

time (sec)

P$_m$S

multiples

Figure 4.   Receiver functions calculated at stations MC22 (a-b) and MC05 (c-d).   (a

and c) Waveform sections showing individual, radial receiver functions in the time range

spanning 5 s before to 40 s after the direct *P* arrival.   The events are ordered by

increasing back azimuth, with back azimuths and epicentral distances for each event shown in the right column. A and B denote clusters of events from Japan and the Fiji-Tonga Islands, respectively (see Figure 3). (b and d) Radial (thick black line) and transverse (thin blue line) receiver functions obtained by simultaneous deconvolution of all high-quality traces recorded at each station (see Table 1). The traces are moveout corrected for P-to-S conversions occurring between 0-500 km depth underneath the stations, with a reference ray parameter of 0.0586 s/km corresponding to earthquakes at ~67º epicentral distance, and they are filtered using a Gaussian filter with a width of 2.0 Hz.
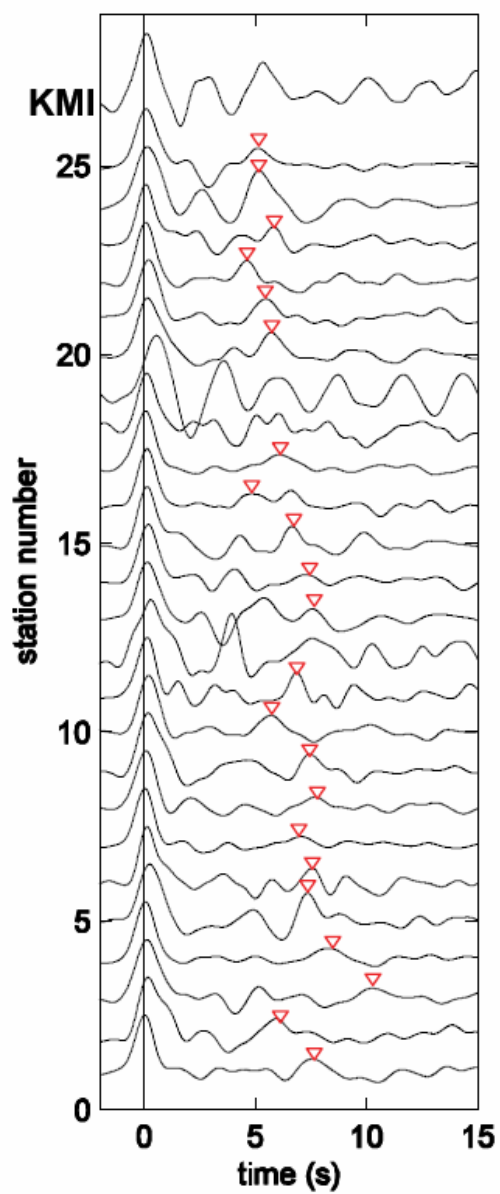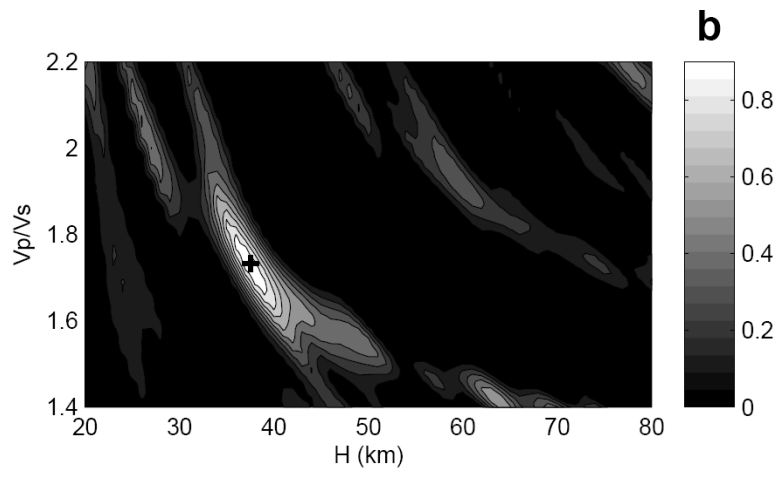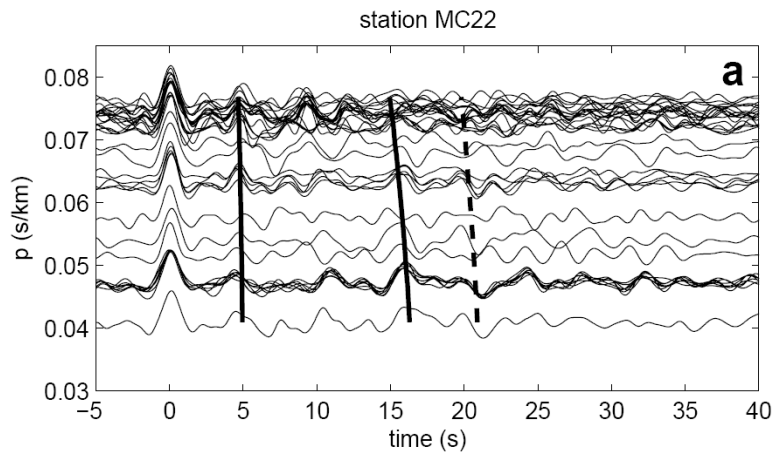
Figure 5. Radial receiver functions from 25 temporary stations and station KMI obtained by simultaneous deconvolution. *P*-to-*S* conversions from the Moho discontinuities are indicated by downward red triangles.
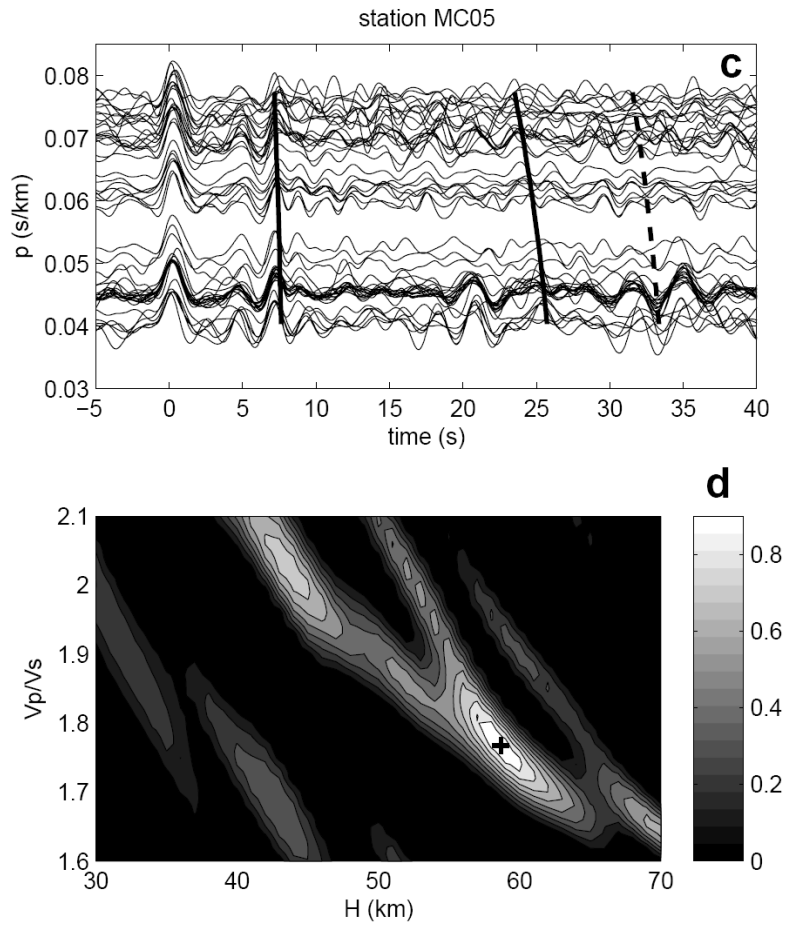
station MC22

a

b

station MC05

Figure 6. Slant-stacking results for stations MC22 and MC05. (a and c) Receiver functions ordered by ray parameter (p) for station MC22 and MC05, respectively, along with predicted travel time curves estimated from the optimum solution of H and V_P/V_S, determined by slant-stacking analysis ($V_P = 6.2$ km/s).   These curves (dashed for arrivals that are more tentative) were generated using a simple, flat-Earth, and one-layer crust model.   (b and d) Solution surfaces constructed by a direct search over V_P/V_S vs. H space. The optimum solution is indicated by a cross; contour lines are spaced at intervals of 0.1. Scale is normalized and all solutions with negative sum are shaded black.
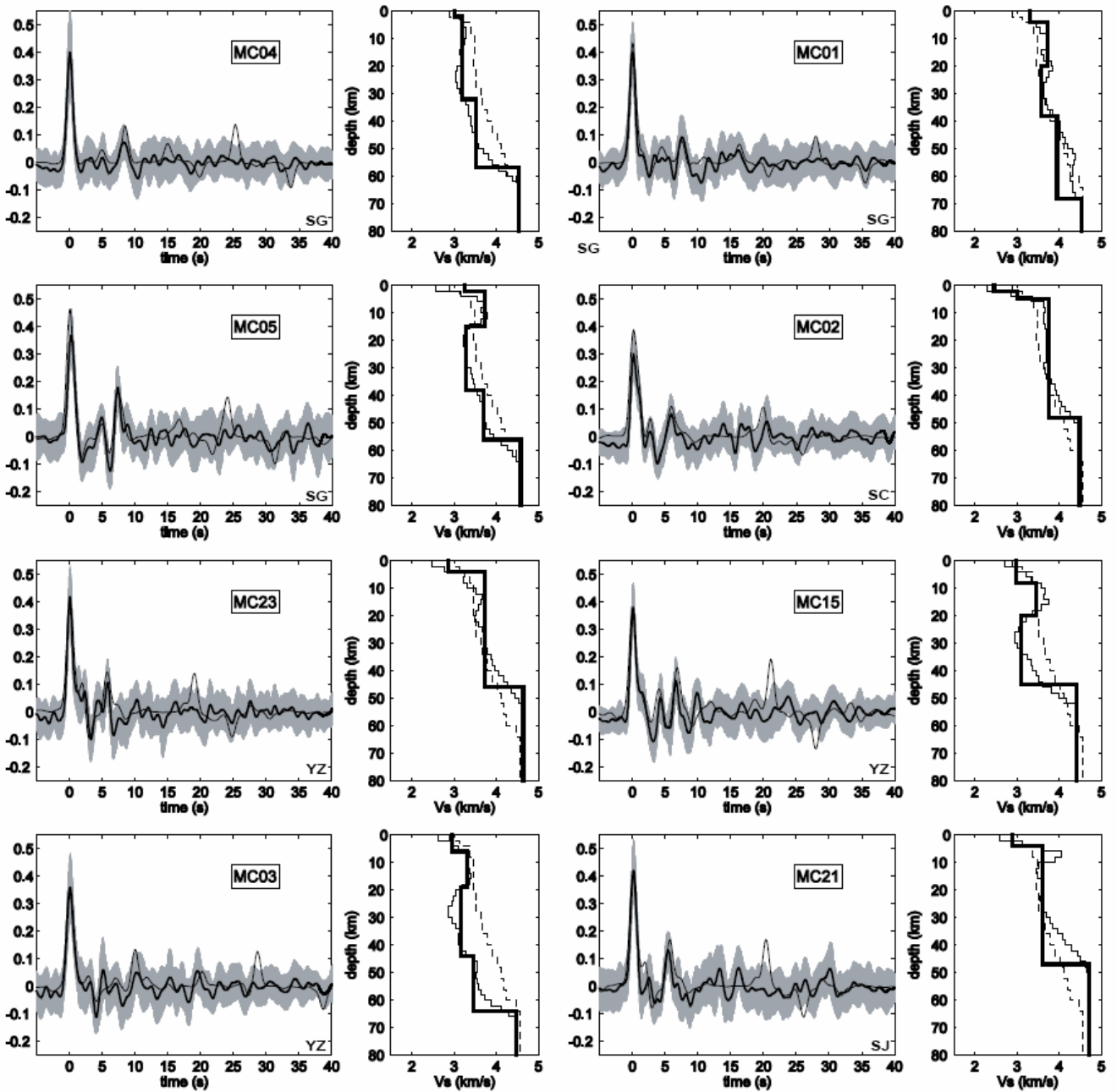
Figure 7. Least-squares inversion and grid-search (i.e., simplified modeling) results

for 8 stations. Results for each station are shown in two panels. The left panel shows

the observed receiver function (thick black lines), its standard deviation ($\pm \sigma$) bounds

(grey shading), and the synthetic receiver function corresponding to the grid-search

solution (thin black line).   The right panel shows the initial model (thin dashed lines),

the preferred solution (thin black lines) from many-layered least-squares inversion, and

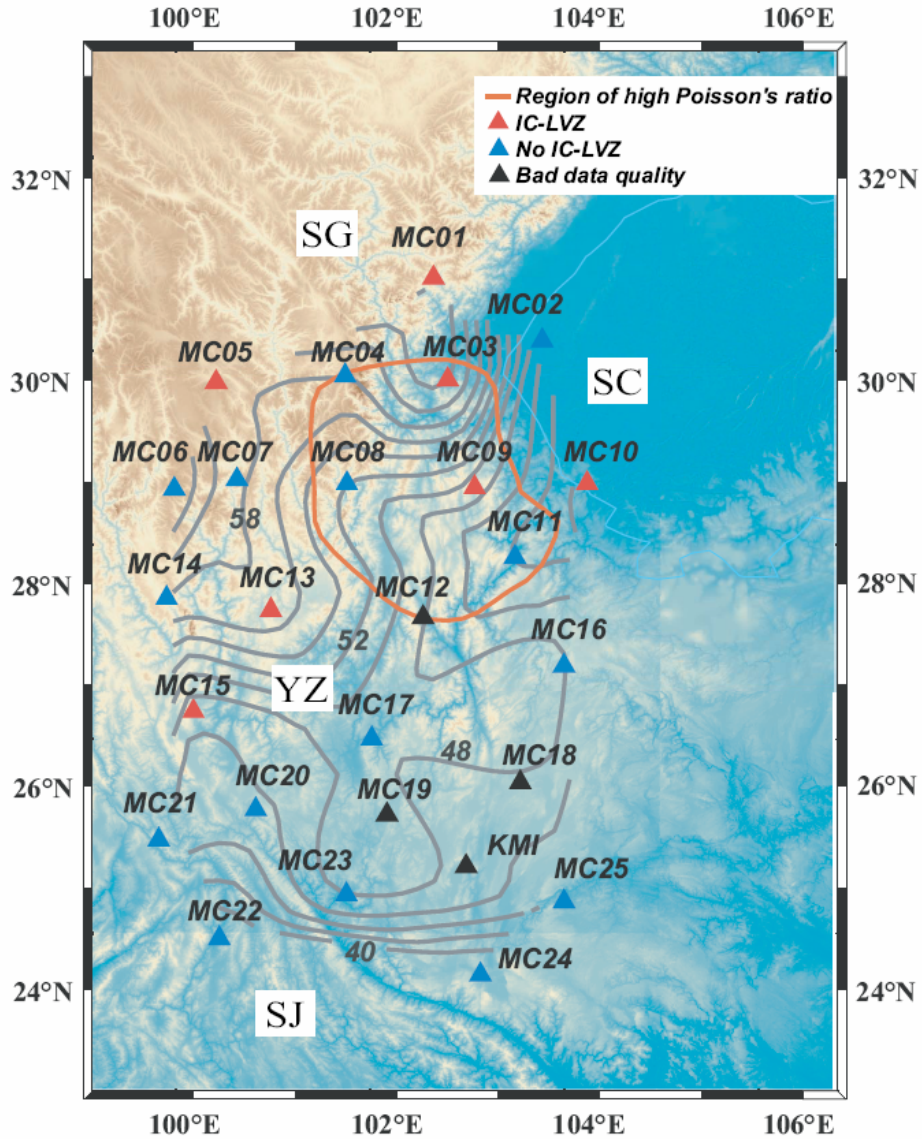the grid-search solution (thick black line).

Figure 8.   Contour map of crustal thickness (in km) from this receiver function study.

The orange line denotes the region of high Poisson's ratio (> 0.30).   The red triangles

represent stations with an obvious IC-LVZ, the blue ones represent stations without

obvious IC-LVZ, and the black ones represent stations without sufficient data quality.

The Sichuan basin is outlined by a thin blue line.   Tectonic labels are the same as in
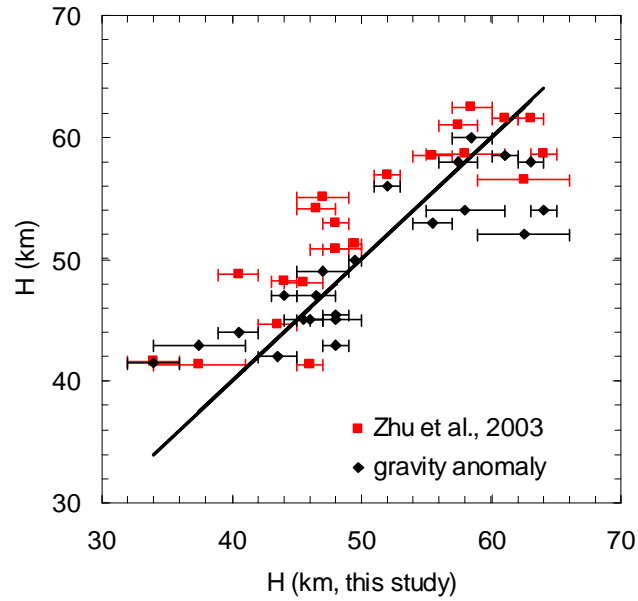
Figure 1.

Figure 9. Comparison between crustal thicknesses obtained in this study, H_{RF}, and those from previous seismic refraction, H_{SR}, and gravity anomaly and deep seismic sounding profile data, H_{GRA} (Zhu et al., 2003, personal communication; Wang et al., 2003). Correlation coefficients are 0.88 between H_{RF}-H_{SR}, and 0.86 between H_{RF}-H_{GRA}.

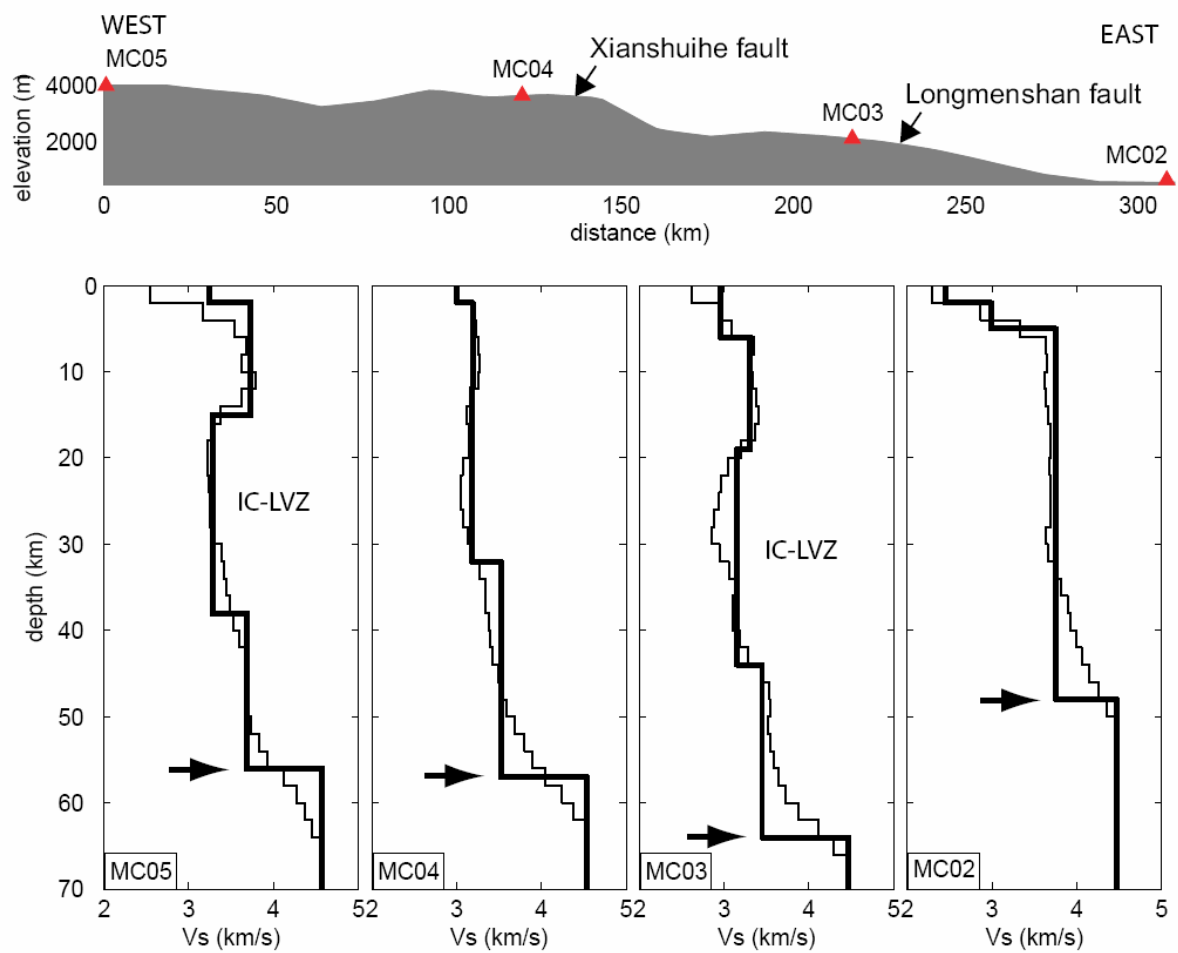Figure 10. Elevation and velocity cross-sections along Line 1 in Figure 1. Top: Topography profile and (projected) locations of the stations (red triangles) and major fault zones. Bottom: *S*-wave velocity models (IC-LVZ = Intracrustal low-velocity zone). The Moho depth (inferred from slant-stacking analysis) is indicated by black arrows.
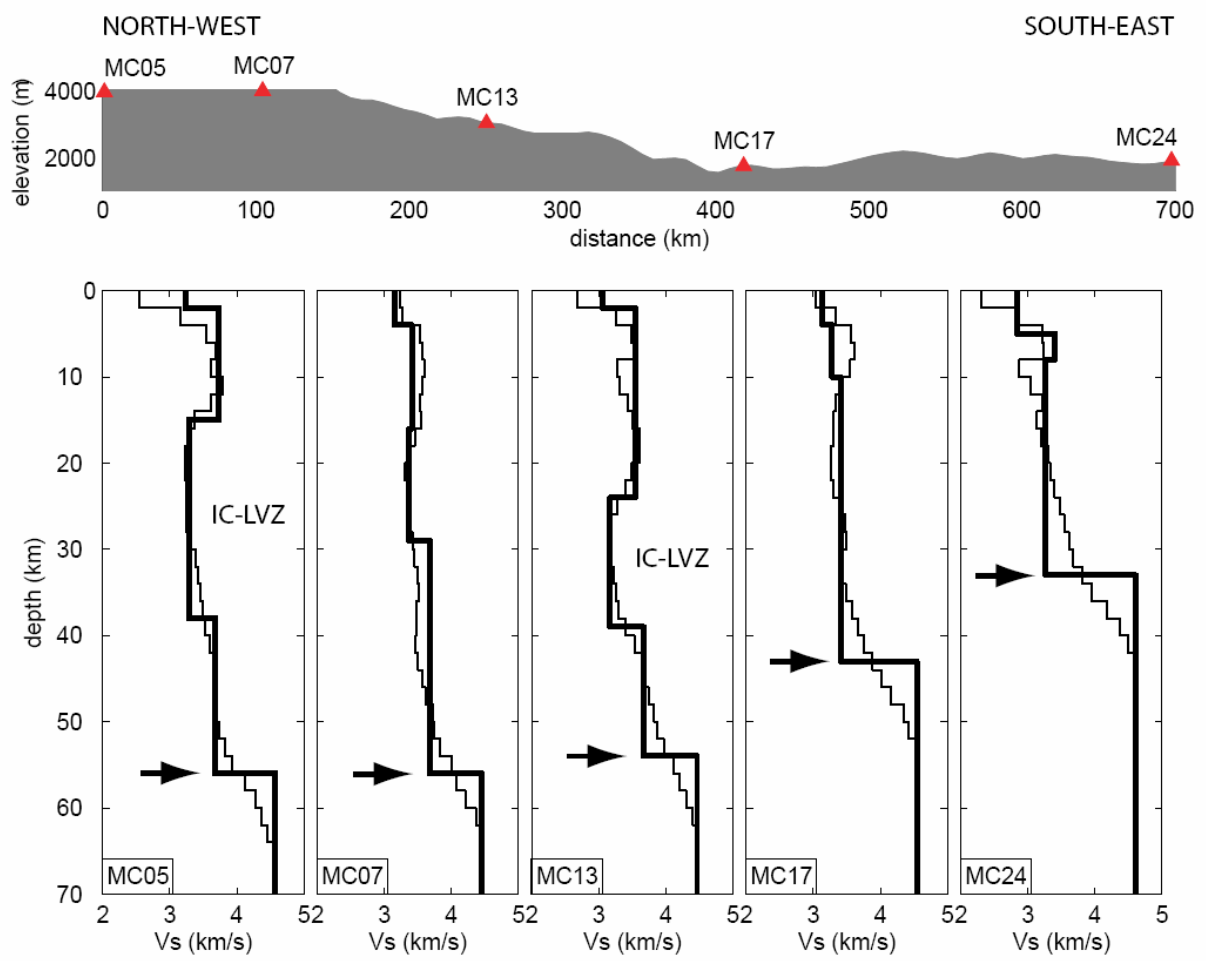
Figure 11.   Same as Figure 10 but for Line 2 in Figure 1.

Table 1. Station information and receiver function results.

Station	latitude (°N)	longitude (°E)	Number of traces	Moho depth #1 (km)[2]	V_P/V_S ratio [2]	Poisson's ratio [2]	Moho depth #2 [3]	Moho depth #3 [4]	Category[5]
MC01	31.0	102.3	70	64.0 ± 1.0	1.66 ± 0.03	0.21 ± 0.01	58.6	54	2
MC02	30.4	103.4	51	46.0 ± 1.0	1.76 ± 0.08	0.26 ± 0.03	54.2	47	1
MC03	30.0	102.5	65	62.0 ± 2.0	1.96 ± 0.05	0.32 ± 0.01	56.6	52	2
MC04	30.1	101.5	57	58.0 ± 1.0	1.90 ± 0.06	0.31 ± 0.02	61	58	2
MC05	30.0	100.2	88 (42)[1]	59.0 ± 1.0	1.76 + 0.03	0.26 ± 0.01	62.5	60	2
MC06	28.9	99.8	57 (24)[1]	64.0 ± 1.0	1.74 ± 0.03	0.25 ± 0.01	61.5	58	2
MC07	29.0	100.4	65	58.5 ± 3.5	1.76 ± 0.15	0.25 ± 0.06	61.5	58.5	2
MC08	29.0	101.5	57	52.0 ± 1.0	1.92 ± 0.05	0.31 ± 0.01	56.9	56	2
MC09	29.0	102.8	32	49.0 ± 1.0	1.93 ± 0.08	0.31 ± 0.02	51.3	50	2
MC10	29.0	103.9	54	40.5 ± 1.5	1.84 ± 0.10	0.29 ± 0.03	48.7	44	2
MC11	28.3	103.1	78 (30)[1]	44.0 ± 1.0	1.95 ± 0.07	0.32 ± 0.02	48.2	47	2
MC12	27.7	102.2	29	-	-	-	56.7	49	3
MC13	27.7	100.8	87	57.0 ± 2.0	1.80 ± 0.05	0.27 ± 0.02	58.5	53	2
MC14	27.9	99.7	69	58.0 ± 2.0	1.73 ± 0.07	0.25 ± 0.03	58.6	54	2
MC15	26.8	100.0	52	47.0 ± 2.0	1.87 ± 0.08	0.30 ± 0.02	55.1	49	2
MC16	27.2	103.6	24	48.5 ± 1.5	1.66 ± 0.07	0.21 ± 0.04	50.9	45	2
MC17	26.5	101.7	39	48.5 ± 0.5	1.79 ± 0.06	0.27 ± 0.02	53	45.5	2
MC18	26.1	103.2	24	-	-	-	52.6	44.5	3
MC19	25.7	101.9	30	-	-	-	53	43.5	3
MC20	25.8	100.6	35	45.5 ± 1.5	1.79 ± 0.08	0.27 ± 0.03	48.1	45	2
MC21	25.5	99.6	51	46.0 ± 1.0	1.70 ± 0.06	0.23 ± 0.03	41.3	45	2
MC22	24.5	100.2	29	37.5 ± 1.5	1.74 ± 0.10	0.25 ± 0.04	41.3	43	1
MC23	24.9	101.5	62	48.0 ± 1.0	1.77 ± 0.07	0.26 ± 0.03	50.9	43	2
MC24	24.2	102.8	62	37.0 ± 5.0	1.90 ± 0.18	0.30 ± 0.05	41.6	41.5	1
MC25	24.9	103.7	59	43.5 ± 1.5	1.68 ± 0.10	0.22 ± 0.05	44.6	42	2
KMI	25.1	102.7	70	-	-	-	48.4	43	3

1. Total number of traces (events) used for receiver function analysis at each station

2. Moho depth, V_P/V_S ratio, and Poisson's ratio from this receiver function study

3. Moho depth from seismic refraction profiles (Zhu et al., personal communication, 203)

4. Moho depth gravity anomaly/deep seismic sounding profile results (Wang et al., 2003)

5. Measures the reliability of the crustal properties derived from slant-stacking analysis; 1 is highest and 3 is lowest, see text for details

Conclusion

Our investigations of the plastic flow of synthetic Mg-calcites and strain heterogeneities in Carrara marble developed during laboratory deformation at temperatures from 400-600° C reveal that:

(1) Mechanical behavior of calcite rocks depends on the deformation mechanism and on their chemical composition. If Mg impurity is present, the flow strength of calcite in the dislocation creep region is increased, but the flow strength in the diffusion creep region does not change. The strengthening effect of Mg solute on the dislocation creep of calcite is due to the solute drag effect.

(2) After compression tests of Carrara Marble, both intragranular and intergranular strain distributions are highly heterogeneous with a strong influence of local microstructure on the strain distributions. High strain values are often observed at twin bands and grain boundaries, indicating these are weak areas and tend to have localized strains. Local strain heterogeneities can be a combination of the activation of multiple slip systems, grain-boundary sliding, substructure development, twinning, and grain-to-grain interactions.

(3) The basic self-consistent (VPSC) model describes global textures well, but does not always predict lattice rotation and deformation of individual grains. To predict the actual deformation of grains within polycrystalline material will require quantitative consideration of the effects of grain-boundary misorientation, local strain/stress state, grain-boundary sliding, and deviations in grain geometry.

237